

# **THE DESIGN OF MOVING MAGNET ACTUATORS FOR LARGE-RANGE FLEXURE-BASED NANOPositionING**

---

**by**

**David B. Hiemstra**

A thesis submitted in partial fulfillment of  
the requirements for the degree of Master of  
Science in Engineering (Mechanical  
Engineering) at The University of Michigan

Advisor:

Professor Shorya Awtar

© David B. Hiemstra 2014

All Rights Reserved

## ACKNOWLEDGEMENTS

Shorya, it will take me the rest of my life to learn all of what you have taught me and see all the ways you have helped me grow. Thank you.

Thank you to many people who collaborated with me during this work, including Gaurav Parmar<sup>1</sup>, Cory Welch, Yangbing Lou, Zhen Wu, Yi Chen, Yilong Wen, and Adrian Adames. Your help, discussions, insights, support, and machine shop time spent with me on this project are invaluable.

Everyone else who supported me during this adventure, especially my family, the Precision Systems Design Laboratory, and all my friends—thank you.

---

<sup>1</sup> A certain portion of this work was done in collaboration with Gaurav Parmar in the Precision Systems Design Laboratory at the University of Michigan. This portion has been published in a journal paper in IEEE/ASME Transactions on Mechatronics [83].

## TABLE OF CONTENTS

<b>ACKNOWLEDGEMENTS</b> .....	<b>iii</b>
<b>TABLE OF CONTENTS</b> .....	<b>iv</b>
<b>LIST OF FIGURES</b> .....	<b>ix</b>
<b>LIST OF TABLES</b> .....	<b>xv</b>
<b>ABSTRACT</b> .....	<b>16</b>
<b>CHAPTER 1 : Introduction and Motivation</b> .....	<b>18</b>
1.1    Lorentz-force electromagnetic actuators .....	19
1.1.1    Moving magnet actuators (MMA) .....	20
1.1.2    Voice coil actuators (VCA) .....	22
1.1.3    Characteristics of Lorentz force actuators .....	24
1.1.4    Applications .....	25
1.2    Nanopositioning .....	27
1.2.1    Large range flexure based nanopositioning .....	27
1.2.2    Research goals and impact.....	30
1.2.3    Challenges in achieving large range nanopositioning .....	32
1.3    Design specifications.....	34
1.3.1    Motion range.....	36
1.3.2    Motion quality.....	36
1.3.3    Speed.....	37
1.3.4    Temperature stability .....	43
1.3.5    Additional considerations .....	43
1.4    Thesis outline .....	44
<b>CHAPTER 2 : Actuators for Large Range Nanopositioning</b> .....	<b>46</b>
2.1    Actuator comparison based on literature survey .....	48
2.2    Actuator comparison using performance indices .....	51
2.2.1    Maximize first natural frequency .....	57
2.2.2    Maximize scanning frequency .....	60
2.2.3    Minimize rise time in point to point positioning application.....	65
2.2.4    Minimize power consumption .....	66

2.2.5	Minimize positioning resolution .....	67
2.2.6	Conclusion .....	68
2.3	Piezoelectric actuators .....	68
2.3.1	Piezoelectric stack actuators .....	70
2.3.2	Piezoelectric stacks with amplification mechanism .....	71
2.3.3	Comparison between electromagnetic and piezoelectric actuators ....	80
2.4	Piezomotors .....	84
2.4.1	Quasi-static piezomotors.....	85
2.4.2	Dynamic piezomotors .....	88
2.4.3	Ultrasonic piezomotors .....	89
2.5	Magnetostrictive actuators .....	91
2.6	Electromagnetic actuators .....	92
2.6.1	Voice coil actuators.....	94
2.6.2	Moving magnet actuators.....	99
2.6.3	Multi-phase electromagnetic actuators (linear motors) .....	103
2.6.4	Additional electromagnetic actuator types.....	104
2.7	Conclusion.....	105
<b>CHAPTER 3 : Prior art concerning moving magnet actuators .....</b>		<b>106</b>
3.1	Common MMA architectures.....	106
3.1.1	Slotting.....	107
3.1.2	Traditional MMA architecture .....	110
3.1.3	Linear motor MMA architecture.....	111
3.1.4	“Air” core MMA architecture.....	113
3.1.5	Slotted MMA (compressor architecture) .....	115
3.2	Additional MMA architectures and design ideas .....	118
3.3	Voice coil actuator designs.....	127
3.4	Coil design.....	130
<b>CHAPTER 4 : Design considerations and methodologies .....</b>		<b>134</b>
4.1	Actuator design considerations .....	134
4.1.1	Force uniformity over stroke .....	134
4.1.2	Armature reaction .....	139
4.1.3	Shorted turn.....	141
4.1.4	Wire selection .....	142
4.1.5	Magnetic saturation of circuit components.....	143
4.1.6	Magnet material .....	144
4.1.7	Radial instability .....	149

4.1.8	Thermal management.....	150
4.1.9	Actuator design considerations map.....	150
4.2	System design considerations.....	153
4.2.1	Open-loop bandwidth.....	153
4.2.2	Actuator force .....	153
4.2.3	Actuator force uniformity .....	154
4.2.4	Mechanical load on flexure bearing.....	154
4.2.5	Thermal management.....	155
4.2.6	System design considerations map .....	156
4.3	Design methodologies .....	158
4.4	Figures of merit .....	160
<b>CHAPTER 5 : Dynamic Actuator Constant .....</b>		<b>162</b>
5.1	Derivation.....	163
5.2	Impact on motion system performance .....	170
<b>CHAPTER 6 : Electromagnetic modeling of an MMA.....</b>		<b>176</b>
6.1	Model neglecting magnetic fringing .....	180
6.2	Models incorporating magnetic fringing via Rotor's method .....	183
6.2.1	Circular flux paths.....	184
6.2.2	Improved magnetic leakage estimation .....	186
6.2.3	Improved magnetic fringing estimation.....	187
<b>CHAPTER 7 : Actuator design and fabrication .....</b>		<b>192</b>
7.1	Detailed design.....	194
7.1.1	Pole piece .....	195
7.1.2	Magnet length .....	196
7.1.3	Magnet radius and coil thickness.....	197
7.1.4	Coil length.....	199
7.1.5	Wire gauge .....	200
7.1.6	Back iron.....	201
7.1.7	Coil bobbin.....	203
7.1.8	Off-axis attraction forces .....	205
7.1.9	Mover shaft .....	206
7.1.10	Summary.....	208
7.2	Practical design considerations .....	208
7.2.1	Mover.....	208
7.2.2	Back iron.....	209
7.2.3	Bobbin.....	210

7.3	Fabrication.....	211
7.3.1	Bobbin.....	211
7.3.2	Coil winding.....	212
7.3.3	Back iron.....	215
7.3.4	Magnets.....	215
<b>CHAPTER 8 : Thermal management system .....</b>		<b>216</b>
8.1	Concept selection .....	218
8.2	Detailed design .....	221
8.2.1	Latent heat sink .....	221
8.2.2	Thermal bridge.....	224
8.2.3	Thermal housing .....	225
8.2.4	TMS thermal model .....	226
8.3	Fabrication.....	231
<b>CHAPTER 9 : Double-parallelogram flexure bearing.....</b>		<b>233</b>
9.1	Detailed design .....	234
9.1.1	Material selection.....	235
9.1.2	Motion stage design .....	235
9.1.3	Beam dimensions .....	236
9.1.4	Off-axis stability .....	239
9.1.5	Bearing dynamics.....	241
9.2	Practical design considerations .....	243
9.3	Fabrication.....	244
<b>CHAPTER 10 : Experimental Results .....</b>		<b>247</b>
10.1	Experimental setup .....	248
10.2	Moving magnet actuator.....	251
10.2.1	MMA static force characteristics .....	251
10.2.2	Effect of bobbin material on dynamic response .....	252
10.3	Thermal management system.....	253
10.4	Nanopositioning .....	254
10.4.1	System characterization .....	255
10.4.2	Nanopositioning performance.....	255
<b>CHAPTER 11 : Innovations in Actuator Design .....</b>		<b>259</b>
11.1	Concentric coil ring magnet (CCRM) moving magnet actuator .....	259
11.1.1	Optimal MMA topology .....	260
11.1.2	Concentric coil radial magnet (CCRM) module.....	263
11.1.3	Single CCRM open face MMA (preferred embodiment) .....	265

11.1.4	Integrated thermal management.....	269
11.1.5	Single CCRM closed face MMA design .....	270
11.1.6	Axially spaced dual CCRM MMA designs .....	272
11.1.7	Radially spaced dual CCRM MMA designs.....	274
11.1.8	Planar topologies.....	276
11.2	Actuator integration with motion system .....	278
11.3	Coil designs .....	279
11.3.1	MMA featuring non-uniform coil windings .....	279
11.3.2	High-efficiency planar coils.....	280
11.4	Voice coil actuator concepts.....	282
11.4.1	Flexure coil leads .....	283
11.4.2	VCA for nanopositioning.....	284
<b>CHAPTER 12 : Conclusion.....</b>		<b>285</b>
<b>REFERENCES.....</b>		<b>287</b>
<b>APPENDIX A: Analytical MMA model MATLAB code.....</b>		<b>309</b>
<b>APPENDIX B: Analytical thermal model for selection of heat pipes .....</b>		<b>316</b>

## LIST OF FIGURES

Figure 1.1: Conventional MMA cross section .....	20
Figure 1.2: Opposite coil winding directions produce unidirectional force in MMA .....	21
Figure 1.3: Off-the-shelf MMAs [6] and [8] .....	22
Figure 1.4: Conventional VCA cross section and off-the-shelf product .....	23
Figure 1.5: Voice coil windings in air gap with radially oriented magnetic field experience force in axial direction .....	23
Figure 1.6: Off the shelf Voice Coil Actuator .....	24
Figure 1.7: Actuator integrated in a mechatronic motion system ([23][24][25]) .....	26
Figure 1.8: Tradeoff between range and resolution in motion systems .....	28
Figure 1.9: Envisioned research impact.....	31
Figure 1.10: Raster scanning over 10mm x 10mm sample (not to scale).....	39
Figure 1.11: Motion profile and force requirements for point to point positioning .....	42
Figure 2.1: Overview of final actuator candidates for large range nanopositioning .....	47
Figure 2.2: Normalized actuator force-stroke and stress-strain curves.....	53
Figure 2.3: Flexure based motion system with amplification mechanism.....	55
Figure 2.4: Comparison of performance index $E/\rho$ for various actuators (estimated maximum and minimum ranges shown).....	60
Figure 2.5: Specific actuation stress vs. actuation strain [93].....	62
Figure 2.6: Comparison between performance indices $E/\rho$ and $\sigma\varepsilon/\rho$ (estimate maximum and minimum ranges shown) .....	64
Figure 2.7: Piezo stack actuator [102] .....	70
Figure 2.8: Piezoelectric stack actuators with amplification a) [109] and b) [102].....	71
Figure 2.9: Piezo stack actuator model .....	72
Figure 2.10: Piezo stack actuator integrated with motion system model .....	73
Figure 2.11: Effect of flexure and amplification mechanism stiffness on piezo actuator displacement and force output .....	74
Figure 2.12: Effect of flexure and amplification mechanism stiffness on piezo actuator blocking force output .....	75
Figure 2.13: Force and displacement of piezo actuator integrated with motion amplification .....	76

Figure 2.14: First resonant frequency vs. free stroke of commercially available mechanically amplified piezo actuators.....	78
Figure 2.15: Blocking force vs. free stroke of commercially available mechanically amplified piezo actuators .....	79
Figure 2.16: First resonant frequency and actuator stroke for an MMA and PZT actuator (Model # P-025.40P).....	82
Figure 2.17: First resonant frequency and actuator stroke for an MMA and PZT actuator (Model # P-056.80P).....	84
Figure 2.18: “Walker” type piezomotor from PiezoMotor AB [114][115].....	86
Figure 2.19: Ultrasonic piezomotor [144] .....	90
Figure 2.20: (Attempt!) at categorization of electromagnetic actuators .....	93
Figure 2.21: VCA in inverted configuration eliminates moving wires and reduces heat transfer to the motion stage at cost of higher moving mass.....	97
Figure 2.22: MMA derived from VCA architecture.....	99
Figure 2.23: Advantages of traditional MMA over VCA for large range nanopositioning .....	102
Figure 3.1: Volumetric force output dependence on magnet material and actuator dimensions (inner actuator diameter, $D$ , and outer diameter $D_o$ ) for slotted vs. non slotted MMA architectures [193] .....	108
Figure 3.2: Conventional MMA cross section.....	110
Figure 3.3: Stacked MMA architecture .....	112
Figure 3.4: Flux focusing MMA [197] .....	113
Figure 3.5: Air core” MMA allows both axial and radial motion .....	114
Figure 3.6: Two axis MMA with maglev force and axial motion [177][56][178] .....	115
Figure 3.7: Two axis MMA with maglev force and axial motion [57].....	115
Figure 3.8: Slotted MMA for compressor applications showing force direction for positive coil current.....	116
Figure 3.9: Highly variable force over stroke plot of typical slotted MMA [199] (top) [200] (bottom).....	118
Figure 3.10: Reduction of cogging force via ferromagnetic end plates [50] .....	119
Figure 3.11: MMA with fixed magnets at axial ends to increase spring force and system resonant frequency [156] .....	120
Figure 3.12: Active end coils [217] .....	121
Figure 3.13: Basic Halbach array.....	122
Figure 3.14: Inversed MMA [218].....	123
Figure 3.15: Stacked inverted MMA .....	124
Figure 3.16: Radial magnet configuration [219].....	125
Figure 3.17: Radial and axial magnet [221].....	126

Figure 3.18: Moving magnet provides simultaneous preload for air bearing and actuation force [55].....	126
Figure 3.19: Single Coil MMA designs.....	127
Figure 3.20: Interleaved circuit designs.....	128
Figure 3.21: Active end coil to reduce inner core saturation of VCA [224] .....	128
Figure 3.22: Flux focusing VCA design [16] .....	129
Figure 3.23: VCA with concentric coils [225]’ .....	130
Figure 3.24: Effects of wire composition on air gap permeability and coil resistance [228] .....	131
Figure 3.25: Graduated coil windings [230].....	132
Figure 3.26: a) Bitter plate coils at the U.S. National High Magnetic Field Laboratory and b) Bitter coil patent [231].....	133
Figure 4.1: Reduction in force and end of stroke due to fringing.....	136
Figure 4.2: Reluctance cogging force of MMA.....	137
Figure 4.3: Typical MMA force over stroke profile .....	138
Figure 4.4: Force over stroke profile for scanning scenario .....	139
Figure 4.5: Armature reaction.....	141
Figure 4.6: “Development of permanent magnet material” [174] .....	145
Figure 4.7: Representative magnetic hysteresis curve.....	146
Figure 4.8: Demagnetization curve.....	147
Figure 4.9: Temperature dependence of demagnetization curve .....	149
Figure 4.10: Actuator-level trade-offs in Lorentz force equation.....	152
Figure 4.11: Cantilevered mover mass and off-axis attractive forces increase loads on bearing.....	155
Figure 4.12: Actuator and system level trade-offs.....	158
Figure 5.1: MMA simplified lumped parameter model.....	164
Figure 5.2: Effect of geometric scaling on MMA performance [83].....	169
Figure 5.3: Dynamic actuator constant (slope) for off-the-shelf MMAs.....	173
Figure 5.4: Dynamic actuator constant vs. stroke for off-the-shelf MMAs.....	173
Figure 6.1: Flux lines in MMA and line evaluated for magnetic flux density calculations in various models .....	177
Figure 6.2: Actual flux paths compared to closed form model assumption .....	180
Figure 6.3: Magnetic flux density, B, in the air gap for various analytical models.....	182
Figure 6.4: Validation of closed form model using non-permeable regions .....	183
Figure 6.5: Improved closed form model using circular fringing paths .....	184
Figure 6.6: Magnetic flux density along evaluation line for lumped parameter model with circular geometries.....	186

Figure 6.7: Closed form model using parallelogram reluctance region between coils...	187
Figure 6.8: Method of investigating the dependency of magnetic flux fringing on air gap size ( $t_g$ ) .....	188
Figure 6.9: Magnetic flux fringing distance dependence on air gap thickness.....	189
Figure 6.10: Analytical model incorporating flux fringing dependence on air gap thickness, $t_g$ .....	189
Figure 6.11: Results of improved closed form model showing air gap flux density, $B$ , along evaluation line for various geometries. Nominal MMA dimensions are in c).....	191
Figure 7.1: CAD rendition of MMA.....	192
Figure 7.2: Fabricated MMA prototype.....	193
Figure 7.3: MMA topology.....	194
Figure 7.4: Effect of pole piece on the dynamic actuator constant.....	196
Figure 7.5: Magnet length and coil separation requirements.....	197
Figure 7.6: Variation in dynamic actuator constant ( $\beta$ ) with varying coil thickness and magnet radius .....	198
Figure 7.7: N52 NdFeB grade ring magnet [260] from K&J Magnetics, Inc.....	199
Figure 7.8: Percentage drop in force constant ( $K_f$ ) at the ends of the stroke and dynamic actuator constant ( $\beta$ ) vs. coil length ( $l_c$ ) .....	200
Figure 7.9: Maximum continuous current and voltage requirement vs. wire diameter ..	201
Figure 7.10: Mover force vs. stroke for $i = 0A$ and $i = 1A$ coil current .....	202
Figure 7.11: Flux Density in the MMA .....	202
Figure 7.12: Bobbin design considerations.....	204
Figure 7.13: Magnet in a) nominal position and b) misaligned by 0.5mm in radial direction .....	206
Figure 7.14: Pultruded carbon fiber shafts from Goodwin.com .....	208
Figure 7.15: Shaft collars constrain magnets to carbon fiber shaft.....	209
Figure 7.16: Back iron split in two “clam shells” for simplified assembly with bobbin	210
Figure 7.17: Bobbin details.....	211
Figure 7.18: a) coil winding initial setup b) start of first coil and c) hand-guided layer-winding .....	213
Figure 7.19: Wound bobbin wrapped with electrical tape .....	214
Figure 8.1: CAD rendition of thermal management system .....	217
Figure 8.2: Fabricated TMS prototype.....	218
Figure 8.3: Primary heat transport paths between MMA and motion stage .....	219
Figure 8.4: TMS functionality diagram with main system components.....	221
Figure 8.5: Latent heat sink .....	222
Figure 8.6: Heat sink insulated walls .....	223

Figure 8.7: Heat pipe working principle .....	225
Figure 8.8: Thermal housing.....	226
Figure 8.9: System thermal resistance network .....	227
Figure 8.10: Thermal resistance of the MMA and housing .....	228
Figure 8.11: Thermal model of the heat sink .....	230
Figure 8.12: Predicted coil temperature versus number of heat pipes .....	231
Figure 8.13: Fabricated thermal management system (ice packs not shown) .....	232
Figure 9.1: Flexure bearing and MMA assembly in CAD.....	233
Figure 9.2: Fabricated flexure bearing.....	234
Figure 9.3: Flexure bearing with MMA mover and encoder assembly .....	234
Figure 9.4: a) CAD cross section and b) fabricated motion stage .....	236
Figure 9.5: Double parallelogram flexure bearing topology and dimensions .....	237
Figure 9.6: Bearing mesh and loading conditions for FEA a) and stress analysis b) .....	240
Figure 9.7: Stiffness comparison of actuator and bearing showing off-axis stability ....	241
Figure 9.8: First four natural frequency modes of mover integrated with flexure bearing at a) 22.4Hz b), 82Hz c), 86.3Hz, and d) 152.8Hz .....	243
Figure 9.9: Removable flexure bearing back plate .....	244
Figure 9.10: Bearing and mover assembly (top) and removable MMA attachment plate (bottom).....	246
Figure 10.1: Detailed CAD of motion system assembly .....	249
Figure 10.2: Single-axis nanopositioning system prototype.....	250
Figure 10.3: Setup for MMA force measurement.....	251
Figure 10.4: (a) Measured force constant (b) Measured force-stroke non-uniformity ...	252
Figure 10.5: Temperature rise of the coil bobbin and the motion stage with (- -) and without (—) the thermal management system .....	253
Figure 10.6: Effect of TMS on optical encoder scale temperature .....	254
Figure 10.7: Open-loop frequency response .....	255
Figure 10.8: Feedback architecture.....	256
Figure 10.9: Closed-loop frequency response .....	257
Figure 10.10: Motion stage response to 2.5mm and 20nm step commands .....	258
Figure 11.1: Optimal MMA magnetic circuit arrangement with ideal assumptions .....	260
Figure 11.2: Cylindrical version of optimal circuit arrangement .....	263
Figure 11.3: Radial magnet concentric coil MMA building block.....	264
Figure 11.4: MMA featuring radial magnet and concentric coil windings cross-section (left) and CAD rendition (right).....	266
Figure 11.5: CAD model of envisioned MMA.....	268
Figure 11.6: Triple coil embodiment .....	269

Figure 11.7: Single CCRM MMA with integrated thermal management .....	270
Figure 11.8: Single CCRM MMA with integrated diaphragm flexure bearing and thermal management system .....	270
Figure 11.9: Single CCRM closed face MMA design .....	271
Figure 11.10: Ironless axially spaced dual CCRM MMA .....	272
Figure 11.11: Axially spaced dual CCRM MMA with center core and back iron .....	273
Figure 11.12: Axially spaced dual CCRM closed face MMA design .....	274
Figure 11.13: Radially spaced dual CCRM open face MMA.....	275
Figure 11.14: Radially spaced dual CCRM semi-closed-face MMA.....	276
Figure 11.15: Single-Axis Planer MMA.....	277
Figure 11.16: Dual axis planar MMA.....	278
Figure 11.17: Integrated actuator and motion bearing configurations.....	279
Figure 11.18: Non-uniform coil increase force uniformity over stroke profile.....	280
Figure 11.19: Planar voice coil in hard drive read head mechanism [278] .....	281
Figure 11.20: Planar coil winding pattern (a) and layout (b).....	282
Figure 11.21: Flexure beam voice coil electrical wire leads .....	283
Figure 11.22: Flexure beams for motion guidance, power supply, and heat transfer.....	284

## LIST OF TABLES

Table 1.1: General characteristics of Lorentz force actuators .....	25
Table 1.2: Motion range and resolution of several commercially available desktop size motion systems.....	29
Table 1.3: Nanopositioning system and component level performance requirements .....	35
Table 1.4: Speed and scanning time requirements for various scanning frequencies at 10mm travel .....	40
Table 1.5: Force requirements for various scanning frequencies at 10mm travel .....	41
Table 2.1: General advantages and disadvantages of final actuator candidates for large range nanopositioning.....	48
Table 2.2: Potential actuators for large range nanopositioning based on literature survey .....	51
Table 2.3: Actuator and system values assuming PZT actuator model # P-025.40P .....	81
Table 2.4: Actuator and system values assuming PZT actuator model # P-056.80P .....	83
Table 2.5: General speed and resolution of piezomotors.....	85
Table 2.6: Speed and resolution of various quasi-static piezomotors. Note that these values cannot be simultaneously achieved. ....	87
Table 2.7: Speed and resolution of various dynamic piezomotors. Note that these values cannot be simultaneously achieved.....	89
Table 2.8: Ultrasonic piezomotor survey.....	91
Table 3.1: General trade-offs of slotted, non-slotted, and coreless MMA architectures	108
Table 5.1: MMA performance specifications from various vendors .....	174
Table 5.2: MMA manufacturers and model numbers.....	175
Table 7.1: MMA final design specifications.....	193
Table 7.2: Selected MMA dimensions.....	195
Table 8.1: Working time per ice pack.....	222
Table 9.1: Bearing specifications.....	237
Table 10.1: Motion system experimental results .....	248

## ABSTRACT

Moving magnet actuators (MMA) are direct-drive, single-phase electromagnetic linear actuators that provide frictionless and backlash-free motion over a range of several millimeters. This work investigates the use of MMAs to simultaneously achieve large range, high speed, and high motion quality in flexure-based nan positioning systems. This work impacts technologies such as scanning probe microscopy and lithography, industrial semiconductor wafer quality control processes, and other applications which rely on nan positioning systems to provide controlled motion with nanoscale precision, resolution and accuracy. Various actuator types are compared to meet system-level requirements and the MMA is chosen as a promising potential candidate. Component and system level design challenges and associated tradeoffs in designing the MMA to meet nan positioning performance are discussed and derived in this thesis. In particular, it is shown that even as the overall size of an MMA is varied, the actuation force remains directly proportional to the square root of the actuator's moving magnet mass and the square root of power consumed. This proportionality constant, identified as the *dynamic actuator constant*, serves as a novel and important figure of merit for MMAs. It describes fundamental performance limits for MMAs and enables the determination of an optimized MMA geometry in a simplified manner. When an MMA is employed in a flexure-based nan positioning system, this constant directly impacts the system-level positioning performance in terms of range, resolution, speed, and temperature control. This highlights the significance of incorporating a thermal management system for heat

dissipation, minimizing noise and harmonic distortion in the current driver, choosing a low ground vibration setting, and improving the force-stroke uniformity of the actuator.

Based on this understanding, a single-axis nanopositioning system that simultaneously achieves 10mm range, 4nm resolution, open-loop natural frequency of 25Hz, and temperature rise of less than 0.5°C, is designed, fabricated, and tested. The significance of the dynamic actuator constant is experimentally validated. A novel thermal management system is tested to successfully mitigate heat dissipation. Preliminary controller design and closed-loop operation highlight the potential of MMAs in large range, high speed nanopositioning. These results point to the importance of achieving greater values of the dynamic actuator constant while maintaining low force–stroke non-uniformity. This motivates the development of actuators with a higher dynamic actuator constant. A novel MMA architecture and other MMA and VCA innovations are presented to achieve a significantly higher dynamic actuator constant and improve motion system performance.

## CHAPTER 1: Introduction and Motivation

Moving magnet actuators (MMAs) are direct-drive, single-phase linear electromagnetic actuators of the Lorentz force type which provide frictionless and backlash-free motion over a range of several millimeters. This work aims to investigate, quantify, and overcome limitations of moving magnet actuators to achieve large range and high speed positioning with nanometric resolution, precision, and accuracy (referred to as nanometric *motion quality*). This is of particular relevance in achieving large range nanopositioning performance in flexure based nanopositioning systems. This work also applies to electromagnetic actuator design for high precision flexure-based motion systems and electromagnetic actuator design in general.

In this chapter, a brief overview of single-phase Lorentz force type actuators is first presented, including their operation and conventional applications. Next, nanopositioning systems and the need for larger motion range capabilities and resulting required actuation technology are discussed. Nanopositioning system-level and actuator-level design specifications used in this work follow. Finally, an overview of the presented work in this thesis, the envisioned impact (see Figure 1.9), and the focus of each chapter is described.

It is assumed that the reader is proficient in the fundamentals of electromagnetism and electrodynamics. For a well presented undergraduate reference see [1] and for electromagnetic actuator design see [2]. Additional good design references are [3][4].

## 1.1 Lorenz-force electromagnetic actuators

An actuator provides a mechanical action in response to an electrical input. More specifically, an actuator is an “energy converter which transforms energy from an external source into mechanical energy in a controllable way” [5]. One type of actuator, the Lorenz force actuator, utilizes the interaction between a current-carrying coil and permanent magnet to generate force and subsequent displacement. A moving magnet actuator (MMA) and the closely related voice coil actuator (VCA) are common Lorenz force actuators. This section gives a general overview of these actuators and highlights their potential in achieving the nanopositioning requirements discussed in Section 1.3. Both types of actuators are generally characterized by high accelerations and speeds, good motion quality, light weight, and linear force response in regard to input current and stroke. The moving coil in a VCA and moving magnet in an MMA give rise to the general differentiators between them, namely VCAs are cogging- and hysteresis-free, and MMAs have good thermal attributes and true frictionless motion.

Despite the above-listed desirable qualities of electromagnetic actuators, similar or comparatively good qualities may be found in other types of actuators as well. Indeed, it is challenging to quantitatively compare and fairly declare a “winner” between actuator types. One goal of this work is to better quantify such attributes, and provide a systematic and quantitative comparison between actuator types (see Chapter 2). The actuator comparison shows MMAs to be a very good candidate for achieving large range nanopositioning and is therefore the focus of this work.

### 1.1.1 Moving magnet actuators (MMA)

An MMA of the traditional single phase, slot-less architecture is shown in Figure 1.1. An axially-magnetized cylindrical permanent magnet sandwiched between two iron pole-pieces forms the mover. The stator consists of a back iron along with two oppositely wound coils on a bobbin connected in series. The interaction between magnetic flux from the permanent magnet and current in the coils produces an output force in the motion axis axial direction.

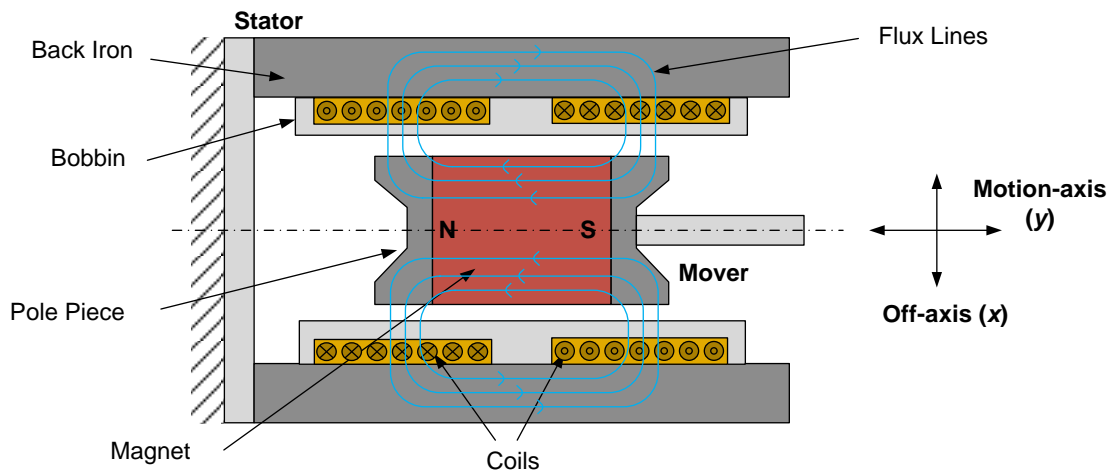


*Figure 1.1: Conventional MMA cross section*

This MMA is single phase, meaning that there is no switching circuitry between coils. An MMA is fundamentally a single phase actuator; however they are often “stacked” axially in series using multiple phase coil windings for greater travel range, as will be discussed further in Chapter 2. This architecture is slot-less, meaning that the coils are not recessed in the back iron. Slotted designs minimize the magnetic air gap and increase force at the expense of additional cogging forces. Cogging forces, which are generally detrimental to positioning performance (see section 4.1.1), are reluctance forces

acting between the mover and other magnetically permeable materials in the actuator. This causes an additional force to the Lorentz force which acts over the actuator stroke. Slotted MMA designs are further discussed in sections 2.6.2 and 3.1.5. MMAs are generally direct-drive actuators, meaning that they do not require a transmission.

The Lorentz force,  $F$  [N], is described by  $F = il \times B$ , where  $i$  is the current in the coil [A],  $l$  is the length of the wire [m], and  $B$  is the magnetic field density [T] in which the wire resides (in this case, the air gap). The resulting force is therefore proportional to current magnitude. The conventional MMA can be simplified as illustrated in Figure 1.2, where an axially-magnetized magnet is positioned between two loops of wire with current flowing in opposite directions. Magnetic flux loops leave and enter the north and south poles of the magnet. Where a magnetic flux intersects the current in the wire loop, a Lorentz force is produced on the wire and magnet the axial (i.e. motion axis) direction.

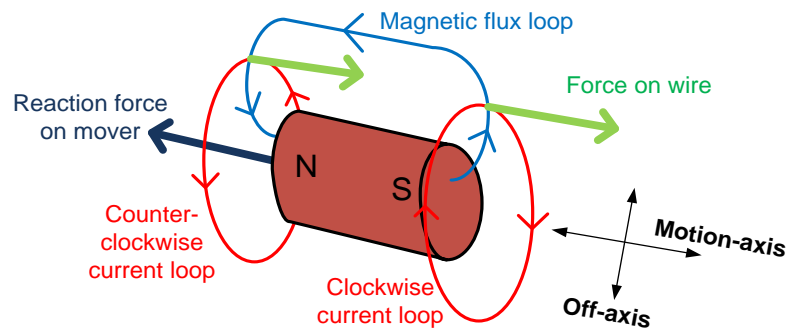


*Figure 1.2: Opposite coil winding directions produce unidirectional force in MMA*

An example of an off-the-shelf MMA [6] is shown in Figure 1.3a. The coils are wrapped on a plastic bobbin fit concentrically inside the back iron. Note that the mover is sticking to the back iron—this off-axis (radial) attraction between the back iron and mover must be counteracted by a bearing [7]. For example, an MMA from H2W

Technologies [8] integrated with a diaphragm flexure bearing is shown in Figure 1.3b. This holds the mover concentric with the back iron.

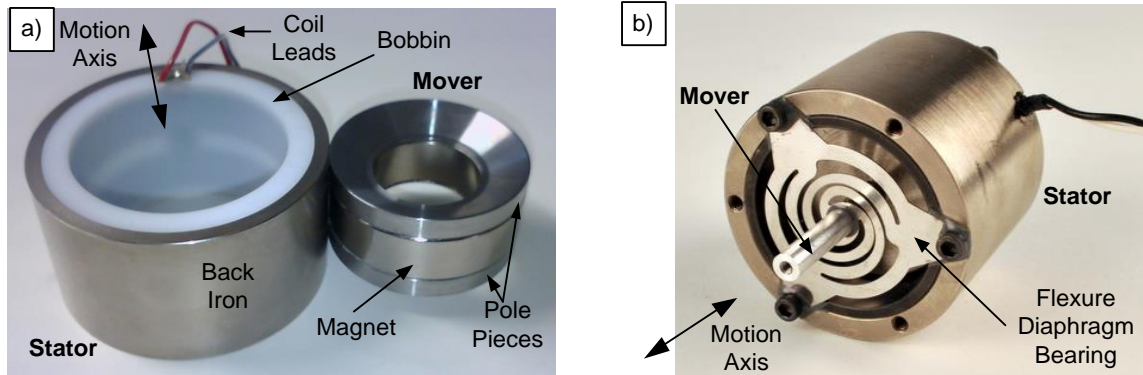
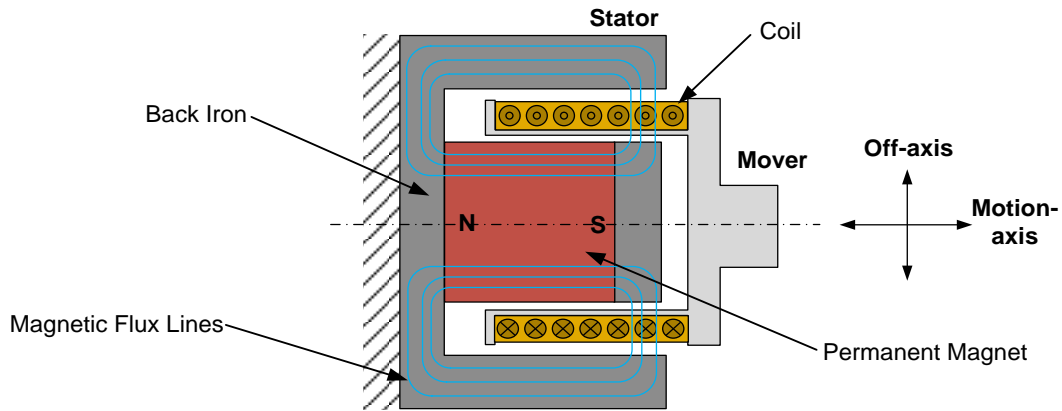


Figure 1.3: Off-the-shelf MMAs [6] and [8]

### 1.1.2 Voice coil actuators (VCA)

The voice coil actuator (VCA) is closely related to the MMA, distinguished by a stationary magnet and moving coil. A cross-section of a typical VCA is shown in Figure 1.4. An axially-magnetized cylindrical permanent magnet and integrated tubular back iron form the stator, and a coil wound on a bobbin forms the mover.



*Figure 1.4: Conventional VCA cross section and off-the-shelf product*

As expected, the Lorentz force on the voice coil (Figure 1.5) is similar to that of the MMA, however with only one set of coil windings. In this case, the coils form the mover and a stationary permanent magnet (not shown) provides the air gap magnetic flux.

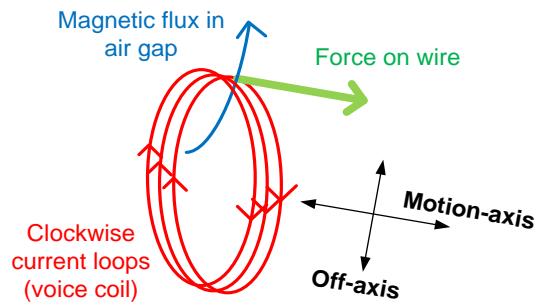


*Figure 1.5: Voice coil windings in air gap with radially oriented magnetic field experience force in axial direction*

An example of an off-the-shelf VCA from BEI Kimco (Figure 1.6) shows a steel back iron and copper coil wound on an aluminum bobbin.



*Figure 1.6: Off the shelf Voice Coil Actuator*

### 1.1.3 Characteristics of Lorentz force actuators

Lorentz force actuators have several key attributes which are summarized in Table 1.1. For example, VCAs can achieve very high acceleration and speed with high precision and accuracy over a several millimeter range [9][10][11][12]. This also holds true for MMAs. VCAs are cogging-free, have low variation of coil force over stroke when there is current applied, are hysteresis-free, and have a linear force with respect to current [13][14][15][16]. These attributes make them well-suited for feedback control which plays an important role in achieving high precision motion. MMAs also have these attributes, although MMAs generally exhibit some cogging forces and off-axis bearing loads due to the attractive forces between the magnet and field assembly (i.e. back iron) as described further in section 4.1.1 [7][17]. They also have potentially greater eddy current and hysteresis losses than VCAs due to the changing magnetic field while the mover is in motion. However, in return, MMAs have several additional advantages. MMAs have superior heat rejection as compared to VCAs due to the mechanically connected coil and outer housing assembly, as well as no disturbance-inducing and fatiguing moving coil leads [18][19][20][21]. Also, the configuration of an MMA allows placement of coil outside the working gas space in compressors which reduces outgassing

and gas contamination [20][22]. These characteristics, as explained in more detail in Chapter 2, make them good candidates for achieving the desired specifications required for large range nanopositioning outlined in section 1.3.

*Table 1.1: General characteristics of Lorentz force actuators*

<b>VCA</b>	<b>MMA</b>
High acceleration and speed	
High precision, resolution and accuracy (due to contactless and friction-free motion)	
Several millimeter travel range	
Linear current-force response	
Low variation of force over stroke	
Cogging-free	No moving leads
Hysteresis-free	Good heat rejection
Light weight	
Low cost	

#### 1.1.4 Applications

Lorentz force actuators are used in a wide variety of applications and are often integrated in mechatronic motion systems. Mechatronic motion systems comprise an actuator and bearing along with a sensor, driver, and control logic and hardware to produce controlled motion [5]. Feedback control is often implemented in applications demanding higher levels of precision. The interdependence of the actuator and mechatronic system components is illustrated in Figure 1.7.

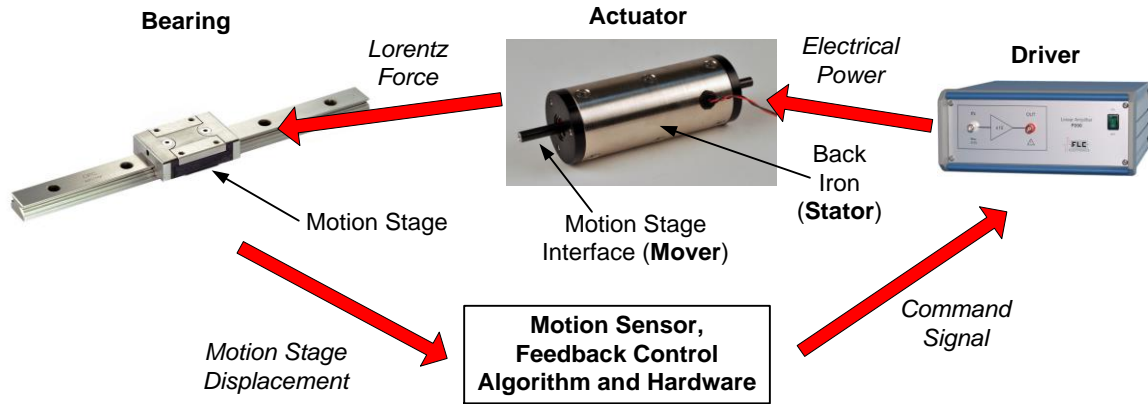


Figure 1.7: Actuator integrated in a mechatronic motion system ([23][24][25])

VCA, which are named after their traditional use as audio speaker cone drivers, are still widely used for this application [26][27][28]. Further application examples include automotive valves and transmissions [29][30][31], thermo-acoustic refrigerators [32], cryo-coolers [33], haptic feedback devices [34][35], and vibration generators [36]. Some higher precision applications include hard drive read head actuation [37][38][39], high precision positioning stages [40][41][12][42], medical devices [43] and optics [44][45][46].

MMA are widely used as well, albeit in more niche applications where lack of moving wire leads, heat rejection capability or coil protection is important. Some examples include robotic applications, vibration generators, actuator human interface devices [47], air-compressors, fluid pumps and Stirling cryo-coolers [48][49], engine valves [50], artificial heart pump drives [51], haptic feedback [52], and wave energy capture devices [53]. A few especially high precision applications include robotic applications [47], precision stages [54][55], [56][57] and micro robots [58].

## 1.2 Nanopositioning

A nanopositioning system is a mechatronic motion system capable of producing nanometric *motion quality*, which is defined here as nanometric (<10nm) precision (repeatability of motion), accuracy (lack of error in motion), and resolution (minimum incremental motion) [59][60][61]. As with most mechatronic motion systems, a nanopositioning system generally comprises a bearing for motion guidance, actuator(s), sensor(s), driver(s), and control logic and hardware. Closed-loop operation is necessary to achieve nanometric motion quality over the desired frequency range [60].

Due to their nanometric motion quality, nanopositioning systems are employed in various sensitive techniques to provide relative scanning motion between a probe or microscope head and substrate. These include scanning probe microscopy [62], scanning probe lithography [63], nanometrology [64], and hard-drive and semiconductor inspection and metrology [65]. Several applications of these techniques is provided in [66]. These technologies have played a critical role in the growth in nanotechnology and electronics over the past few decades by enabling visualization, manipulation, fabrication and measurement of matter on the nanoscale [60]. The motion quality of the nanopositioning system often directly determines the resolution and registration (i.e. how well a desired pattern can be reproduced), and therefore directly affects the quality, functionality, and product yield of the specific metrology, inspection, or lithography applications..

### 1.2.1 Large range flexure based nanopositioning

One significant limitation of existing off-the-shelf desktop size nanopositioning systems is their relatively small motion range [67]. This is readily apparent in Figure 1.8,

showing the range vs. motion quality of a representative selection of commercially available motion systems. The nanopositioning systems plotted are listed in Table 1.2. While existing nanopositioning systems are capable of nanometric (<5nm) motion quality, their motion range is limited to a few hundred microns per axis [68]–[71]. On the other hand, traditional motion systems (usually based on rolling element bearings) can provide large range (~1 to 100mm), but are limited to a motion quality of ~100nm due to friction and backlash in system components [62], [72]–[77].

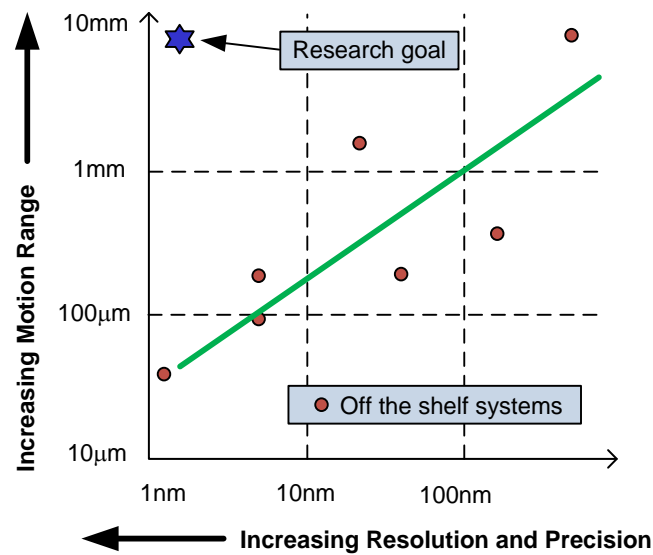


Figure 1.8: Tradeoff between range and resolution in motion systems

*Table 1.2: Motion range and resolution of several commercially available desktop size motion systems*

<b>Product</b>	<b>Range [<math>\mu\text{m}</math> x <math>\mu\text{m}</math>]</b>	<b>Resolution [nm]</b>	<b>Precision [nm]</b>
PhysikInstrumente, P-542.2 [68]	200 x 200	0.7	5
PhysikInstrumente, P-629.2 [69]	1800 x 1800	3.5	28
Queensgate, NPS-XY-100A [70]	100 x 100	0.5	5
Mad City Labs, NanoBio200 [71]	200 x 200	0.4	N/A
Piezosystem Jena, Nano PXY200 [78]	200 x 200	4	45
nPoint, NPXY400A [76]	400 x 400	1.5	200
Asylum Research, Cypher	40 x 40	1.0	N/A
Discovery Tech., NTS10 [77]	10000 x 10000	50	500

Overcoming the limited motion range of nanopositioning systems could significantly increase the achievable area-coverage in scanning nanometrology and direct-write nanomanufacturing, potentially leading to large-scale industrial applications of these techniques. For example, while novel engineered nano-materials have been fabricated in research labs as small (typically between 10-100 $\mu\text{m}$ ) proof-of-concept demonstration units, scaling up their size and production for practical use by consumers remains a manufacturing challenge [79]. Size and throughput limitation is a direct consequence of the small patterning field of current nanopositioning systems. Attempts to increase the field of patterning via a step and repeat process [67][80][81] compromises the patterning speed and also results in registration errors (also known as stitching error) between the steps. Low patterning speed limits the process throughput and registration error which is highly detrimental to the functionality of these nano-patterned devices as they require nanometric feature registration over their entire patterning field.

Furthermore, large range, high speed, flexure based nan positioning systems could enable the use of scanning probe techniques in practical industrial settings, such as in-line inspection, and metrology and process control in semiconductor [64][79], LCD flat-panel [79], and hard drive [82] manufacturing industries.

### 1.2.2 Research goals and impact

Achieving large range flexure based nan positioning forms a broad research goal and overall motivation for this work. To meet this overall goal, the goal and focus of this thesis is to investigate actuation technology, specifically the feasibility of using moving magnet actuators, to enable large range nan positioning performance which then impacts several potential applications. The envisioned impact of this research is summarized in Figure 1.9. In this work, the traditional MMA architecture is explored and a novel design promising significantly higher performance is introduced. In future work, the MMA is to be integrated with novel large range XY nan positioning systems [59] to demonstrate large range, high speed nan positioning performance. The systems are then incorporated into various metrology instruments and industrial equipment. These tools will offer significant improvements in nanomanufacturing, imaging, and metrology capabilities, enabling advances in semiconductor, hard drive, and materials manufacturing, and basic research.

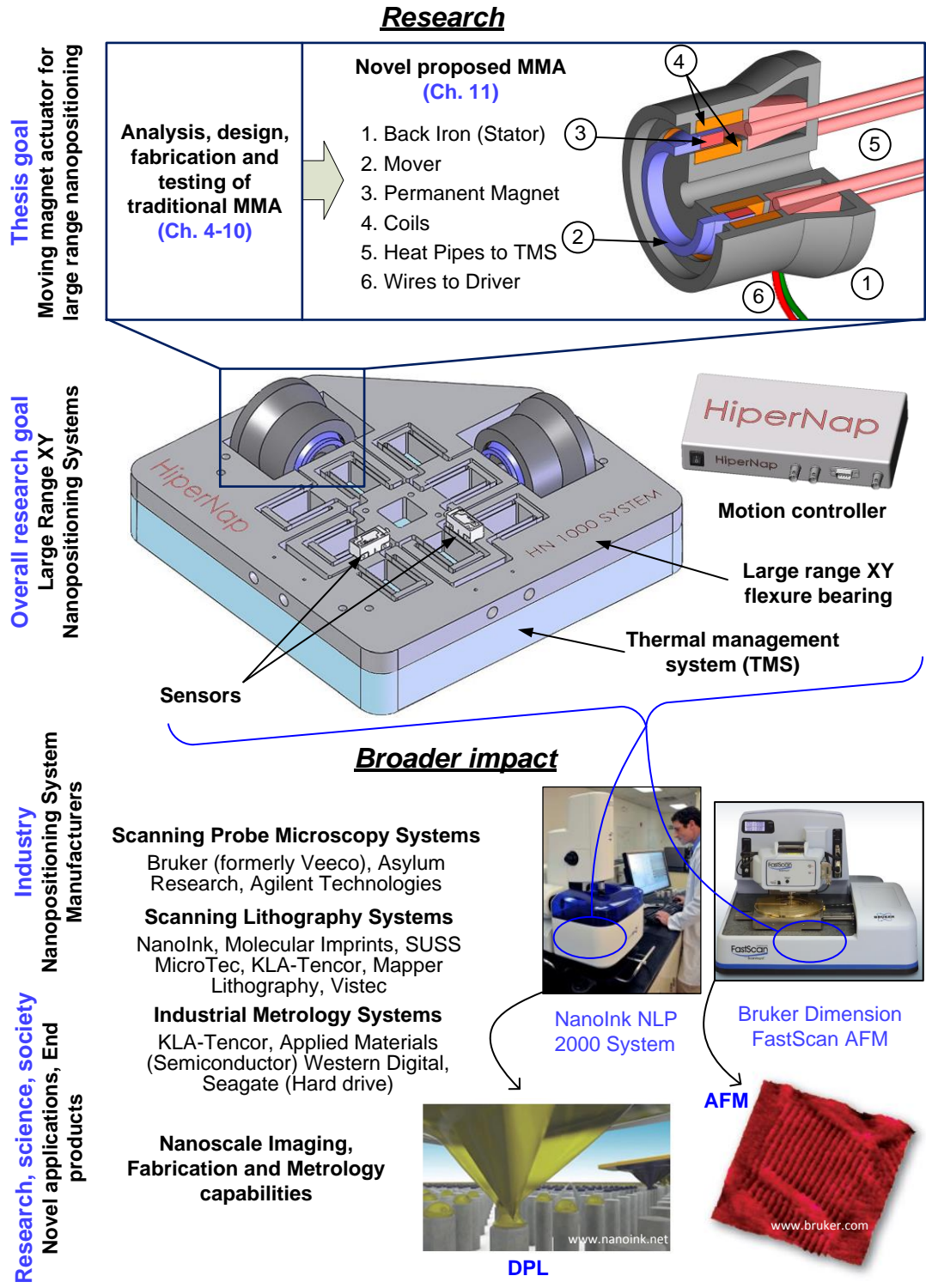


Figure 1.9: Envisioned research impact

### 1.2.3 Challenges in achieving large range nan positioning

There are several fundamental challenges in simultaneously achieving large range, high motion quality, and high speed in nan positioning systems [59][83]. These arise from limitations of the individual components, their mechanical integration and physical interaction, and the closed-loop operation of the overall motion system. Of the typical components in a nan positioning system (bearing, actuator, sensor, driver, and control logic and hardware), one of the most significant remaining challenges lies within actuator technology, which this thesis aims to address. In general, the actuator must provide large range ( $>10\text{mm}$ ), high resolution ( $<10\text{nm}$ ), and low heat ( $<10\text{W}$ ) generation. Surveyed available actuator products do not meet these requirements. For example, piezo stack actuators cannot achieve the motion range, piezo inertial drive types suffer from motion jitter and low fatigue life, and lead screw rotary drives cannot achieve the required resolution. Of the electromagnetic type, mover mass and/or moving wire disturbance may also degrade the nan positioning system performance. Further details and a comparison of actuators used in nan positioning and their potential in achieving large range nan positioning is discussed in Chapter 2.

Besides actuation technology, other significant challenges in achieving large range nan positioning include bearing, sensor, and controller design. Non-contact bearings are most often used in nan positioning systems to avoid friction and backlash [84][85]. Flexure bearings are a natural choice, as their monolithic (jointless) construction has inherently high motion quality, design simplicity, vacuum compatibility, low-cost, long life, and compact size. Several commercial nan positioning systems in Table 1.2 are based on flexure bearings. Other non-contact bearings such as magnetic and aerostatic bearings have also been investigated for achieving large range nan positioning

[86][87][88]. However, given the design and cost advantages of flexure bearings and their adequate stroke (~10mm) for the above mentioned applications, the focus of this thesis is flexure-bearing based motion systems. Recent work in [89][59] presents a novel physical system layout using a parallel-kinematic XY flexure bearing that provides a high degree of decoupling between the two motion axes by avoiding geometric over-constraints. This novel layout addresses several of the above mentioned challenges faced in bearing and sensing technology and the system integration. This also eliminates challenges and drawbacks associated with the most common approach to overcoming range limitation by mounting a “fine” flexure-based nanopositioning system on top of a “course” large-range traditional motion system [89]. Therefore, in this work, dual stage actuation schemes are not considered.

There exist several sensing options that are capable of the desired range, speed, precision, and resolution [90]. One of these—a linear optical encoder—is used in this work.

Considering controller design, elimination of backlash and friction in the motion system is critical in achieving nanometric motion quality. Presence of these non-deterministic effects otherwise make feedback control design particularly difficult and restrict the motion quality [75]. While advanced design and control methods have demonstrated steady-state nanometric precision and resolution in point-to-point positioning, tracking dynamic command profiles that involve frequent direction reversal is still an unmet challenge and is addressed further in [91].

### **1.3 Design specifications**

To define proper actuator design specifications it is important to understand the overall nan positioning system performance requirements. The relationship between actuator-level and system-level requirements is important given the system's sensitive nature and high degree of component interrelations. From an end-user's perspective (i.e. scanning probe microscopy / lithography techniques, or semiconductor and/or hard drive manufacturing requirements), large range nan positioning generally requires achieving four goals simultaneously, namely 1) large motion range, 2) nanometric motion quality (both for dynamic and quasi-static motion profiles), 3) high speed, and 4) temperature control and stability. These requirements result in many system level design trade-offs which are examined in depth in Chapter 3. The overall nan positioning system specifications and their impact on individual component requirements are summarized in Table 1.3 and discussed in the following subsections. In general, all components of the nan positioning system should have high bandwidth, dynamic range, and / or equivalently fast response time, no friction, low heat generation and / or good heat rejection, and high mechanical stiffness in non-motion directions. Due to the parallel kinematic flexure bearing technology mentioned above, the actuators and sensors in this work are assumed to only require a single axis of motion. The motion system level specifications chosen reflect typical representative numbers or order of magnitude estimates.

Table 1.3: Nanopositioning system and component level performance requirements

Motion system level specification		Motion Range	Motion Quality			Speed	Temperature stability
			Resolution	Precision	Accuracy		
		10mm	1nm	1nm	1nm	1m/s	+/- 0.1°C
Component level specifications	Actuator	10mm	Frictionless or high force with high dynamic range High force, Low mass (high bandwidth) High force uniformity over stroke	Frictionless or high force with high dynamic range High force, Low mass (high bandwidth) High force uniformity over stroke	Low heat generation Good heat rejection and/or decoupling of heat from motion stage	High force Low moving mass	Low heat generation Good thermal dissipation
	Bearing	10mm High stiffness and small error motions in bearing direction(s)	Good vibration isolation between bearing and environment No friction High stiffness in motion direction (to enable better disturbance rejection)	Good vibration isolation between bearing and environment No backlash and friction	Low heat sensitivity Small error motions Low stiffness in motion direction (decrease steady state error)	Low moving mass	Low heat sensitivity Low CTE material Isolation from heat source
	Sensor	10mm	1nm	1nm	Low heat sensitivity Sensor isolated from heat	High speed / bandwidth	Low thermal drift
	Controls / Driver	High SINAD / dynamic range	Low noise and distortion; High SINAD / dynamic range; Real time control			High clock speed and loop rate	-

### 1.3.1 Motion range

To demonstrate large range nanopositioning capability, a representative desired motion range of 10mm per motion axis is chosen. This requires that the actuator, bearing, and sensor to have a minimum 10mm range as well, assuming no amplification mechanism is used. Additionally, in the case of a flexure bearing, the bearing should have high stiffness and low error motion in the bearing directions over the stroke. Furthermore, a large stroke can require a finite force in the motion direction due to the motion-direction flexure stiffness as well as finite force to accelerate the motion stage to achieve high speeds. These forces must be matched by the actuator force, driver, and power supply capabilities.

### 1.3.2 Motion quality

Along with large motion range, nanopositioning performance of 1nm motion resolution, precision and accuracy is typically desired. In a nanopositioning system utilizing a flexure bearing, the main inhibitors of motion resolution and precision are due to sensor noise, driver noise and signal distortion, motion disturbance due to ground vibrations, and component nonlinearities, which must all be mitigated via feedback control. To maintain this assumption, it should be ensured that all other system components in addition to the bearing be frictionless. In particular, the actuator should have either no friction, or should be capable of large force that can be precisely controlled by current or voltage to move the stage with the desired motion quality in spite of any friction present in the actuator or system. The distinction here between continuous actuators and stepping actuators is important and is discussed in depth in Chapter 2. As discussed in Chapter 4, high system bandwidth is critical for good disturbance rejection

by the controller to achieve high motion quality. This is can be achieved by high actuator force output and low moving mass for a given flexure stiffness. Alternatively this can be achieved by a high stiffness in the motion direction. Additionally, the actuator should minimize cogging to reduce harmonic distortions of the force output. The motion stage should have low moving mass to maximize system bandwidth. The bearing should have high stiffness in off-axis directions and good vibration isolation to minimize disturbance of the motion stage Damping also can be selectively chosen to improve motion quality. While negatively impacting disturbance rejection capability, low stiffness in the motion direction is desirable because it leads to small steady state errors which determine accuracy.

Actuator heat output can significantly reduce positioning accuracy due to expansion of mechanical elements and thermal drift of sensors, apart from causing structural problems due to distortion. With this in mind, the actuator should have low heat generation and good heat rejection, and thermal decoupling between heat source and motion stage. The bearing should have low sensitivity to thermal fluctuations and should also keep the critical components such as flexure beams and motion stage thermally isolated from the actuator heat source.

Low noise and distortion of the driver and power supplies, as well as a high signal-to-noise and distortion ratio (SINAD) in the driver is critical. The controller hardware should have real time control capability.

### 1.3.3 Speed

In addition to maintaining nanometric motion quality over large ranges, high scanning speed and / or fast response time is also desirable to maximize device

throughput or reduce end user wait time. This implies for high accelerations, which in general means that the actuator must provide a high force output and a low moving mass, the bearing must have low moving mass, the sensor have high speed capability and / or bandwidth, and the electronics and controls hardware have a high clock speed and loop rate. The bandwidth of the flexure can be increased by increasing flexure stiffness and therefore its first resonant frequency. Adequate damping enables operation up to frequencies higher than the flexure first natural resonant frequency, which translates to higher achievable scanning speed and increased disturbance rejection. However this trades off with a higher actuation effort requirement at low frequencies and increased potential for steady state errors. System rise time also increases for point to point positioning scenarios. To decrease rise time, the flexure stiffness should be reduced at the expense of reduced disturbance rejection capability.

To estimate required actuation speeds for this work, a representative desired scanning path is assumed based on a 10mm x 10mm device size with nano-scale features separated by 10nm (Figure 1.10a). The scanning motion occurs along the y-axis, where a sinusoidal scanning motion profile is assumed (Figure 1.10b).

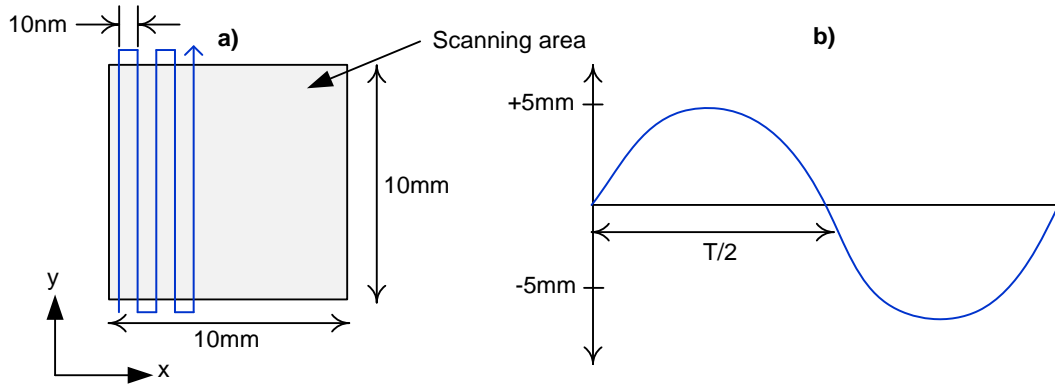


Figure 1.10: Raster scanning over 10mm x 10mm sample (not to scale)

As shown in Figure 1.10a the total number of lines of the scanning profile,  $n$ , for a given side length,  $X$ , and step size,  $\Delta x$ , is

$$n = \frac{X}{\Delta x} = \frac{10\text{mm}}{10\text{nm}} = \frac{10 \cdot 10^{-3}\text{m}}{10 \cdot 10^{-9}\text{m}} = 10^6 \quad (1.1)$$

and the total number of scanning cycles is therefore  $n/2$  assuming both forward and backward stroke directions are needed in the particular application. It should be noted that this ratio corresponds roughly to the desired dynamic range of the nanopositioning system. For a side length of  $X = 10\text{mm}$  and step size  $\Delta x = 10\text{nm}$  there are 500,000 cycles. This corresponds to a scanning time [hours] of

$$\frac{n}{2} \cdot \frac{1}{f} \cdot \frac{1}{3600} = \frac{n}{7200f} \quad (1.2)$$

where frequency  $f$  is measured in Hz. For the motion profile as defined in Figure 1.10b,  $x$ , [mm], the speed,  $\dot{x}$  [mm/s], and acceleration,  $\ddot{x}$  [mm/s<sup>2</sup>], are given by

$$\begin{aligned}
x &= \frac{X}{2} \sin(2\pi ft) \\
\dot{x} &= \frac{X}{2} (2\pi f) \cos(2\pi ft) \\
\ddot{x} &= -\frac{X}{2} (2\pi f)^2 \sin(2\pi ft)
\end{aligned} \tag{1.3}$$

where  $f$  is the desired scanning frequency. This corresponds to a maximum and root mean squared speed [mm/s] and acceleration [mm/s<sup>2</sup>] of

$$\begin{aligned}
\dot{x}_{\max} &= X \pi f \\
\dot{x}_{RMS} &= \frac{\sqrt{2}}{2} X \pi f \\
\ddot{x}_{\max} &= 2X \pi^2 f^2 \\
\ddot{x}_{RMS} &= \sqrt{2} X \pi^2 f^2
\end{aligned} \tag{1.4}$$

The speed and acceleration of the motion stage and required scanning time for various scanning frequencies are listed in Table 1.4. Scanning at 50Hz results in total scanning time of ~3 hours.

*Table 1.4: Speed and scanning time requirements for various scanning frequencies at 10mm travel*

Frequency [Hz]	Max. speed [m/s]	RMS speed [m/s]	Max. acc. [m/s <sup>2</sup> ]	RMS acc. [m/s <sup>2</sup> ]	Scanning time [hours]
1	0.03	0.02	0.20	0.14	139
5	0.16	0.11	4.93	3.49	28
10	0.31	0.22	19.74	13.96	14
50	1.57	1.11	493.48	348.94	3
100	3.14	2.22	1973.92	1395.77	1

In typical scanning applications, the nanopositioning system provides the relative scanning motion between a probe or energy-beam and a substrate. Subsequently forces of interaction between the mover and substrate are very small compared to the spring force

of the flexure bearing and the inertial force associated with the moving mass. This is unlike other motion systems that are used in traditional manufacturing, where the external loads are considerable compared to the bearing and inertial forces. Therefore load capacity in addition to inertial forces due to the motion stage itself is not considered.

The maximum inertial force,  $F_{max}$  [N], for a given mass of the motion stage,  $m_s$  [kg], and mass of the mover of the actuator,  $m_a$  [kg], is given by Equation (1.5). Here  $m_a$  is assumed to be negligible.

$$F_{max} = 2X\pi^2 f^2 (m_s + m_a) \quad (1.5)$$

The maximum force requirement for various scanning frequencies and motion stage masses are listed in Table 1.5. The importance of minimizing the motion stage mass to reduce inertial forces is apparent. Note the stiffness of the flexure bearing is not included in these calculations, which will increase low frequency force requirements and reduce force requirements near the first natural resonance frequency.

*Table 1.5: Force requirements for various scanning frequencies at 10mm travel*

Frequency [Hz]	Max. acc. [m/s <sup>2</sup> ]	Inertial Force [N] ( $m_s = 500\text{g}$ )	Inertial Force [N] ( $m_s = 5\text{kg}$ )
1	0.20	0.10	0.99
5	4.93	2.47	24.67
10	19.74	9.87	98.70
50	493.48	246.74	2467.40
100	1973.92	986.96	9869.60

It is also important to consider a point to point positioning scenario. In this case, it is often desired to minimize response time. Assuming a triangular velocity profile, the position, acceleration, and force requirements are shown in Figure 1.11.

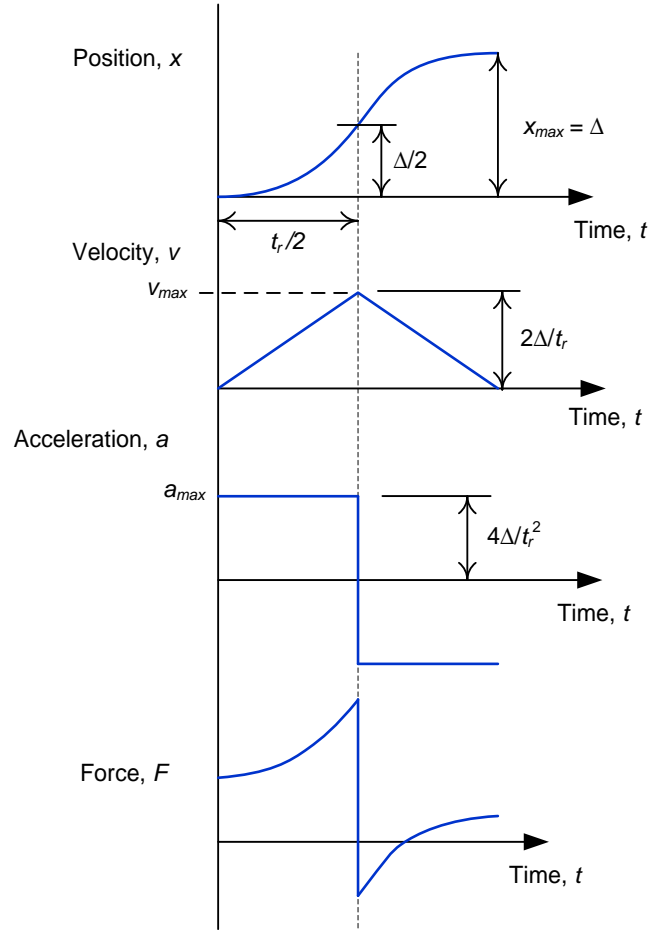


Figure 1.11: Motion profile and force requirements for point to point positioning

The maximum velocity occurs at  $t = t_r/2$ , half the distance to the target ( $x = \Delta/2$ ). Maximum velocity is given by (1.6).

$$\dot{x}_{\max} = \frac{2\Delta}{t_r} \quad (1.6)$$

Similarly, the maximum acceleration is given by (1.7).

$$\ddot{x}_{\max} = \frac{4\Delta}{t_r^2} \quad (1.7)$$

For a given flexure-based positioning system, the required maximum acceleration gives an estimate for the maximum force requirement. This approach is taken in Section 2.2.

#### 1.3.4 Temperature stability

In this work, temperature stability of  $\pm 1^\circ\text{C}$  at the motion stage and sensor is targeted. The importance of thermal management in precision engineering, in general, and nanopositioning systems, in particular, is well-known and has been extensively reported in the literature. Temperature rises and spatial thermal gradients can lead to significant internal stresses and distortion in the mechanical structure and assembly [92]. Also, a temperature rise can cause loss in accuracy of the sensors, which cannot be compensated by using feedback control. All these factors adversely affect the precision and accuracy of the nanopositioning system. In general, actuators and sensors generate heat which can become a significant limitation in motion system performance [90]. From an end user's standpoint, it is important that the motion stage remain at a controlled, consistent temperature. This reduces any thermal fluctuations in the sample, wafer, or hard drive read head, depending on the application, which would otherwise cause inaccurate data or defective components. Heat generation (i.e. power consumption) should be minimized or mitigated in the actuator, and heat flow management should be considered in the system level design. Specifics of these trade-offs are addressed in Chapter 8.

#### 1.3.5 Additional considerations

In some applications, it may be required that the nanopositioning system does not introduce significant electric or magnetic fields in the environment. Vacuum

compatibility also may be required, especially for semiconductor applications. The system should be comparable in cost to other nan positioning systems (< \$100,000) and have “desktop-size” dimensions (for example, fit within 500 mm x 500mm square) and packaging.

#### **1.4 Thesis outline**

To investigate the feasibility of using MMAs to simultaneously achieve large range, high speed, and high motion quality in flexure-based nan positioning systems, the following work and corresponding outline of the thesis is presented here.

In this chapter, Lorentz force actuators, namely moving magnet actuators (MMA) and their close relative voice coil actuators (VCA) are introduced. Their operation, advantages and disadvantages, and conventional applications are discussed. This highlights their potential in meeting the performance requirements for large range nan positioning. Nan positioning systems are then discussed in more detail. Finally, the required system- and actuator-level design specifications required in meeting demands of large range nan positioning are proposed.

Chapter 2 compares Lorentz force actuators with other types of existing actuators and attempts to summarize their respective potential in meeting the proposed design specifications. The particular potential of MMAs is shown.

Chapter 3 examines MMA prior art. Based on the prior art, the MMA design concept for this work is proposed.

Chapter 4 discusses inherent trade-offs in the performance specifications of an MMA and their impact on the performance of flexure-based nan positioning systems.

Chapter 5 derives a new figure of merit that captures the dynamic performance of the actuator which is used for subsequent actuator design and optimization. Performance trade-offs at the motion system level are quantitatively identified in terms of the individual performance of the actuator, actuator driver, flexure bearing, and thermal management system.

Chapter 6 develops and evaluates analytical model for design purposes. Based on these results, finite element analysis is used for subsequent design work.

Chapter 7, Chapter 8, and Chapter 9 describe the detailed design and fabrication of the proposed MMA, thermal management system, and flexure bearing, respectively.

Chapter 10 presents the assembly of the complete experimental set-up. Experimental results of the MMA, thermal management system, and complete motion system, including closed loop design and operation highlight the potential of the proposed actuator in large-range nanopositioning.

Chapter 11 presents innovative MMA and VCA designs to address performance limitations and challenges identified in this work and to improve performance upon the traditional MMA architecture.

Chapter 12 summarizes the primary findings and results of this work and discusses future work.

## **CHAPTER 2: Actuators for Large Range Nanopositioning**

Actuators in a nanopositioning system must be able to simultaneously meet the desired system-level requirements outlined in Section 1.3, namely motion range, motion quality, speed, and temperature stability. This chapter compares several existing linear actuation technologies and discusses their potential in achieving the performance goals in this work. As mentioned previously, dual-stage actuation schemes are not considered here. Due to the enormous variety in actuator types, configurations, figures of merit, design criteria and trade-offs, etc., first a high level comparison of actuators based on literature survey and performance indices method is considered. This narrows the potential choices to piezoelectric, magnetostrictive and electromagnetic actuators. These actuators are then considered individually in further detail. The single phase, non-slotted moving magnet actuator (MMA), introduced in Chapter 1, shows potential for large range nanopositioning and is therefore chosen as the focus of this thesis. Note that all product data listed here has been obtained from various sources (catalogs, datasheets, company websites, etc.). There is no guarantee of accuracy in this externally obtained data and may be subject to change or revision.

Based on the findings in this chapter, an overview of actuator general strengths and weaknesses in regards to the above-mentioned nanopositioning specifications is shown in Figure 2.1. This figure is discussed in more detail in the following sections, however it suggests moving magnet actuators to be the most promising overall selection to meet the four system performance specifications. For example, piezo stack actuators alone cannot achieve the motion range and their force and resonant frequency reduce to

values comparable to MMA if an amplification mechanism is used to increase their stroke. Amplified piezo stack actuators are, however, a comparable candidate. Magnetostrictive actuators feature similar limitations to piezo types. Piezo inertial drive and piezomotor types have low speeds, low motion quality due to motion jitter, and low fatigue life. Lead screw drives cannot achieve the required resolution or speed. Of the electromagnetic type, mover mass and/or moving wire disturbance may also degrade the nanopositioning system performance. Compared to voice coil actuators, moving magnet actuators stand out as the best overall potential candidate due to their better thermal management and lack of moving wires Table 2.2 describes these general advantages and disadvantages for various actuator types examined in this chapter.

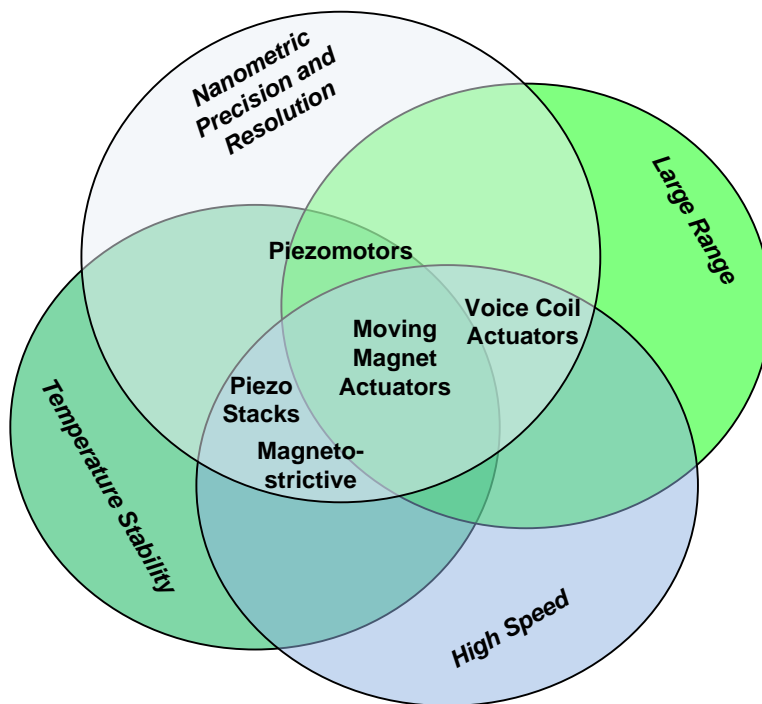


*Figure 2.1: Overview of final actuator candidates for large range nanopositioning*

*Table 2.1: General advantages and disadvantages of final actuator candidates for large range nanositioning*

Actuator type	Advantages	Disadvantages
Piezoelectric: stack with amplification	<ul style="list-style-type: none"> <li>• High precision / resolution</li> <li>• Low heat output</li> <li>• High speed for smaller motion amplification</li> </ul>	<ul style="list-style-type: none"> <li>• Drift</li> <li>• Hysteresis</li> <li>• Low force and resonant frequency at large motion amplification</li> </ul>
Piezoelectric: stepping type / piezomotor	<ul style="list-style-type: none"> <li>• Large travel range</li> <li>• High precision / resolution (however only at specific location; not during travel)</li> <li>• Low heat output</li> </ul>	<ul style="list-style-type: none"> <li>• Jitter</li> <li>• Fatigue</li> <li>• Low speeds</li> </ul>
Electromagnetic: Moving magnet type (MMA)	<ul style="list-style-type: none"> <li>• High precision / resolution</li> <li>• Large travel range</li> <li>• High speed</li> <li>• Good thermal management</li> </ul>	<ul style="list-style-type: none"> <li>• Magnetic hysteresis</li> <li>• Higher moving mass</li> <li>• Off-axis attraction</li> <li>• High heat output</li> </ul>
Electromagnetic: Moving coil type (VCA)	<ul style="list-style-type: none"> <li>• High precision / resolution</li> <li>• Large travel range</li> <li>• High speed</li> </ul>	<ul style="list-style-type: none"> <li>• Moving wires</li> <li>• Heat dissipation at mover</li> <li>• Poor thermal management</li> <li>• High heat output</li> </ul>
Magnetostrictive	<ul style="list-style-type: none"> <li>• High precision / resolution</li> <li>• Low heat output</li> <li>• Higher operating temperature than piezo (380C vs. 165-300C)</li> </ul>	<ul style="list-style-type: none"> <li>• Drift</li> <li>• Hysteresis</li> <li>• Higher currents used for control compared to high voltages in piezo</li> <li>• Continuous current or permanent magnets required for static displacement unlike in piezoelectric</li> </ul>

## 2.1 Actuator comparison based on literature survey

Some of the most common classes of actuators are electromagnetic, electrostatic, piezo-ceramic, shape memory alloy, magnetostrictive, thermal expansion, hydraulic,

pneumatic, and organic actuators such as muscle [90][93][5]. Based on a survey of commercial products, conventional practice, as well as the discussion in [66], the most common actuators for macroscopic (i.e. desktop size) precision motion systems are piezoelectric and electromagnetic actuators. For microscopic (i.e. MEMS scale to millimeter sized) nanopositioning systems there are many other types used, such as electrostatic, thermal, magnetostrictive and electrochemical actuators [66][60]. However, before assuming that piezoelectric or electromagnetic actuators are the best solutions for the desired large range nanopositioning performance, a survey of actuator design literature was conducted to validate that these are indeed the best options. This makes sense especially considering the opinion expressed in [94] that all actuators have respective advantages and disadvantages, with no single type necessarily being the best. This prior art search was conducted with the goal that it may lead to additional candidates, or provide insights as to which of the two (piezoelectric or electromagnetic) would be better for achieving large range nanopositioning, if they are indeed are the best choices.

Due to the large number of actuator configurations and varieties, applications, and corresponding actuator requirements, the literature presents many tradeoffs, approximations, and opinions. Selecting an actuator based on a survey of literature discussing individual actuator types, or even on literature which specifically compares classes of actuators, becomes largely non-quantitative and subjective, if not overwhelming. One reason is that there is a large variety of performance specifications for which the actuators are designed. Common performance specifications of actuators include motion range, motion resolution, force, response time, speed, size, weight, power consumption, pressure, strain, density, and efficiency. These performance specifications are used in good actuator overviews and comparisons such as in

[60][90][66][93][35][94]. However, many other performance specifications are also used in the literature. For example, [95] lists material reliance and reversibility. In [96] there is force density, drive voltage and reliability. [90] uses actuator power densities. In [35] also are mentioned compliance, material overhead, and stiffness.

The various performance metrics identified in the literature is sorted into the corresponding four system level performance metrics for large range nanopositioning in this work (Table 2.2). The most suitable actuators for each performance metric from the literature survey are listed. From sources which included an overview of various actuators, the winners of each category were selected. We see that in general, the best actuators for achieving large range are electromagnetic and piezo stepping types. For high motion quality the best are generally electromagnetic and piezoelectric. For high speed the best appear to be shape memory alloy (SMA), hydraulic, thermal, and electromagnetic. There appeared to be no consistent best choice for achieving temperature stability, however electromagnetic actuators were generally not chosen. It could therefore be reasonable to suggest that piezoelectric and perhaps electromagnetic are the best overall solutions, however this is quite qualitative. The next section describes a more quantitative method for selecting an appropriate actuator.

Table 2.2: Potential actuators for large range nanositioning based on literature survey

System level nanositioning specification (see Section 1.3)	Potential corresponding actuator level specification	Tentative best actuators for each system level specification based on literature review
Large range	Travel range, strain	<ul style="list-style-type: none"> <li>• Piezo inchworms, dual stage piezo-electric, electromagnetic [66]</li> <li>• Electromagnetic, pneumatic, piezo inchworm, muscle [35]</li> <li>• Electromagnetic, SMA, Piezo stack [96]</li> <li>• Inchworm/ultrasonic/quasi-static piezo-electric, dual stage piezo-electric, electromagnetic [94]</li> </ul>
High speed	Bandwidth, speed, power density, force density, response / settling time	<ul style="list-style-type: none"> <li>• Hydraulic, SMA [90]</li> <li>• Thermal, electrostatic, piezo-electric, electromagnetic [66]</li> <li>• Hydraulic, SMA, electromagnetic, piezo-electric [35]</li> <li>• Thermal, SMA [95]</li> <li>• SMA, electromagnetic [96]</li> </ul>
High motion quality	Resolution, accuracy, precision, range to resolution ratio [66]	<ul style="list-style-type: none"> <li>• Electrostatic, piezoelectric, electromagnetic [66]</li> <li>• Electromagnetic [35]</li> <li>• Piezo-electric, hydraulic, dual stage piezo-electric [94]</li> </ul>
Temperature stability	Efficiency, power density	<ul style="list-style-type: none"> <li>• Pneumatic, magnetostrictive [35]</li> <li>• Electrostatic, piezo-electric, electrostrictive [95]</li> <li>• Piezo better than electromagnetic under 30W (due to increasing Joule heating with reducing coil wire thickness) [97]</li> </ul>

## 2.2 Actuator comparison using performance indices

Classes of actuators can be compared in a quantitative manner using actuator *performance indices*. Performance indices are defined as “actuator characteristics which measure its effectiveness in performing a given function” to “guide the selection of an appropriate type of actuator for a given application” [93]. This method, pioneered in [93],

is harnessed in this section as a method for selecting the appropriate actuator type. The performance indices method can at least suggest which actuator classes are most suitable for an application, if not give an outright best actuator class. Performance indices for a given application are derived via analytical system models, which are subsequently evaluated via actuator performance characteristics to determine which actuator classes best achieve system requirements.

Examples of actuator performance characteristics include maximum actuation stress  $\sigma_{max}$  (maximum actuation force per actuator cross sectional area), maximum actuation strain  $\varepsilon_{max}$  (maximum actuator stroke per actuator length), actuator mass density  $\rho$  (ratio of total actuator mass to total actuator volume) and minimum strain resolution  $\varepsilon_{min}$  (smallest step increment of the actuation strain). It should be noted that these characteristics are significantly different, although analogous, from conventional material stress, strain, and density. Other performance characteristics include actuator modulus,  $E$ , maximum operation frequency, maximum power density, and power efficiency. Numerical data for these performance characteristics for many actuator types is listed in [93] and is sourced from manufacturers and known theoretical limits. Plots of these performance characteristics show relative strengths and weaknesses between actuator classes and give insightful order of magnitude estimates of performance differences. It should be noted that moving magnet actuator performance characteristics are within the ranges given for moving coil transducers (i.e. voice coil actuators) in the data in [93].

Actuator performance indices predicting system performance for a specific application are derived from system analytical models. By examining the indices that affect system performance, the combination of actuator performance characteristics most important to that specific application are obtained. Consulting the aforementioned plots

of actuator performance characteristics leads to the most appropriate actuator, or points to important tradeoffs in actuator selection.

An actuator's force output can be characterized as shown in Figure 2.2. Similarly, the performance characteristics of stress ( $\sigma$ ) and strain ( $\epsilon$ ) can be plotted. A change in force given a change in displacement (when the control signal to an actuator is held constant) can be described by its stiffness,  $K_a$ . The analogous term when stress and strain are considered is the actuator's modulus,  $E$ . For some types of actuators, for example piezo-based actuators, their modulus places a bound on their achievable stroke work ( $F_{max}x_{max}$ ). As soon as their stroke increases, the achievable force drops. On the other hand, with other actuators such as hydraulic actuators, their achievable stroke work is independent of their modulus. Their force can remain constant all the way to maximum stroke, after which their force drops with their modulus.

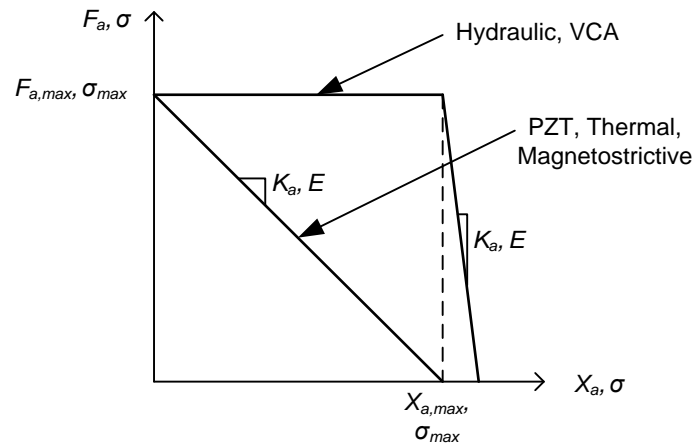


Figure 2.2: Normalized actuator force-stroke and stress-strain curves

Based on Figure 2.2, the actuator force over stroke can be modeled in general by

$$F_a = F_{a,max} - K_a(x)x_a \quad (2.1)$$

where  $K_a(x)$  captures the change in force over stroke.  $K_a(x)$  is a constant in the case of PZT actuators. This model can therefore capture whether the actuator is a force-based or displacement-based actuator, and incorporates the actuator's modulus. This model assumes that the actuator can produce bi-directional force, which is not true for all actuator classes. This is discussed in [93].

For the application in this work, actuator performance indices representative of a large range nanopositioning system are derived. To meet system requirements outlined in Section 1.3, several scenarios and design goals are examined, namely to maximize system first resonant frequency, maximum scanning frequency, minimize point to point positioning response time, and minimize power input. A flexure-based nanopositioning system comprising an actuator, motion amplification mechanism, motion stage, and flexure bearing, is shown in Figure 2.3. The actuator has displacement  $x_a$ , stiffness  $K_a(x)$ , and mass  $m_a$ . The motion stage displaces by  $x$  and has mass  $m$ . The mechanical stiffness of the flexure guiding the motion stage is represented by a spring with spring constant  $K$ . An amplification mechanism with motion amplification  $N$ , lever arm length  $L$ , torsional stiffness  $K_m$ , and evenly distributed mass  $m_m$ , is included to capture the possibility of using motion amplification allowing the realistic comparison of different actuator classes. For example, the relatively small motion range of piezoelectric actuators can be increased using a flexure based amplification mechanism.

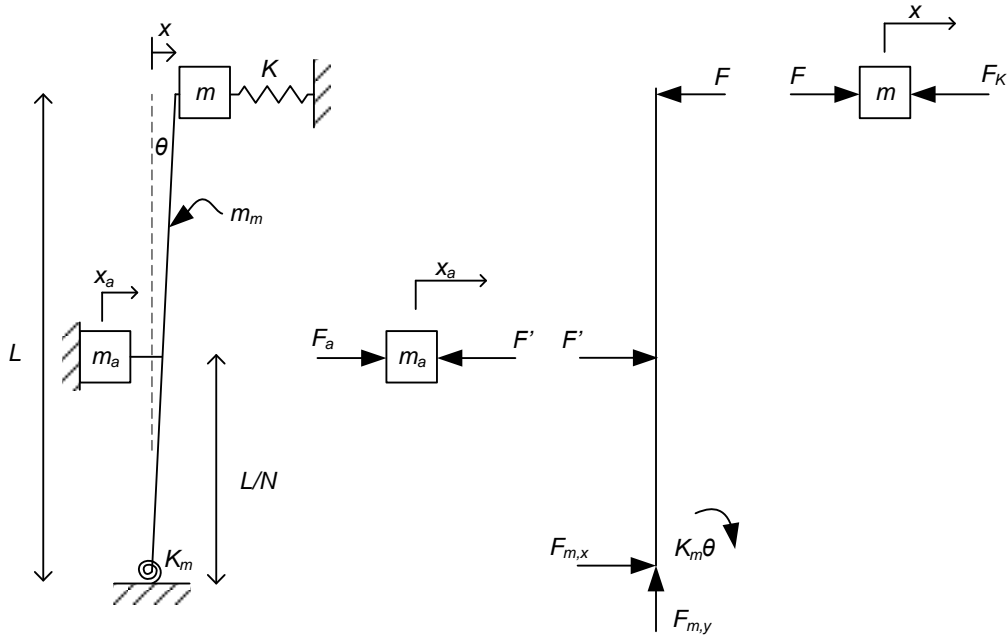


Figure 2.3: Flexure based motion system with amplification mechanism

An actuator displacement,  $x_a$ , results in displacement,  $x$ , of the motion stage via the amplification mechanism lever arm and is related by

$$\frac{x}{L} = \frac{x_a}{L/N} \rightarrow x_a = \frac{x}{N} \quad (2.2)$$

This gives the actuator velocity and acceleration as

$$\dot{x}_a = \frac{\dot{x}}{N}; \ddot{x}_a = \frac{\ddot{x}}{N} \quad (2.3)$$

Assuming a small angle approximation, motion stage displacement,  $x$ , is related to the angle made by the lever arm,  $\theta$ , by

$$\frac{x}{L} = \sin \theta \approx \theta; \frac{\ddot{x}}{L} \approx \ddot{\theta} \quad (2.4)$$

Summing the torques about the lever arm pivot gives Equation (2.5).

$$\begin{aligned}
F' \frac{L}{N} - FL - K_m \theta &= I_m \ddot{\theta} = \frac{m_m L^2}{3} \ddot{\theta} \\
\rightarrow F &= \frac{F'}{N} - \frac{K_m}{L^2} x - \frac{m_m}{3} \ddot{x}
\end{aligned} \tag{2.5}$$

Actuator free body diagram of Figure 2.3 gives the actuator equation of motion, Equation (2.6).

$$\begin{aligned}
F_a - F' &= m_a x_a = \frac{m_a}{N} \ddot{x} \\
\rightarrow F' &= F_a - \frac{m_a}{N} \ddot{x} = F_{a,\max} - \frac{K_a(x)}{N} x - \frac{m_a}{N} \ddot{x}
\end{aligned} \tag{2.6}$$

Likewise, the motion stage free body diagram gives the motion stage equation of motion, Equation (2.7).

$$m\ddot{x} = F - F_K = F - Kx \tag{2.7}$$

Substituting Equations (2.5) and (2.6) into Equation (2.7) gives the motion stage equation of motion, Equation (2.8), where the effective actuator force  $F_a / N$  must equal the sum of the inertial and spring forces.

$$\begin{aligned}
m\ddot{x} &= \frac{F_{a,\max}}{N} - \ddot{x} \left( \frac{m_a}{N^2} + \frac{m_m}{3} \right) - x \left( \frac{K_a(x)}{N^2} + \frac{K_m}{L^2} + K \right) \\
\rightarrow \ddot{x} \left( \frac{m_a}{N^2} + \frac{m_m}{3} + m \right) + x \left( \frac{K_a(x)}{N^2} + \frac{K_m}{L^2} + K \right) &= \frac{F_{a,\max}}{N}
\end{aligned} \tag{2.8}$$

Several actuator relations establish a link between actuator and system performance and result in appropriate performance indices [93]. An actuator must achieve displacement  $x_a$ , but is limited by its maximum actuator displacement. Therefore actuator displacement is governed by maximum actuator strain as Equation (2.9), where  $L_a$  is the length of the actuator.

$$x_a \leq \varepsilon_{\max} L_a \quad (2.9)$$

Likewise, maximum actuation force is related to maximum actuation stress by Equation (2.10), where  $A_a$  is the cross sectional area of the actuator.

$$F_a \leq \sigma_{\max} A_a \quad (2.10)$$

Actuator mass can be written as

$$m_a = \rho A_a L_a \quad (2.11)$$

Combining Equations (2.9), (2.10), and (2.11) relates actuator output force to actuator mass in Equation (2.12). Output force is limited by the maximum specific stress, strain, and mass density of an actuator class for a given actuator displacement,  $x_a$ .

$$m_a \geq \frac{\rho}{\sigma_{\max} \varepsilon_{\max}} F_a x_a \rightarrow F_a \leq \frac{m_a}{x_a} \frac{\sigma_{\max} \varepsilon_{\max}}{\rho} \quad (2.12)$$

### 2.2.1 Maximize first natural frequency

It is desirable to maximize the first natural frequency of a flexure based motion system to improve disturbance rejection capability as discussed in Section 4.2.1. Based on the assumed spring-mass motion system, the system first resonant frequency is approximated by the ratio of spring and inertial forces in Equation (2.8), resulting in Equation (2.13). Examining the numerator, it is clear that all system springs should be stiff. According to the denominator, all system masses should be small. However, it is important to note the dependence on amplification  $N$ —its significance depends on how actuator mass  $m_a$  compares to the payload  $m$  and amplification mass  $m_m$ , as well as how the actuator stiffness  $K_a$  compares to the system stiffness  $K$  and amplification mechanism stiffness  $K_m$ . Assuming comparable magnitudes of the three masses and low actuator

stiffness, for large  $N$  the dependence of first resonant frequency on  $N$  becomes negligible. However, for systems employing actuators with high intrinsic stiffness and low mass, such piezoelectric actuators, the dependence on  $N$  is not insignificant. This results in a  $1/N$  dependence of natural frequency which is discussed in Section 2.3.2. The relation can also be thought of the system natural frequency,  $K/m$ , which is reduced by an attenuation factor which depends on the ratios of actuator stiffness and mass to system stiffness and mass.

$$\omega_n^2 = \frac{\frac{K_a(x)}{N^2} + \frac{K_m}{L^2} + K}{\frac{m_a}{N^2} + \frac{m_m}{3} + m} = \frac{K}{m} \frac{\frac{K_a(x)}{N^2 K} + \frac{K_m}{KL^2} + 1}{\frac{m_a}{N^2 m} + \frac{m_m}{3m} + 1} \quad (2.13)$$

To derive an appropriate performance index, assuming  $x=Nx_a$ , the system first resonant frequency can be written as

$$\omega_n^2 = \frac{\frac{K_a(x)x_a^2}{x^2} + \frac{K_m}{L^2} + K}{\frac{m_a x_a^2}{x^2} + \frac{m_m}{3} + m} \quad (2.14)$$

For initial analysis, some approximations are made. Assume the actuator stiffness,  $K_a(x)$ , is a constant and equal to  $EA_a/L_a$ . This is a good estimate for obtaining the natural frequency, as the actual force over stroke curve is inconsequential. The system and amplification mechanism stiffness and mass are here assumed to be negligible. As seen in further analysis, however, the payload mass and amplification mechanism stiffness have a significant effect on the obtainable natural frequency. With these assumptions, and substituting in (2.11) for the actuator mass, the first resonant frequency simplifies to

$$\omega_n^2 = \frac{K_a(x)}{m_a} = \frac{E \frac{A_a}{L_a}}{\rho A_a L_a} = \frac{E}{\rho L_a^2} \quad (2.15)$$

Therefore, for appropriate actuator size constraints length  $L_a$ , the performance index comprising the ratio of actuator modulus  $E$  and mass density  $\rho$  should be maximized. This performance index,  $E/\rho$ , has units of  $\text{m}^3 / \text{kg}$ . According to tabulated actuator performance characteristics in [93], and plotted in Figure 2.4, actuators that have the largest value of  $E/\rho$  are the strain-based actuators: piezoelectric, shape memory alloys, magnetostrictive, and thermal expansion actuators. Hydraulic and pneumatic actuators follow, with electromagnetic types last. It should be noted that while piezoelectric type actuators appear to be best suited for maximizing the first natural frequency in this analysis, a closer examination in Section 2.3.3 shows this to be inaccurate for large motion ranges (i.e. large motion amplification), where electromagnetic actuators are similar in performance. The contribution to the blocking force on the piezoelectric element from the amplification mechanism significantly reduces the achievable natural frequency for large amplification, which is not accounted for in this analysis.

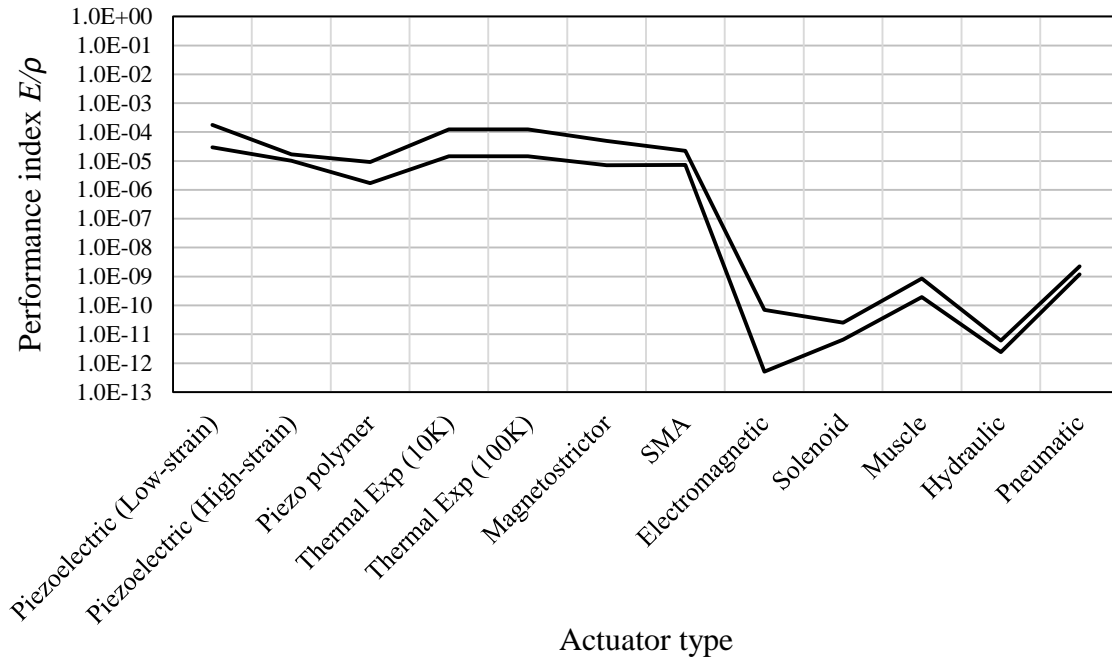


Figure 2.4: Comparison of performance index  $E/\rho$  for various actuators (estimated maximum and minimum ranges shown)

### 2.2.2 Maximize scanning frequency

Assuming a sinusoidal motion profile in Section 1.3.3, motion stage acceleration is related to desired scanning frequency and stroke as

$$\begin{aligned} x(t) &= \Delta \sin(2\pi ft) \\ \rightarrow |\ddot{x}(t)| &\leq 4\Delta\pi^2 f^2 \end{aligned} \quad (2.16)$$

Substituting in the system equation of motion, Equation (2.8), and assuming at a given point in time  $\sin(2\pi ft) = -1$ , scanning frequency is limited by

$$f^2 = \frac{\frac{F_a}{N} + \Delta\left(\frac{K_a(x)}{N^2} + \frac{K_m}{L^2} + K\right)}{4\Delta\pi^2\left(\frac{m_a}{N^2} + \frac{m_m}{3} + m\right)} \quad (2.17)$$

Combined with actuator relation (2.12), we see that the scanning frequency is limited by the actuator and system properties as

$$f^2 = \frac{\frac{\sigma_{\max} \varepsilon_{\max}}{\rho} \frac{m_a}{\Delta^2} + \Delta \left( \frac{K_a(x)}{N^2} + \frac{K_m}{L^2} + K \right)}{4\pi^2 \left( m + \frac{m_a}{N^2} + \frac{m_m}{3} \right)} \quad (2.18)$$

In this case, the ratio of the first term in the numerator to the denominator, as well as the ratio of the second term in the numerator to the denominator, should be maximized. The second ratio is the system natural frequency examined in the last section. Examining the first ratio alone, we see that the lower bound on scanning frequency is

$$f^2 \geq \frac{\frac{\sigma_{\max} \varepsilon_{\max}}{\rho}}{4\pi^2 \Delta^2 \left( \frac{m}{m_a} + \frac{1}{N^2} + \frac{1}{3} \frac{m_m}{m_a} \right)} \quad (2.19)$$

Therefore it is desirable to maximize the ratio  $\sigma_{\max} \varepsilon_{\max} / \rho$ . This ratio is the maximum specific work (i.e. work per unit mass) of an actuator, in Joules per kilogram. According to [93], this performance index is common in applications where weight or inertial forces should be minimized, which is appropriate. It should be noted that the mass density assumes the entire actuator mass, not only the mover, however this is assumed adequate for initial comparisons. Comparing maximum specific actuation stress ( $\sigma_{\max} / \rho$  [Nm/kg]) versus maximum actuation strain ( $\varepsilon_{\max}$  [-]) in Figure 2.5 suggests which actuator classes best meet this performance index. The original is Figure 7 in [93]. The actuators toward the upper right of the plot have the maximum specific work. An ideal mechanism can move the performance of an actuator along a line of constant  $\sigma \varepsilon / \rho$  [Jkg<sup>-1</sup>], which are diagonal lines with slope of -1 [93]. Therefore, actuators with similar  $\sigma \varepsilon / \rho$  but different maximum strain and stress can potentially be used for an application

through use of an amplification mechanism. However, as noted above, the amplification mechanism torsional stiffness and mass may reduce accuracy of this assumption.

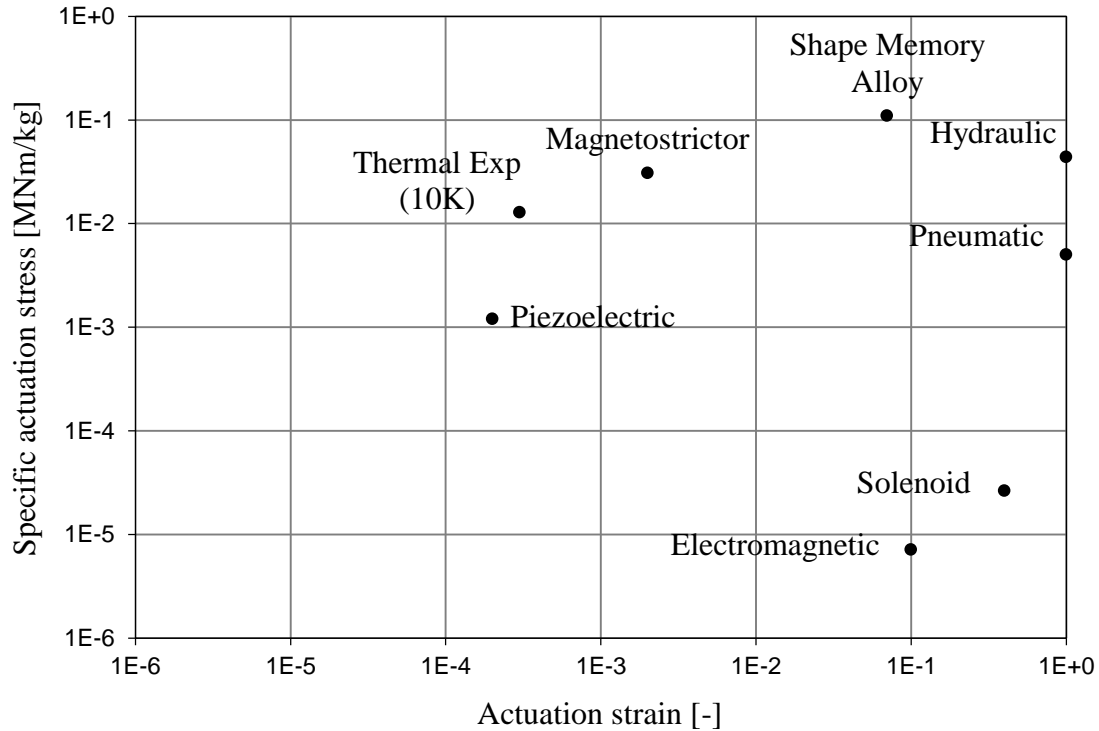


Figure 2.5: Specific actuation stress vs. actuation strain [93]

According to Figure 2.5, shape memory, hydraulic and pneumatic are the best actuator choices to maximize specific work output. The specific work of thermal, piezoelectric, and electromagnetic actuators follow, and are roughly the same, where the latter has larger stroke (i.e. strain) with lower force per mass (i.e. specific stress), and the former have smaller stroke with higher force per mass. These actuators, through use of an amplification mechanism, compete with one another for maximizing the performance index for this application. Hydraulic and pneumatic classes are ruled out based on positioning resolution discussed in Section 2.2.5. This leaves magnetostrictor actuators as

the second best choice, followed by thermal, piezoelectric, and electromagnetic actuators competing for the best choice to maximize scanning frequency.

According to Equation 2.19, the specific work density should be maximized regardless of system properties which depend on the desired stroke,  $\Delta$ , and the mass ratios in the denominator. Interestingly, however, if the payload mass,  $m$ , and the amplification mechanism mass,  $m_m$ , are assumed negligible, the equation above reduces to the performance index,  $E/\rho$ , which is the same result as when only the resonant frequency term is considered like in the previous section. This may imply that the specific actuator work is a more general (and therefore more accurate for the use of broad comparisons) indicator of actuator performance in a scanning motion profile scenario. It accounts for the fact that the actuator must produce work to achieve the desired stroke, even at high frequencies, even if the actuator has high intrinsic natural resonant frequency (i.e. high stiffness  $K_a$ ). These two performance indices are compared in Figure 2.6. Both performance indices indicate similar conclusions for non-strain-based actuators, however shows a large difference for strain-based actuators such as PZT. This trend mirrors the results in Section 2.3.3 when the effect of system and amplification mechanism stiffness and mass are included, showing PZT and electromagnetic actuators to compete with each other.

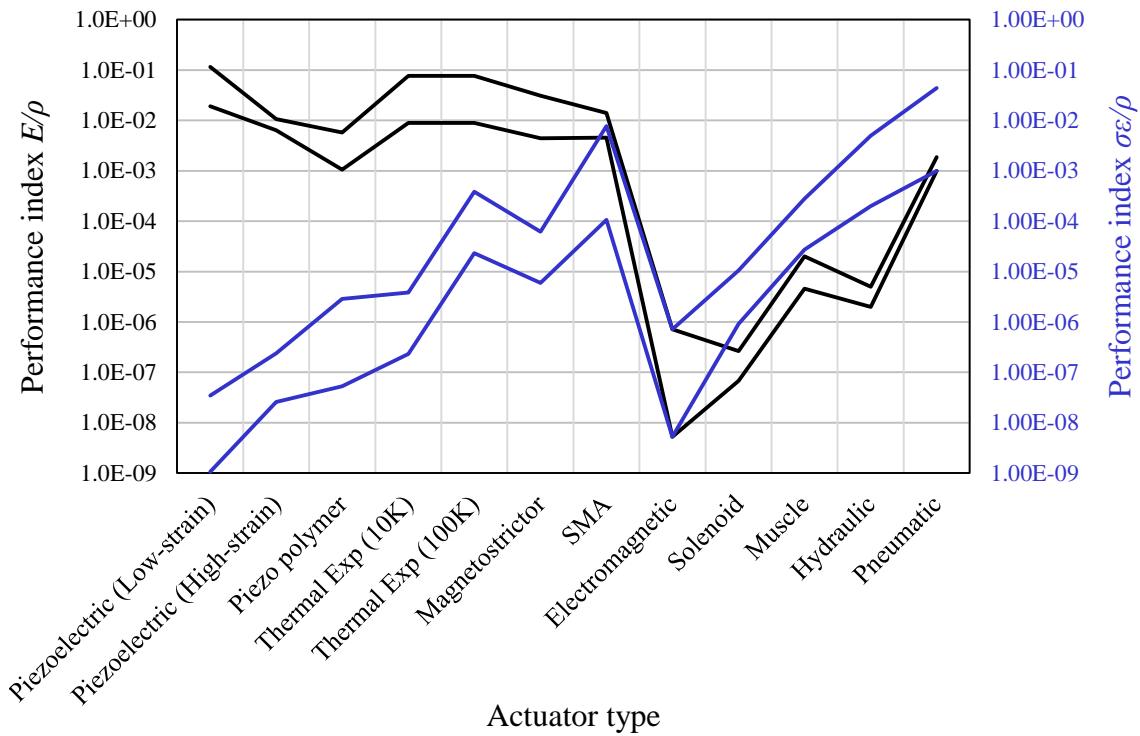


Figure 2.6: Comparison between performance indices  $E/\rho$  and  $\sigma\epsilon/\rho$  (estimate maximum and minimum ranges shown)

It is also interesting to note a non-dimensional stroke-work coefficient  $C_s$  ranging from 0 to unity which is defined in [93] to account for the fact that some actuators, such as PZT, cannot produce maximum stress over their entire stroke. For example, hydraulic actuators have a  $C_s$  of 1, whereas PZT have  $C_s = \sim 0.5$ . This potentially accounts for the effect of actuator stiffness,  $K_a$ , and may validate the assumption of  $K_a=0$  for the analysis examples in [93]. Therefore, in this case the term  $C_s \sigma_{\max} \epsilon_{\max} / \rho$  may be the more appropriate performance index. However, the stroke-work coefficient ranges from 0.25-1 (factor of 4), so it actually has a negligible effect on the results given that the specific work for different actuator classes range several orders of magnitude.

### 2.2.3 Minimize rise time in point to point positioning application

In this section we examine a point to point positioning application where the goal is to minimize response time, assuming a triangular velocity profile described in Section 1.3.3. Substituting in the maximum position and acceleration requirements into Equation (2.8) gives the maximum force requirement as

$$\frac{F_{a,\max}}{N} = \frac{4\Delta}{t_r^2} \left( m + \frac{m_a}{N^2} + \frac{m_m}{3} \right) + \frac{\Delta}{2} \left( \frac{K_a(x)}{N^2} + \frac{K_m}{L^2} + K \right) \quad (2.20)$$

Rearranging, we find the minimum response time to be

$$t_r^2 \leq 4\Delta \frac{m + \frac{m_a}{N^2} + \frac{m_m}{3}}{\frac{F_a}{N} - \frac{\Delta}{2} \left( \frac{K_a(x)}{N^2} + \frac{K_m}{L^2} + K \right)} = 4 \frac{m_a \left( \frac{m}{m_a} + \frac{1}{N^2} + \frac{1}{3} \frac{m_m}{m_a} \right)}{\frac{\sigma_{\max} \varepsilon_{\max}}{\rho} \frac{m_a}{\Delta^2} - \frac{1}{2} \left( \frac{K_a(x)}{N^2} + \frac{K_m}{L^2} + K \right)} \quad (2.21)$$

In this case, it is always desirable to minimize the spring stiffness and actuator stiffness, unlike in the scanning scenario. Assuming that in an optimal scenario, the stiffness is zero, the maximum response time is given by Equation (2.22).

$$t_r^2 \leq 4\Delta^2 \frac{\rho}{\sigma_{\max} \varepsilon_{\max}} \left( \frac{m}{m_a} + \frac{1}{N^2} + \frac{1}{3} \frac{m_m}{m_a} \right) \quad (2.22)$$

We see that the specific work density ( $\sigma\varepsilon/\rho$ ) of the actuator should be maximized to minimize response time. Therefore, the potential actuator classes are the same as in the case of maximizing scanning frequency (Section 2.2.2). Similar to the above analysis, the mass ratios and  $1/N^2$  term may significantly impact the final optimal actuator selection, however the specific work density should be maximized regardless of system properties.

#### 2.2.4 Minimize power consumption

To satisfy thermal considerations outlined in Section 1.3.4, the power input to the motion system which is dissipated as heat should be minimized. Power is limited by actuator force and velocity as

$$P \leq F_{a,\max} \dot{x}_{a,\max} = \frac{F_{a,\max} \dot{x}_{\max}}{N} \quad (2.23)$$

For a point to point positioning scenario, substituting in from Equation (2.20) relates the power requirement to response time and system properties as

$$\begin{aligned} P &\leq \frac{2\Delta}{t_r} \left[ \frac{4\Delta}{t_r^2} \left( m + \frac{m_a}{N^2} + \frac{m_m}{3} \right) + \frac{\Delta}{2} \left( \frac{K_a(x)}{N^2} + \frac{K_m}{L^2} + K \right) \right] \\ &= \frac{8\Delta^2}{t_r^3} \left( m + \frac{m_a}{N^2} + \frac{m_m}{3} \right) + \frac{\Delta^2}{t_r} \left( \frac{K_a(x)}{N^2} + \frac{K_m}{L^2} + K \right) \end{aligned} \quad (2.24)$$

Assuming that the response time should be small (i.e.  $t_r \ll 1$ ) power is dominated by inertial terms and is estimated as

$$P \leq \frac{8\Delta^2}{t_r^3} m_a \left( \frac{m}{m_a} + \frac{1}{N^2} + \frac{1}{3} \frac{m_m}{m_a} \right) \quad (2.25)$$

For a given actuator mass  $m_a$ , reducing system response time trades off with higher actuator power output. Therefore, actuator specific work should be maximized (according to the conclusions in Section 2.2.3), and system thermal management should be carefully considered. This also implies that the stage and amplification mechanism masses should be small compared to the actuator mass. Other metrics for minimizing power requirements in reciprocating motion applications such as stroke work and power efficiencies are explored further in [93].

### 2.2.5 Minimize positioning resolution

The positioning system must also achieve high motion quality. Therefore, actuator classes are compared based on required motion quality outlined in Section 1.3.2. Two main actuator characteristics are considered which affect the system positioning resolution, precision, and accuracy. First, the number of distinct positions through which an actuator can step compared to its stroke (effectively its dynamic range). Second, the minimum step size, which corresponds to minimum resolution. These characteristics are compared by considering the plot of minimum strain resolution and actuator strain (see Figure 8 in [93]). Lines of slope +1 give the number of steps an actuator can achieve i.e. its dynamic range. Based on Section 1.3.2, the minimum required actuator dynamic range is  $10^6$ . No actuators explicitly meet this requirement (notice there are no actuators which lie along the  $10^6$  diagonal line in the figure). This is most likely because the actuators listed are only examined based on their inherent characteristics without using feedback control (i.e. the stated actuator positioning resolution was measured using open loop control, although effective closed loop control can further increase dynamic range). Actuators which most closely meet dynamic range requirement lie along the  $10^5$  line. These are piezoelectric, magnetostrictor, electromagnetic, pneumatic, and hydraulic actuators. The latter two are ruled out based on previous analysis. This leaves piezoelectric, magnetostrictor, and electromagnetic actuators as potential candidates. Next, actuator minimum positioning strain (i.e. positioning resolution) is considered. According to the same figure, actuator classes which enable the smallest step sizes are piezo, magnetostrictor, and electromagnetic, in that order. Assuming standard actuator lengths, electromagnetic actuator minimum positioning resolution lies in the 100nm range. This means that for this nanopositioning application, electromagnetic actuators

could be considered the limiting class, with piezo and magnetostrictor actuators as the optimal choices.

### 2.2.6 Conclusion

Based on the above examined requirements in this application, the performance indices method suggests that the classes which best simultaneously meet these requirements are piezoelectric, magnetostrictor, and electromagnetic actuators. These actuators have lower work density than other types, however have good resolution and speed capabilities. Electromagnetic actuators appear to be a good “compromise” actuator, as they often came in the middle of the extremes, and are suitable for medium to large stroke applications. One drawback would be that closed loop operation is required, placing more emphasis on the control scheme and power source in maintaining nanometric motion quality. Piezoelectric actuators appear better suited for open loop high precision control with better resolution capability. While this analysis helps narrow down potential actuator types, it only gives order of magnitude estimates. Many factors were not considered. For example, the total mass of the actuators were used, not just the mover. Packaging considerations are largely neglected. Importantly, this discussion does not consider actuators with infinite length capability, such as stepping type (e.g. inchworm) piezomotors, linear multi-phase electromagnetic motors, and dual stage actuation schemes. Therefore, a more in-depth discussion of some of these types as well as the three top actuator types identified in this section follows.

## 2.3 **Piezoelectric actuators**

Piezoelectric actuators utilize the inverse piezoelectric effect, where an applied electric field results in a mechanical strain of a crystalline material. By far the most

commonly used piezoelectric material is ceramic lead zirconate titanate (PZT). PZT is popular for having greater sensitivity and higher operating temperature than other piezo-ceramics, and is relatively mechanically strong, chemically inert and inexpensive to manufacture. Piezoelectric actuators have been the most commonly used for nanopositioning [60] for their several advantages [98] including backlash and frictionless motion, resolution that is in practice limited only by electronic and mechanical noise, high force due to high stiffness, high operating bandwidth generally only limited by the current rating of the controller, and low power dissipation.

However, due to a low strain limit of  $\sim 0.1\%$  [99], in practice the displacement of PZT is very small, around  $\sim 10\mu\text{m}$ . This is arguably the largest disadvantage of piezoelectric actuation [60]. Achieving large displacements using standalone PZT requires large packaging size requirements; for example a  $100\mu\text{m}$  displacement implies a device 100 mm long [98]. Therefore, many applications use motion amplification or various forms of repeated stepping motions [100] to increase the motion range. Another large drawback of PZT is hysteresis and drift. These can cause changes in the desired displacement of 10 to 15% of the motion range. This means that in practice, PZT actuators often require closed loop control, despite their high resolution while operating in open loop. These effects also reduce cycle life [96]. Additional drawbacks of PZT include a fairly low Curie temperature ( $150\text{-}300^\circ\text{C}$ ), which is the temperature above which alignment of the electric dipoles is lost. The maximum operating temperature of PZT is generally half of the Curie temperature. PZT is also poor in tension often requiring pre-loading [98].

The main types of piezoelectric actuators used for nanopositioning are piezo stack actuators (sometimes with mechanical motion amplification), and quasi-static,

dynamic or resonant (ultrasonic) piezo actuators. These actuators are described next. The layout and operation of these actuators are such that they help overcome some of the above mentioned drawbacks, including the small displacement.

### 2.3.1 Piezoelectric stack actuators

To increase the motion range, multiple piezoceramic plates can be stacked to form piezoelectric stack actuators [90]. The stack is often enclosed in a housing to provide structural support, and internal preload using springs ensures bi-directional motion. The voltage requirement is usually 100V to 1000V depending on the type of PZT used. The electrical connections are distributed in parallel to the piezoceramic plates to decrease the drive voltage requirement. An example piezoelectric stack actuator [101] is shown in Figure 2.7. Piezoelectric drivers generally feature high voltage (100-1000V) and low current (~1-2A) and are in the ~\$1000 range.

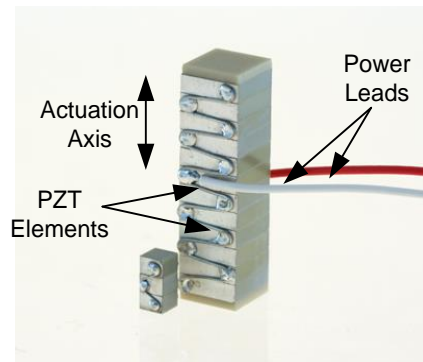


*Figure 2.7: Piezo stack actuator [102]*

However, despite their increased motion range, most commercially available piezo stack actuators still have too small of stroke (~200 $\mu$ m) for large range nanopositioning [60][101][103]. This is limited mainly for the practical reason that due to

the low strain of piezoelectric materials, as mentioned above, achieving a 10mm travel range with a PZT stack actuator would require it to be 10m in length.

### 2.3.2 Piezoelectric stacks with amplification mechanism

To increase the motion range, piezoelectric stack actuators may be integrated with suitable flexure-based motion transmissions that amplify their range [104][105][106][90]. Off the shelf examples are shown in Figure 2.8 (see patent [107]). The range of these actuators seen in datasheets is generally up to 1mm [108][102][109] and in some cases 2-10mm [110].

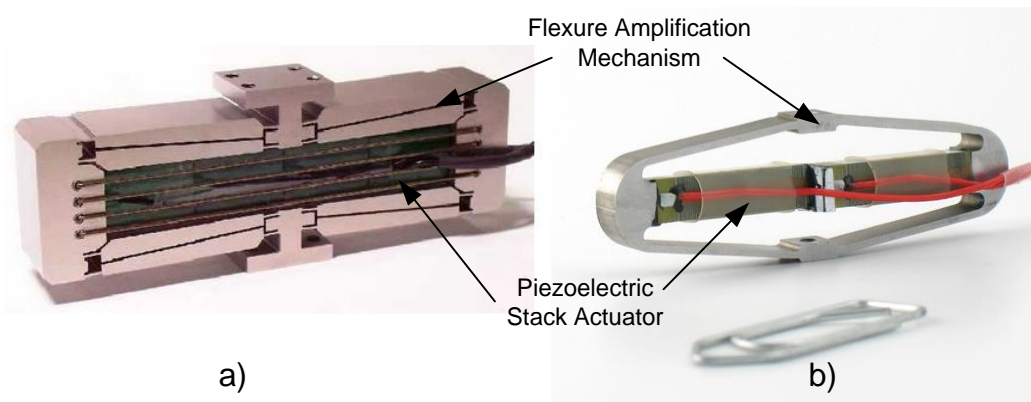


Figure 2.8: Piezoelectric stack actuators with amplification a) [109] and b) [102]

As amplification mechanisms can increase the stroke close to that required for this work, the implications on system performance is therefore investigated in detail. It is found that amplifying the motion significantly decreases the output force and adversely affects dynamic performance, potentially making it a less attractive choice [96] compared to other actuation types. To investigate the effect of motion amplification on the system performance, a piezo actuator can be represented by its stiffness as shown in Figure 2.9. Under no load, the actuator has maximum free displacement  $x_0$ . Conversely, at zero

displacement, the actuator has a maximum blocking force  $F_0$ . The actuator force  $F_a$  and actuator displacement  $x_a$  operate between these two extremes. The stiffness of the actuator is represented by  $K_a = F_0 / x_0$ . The free displacement is dictated by the applied voltage from the power supply as  $x_0 = K_p V$ , where  $K_p$  is the piezo expansion coefficient  $V$  is the applied voltage. Increasing supply voltage shifts the operating line upward. The blocking force can be expressed as  $F_0 = \bar{K}_p V$ , where  $\bar{K}_p = K_a K_p$ .

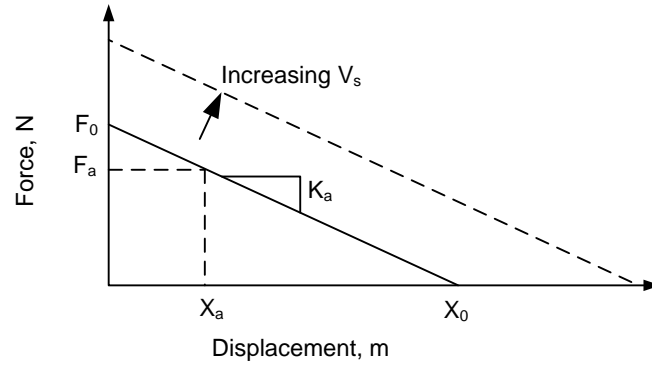


Figure 2.9: Piezo stack actuator model

Based on Figure 2.9, the actuator force,  $F_a$ , can be written as

$$F_a = F_0 - K_a x_a = \bar{K}_p V_s - K_a x_a \quad (2.26)$$

Rearranging gives the actuator displacement,  $x_a$ , as

$$x_a = \frac{1}{K_a} (F_0 - F_a) = x_0 - \frac{1}{K_a} F_a \quad (2.27)$$

Piezo stack actuators are often integrated with a flexure bearing and amplification mechanism to increase motion range. To examine the effects of motion amplification and to compare performance with other potential competing actuator classes, the above piezo force and displacement relations are included in the system model in Section 2.2. The free body diagram of actuator and piezo spring stiffness,  $K_a$ , are illustrated in Figure 2.10.

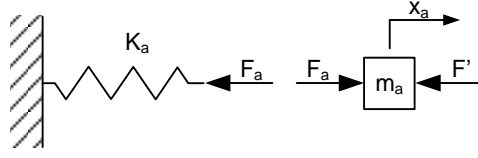


Figure 2.10: Piezo stack actuator integrated with motion system model

Substituting Equation (2.26) into the system equation of motion, Equation (2.8), gives

$$\begin{aligned}
 m\ddot{x} &= \frac{F_a}{N} - \ddot{x}\left(\frac{m_a}{N^2} + \frac{m_m}{3}\right) - x\left(\frac{K_m}{L^2} + K\right) \\
 \rightarrow \ddot{x}\left(m + \frac{m_a}{N^2} + \frac{m_m}{3}\right) + x\left(\frac{K_m}{L^2} + K + \frac{K_a}{N^2}\right) &= \frac{\bar{K}_p V}{N}
 \end{aligned} \tag{2.28}$$

Simplification of this relation leads to several insights. In quasi-static conditions,  $\ddot{x} \approx 0$ , and the equation of motion simplifies to Equation (2.29). If the amplification mechanism joint stiffness  $K_m$  and flexure bearing stiffness  $K$  are very small compared to the piezo stiffness, then  $x = Nx_0$  as expected and the piezo reaches its free displacement. However, in practice, this implies that  $K_m$  and  $K$  contribute significantly to the blocking force. For finite  $K_m$  and  $K$  and  $N \gg 1$  the expected motion amplification  $N$  of the piezo stack is reduced by an additional factor as  $\sim 1/N^2$ . This leads to a smaller than expected stroke, approaching  $x = x_0 / N$ , due to the amplified blocking force that the flexure and amplification mechanism generate..

$$x = \frac{\frac{\bar{K}_p V}{N}}{\frac{K_m}{L^2} + K + \frac{K_a}{N^2}} = Nx_0 \frac{K_a}{K_a + N^2\left(\frac{K_m}{L^2} + K\right)} \tag{2.29}$$

The contribution of  $K_m$  and  $K$  to the blocking force also affect the actuator output force. Substituting Equation (2.29) for (2.26) gives Equation (2.30). If  $K_m$  and  $K$  go to 0, then the force becomes 0 for all  $N$  as the piezo fully extends. The expected output force  $F = F_0 / N$  is further reduced for small  $N$  and converges for large  $N$ .

$$F_a = F_0 - K_a x_a = F_0 \left(1 - \frac{x_a}{x_0}\right) = F_0 \left(1 - \frac{x}{Nx_0}\right)$$

$$F = \frac{F_a}{N} = \frac{F_0}{N} \left(1 - \frac{K_a}{K_a + N^2 \left(\frac{K_m}{L^2} + K\right)}\right) = \frac{F_0}{N} \left(\frac{1}{1 + \frac{1}{N^2} \frac{K_a}{K_m / L^2 + K}}\right) \quad (2.30)$$

The effect of flexure and amplification mechanism stiffness on actuator displacement for changing amplification is summarized in Figure 2.11. Increased amplification causes the piezo to become blocked with less displacement possible, smaller than the expected  $NX_0$ .

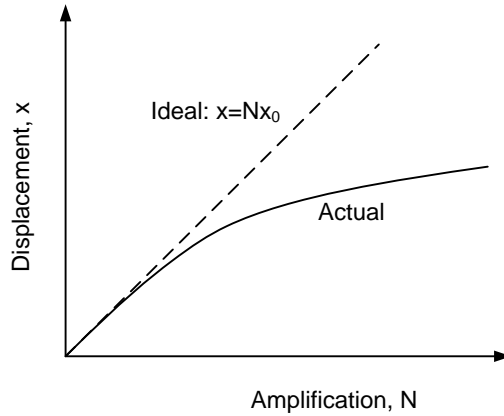


*Figure 2.11: Effect of flexure and amplification mechanism stiffness on piezo actuator displacement and force output*

The amplification mechanism and flexure stiffness  $K_m$  and  $K$  also affect the actuator output force. Rearranging actuator force relation (2.26) gives (2.30) and

substituting (2.29) into (2.30) describes the force acting on the motion stage. As expected, if  $K_m$  and  $K$  are large compared to the piezo stiffness, then the actuator force approaches the blocking force of  $F = F_0 / N$ . However, for finite  $K_m$  and  $K$ , the output force  $F = F_0 / N$  is further reduced for small  $N$  and converges for large  $N$ .

$$F_a = F_0 - K_a x_a = F_0 \left(1 - \frac{x_a}{x_0}\right) = F_0 \left(1 - \frac{x}{Nx_0}\right) \quad (2.31)$$

$$F = \frac{F_a}{N} = \frac{F_0}{N} \left(1 - \frac{K_a}{K_a + N^2 \left(\frac{K_m}{L^2} + K\right)}\right) = \frac{F_0}{N} \left(\frac{1}{1 + \frac{1}{N^2} \frac{K_a}{K_m / L^2 + K}}\right) \quad (2.31)$$

The effect of flexure and amplification mechanism stiffness on actuator force output for changing amplification is summarized in Figure 2.11. Increased amplification causes lower than expected blocking force  $F_0/N$  for small amplification.

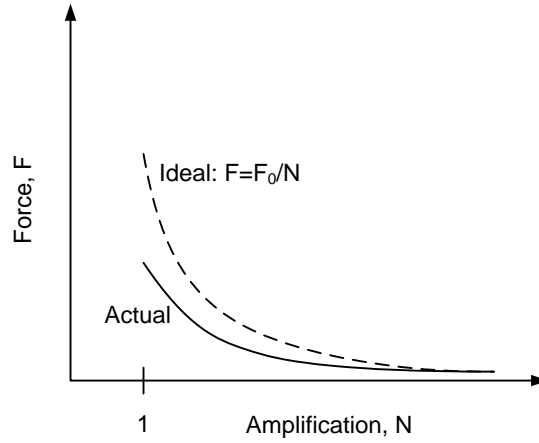


*Figure 2.12: Effect of flexure and amplification mechanism stiffness on piezo actuator blocking force output*

The effect of motion amplification can also be visualized in Figure 2.13. The achievable motion range of a piezo actuator flexure based amplification mechanism will

be  $x_A$ , which occurs where the system spring curve and actuator stiffness line intersect. Amplifying the displacement of the piezo actuator by  $N$  times shifts the effective actuator stiffness line. This will deliver a displacement  $x_B$  which is smaller than expected improvement in the overall achievable motion range,  $Nx_A$ . It is important to note that as amplification  $N$  increases, displacement increases as expected, if  $K + K_m/L^2$  is smaller than  $K_a$ . As noted earlier, the piezo effective stiffness drops with  $N$ , and so when the actuator stiffness and system stiffness become equal, there will no longer be an increase in displacement for increase in  $N$ . If the flexure and amplification mechanism stiffness dominates the piezo stiffness, amplification will result in a decrease in achievable displacement.

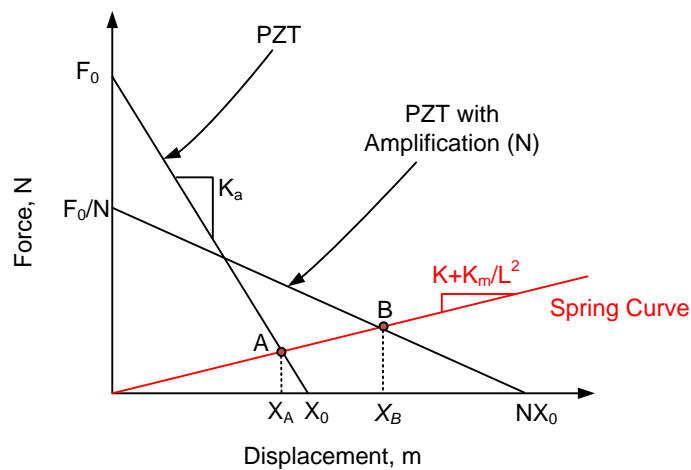


*Figure 2.13: Force and displacement of piezo actuator integrated with motion amplification*

Next, the effect on amplification of effective system first resonant frequency is examined. From Equation (2.28), the system open loop bandwidth is approximated by the ratio of spring to inertial stiffness as

$$\omega_n^2 = \frac{\frac{K_a}{N^2} + \frac{K_m}{L^2} + K}{m + \frac{m_a}{N^2} + \frac{m_m}{3}} \quad (2.32)$$

For a typical piezo actuator system, the actuator stiffness is much greater than the flexure and amplification mechanism stiffness, so  $\frac{K_a}{N^2} \gg \frac{K_m}{L^2}$  and  $\frac{K_a}{N^2} \gg K$ . Also, the piezo mass is small compared to the motion stage mass, giving  $\frac{m_a}{N^2} \ll m$ . With these assumptions, (2.32) reduces to (2.33) which suggests that the first resonant frequency scales with  $1/N$ .

$$\omega_n^2 \approx \frac{\frac{K_a}{N^2}}{m + \frac{m_m}{3}} \rightarrow \omega_n \approx \frac{1}{N} \sqrt{\frac{K_a}{m + \frac{m_m}{3}}} \quad (2.33)$$

These findings are checked against specifications of available actuators using piezoelectric stacks and flexure based motion amplification. These actuators are sold by [CEDRAT Technologies](#), [Dynamic Structures LLC](#), and [PI](#), among others. Figure 2.14 shows the free (i.e. no load) natural resonant frequency versus free (unblocked) stroke [110][111][108]. The  $1/N$  trend is clearly seen. The only mechanism achieving 10mm range (from Dynamic Structures LLC) predicts ~70 Hz resonant frequency.

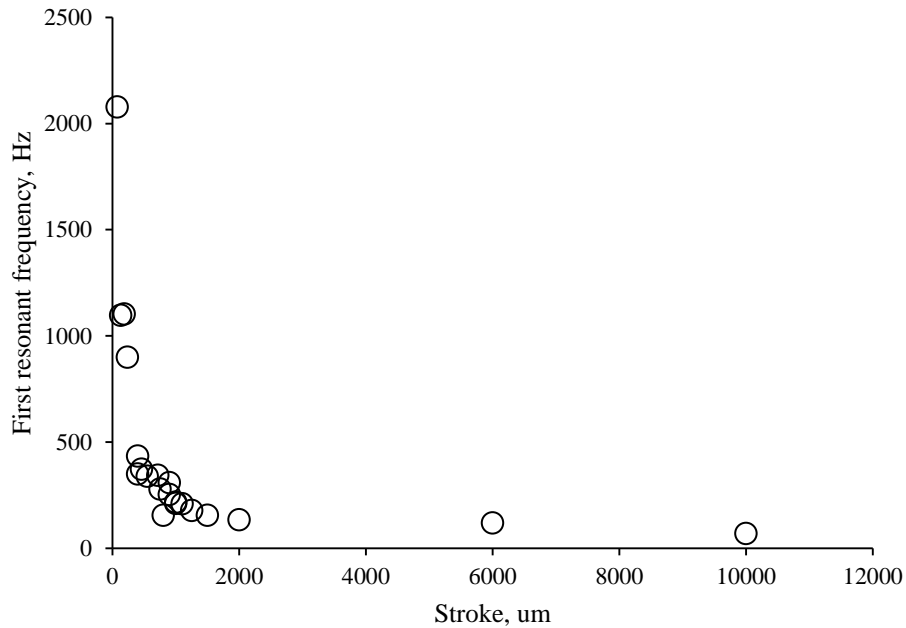


*Figure 2.14: First resonant frequency vs. free stroke of commercially available mechanically amplified piezo actuators*

Similarly, according to the product datasheets, available blocking force decreases with amplification. Figure 2.15 shows blocking force compared to stroke for various commercial actuators, which supports the  $\sim 1/N$  trend identified above. It should be noted that the available force in these commercial actuators drops significantly for large amplifications. For example, the blocking force for the 10mm actuator from Dynamic Structures is only 20N. This implies low achievable accelerations, especially for larger payloads.

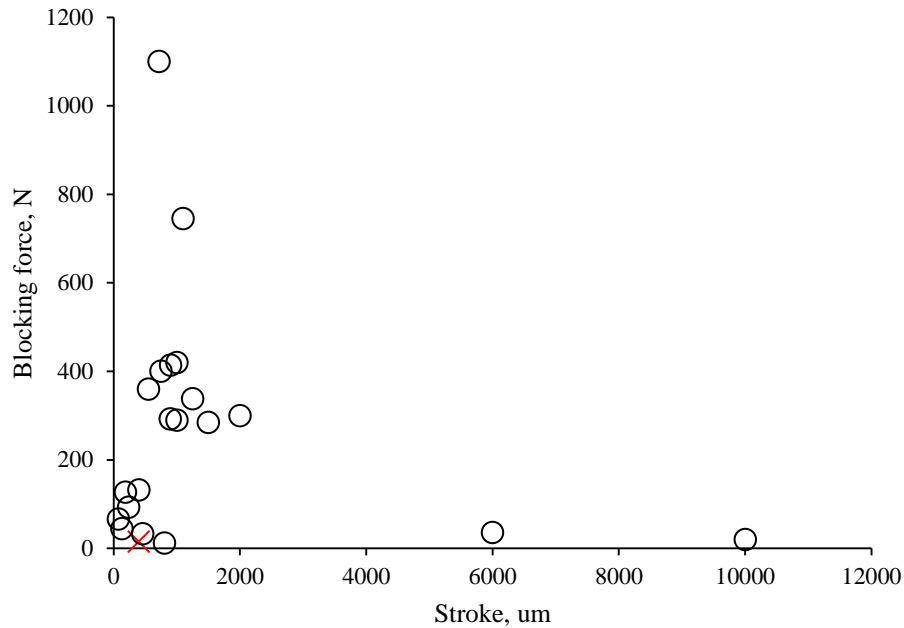


*Figure 2.15: Blocking force vs. free stroke of commercially available mechanically amplified piezo actuators*

It is important to mention that in many designs, the amplification mechanism may be integrated such that it simultaneously serves as the flexure bearing and provides motion guidance for the motion system [104]. In these cases, the stroke of the motion system is indeed amplified to be  $N$  times that of the actuator, but the natural frequency of the motion system scales inversely with  $N$ . Using the example of reference [104], when an off-the-shelf piezoelectric stack actuator with  $80\mu\text{m}$  free stroke and  $6\text{KHz}$  natural frequency is used with an amplification factor of 16 to increase its free stroke to  $1.2\text{mm}$ , its natural frequency drops to about  $86\text{Hz}$ . Even though difficult to achieve, a greater transmission ratio would lead to an even lower natural frequency, thus limiting the dynamic performance. Furthermore, to achieve high transmission ratios and yet maintain an overall compact motion system footprint, these designs exploit kinematic nonlinearities in the transmission mechanism. This produces a transmission ratio that changes

considerably, especially over a large motion range, as well as introduces the possibility of over-constraint [112]. Moreover, the elastic deviation of a flexure-based transmission from true kinematic characteristics leads to “lost motion” between the actuator and motion stage [106].

### 2.3.3 Comparison between electromagnetic and piezoelectric actuators

According to Section 2.2.1, to maximize the system first natural frequency, the ratio of the actuator’s modulus and density,  $E/\rho$ , should be maximized. Piezo-type actuators have the highest values by far. However, it was noted that the effect of the system and amplification mechanism stiffness and mass is not taken into account, which are significant in practical applications. Therefore, in this section, the first resonant frequency of PZT and electromagnetic type actuators is examined more closely. It is found that the first natural frequency for PZT actuators decreases for large amplification factors, approaching that expected for electromagnetic actuators. Therefore PZT actuators have a less clear advantage over electromagnetic actuators when considering first resonant frequency, unlike concluded in Section 2.2.1.

The achievable first natural frequency using an amplified piezo stack actuator, Equation (2.32), is compared to the predicted natural frequency of a general actuator, Equation (2.13). The significant difference is the values of actuator stiffness and mass. The achievable stroke of a PZT actuator is governed by Equation 2.30 which depends on the system blocking forces and is smaller than the expected  $x_a N$ . Here two examples are compared using estimated realistic actuator and system stiffness and mass values. In the first case, a PZT stack actuator from PI (Model # P-025.40P) is selected, which has a stiffness of 220 N/ $\mu\text{m}$  and nominal displacement of 60 $\mu\text{m}$ . This actuator line is for high

dynamic and force operation, and is roughly the middle of the road in terms of stiffness, displacement, and blocking force of the offered products. The rest of the assumed values of the system and actuator variables are listed in Table 2.3.

Table 2.3: Actuator and system values assuming PZT actuator model # P-025.40P

Property	PZT	EM
Actuator stiffness, $K_a$ , (N/m)	220000000	200
Flexure stiffness, $K_f$ (N/m)	1000	1000
Amplification mechanism torsional stiffness, $K_m$ (Nm/rad)	10	10
Amplification mechanism arm length, $L$ (m)	0.1	0.1
Actuator moving mass, $m_a$ (kg)	0.1	0.5
Payload mass, $m$ (kg)	0.5	0.5
Amplification mechanism total mass, $m_m$ (kg)	0.1	0.1
Nominal actuator stroke, $x_a$ (m)	0.00006	0.01
Desired system motion range, $x$ , (m)	0.01	0.01

The resulting first natural frequencies of the amplified piezo and electromagnetic actuators are compared in Figure 2.16 for varying amplification,  $N$ . The predicted stroke as a function of  $N$  is overlaid. The decrease in first resonant frequency of the piezo actuator, scaling as  $1/N$ , is clearly seen. This is because the actuator stiffness term dominates, and the mass term is small compared to system masses (especially for high  $N$ ). Likewise, the independence of first resonant frequency to  $N$  for the electromagnetic actuator is seen, which is largely due to the low actuator stiffness.

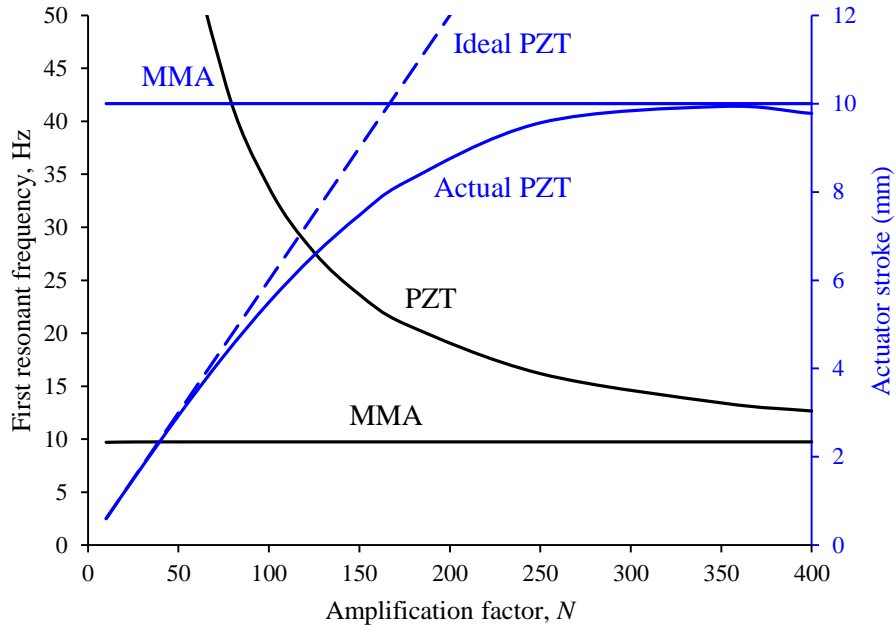


Figure 2.16: First resonant frequency and actuator stroke for an MMA and PZT actuator (Model # P-025.40P)

The stroke of the PZT would ideally reach 10mm with an amplification factor of  $\sim 175$ , however due to the blocking forces from the amplification mechanism, 10mm displacement is not achieved until  $N=350$ . At this point, the first resonant frequency of the system with a PZT actuator drops near that of the system employing an electromagnetic actuator.

The flexure stiffness is very small ( $5\text{N}/5\text{mm} = 1000\text{N/m}$ ), however is chosen so in order to feasibly achieve 10mm with the chosen PZT actuator. At higher flexure stiffness, the PZT displacement curve drops further, never reaching 10mm. Such low flexure stiffness is detrimental to disturbance rejection capabilities.

This suggests that piezo actuators show significantly higher resonant frequency for small  $N$  (i.e smaller motion ranges). As  $N$  increases, however, the frequency of the MMA and piezo driven systems converge. This means that the advantage of piezo may

be lost for larger amplification. Additionally, a significantly higher amplification ratio may be required than expected to achieve the desired motion range, and in this example, may never be achieved without very low flexure stiffness. This further reduces the system natural frequency.

A second example is examined with a higher payload mass (0.75kg) and higher flexure stiffness (80N/5mm = 16000N/m), for better disturbance rejection. This would be impossible for the PZT actuator selected above to achieve. To assess feasibility, one of the largest PZT stack actuators found offered from PI is selected (Model # P-056.80P), featuring a 570 N/ $\mu$ m stiffness and nominal displacement of 120 $\mu$ m. This actuator is quite large (OD of 56mm and length of 116mm). The assumed system properties are listed in Table 2.4.

*Table 2.4: Actuator and system values assuming PZT actuator model # P-056.80P*

Property	PZT	EM
Actuator stiffness, $K_a$ , (N/m)	570000000	200
Flexure stiffness, $K_f$ (N/m)	16000	16000
Amplification mechanism torsional stiffness, $K_m$ (Nm/rad)	20	20
Amplification mechanism arm length, $L$ (m)	0.1	0.1
Actuator moving mass, $m_a$ (kg)	0.1	0.5
Payload mass, $m$ (kg)	0.75	0.75
Amplification mechanism total mass, $m_m$ (kg)	0.1	0.1
Nominal actuator stroke, $x_a$ (m)	0.00012	0.01
Desired system motion range, $x$ , (m)	0.01	0.01

The resulting first natural frequencies of the amplified piezo and electromagnetic actuators are shown in Figure 2.17. In this case, the 10mm stroke is achieved with an amplification of  $N=125$ . The natural frequency still approaches that of the electromagnetic actuator (40Hz vs. 22Hz), however is a significant improvement.

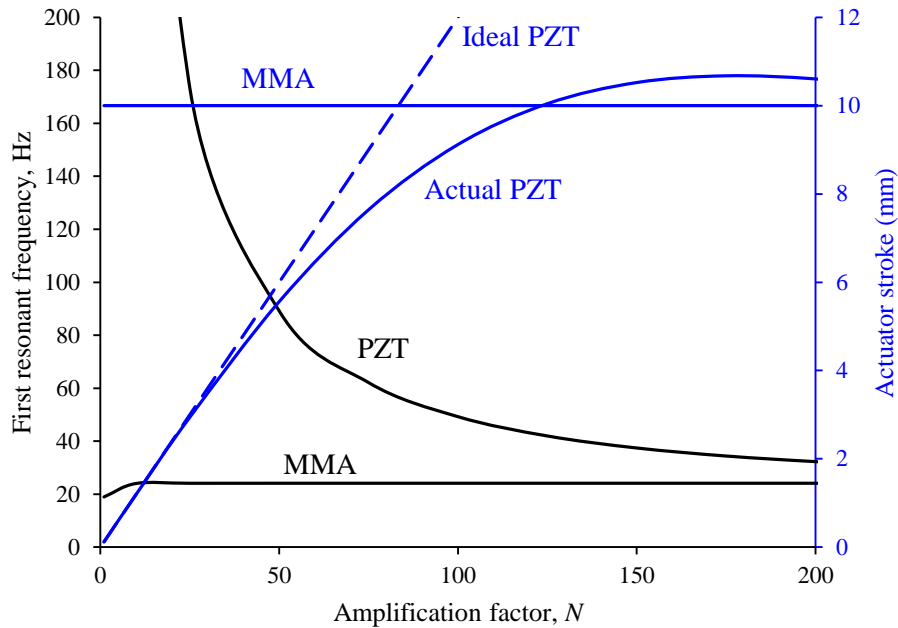


Figure 2.17: First resonant frequency and actuator stroke for an MMA and PZT actuator (Model # P-056.80P)

These examples suggest that for large required stroke, amplified piezo actuators and electromagnetic actuators are potentially comparable selections, if considering only the system first natural frequency. Piezo types may be better assuming large actuator stack sizes.

## 2.4 Piezomotors

Another type of piezoelectric actuator, in general called a piezomotor, overcomes the limited range of piezoceramics by employing a repetitive actuation pattern to generate theoretically infinite displacement. Unlike in piezoelectric stack actuators, which importantly exhibit zero friction during operation, in quasi-static piezomotors, friction is critical in producing the relative motion between the piezoceramic element(s) and a secondary body. The piezoceramic element is often a component of the stator and the

secondary body is the mover. The layout and actuation pattern distinguishes between types, in general quasi-static, dynamic, and ultrasonic. Although some piezomotors come close to meeting large nanopositioning requirements, their general limitation is low speeds and/or poor positioning resolution during travel. A summary of the speed and resolution of some representative prior art surveyed is given in Table 2.5. It shows a general trade-off between speed and resolution.

*Table 2.5: General speed and resolution of piezomotors*

Type	Speed (mm/s)	Resolution <sup>2</sup> (nm)	References
Quasi-static	2-20	1-5	[60], [66], [94], [113]–[119]
Dynamic	20-40	5	[120]–[127]
Ultrasonic	100-800	50-160	[94], [119], [128]–[133]

#### 2.4.1 Quasi-static piezomotors

The quasi-static piezomotor employs a repetitive actuation pattern most often based on either an “inchworm” or “walking” principle. Quasi-static piezomotors are distinguished by the fact that the actuation pattern is driven at frequencies lower than the resonant frequency of the piezoceramic element. The “inchworm” quasi-static piezomotor is arguably the most common type. It was introduced in the 1960’s [134] (see [113] and [97] for detailed history). These actuators function like their name implies, where the motion is generated through a succession of coordinated clamp/unclamp and extension/contraction step cycles [135][136]. While in a clamped position, the

---

<sup>2</sup> This is most often “static” resolution. Resolution at higher speeds is lower.

piezoceramic elements can also be operated in a “fine” positioning mode to achieve small-displacement, high-resolution positioning, analogous to using a standard PZT actuator. Inchworm piezoelectric actuators have long been manufactured by Burleigh Instruments [137][138][139][140]. Another quasi-static type, “walking” quasi-static piezomotors, produce a motion mimicking legs walking. Some products which use this principle include those from PiezoMotor AB [114][115] (shown in Figure 2.18) and PiezoWalk piezomotors from Physik Instrumente GmbH.

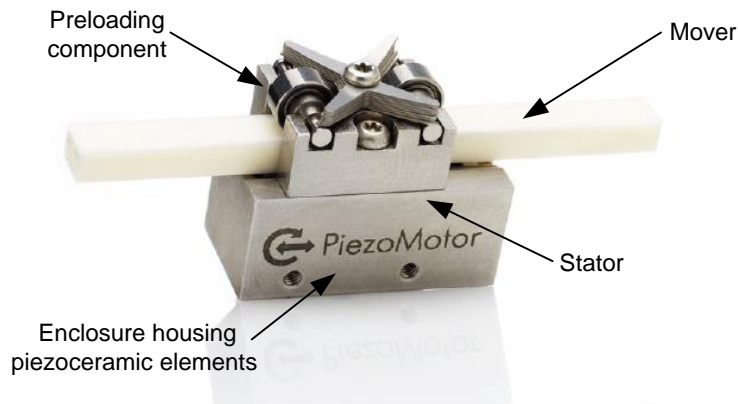


*Figure 2.18: “Walker” type piezomotor from PiezoMotor AB [114][115]*

While these actuators show promise for large range nanopositioning as they can achieve both over a 10mm travel range and nanometric resolution, they suffer from two main drawbacks. The surveyed quasi-static piezomotors types have operating speeds of less than 10 mm/s, significantly below the desired 1m/s requirement. The individual step sizes of the piezomotors are in the range of 10nm to 1 $\mu$ m. Generally, a larger step size enables higher speeds at the tradeoff of lower motion resolution. The speeds of several reported piezomotors are summarized in Table 2.6. For example, the Burleigh products have a maximum speed of 2mm/s. Those listed by PiezoMotor AB [114][115] feature

maximum speeds of 20mm/s and resolution under 1nm (however only in “fine” positioning mode). PiezoWalk piezomotors from Physik Instrumente GmbH feature 1 mm/s speed and 5nm (again, only in “fine” positioning mode) resolution over 10 mm range [116][117]. Another inchworm piezomotor reported by Fujitsu Laboratories for AFM applications has a travel range 5 mm with a minimum step size of 5 nm and a maximum step size of 3 $\mu$ m [118] [119]. It was only used for low speed positioning.

*Table 2.6: Speed and resolution of various quasi-static piezomotors. Note that these values cannot be simultaneously achieved.*

Reference	Speed (mm/s)	Fine positioning resolution (nm)
Burleigh products [113]	2	N/A
[114][115]	20	1
[116][117]	1	5
[118] [119]	N/A	5

The second main drawback of quasi-static piezomotors is that they are not suitable for high-speed scanning dynamic scenarios where nanometric motion quality has to be maintained along the entire motion profile at high speeds. This is because of the impact-induced axial vibrations during steps, often termed as “glitch”, which is typically of the order of 50nm [60][139][100]. The glitch becomes more prominent at higher speeds. Additionally, in addition to axial glitch, according to [139] there is also glitch in the lateral direction on the order of 1 $\mu$ m. Due to glitch, the nanometric resolution specified by many available products can only be achieved in the clamped, non-stepping “fine” positioning mode. The loss in resolution at higher speeds would be unacceptable for scanning applications and does not meet the requirements outlined in Section 1.3. Contamination of the mover surface can also limit practically achievable resolution to tens to hundreds of nanometers [66]. Another concern is the fatigue life of quasi-static

actuators. The estimated life of millions of cycles in [139] translates to a life time travel range as low as 200m in [60]. In the proposed 10mm x 10mm scanning profile, this would limit the nanopositioning system to ~60 full scans before requiring replacement. Actuator life time could be increased at the cost of lowering scanning speeds.

One advantage of quasi-static actuators is their large (up to 500N or more) holding forces [60][66][113][94]. Also, due to spring assisted preloading, no power is consumed or heat generated when holding a constant position.

#### 2.4.2 Dynamic piezomotors

As opposed to quasi-static piezomotors, dynamic piezomotors exploit inertia and the difference in dynamic and static friction to produce discrete “slipping” steps, which may be repeated indefinitely giving infinite range [120]. They are often called impact drive piezomotors. Some of these actuators can achieve faster speeds than quasi-static piezomotors, at the tradeoff of lower clamping forces and larger step sizes. Table 2.8 lists speeds and motion resolution of several reported dynamic piezomotors. Cedrat Technologies SE offers impact drive piezomotors with up to 20mm/s and resolution under 5nm [121][122]. They also list prototype actuators with speeds over 50mm/s, resolution under 1nm, and over 3mm travel range. Speeds of 40mm/s and holding force of 4N and (static) positioning resolution 5nm are reported in [123][124]. Others with smaller step sizes achieve very high resolution, at the expense of slower speeds—5 mm/s, 20mm range, atomic resolution reported in [125][126] (based on patent [141]). In [120], steps were smaller than 100nm with maximum velocities of 2 mm/s. With step sizes down to 40nm, the piezomotor [127] has speeds of 0.2mm/s. However, these actuators

have generally the same drawbacks as quasi-static piezomotors, namely low speeds and high resolution only during quasi-static holding (“fine” positioning) mode.

*Table 2.7: Speed and resolution of various dynamic piezomotors. Note that these values cannot be simultaneously achieved.*

Reference	Speed (mm/s)	Fine positioning resolution (nm)
[121][122]	20	< 5
[121]	50	< 1
[123][124]	40	5
[125][126]	5	< 1?
[120]	2	N/A (100nm step size)
[127]	0.2	N/A (40nm step size)

### 2.4.3 Ultrasonic piezomotors

Ultrasonic piezomotors excite resonant bending modes of a piezoceramic element in the ultrasonic frequency range which combine to produce a repeating elliptical stepping motion. Some of the first were developed at IBM in 1973 [142] and in the former Soviet Union [143], and commercially by Nanomotion [144] (see Figure 2.19). A common application is automatic focus drive for camera lenses. A survey of ultrasonic piezomotors is shown in Table 2.8. While ultrasonic actuators provide much higher speeds (100-500mm/s), they have much lower force capability (<10N) [66][142]. Due to preloading of the piezoceramic element against the guide track, there is a tradeoff between force and speed. For example, in [131], the reported 600mm/s speed with 10N force reduces to 300mm/s for a 50N force. A similar trend is reported in [145].

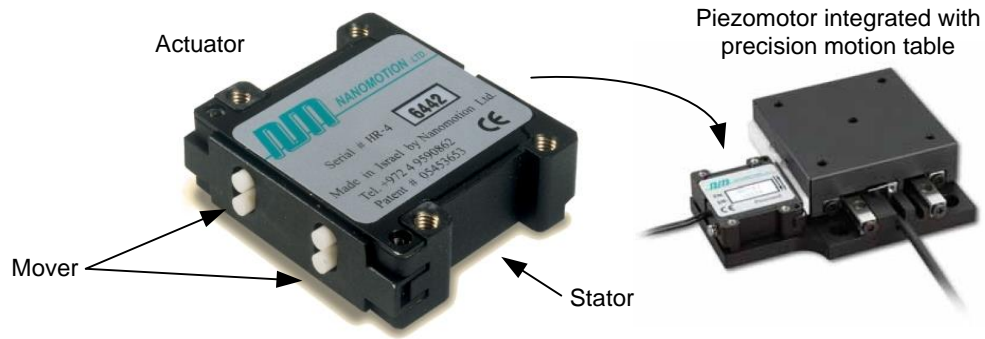


*Figure 2.19: Ultrasonic piezomotor [144]*

Dynamic piezomotors have also been reported driven at ultrasonic resonance to achieve higher speeds. For example, speeds of 800mm/s [146], 280mm/s [145] and 140mm/s [147] are reported.. While ultrasonic piezomotors come much closer to achieving the speed requirement and meet the motion range requirement for large range nanopositioning, the main drawback of ultrasonic motors is that this increase in speed comes at the cost of decreased motion quality [94][142]. Due to the use of resonance or generation of surface waves, they are not suitable for direct precise positioning [120] and cannot simultaneously provide nanometric resolution, large output force and large range [119]. This is validated as shown in Table 2.8. Despite high speeds, the motion resolution is well above the 10nm requirement.

Table 2.8: Ultrasonic piezomotor survey

Reference	Speed (mm/s)	Resolution (nm)	Output force (N)
[128]	500	N/A	5
[129]	600	N/A	6
[119]	470	N/A	N/A
[130]	500	300 (step size)	4
[131]	800	50	5
[132]	250	100	3.5
[133]	100	3000 (step size)	20
[94]	N/A	160	Low

Another drawback is heat generation in the piezoceramic elements when driven at high frequencies. Temperatures have been reported to rise up to 120°C which can degrade performance through depoling of the piezoceramic [142][148]. Additionally, ultrasonic piezomotor electronics can be complex [133]. Like quasi-static piezomotors, they have potentially low fatigue life [60].

## 2.5 Magnetostrictive actuators

According to the analysis in Section 2.2, actuators based on the effect of magnetostriction are also a potential candidate for achieving large range nanopositioning. These actuators have been used in many short stroke (under 100µm) precision applications [149][150]. However, in general, the strengths and limitations of magnetostrictive materials are similar to that of piezoelectric materials, and therefore the actuators have similar challenges in meeting the large range nanopositioning requirements. A good overview and comparison to piezoceramics are found in [151][152][153]. While in theory magnetostrictive materials have the advantage of higher energy densities than piezoelectric materials [95][152], they are more difficult to use

practically [152]. This is reflected by the limited commercial suppliers. According to [152], several additional differences between magnetostrictive actuators and piezo actuators include a higher Curie (i.e. operating) temperature than piezo (380C vs. 165-300C), Higher currents used for control compared to high voltages in piezo, and that continuous current or permanent magnets are required for static displacement unlike in piezoelectric materials which hold charge and therefore displacement.

## **2.6 Electromagnetic actuators**

A moving electron produces a magnetic field, which in turn imparts a force on another moving electron. Actuators that utilize this force form a large and diverse family making classification challenging. An attempt, however, is made here (Figure 2.20). In this section, first the families of magnetic field actuators are described. Of these, several promising types of actuators for large range nanopositioning are identified. These include single phase voice coil actuators, moving magnet actuators, and multi-phase electromagnetic actuators. These three are compared in further detail next. Based on the comparison, the single-phase MMA appears to be the most suitable selection for achieving large range nanopositioning.

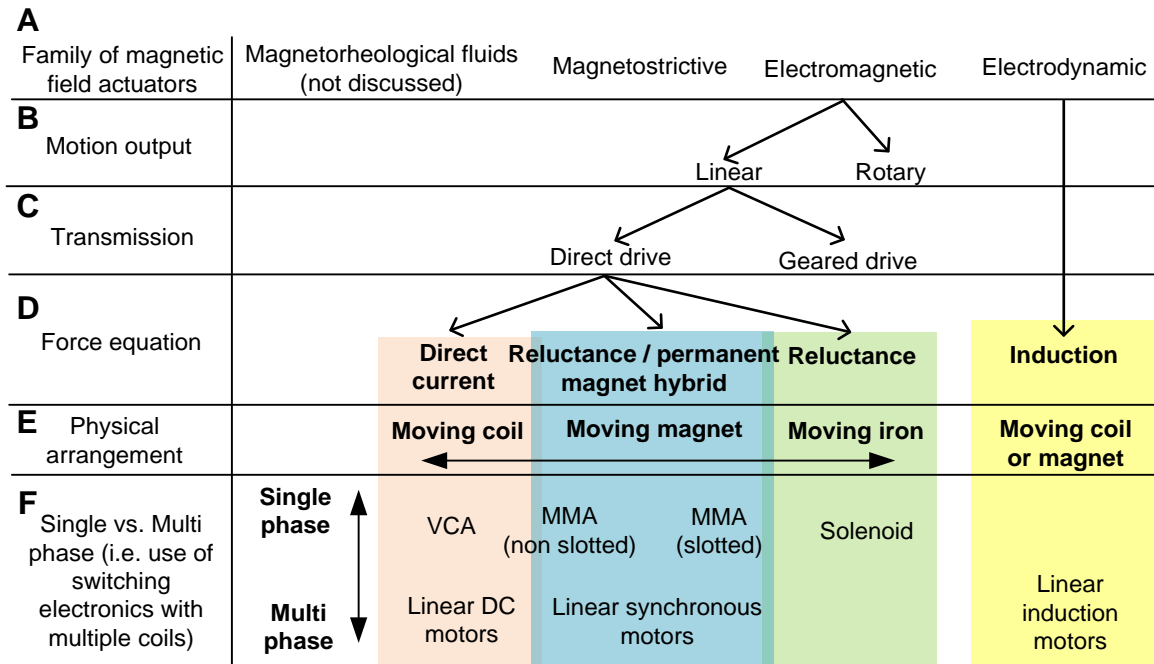


Figure 2.20: (Attempt!) at categorization of electromagnetic actuators

In general, actuators that use magnetic fields can be classified as electromagnetic, electrodynamic, magnetostrictive and magnetorheological (MR) [90][152] (Figure 2.20A). The first two types will be examined in this section. The third type was discussed in the previous section. The fourth type, MR fluids, which are non-permeable fluids with suspensions of magnetizable particles, is not discussed here. Of the first two types, electromagnetic and electrodynamic actuators can generally be further sorted into direct or geared drive, and rotary or linear types [154][155] (Figure 2.20B). Of these, linear direct drive actuators are considered for large range nanopositioning due to the absence of friction and backlash otherwise introduced by transmissions (Figure 2.20C). This category of actuators are especially varied, partly from the customized nature of the applications [154]. There are generally two ways to sort linear direct drive electromagnetic actuators. The interchangeable classification methods can easily lead to

confusion so a visual comparison is attempted. The first categorization method is based on the general force equation of the actuator (Figure 2.20D). This leads to four subcategories; direct current, reluctance / permanent magnet hybrid, reluctance, and induction [154]. The first type uses the Lorentz  $i\ell \times B$  force (where permanent magnets produce a magnetic field in which current carrying wires reside) [90]. Consequently, these actuators are also known as Lorentz force actuators. The second uses a combination of the Lorentz force and the  $1/2 i^2 dL/dx$  reluctance force (where attractive forces between two ferromagnetic materials are produced in order to minimize the magnetic reluctance). The third uses only the reluctance force. The fourth, which more suitably falls under the higher-level electrodynamic actuator family, uses induction (for example, in eddy current brakes where a moving conducting material in a magnetic field experiences a decelerating force due to generated eddy currents). The second categorization method for linear direct drive electromagnetic actuators is by physical configuration (Figure 2.20E). This is often more intuitive. For example, voice coil and non-slotted moving magnet actuators, solenoids, and slotted moving magnet actuators, would fall into three respective subcategories of moving iron, moving coil, and moving magnet actuators [49][156]. These three categories, which are most suitable for large range nanopositioning, are examined in detail in the following sections.

### 2.6.1 Voice coil actuators

Voice coil actuators fall in the categories of direct current or moving coil actuators. A summary of voice coil actuators is given in Section 1.1.2. Besides the VCA shown in Figure 1.4, some common additional configurations are discussed in [157][158][159][13][160][161]. VCAs are used for many high precision motion control applications. This is in part due to having theoretically infinite resolution due to non-

contact construction. The resolution is limited by feedback controller design and amplifier electronics. Some examples of VCAs used for high precision applications include [162], which presents a VCA driven AFM scanner with 1nm resolution, comparable to a PZT actuator also tested. It features 50Hz system open loop bandwidth. However it only has a 10 $\mu$ m range. In [163], a VCA features 4mm stroke with 20nm resolution only limited by the sensor. Reference [11] presents a comparison of VCA and solenoids with 1mm range with resolution below 1nm. The dynamic performance of the VCA in [164] is particularly emphasized. Over a range of 1mm, 2nm static resolution, and 50nm dynamic resolution is achieved. The system open loop bandwidth is 11Hz. Steady state positioning resolution under 4 nm RMS for response to 500  $\mu$ m and 20 nm step commands is shown in [59]. Furthermore, dynamic resolution over a 5mm diameter circle at 1 Hz of 12 nm RMS is achieved. It is important to note most of these references did not state the measured resolution during actuation, only the static resolution. There are also many examples of VCAs used in hard drive read head actuation with very high speeds and precision [37][38][39][160].

Clearly VCAs can achieve the desired nanometric motion quality (~1nm). However, from the examples above, it is not readily apparent if the desired high speed for large range nanopositioning (1m/s) over a 10mm range is possible. As a simple check, BEI Kimco's Voice Coil selection guide [16] is followed to select an appropriate actuator. According Table 1.5, the VCA for 50Hz scanning and 50g stage mass should be able to provide over 25N peak force over 10mm range. As there are no friction and loading forces, only the peak force capability must be checked. Two VCAs listed in the selection guide could achieve this. Model LA15-26-000A [165] has a 45N peak force and 25mm range. However, when the 65g mover is included in the inertial force calculation, the peak force requirement increases to 56N. Therefore, this VCA model does not satisfy

the force requirement, although it comes close. The stroke of this VCA is much longer than required and suggests that with design optimization, the actuator could achieve the force requirement. Alternatively, model LA12-17-000A [166] also has a 45N peak force, however with a smaller stroke (7.6mm). The mover is correspondingly a lower mass (32g). With the mover mass included, the peak force requirement is 40N, which the actuator can provide. In fact, if Table 1.5 is adjusted to account for a 7.6mm range, the peak force requirement (with mover included) is only 28N. This, plus the fact that BEI Kimco's method of estimating maximum acceleration and peak force requirements underestimates values as a safety factor, means that the VCA could be well suited to meeting the speed and range requirements for large range nanopositioning.

Despite these promising qualities, VCAs feature several key drawbacks. One is heat output and thermal management [167]. In a VCA, peak force is generally determined by heat management capability. This has been a long standing problem in speaker design. Heat generated in the coil must be removed through conduction or convection to the air, or through the mover to the motion stage (Figure 2.21a). Heat output to the motion stage is particularly undesirable in precision applications. This is even more pronounced in vacuum environments where there is no convection.

Disturbance from moving wires is another potential drawback of VCA (Figure 2.21a). Non-deterministic disturbance due to the moving coil wires degrades motion quality [168]. For example, moving wire leads has been a well-documented source of disturbance making achieving nanometric motion quality more difficult in hard drive read-head actuators at minimum requiring more complicated control schemes [160], [168]–[172]. Additionally, moving wires can also reduce actuator life and can limit the achievable stroke [168][20].

To overcome the problem of moving wires and heat generation being transported to the motion stage (Figure 2.21a), the voice coil is sometimes employed in an inverted configuration [59][164] (Figure 2.21b). There are no moving wires, and heat flow can be directed away from the motion stage. However, it adds the large mass of the magnet and back iron to the motion stage. For example, for a typical voice coil actuator with a mover mass of ~50g, the field assembly has a mass of ~300g—roughly a six times increase in mass if used in the inverted configuration [33]. The larger mass reduces system open loop bandwidth. For these reasons, VCA is not included as a candidate for achieving large range nanopositioning.

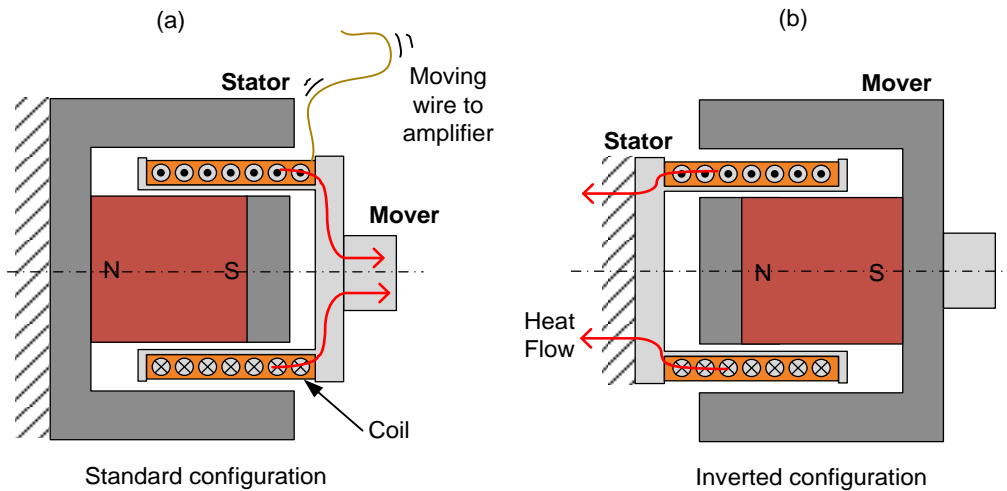


*Figure 2.21: VCA in inverted configuration eliminates moving wires and reduces heat transfer to the motion stage at cost of higher moving mass*

The moving mass of the inverted VCA could be reduced as described in the following thought experiment. By introducing a cut (Figure 2.22a) in the end face of the back iron, the outermost ring of the back iron could be held stationary (Figure 2.22b), significantly reducing the moving mass. However, this new air gap reduces the magnetic circuit flux (hence output force), as well as causes high off-axis forces due to the small

air gap separation. These problems could be alleviated in another step (Figure 2.22c) in which an oppositely wound extension of the coil is introduced in the new air gap. Although the second coil further reduces flux density in the air gap due to the larger effective air gap, the flux now contributes to useful work. Additionally, the larger effective air gap now significantly reduces off-axis attractive forces. This configuration is the moving magnet actuator introduced in Chapter 1, which embodies all the benefits of the inverted voice coil and also has a significantly lower moving mass since the relatively heavy back-iron remains static along with the coil. Furthermore, heat transfer is significantly improved due to the back iron.

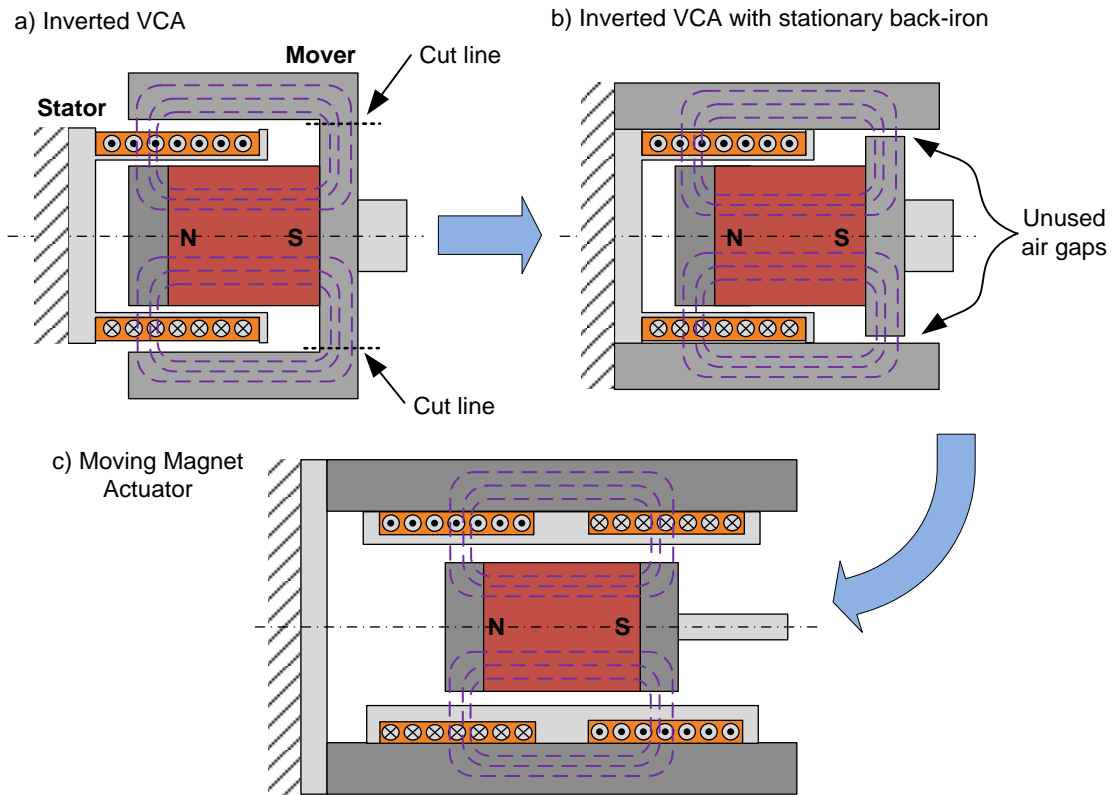


Figure 2.22: MMA derived from VCA architecture

## 2.6.2 Moving magnet actuators

Moving magnet actuators can generally be classified as direct current or reluctance / permanent magnet hybrid electromagnetic actuators, depending on the topology of steel (or lack thereof) in the magnetic circuit. This forms the general variations of slotted, non-slotted, and coreless / ironless architectures discussed below. All MMAs benefit from improved heat dissipation, heat isolation from the motion stage, and no moving wires. They are therefore truly non-contact, frictionless actuators. While the mover is usually heavier than an equivalent VCA, it is significantly lighter than a VCA used in the inverted configuration. Given the general trends below, and more

detailed discussion in the next chapter, MMAs are deemed to be best suited for achieving large range nanopositioning compared to other actuator types. The single phase, non-slotted MMA architecture is of particular interest.

Tradeoffs associated with slotted, non-slotted, and coreless architectures are detailed in Chapter 3, however a brief description is given here. Slotting refers to the introduction of ferromagnetic material around the coil windings to increase magnetic circuit flux. This results in higher volumetric force and higher accelerations, speeds, and load bearing capability. However, the tradeoff is that slotted MMAs have higher cogging forces i.e. large variations in output force over stroke. The higher magnetic fields can make the coil self-inductance, magnetic hysteresis and eddy current losses larger, increasing power requirements and potential force response lag. Ironless or coreless topologies feature no ferromagnetic material besides the magnet, having neither a core, back iron, or slotting. This eliminates hysteresis, off-axis attraction, eddy current generation and cogging at the expense of a lower force output. Many MMA designs compromise between the two, for example, the traditional MMA has a core and back iron, however no slotting, which improves volumetric force output but introduces some cogging [173].

The traditional MMA architecture was introduced in Chapter 1. It is a single phase, non-slotted architecture, with a ferromagnetic back iron and pole pieces. This type falls in the direct current actuator category. In a literature survey of electromagnetic actuators for nanopositioning applications, while there are other related MMA architectures used, surprisingly none using the traditional MMA architecture were found. The main advantages of the traditional MMA over VCA is shown in

Figure 2.23. Given MMAs positive attributes of good thermal management, potential for nanometric motion quality (including lack of moving wires), and >10mm range, perhaps the most significant concern is speed capability, as the mover of an MMA is generally heavier than in a voice coil. It was only with the introduction of Neodymium-Iron-Boron (NdFeB) magnets in the 1980's that made the moving magnet mass comparable to moving coils due to a high remanent magnetization [160][174]. However, the mass of the magnet is still a notable trade-off compared to VCA [19]. Therefore, similar to with VCA, it is checked whether MMA can achieve the speed requirements outlined in Section 1.3.3 following BEI Kimco's actuator selection guide. The only MMA model listed by BEI Kimco is LA16-19-001A [175]. It has 22.4N peak force over 12mm range, which comes close to meeting the 25N inertial force requirement. However, when the 100g mover mass (roughly 2x the mass of the corresponding VCA) is factored in, it results in a 74N force requirement, which the MMA does not achieve. Model NCM03-20-089-2LB [176] from H2W Technologies has a much higher peak force capability of 119N over a 6.4mm range. With the smaller range and moving mass, the peak force requirement is calculated to be 94N, which the MMA adequately achieves. Given that the MMA meets speed requirements, can show nanometric motion quality, has better heat characteristics, no moving wires, and can achieve the desired motion range, the traditional MMA becomes a potential candidate for this work.

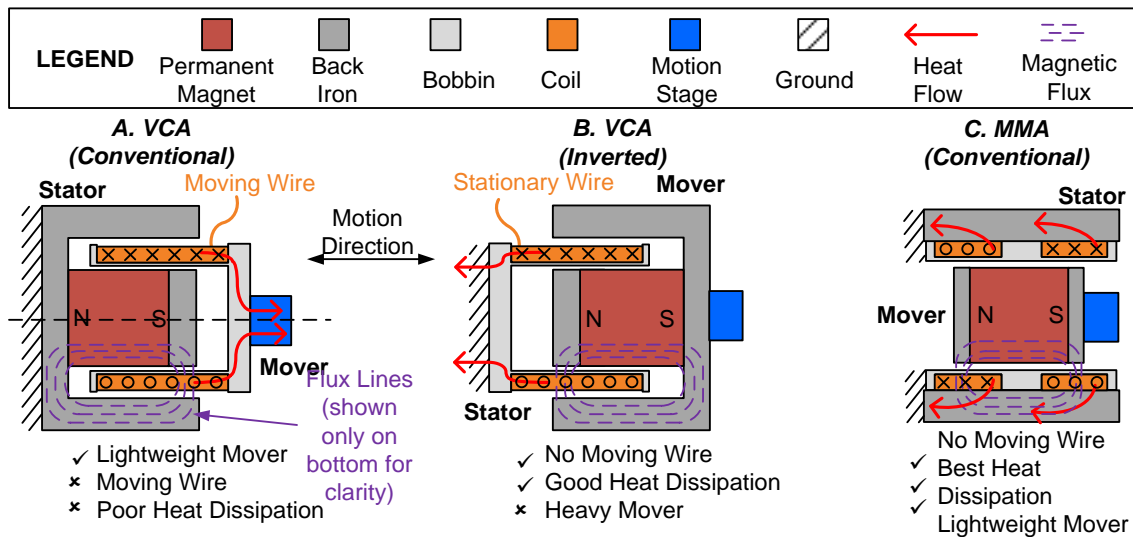


Figure 2.23: Advantages of traditional MMA over VCA for large range nanopositioning

Another common MMA architecture, similar to a linear motor, results when the traditional MMA architecture is “stacked” axially. The main advantage of this design is that the magnetic field is more highly focused in middle pole piece. However for reasons discussed in Chapter 3, this design is less suitable for flexure based systems and presents only a small if any overall improvement in performance to traditional MMA.

Several MMAs found in the literature for nanopositioning are of the ironless / coreless “air core” type. They are used either for 2-axis XY motion or simultaneous Z-direction magnetic levitation bearing force with single axis actuation. For example, the “air core” MMAs in [177][56][178] presents 5 nm resolution, velocity of 0.5 m/s and acceleration of 30 m/s<sup>2</sup>. Power consumption is only 15 mW per actuator. This is over a small motion range of ~200µm, however. Several others include [61][87][179] which also achieve nanometric motion quality. Therefore this type of MMA is also selected as a potential candidate.

Another common type of MMA is single phase with a slotted configuration. This architecture is very often seen in compressor type applications, for example cryocooler [180] and artificial heart pumps [181]. As discussed in Chapter 3, while this configuration achieves high speeds and large range, it is not generally suitable for fine position control [93] as its force over stroke profile is highly variable, similar to that of a solenoid. Therefore this design is not selected.

### 2.6.3 Multi-phase electromagnetic actuators (linear motors)

The actuators discussed so far have been single phase, meaning the actuator has only one set of independent coil windings. However, the magnetic circuits can also be used in multi-phase configurations. Replicating either the coil windings or the permanent magnets along the stroke axis can overcome the inherent finite stroke of VCA and MMA. This is a particularly interesting point given the large motion requirement in this work. The coils are often commutated using brushes, Hall-effect sensors, or feedback from position sensors [182]. In general there are linear induction motors (electrodynamic type) which feature moving coils, linear DC motors, which are also often moving coil, and linear synchronous motors, which are often moving magnet (Figure 2.20). A good overview of the different configurations is found in [183]. In this section, linear synchronous motors, or in general permanent magnet linear motors, are discussed. This is because they have no moving wires that must travel over long distances and can cause motion disturbance. They are also brushless, which eliminates friction.

One general non-slotted permanent magnet linear motor can be envisioned by taking the “stacked” MMA topology and repeating the windings axially. Examples include [184][185][53][58]. Halbach array topologies are also commonly used as they are

self-shielding (meaning the magnetic flux is self-contained inside of the actuator reducing stray magnetic fields into the environment) and can have higher flux densities [186] which improves power efficiency [92]. Examples of Halbach array types include [187][88]. A slotted permanent magnet linear motor is envisioned by axially replicating the single phase slotted architecture described in Figure 3.8. Examples include [51] and [188]. Due to slotting, the small air gap has a high magnetic field (0.6–0.8 times the magnet’s remanent magnetization) [182]. Similar to single phase slotted MMAs, the velocity and acceleration capabilities of such motors are typically around 4m/s and 50m/s<sup>2</sup>, and the closed-loop position bandwidth may be around 30 Hz [49].

While these multi-phase actuators have the potential for infinite motion range and high speeds, they are not necessarily best suited for large range nanopositioning. One reason is simple, in that many single phase architectures can already provide the required ~10mm stroke. Additionally, the drawbacks of cogging still remain [17][185][55][49][189]. These can be minimized in slot-less stator constructions, however there will still be force ripple due to winding variation. Multi-phase windings also require the use of more complicated electronics and controls for phase switching [25][92].

#### 2.6.4 Additional electromagnetic actuator types

As mentioned earlier, electromagnetic actuators form a large and diverse family. Besides the main types mentioned so far, there are other designs as well. For example, Sawyer motors are well known for their versatile XY motion capability. However, they suffer from inherent cyclic errors as well as constraints imposed by the umbilical cord [190][191]. Pure reluctance types such as solenoids are generally not used for fine

position control due to their inherent instability, uni-directional force output (or use of return spring), and non-linear force over stroke response [20]. However these have also been explored [192].

## **2.7 Conclusion**

Several actuator classes are considered in meeting requirements for large range nanopositioning, namely motion range, motion quality, speed, and temperature stability. Based on qualitative and quantitative comparisons, the most promising actuators are narrowed down to piezo stack actuators with motion amplification, and single phase linear electromagnetic actuators of the moving magnet type. Magnetostrictive actuators are considered, however they are a less promising choice compared to piezo. Amplified piezo stacks and moving magnet actuators appear similar within order of magnitude estimates when considering system natural frequency, scanning speeds, and point to point positioning rise time. PZT have generally higher power efficiencies, however electromagnetic actuators can come close. Piezo actuators feature high resolution in open-loop control, however electromagnetic types are comparable when operated in closed-loop control (and in this application would be implemented regardless). Electromagnetic actuators feature more desirable stroke lengths, enabling direct-drive operation and eliminating the need and complexity for a flexure-based amplification mechanism. This may enable more design flexibility as well. Given the close competition, MMA is chosen in this work. The general conclusions from this actuator overview are shown in Figure 2.1.

## **CHAPTER 3: Prior art concerning moving magnet actuators**

Moving magnet actuators (MMA) are chosen as the best potential candidate for achieving large range nanopositioning, however they present a wide variety of topologies and design possibilities. While appearing relatively simple, these actuators can be deceptively challenging to design, as many design considerations such as linearity of force over the stroke, hysteresis, coil inductance, off-axis instability, heat management, manufacturability, etc. become important. These design considerations are described in more detail in Chapter 4. These are especially important given that there appear to be no major advantage between some configurations of magnet and coils in terms of force production [160]. As well put in [14], “almost any design can be made to work, but not very well.”

Therefore, in this chapter, in preparation for designing an optimal actuator for large range nanopositioning, prior art of MMAs along with their possible advantages and disadvantages are discussed. Some prior art in voice coil actuators and coil design is also presented, as these ideas could be incorporated in MMA design. From the variety of actuators considered in this chapter, an MMA of conventional architecture (first introduced in Chapter 1) is selected.

### **3.1 Common MMA architectures**

Despite the wide variety of MMA topologies and configurations, MMAs in the prior art can be sorted into four general categories. The architectures are referred to here

as traditional, linear motor, ironless / coreless, and slotted compressor designs. These designs are differentiated in part by how ferromagnetic materials such as steel are used in the actuator's magnetic circuit, giving rise to slotted, non-slotted, and coreless architectures. Slotting is first discussed.

### 3.1.1 Slotting

As mentioned in the previous chapters, slotting in an electromagnetic actuator refers to the introduction of ferromagnetic material around the coil windings to increase magnetic circuit flux. The main trade-offs of slotted, non-slotted, and coreless architectures are discussed as it appears to be one of the main factors affecting performance. The trade-offs are summarized in Table 3.1. In general, a slotted MMA has higher volumetric force output at the expense of higher cogging forces. Cogging forces act on the mover to “restore” it to a certain position which can be undesirable for large range nanopositioning (see Section 4.1.1). Non-slotted and coreless designs have reduced cogging forces at the expense of lower volumetric force output. Slotting is found in both single and multi-phase designs. The higher volumetric force of slotted MMAs compared to coreless designs is apparent in Figure 3.1, in which actuator force output per volume for slotted and non-slotted designs is compared [193].

Table 3.1: General trade-offs of slotted, non-slotted, and coreless MMA architectures

	Slotted	Non-Slotted	Coreless (i.e. ironless)
Pros	<ul style="list-style-type: none"> <li>• High volumetric force output</li> </ul>	<ul style="list-style-type: none"> <li>• Low cogging</li> <li>• Low coil inductance</li> </ul>	<ul style="list-style-type: none"> <li>• No cogging</li> <li>• No/low hysteresis</li> <li>• No off-axis attraction</li> <li>• Low coil inductance</li> <li>• Multi-axis motion easier to implement</li> </ul>
Cons	<ul style="list-style-type: none"> <li>• Cogging / force ripple</li> <li>• Hysteresis</li> <li>• Off-axis attraction</li> <li>• High coil inductance</li> <li>• High eddy current losses in iron and magnet</li> </ul>	<ul style="list-style-type: none"> <li>• Off-axis attraction</li> <li>• Moderate hysteresis</li> <li>• Higher coil inductance</li> <li>• Higher eddy current losses in iron and magnet</li> </ul>	<ul style="list-style-type: none"> <li>• Low volumetric force output</li> <li>• Possible higher force variation due to lack of flux focusing</li> <li>• Without back iron actuator is not magnetically shielded</li> </ul>

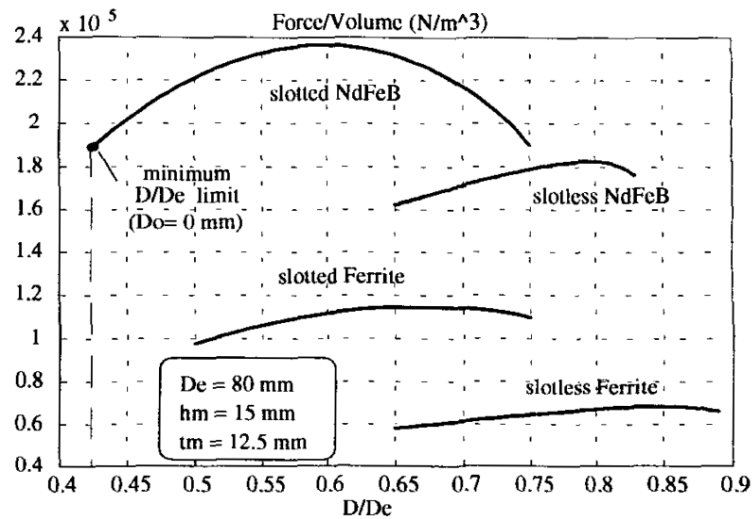


Figure 3.1: Volumetric force output dependence on magnet material and actuator dimensions (inner actuator diameter,  $D$ , and outer diameter  $D_o$ ) for slotted vs. non slotted MMA architectures [193]

In the slotted MMA (see MMA compressor example in Figure 3.8), coils are recessed in the back iron to decrease the effective magnetic air gap. This significantly increases circuit flux density and force output. By introducing slotting, non-slotted MMA architectures such as the MMA introduced in Chapter 1 (see Figure 3.2) would also have these benefits. The higher volumetric force of slotted MMAs enables higher accelerations, speeds, load bearing capability, etc. The increase in volumetric force output comes at a cost, however. One is higher cogging forces, which can cause higher order harmonics in the force output which are detrimental to positioning resolution (see Section 4.1.1). These cogging forces are known as force ripple in multi-phase slotted designs. Cogging can be very high, resulting in large variations in output force over stroke, as discussed for single phase slotted MMAs. Through various design methods cogging can sometimes be reduced. For example, in multi-phase slotted MMA designs, cogging can be reduced by skewing the coils or magnets in the axial direction (picture the coils forming a shallow spiral instead of rings) [182][194], using semi-closed slots or magnetic slot wedges, varying air gap length, or using fractional slots per pole [17]. While the increased presence of iron in slotted designs enables the coil magnetic field to be much stronger (due to a lower reluctance path), this can make the coil self-inductance much higher. Higher inductance slows down the current rise which may increase heat generation and reduce acceleration [160]. Also, the increased iron will lead to higher magnetic hysteresis and eddy current losses due to stronger changing magnetic fields. This can increase power input and introduce force response lag.

Some MMA designs, known as coreless topologies, feature no ferromagnetic material besides the magnet, having neither a core, back iron, or slotting (see example in Figure 3.5). This is the other extreme compared to slotted architectures. Coreless topologies result in a lower air gap flux density and therefore lower volumetric force

output (Figure 3.1), however cogging is eliminated. Despite this advantage, it should be noted that variation of force over stroke may be more pronounced due to less flux focusing in the air gaps.

Many MMA designs incorporate features between the two extremes of slotted and coreless and are referred to as non-slotted designs. For example, the traditional MMA has a core and back iron, however no slotting, which improves force output but does introduce some cogging [173]. The traditional design is discussed next.

### 3.1.2 Traditional MMA architecture

The traditional MMA architecture (Figure 3.2), was introduced in Chapter 1. It is a single phase, non-slotted design with ferromagnetic back iron and pole pieces. The MMA can therefore be classified in the direct current (DC) actuator category. The traditional single phase non-slotted MMA forms the basis of the patent [195].

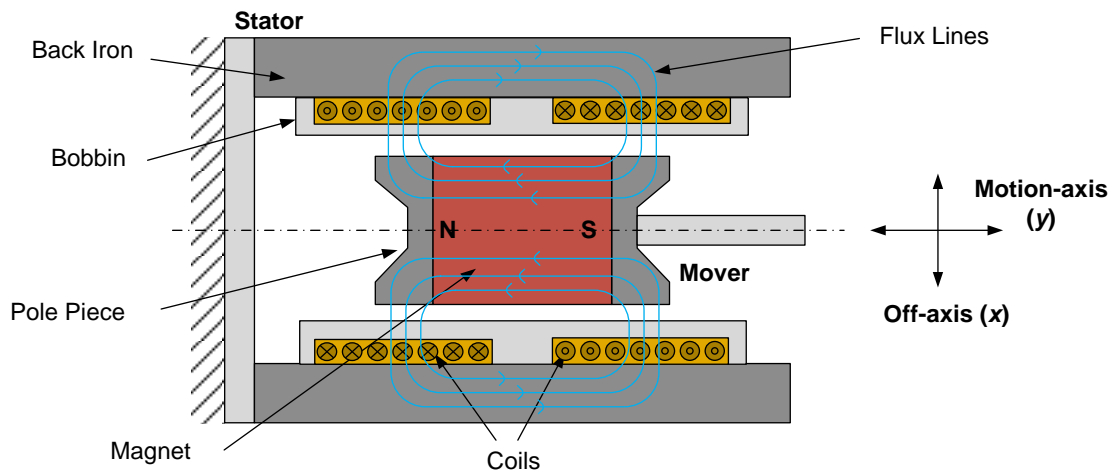


*Figure 3.2: Conventional MMA cross section*

This design features several important characteristics and design considerations. The coils are oppositely wound and therefore the net coil magnetic flux tends to oppose and cancel out. This minimizes armature reaction (i.e. effect of coil magnetic field on permanent magnet circuit, see Section 4.1.2) and coil self-inductance. However, fringing magnetic flux crossing coils through the oppositely wound coils should be minimized. Cogging forces are only from the back iron and are generally linear over the mover's stroke. This can be reduced by extending the back iron length (imagine an infinitely long length—the mover would experience no net axial force due to back iron attraction). Changing magnetic flux in the back iron introduces hysteresis in the current response and mover force, however it is much less than slotted designs. Overall, this architecture features a good balance of force uniformity and force density, design simplicity, manufacturability, low armature reaction and good mechanical interface. Based on this, and compared to other prior art, the traditional MMA architecture was chosen.

### 3.1.3 Linear motor MMA architecture

Another common MMA architecture results when the traditional MMA architecture is “stacked” axially as shown in Figure 3.3. This is a typical configuration for tubular linear motors as discussed previously. The main advantage of this design is that the magnetic field is more highly focused in middle pole piece. Another variation of this architecture uses multiple magnets and magnetization directions, similar to a Halbach array [196].

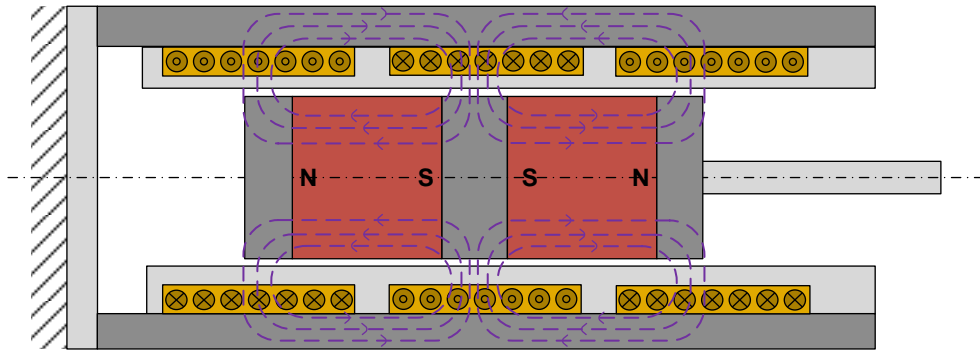


*Figure 3.3: Stacked MMA architecture*

This is the same concept as the “flux focusing” configuration of patent [197] in Figure 3.4. It consists of three coils (2A,B and C) and two magnets (5A and B) sandwiching a central pole piece (6). As mentioned before, the oppositely poled magnets concentrate flux in the center yielding a very high magnetic field (0.6–0.8 times the magnet material’s remanent magnetization value) [182]. Also, due to the flux concentration, fringing in the middle coil may be reduced, leading to better force consistency over the stroke.

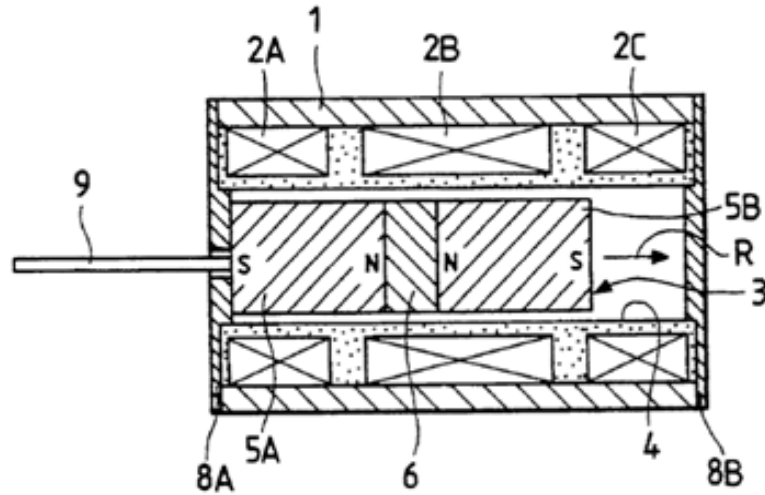


Figure 3.4: Flux focusing MMA [197]

However, this design may not offer a significant performance increase over the traditional MMA. The use of two magnets significantly increases moving mass. If designed without end pole pieces there is a net weight advantage over two traditional configurations stacked on each other, however, this could increase the drop in force over stroke. This would counteract the improvement gained from focusing of flux at the center pole piece. This design is also much longer axially, which increases off-axis torques on the bearing and may require a stronger mover shaft or support from both ends.

#### 3.1.4 “Air” core MMA architecture

Several MMAs found in the literature for nanopositioning are “air core” or coreless / ironless types. This means that besides the magnet there is no magnetically permeable material, including back iron, pole pieces, or slotting. The lack of iron core decreases flux density and force output. Ironless designs can be used to provide 2-axis motion or simultaneous magnetic levitation bearing force with single axis actuation.

The ironless designs in [61][87][179] (Figure 3.5) enable 2-axis motion, in which the mover can travel in the radial direction ( $r$  direction in Figure 3.5) while simultaneously actuated in the axial ( $z$ ) direction. This design is similar to the traditional MMA without a back iron which can therefore tolerate radial displacements. This configuration likely has less consistency of force over the stroke due to fringing. Several high precision applications of this architecture were found, which were listed earlier. [61] achieves  $100\mu\text{m}$  cube travel range,  $\sim 100\text{Hz}$  bandwidth, and nanometric resolution. [87] reports  $100\text{nm}$  accuracy over  $2\text{mm}$  range. [179] has a rotation and translation axis  $80\mu\text{m}$  and  $3.6\text{ mrad}$  and under  $1\mu\text{m}$  positioning noise which is limited by the electronics.

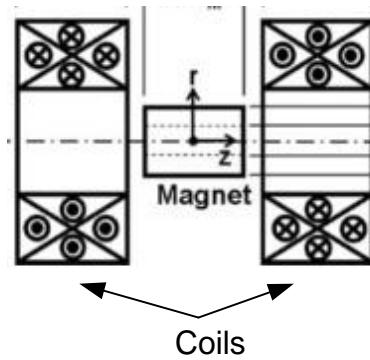


*Figure 3.5: Air core” MMA allows both axial and radial motion*

Another ironless design produces force along two axes using two separate coils. One axis is used for the levitation force in a “maglev” bearing and the second is for positioning actuation. The trade-offs associated with coreless designs hold, and force over stroke may be especially inconsistent. Additionally, due to the arrangement of the coils, flux linkage between them (i.e. mutual inductance) could pose a disadvantage in the design of the control system. [177][56][178] achieves  $5\text{ nm}$  resolution, velocity of  $0.5\text{ m/s}$

and acceleration of  $30 \text{ m/s}^2$  over a range of  $\sim 200\mu\text{m}$ . Power consumption of 15 mW per actuator. Figure 3.6 and Figure 3.7 illustrate two examples of this concept.

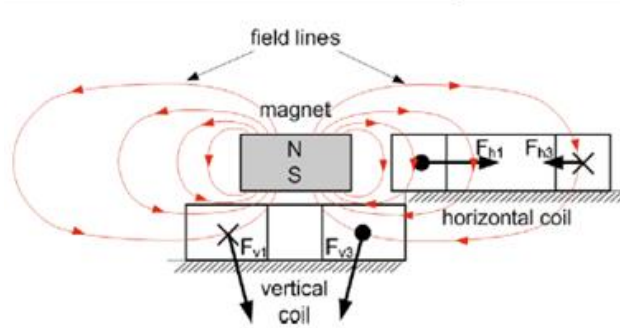


Figure 3.6: Two axis MMA with maglev force and axial motion [177][56][178]

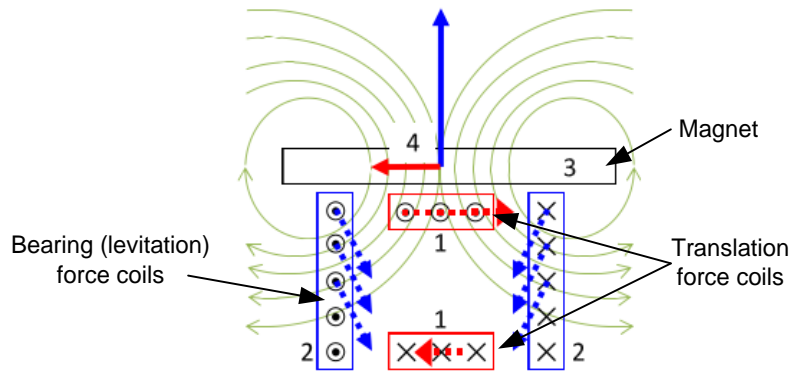
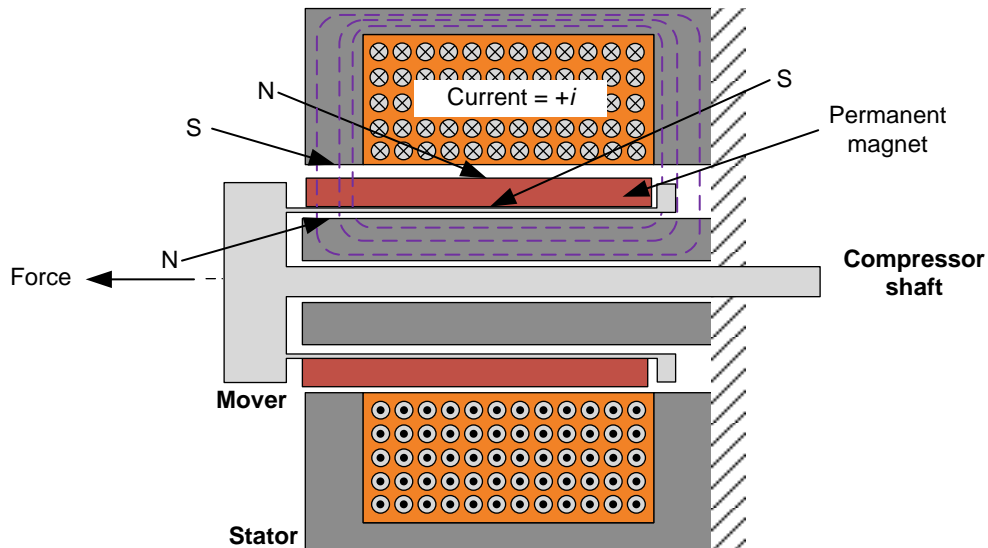


Figure 3.7: Two axis MMA with maglev force and axial motion [57]

### 3.1.5 Slotted MMA (compressor architecture)

Another common type of MMA is a single phase slotted configuration like shown in Figure 3.8. Slotting significantly increases the flux density and force output compared to other architectures. This configuration is commonly called an MMA, however it

should be noted that it is much different than the traditional MMA mentioned above. It is not strictly a direct current type, as the slots which carry the magnetic flux by a recessed coil interact with the magnets, not the coils “directly”. It is probably better classified as a reluctance / permanent magnet hybrid. Additionally, there is only one coil winding instead of two oppositely wound coils. It is however, still a single-phase actuator. A radially oriented ring magnet experiences an axial force as it aligns itself with the magnetic flux loop formed in the iron stator around the coil. One drawback of this is that the full magnetic field of the mover is not used throughout the entire stroke.



*Figure 3.8: Slotted MMA for compressor applications showing force direction for positive coil current*

This architecture is very often seen in compressor applications, for example cryocoolers [180] and artificial heart pumps [181]. In these designs, the mechanical natural frequency (dictated by the total moving mass and system stiffness from return spring or cogging force) is matched to the electrical excitation frequency. High efficiencies are achieved by being driven at resonance, as the actuator only does work

against the compressor load and system losses [49]. This helps achieve high speeds over large travel ranges. For example, a compressor in [198] has a stroke of 16mm at 60Hz. [20] reports up to 65Hz over 10 mm.

While this configuration achieves high speeds and large range, it is not generally suitable for fine position control [93] as its force over stroke profile is highly variable due to the slotted architecture, similar to that of a solenoid. For example Figure 3.9 shows the high variation of force over stroke of a heart pump [199] and valve actuator [200]. Similarly, the cryocooler compressor in [201] (29 hz over 6mm range) has 0N force at 0mm displacement which increases to 40N at 6mm displacement. [202] reports similar, and [20] reports a 25% drop in force over stroke. This is also seen in another related slotted MMA configuration [52], [203]–[206] which features two oppositely poled moving radial magnets that form the mover and a stator that is similar to that in Figure 3.8. This results in a linear spring force profile. Several other permutations of the slotted MMA [18], [207]–[210] (patent [211]) and Halbach array versions [190], [212]–[214] also have similar characteristics.

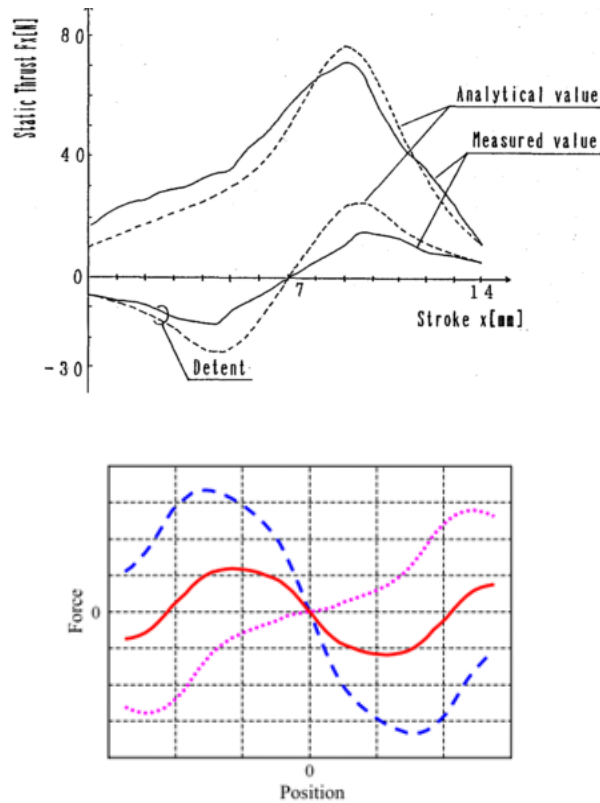


Figure 3.9: Highly variable force over stroke plot of typical slotted MMA [199] (top) [200] (bottom)

### 3.2 Additional MMA architectures and design ideas

Cogging in MMAs can be used as an advantage in some applications. Patent [195] claims selecting the geometry to utilize the cogging force as a magnetic return spring. A VCA version of this idea using magnetic springs is found in [215]. Patent [50] (Figure 3.10) features magnetically permeable material at the axial ends of the back iron so that the mover is attracted to them when traveling away from center position, corresponding to a negative magnetic stiffness as opposed to positive stiffness. This method can counteract the cogging and force loss due to fringing for unidirectional applications as

shown in Figure 3.10a, or eliminate the cogging force for bidirectional applications as shown in Figure 3.10b.

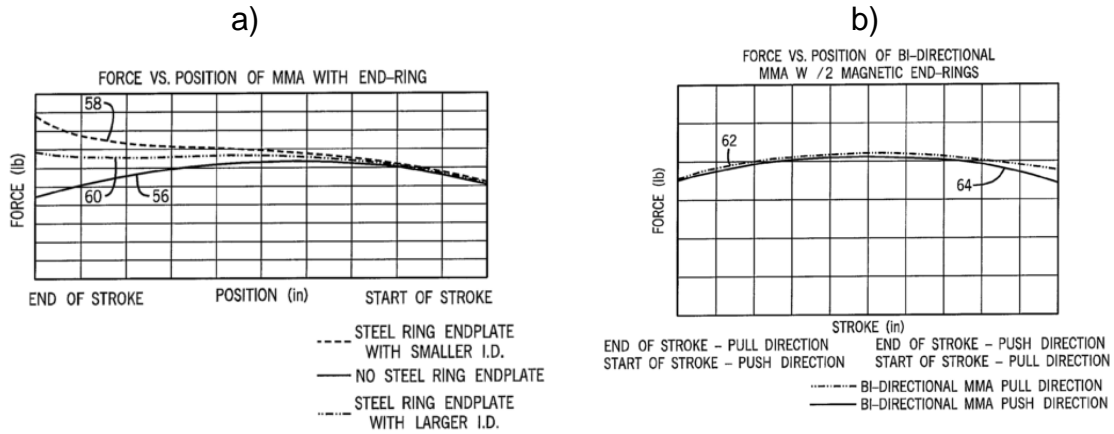
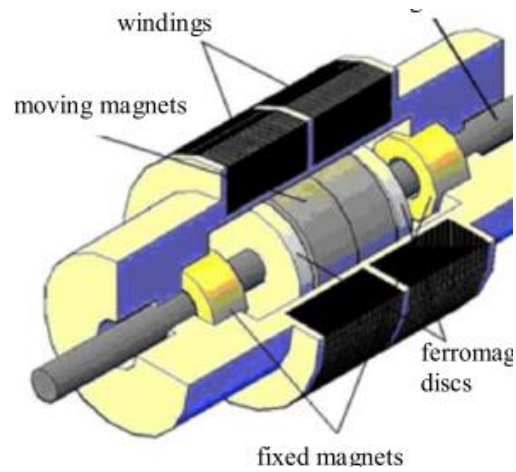


Figure 3.10: Reduction of cogging force via ferromagnetic end plates [50]

A related design described in [156][216][47] features magnets positioned at the MMA axial ends instead of steel rings (Figure 3.11). Instead of an increased attractive force at the end of the stroke to counteract cogging, the magnets create a repelling force. This spring force can increase the resonant frequency of the overall motion system [156]. Potential drawbacks include increased magnetic fields outside of the actuator and increased actuator length.



*Figure 3.11: MMA with fixed magnets at axial ends to increase spring force and system resonant frequency [156]*

Cogging forces can also be actively controlled. Perhaps the most sophisticated method seen giving good real time control of the force stroke profile is shown in [217] (see Figure 3.12). Instead of passive ferromagnetic material or magnets, active coil windings at the end of the stroke reduce the variation of force over stroke, armature reaction, and inductance in a VCA. Drawbacks include increased input power and more complicated control scheme.

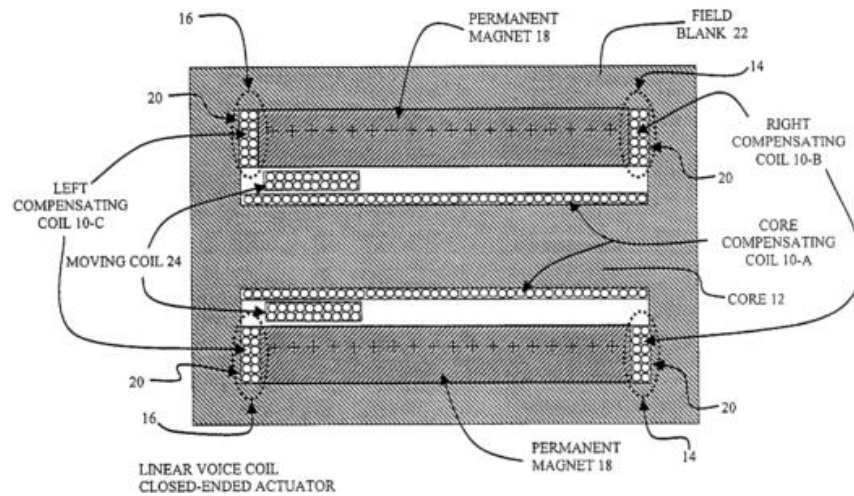
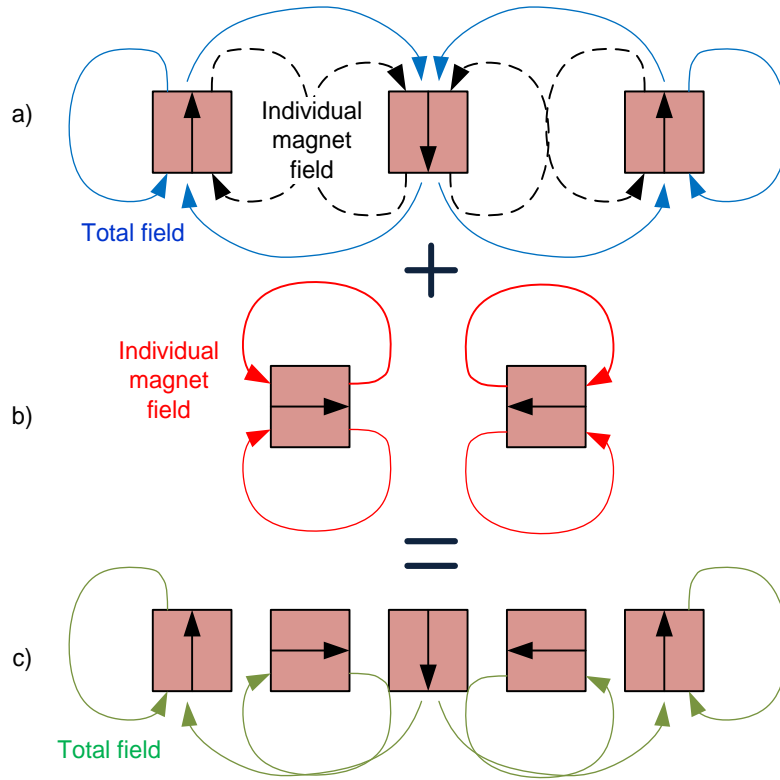


Figure 3.12: Active end coils [217]

Halbach magnet arrays [42] (Figure 3.13) produce a magnet arrangement with essentially no magnetic field on one side, and twice the field strength on the other. This property is interesting because it is somewhat of an approximation of a magnetic monopole, which has not been found in nature. This may add flexibility in a MMA design. The basic Halbach array comprises a magnet arrangement in Figure 3.13a added to the magnet arrangement in Figure 3.13b. The combined field is the “monopole” in Figure 3.13c.



*Figure 3.13: Basic Halbach array*

An interesting embodiment of the conventional MMA, an “inversed” MMA [218], is shown in Figure 3.14. The coil is in the radial interior and a tubular axial magnet with pole pieces ride on the outside. This arrangement enables easy access to the mover, eliminates the need for a cantilever shaft connecting the mover to the motion stage, and exposes the coils to better air flow resulting in better cooling. This arrangement still has the advantage of little armature reaction due to the oppositely wound coils. However the inner core is susceptible to saturation due to a much smaller cross sectional area, which would limit force capabilities. It is also not self-shielded as significant magnetic field lines may be external to the actuator.

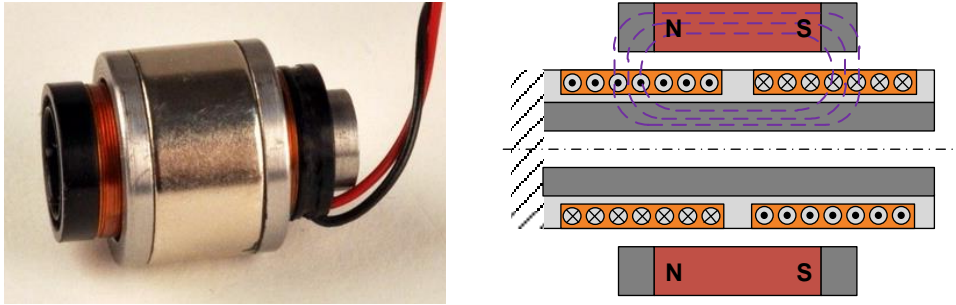


*Figure 3.14: Inversed MMA [218]*

Following this design direction, an MMA as shown in Figure 3.15 can be envisioned. As compared to the above design, for the same mover size, this would reduce the flux through the center by roughly half, and ensures that any flux leakage around the outside diameter in above is utilized by placing the extra coils. Some drawbacks of this of course are larger actuator diameter, higher complexity, and the advantage of easy mechanical interface is lost.

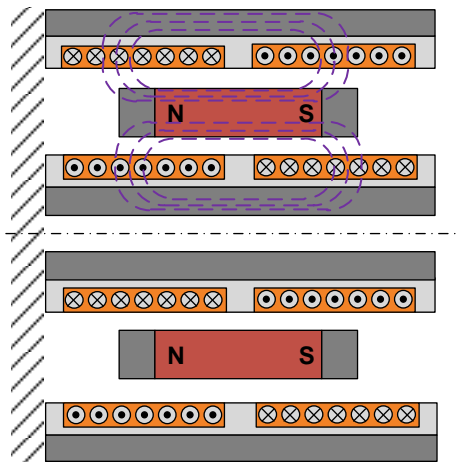


*Figure 3.15: Stacked inverted MMA*

All MMAs presented so far use axially magnetized magnets. However, several existing designs use radially oriented magnets, or combinations of both types. It should be noted that in general, it is more difficult to magnetize and assemble radial magnets [182]. Ring magnets may also have lower remanent magnetization because it is more difficult to create a radial field when magnetizing the sintered magnetic material. Arc segments can be used to approximate a ring, however the assembly is more complicated and may require a keeper ring which increases the air gap.

The MMA in Figure 3.16 has a mover consisting of two radially-oriented ring magnets which move along a central stationary steel core [219]. This design is analogous to the traditional MMA. However, this design has no pole pieces, which reduces the moving mass. As the center core is fixed instead of moving, total moving mass is further reduced. The center core will be susceptible to saturation, which is avoided in the designs employing axial magnets. The air gaps between the magnets and inner core decreases

circuit flux and hence force output. Furthermore, the air gap is small, meaning there are high radially acting forces between the magnets and inner core. Therefore this design is sensitive and prone to radial misalignment. This also puts large forces on the magnets, which would most likely require a structural support like a ring. A ring will also increase the air gap size, reducing force output. Good mechanical interface with the mover may be difficult to achieve. The additional coil could increase the inductance, however because it is oppositely-wound, it may actually be lower. A derivation of this design features a moving central core which eliminates the inner air gap and reduces off axis attraction in [48][220].

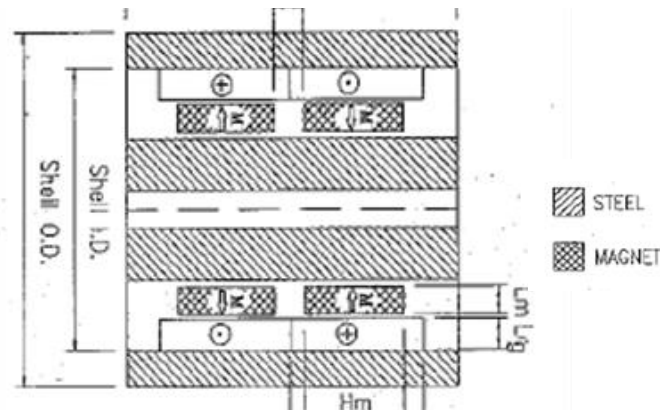


*Figure 3.16: Radial magnet configuration [219]*

Patent [221] shown in Figure 3.17 is similar to that of Figure 3.16 only it replaces the steel central core by an axially oriented magnet (44) sandwiched between the two radial magnets (40, 42) to act as a pathway for magnetic flux. This is essentially a Halbach design, where the interior of the mover has a very low magnetic field. Also see [212][213][214][190] for similar multi-phase versions. This design avoids inner core saturation, however the effective air gap reluctance increases due to the added magnet.

Assembly of this architecture would be difficult, as the magnets have to be placed near each other with different polarities and cannot be magnetized prior to assembly.

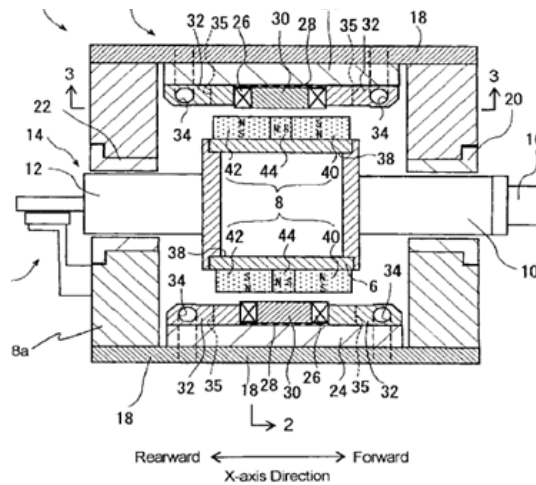


Figure 3.17: Radial and axial magnet [221]

An MMA of planar configuration [55] uses the resulting off-axis reluctance force to provide preloading for an air bearing. This design benefits from using axial magnets compared to ring magnets. The moving iron core has a high moving mass. This configuration has drawbacks associated with planar designs.

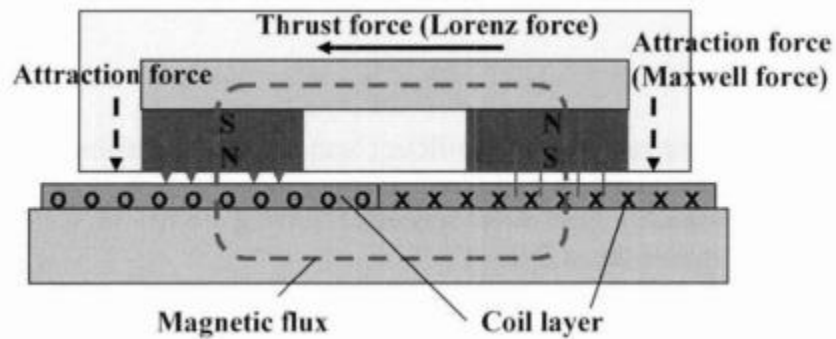
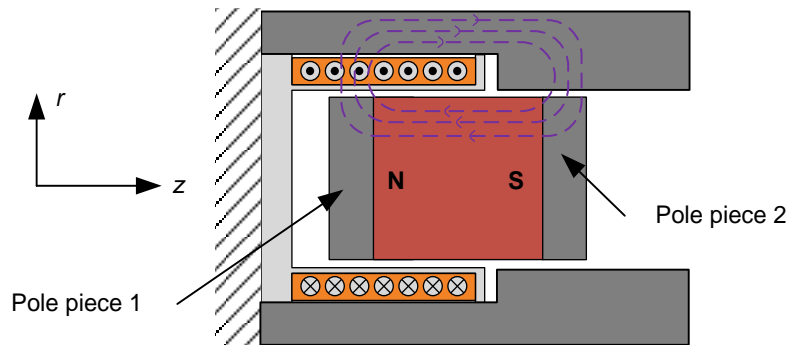


Figure 3.18: Moving magnet provides simultaneous preload for air bearing and actuation force [55]

The MMA configuration in Figure 3.19 can be envisioned during the thought experiment showing how a VCA is related to an MMA (see Figure 2.22). This design has one coil (for pole piece 1) and a step in the back iron to reduce the second air gap for pole piece 2. This results in high off-axis reluctance forces. Another significant potential drawback is increased non-symmetrical axial (and radial!) cogging force between the pole pieces and back iron. There will also be increased flux fringing between pole piece 1 and the back iron.



*Figure 3.19: Single Coil MMA designs*

### 3.3 Voice coil actuator designs

An interesting VCA configuration is the interleaved circuit (Figure 3.20) [222][215][223][161]. It can be seen that in a conventional MMA all flux from the permanent magnet flows through the center core, the back of the stator, and through the outer back iron. By splitting the magnet in half axially and sandwiching a pole piece between them, two separate flux circuits are created with two air gaps. This reduces the flux at all cross sections of the inner core and back iron, enabling higher force. A mover coil with two opposite windings in series (like in the traditional MMA) is employed. Also

due to the opposing coil windings, the inductance and armature reaction is significantly reduced [16].

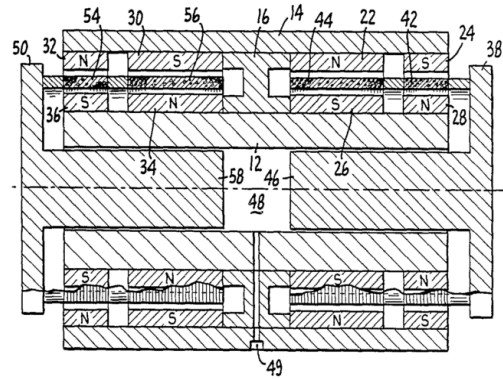


*Figure 3.20: Interleaved circuit designs*

Magnetic saturation can also be reduced by introducing an active end coil [224] in a VCA as shown in Figure 3.21. The active coil current is regulated to counteract the main field in the inner core.

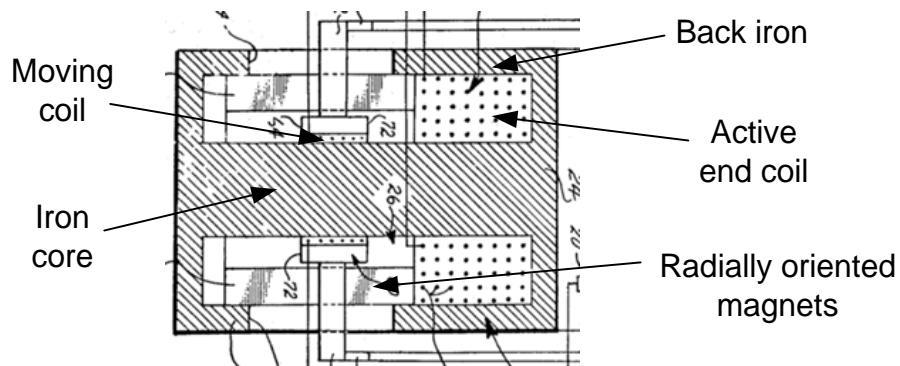


*Figure 3.21: Active end coil to reduce inner core saturation of VCA [224]*

The “flux focusing” VCA configuration (Figure 3.22) can produce higher force than conventional designs. Air gap flux densities equal than or greater than remanent magnetization are achieved [215]. This is done by using two overlaid magnetic circuits

and a small air gap [158]. Another type uses a radial magnet outside of the air gap to focus the flux in the air gap [16].

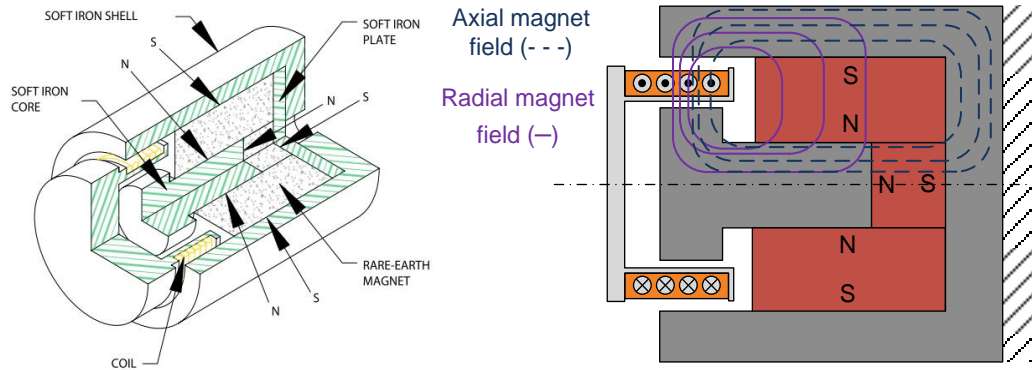


*Figure 3.22: Flux focusing VCA design [16]*

A design featuring concentric coils is presented in Figure 3.23 [225]. According to the patent, it is advantageous to standard VCAs because one magnetic flux circuit can be used to actuate several different coils simultaneously, reducing the total magnetic material. If the coils were constrained together, some additional benefits may include a shorter axial length for the same number of coils than traditional axially stacked VCAs.

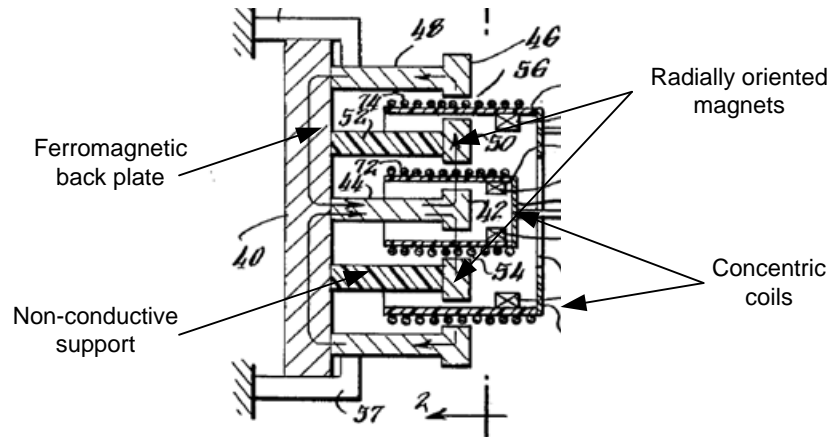


Figure 3.23: VCA with concentric coils [225]

### 3.4 Coil design

In most electromagnetic actuator applications, copper wire is layer wound on a bobbin to form the coil. The wire is round, and is often coated with a bonding agent that when heated after winding, cures to create a rigid coil. Square or flattened wire can increase effective coil density. See Chapter 8 in [2] for a helpful overview on coil design. In this section several ideas that could improve performance over a conventional coil are found in prior art and are described here.

The effective air gap where the coils reside could be reduced (to increase actuator force) by increasing the magnetic permeability of the coil. Several sources have suggested combining ferromagnetic materials with the copper of the windings. The main drawbacks of these methods are that 1) the electrical resistance of iron is over 5 times that of copper so the higher resistance can offset the gain from increased force. The increased heating could damage the insulation and decrease system performance. 2) Iron windings would also increase hysteresis in the coil current 3) Cogging forces could significantly

increase. Reference [226] suggests using pure iron windings. Reference [227] suggests using iron-cored copper wire, as currents flow primarily on the surface. These suggestions are somewhat refuted by [228] in which the effect of iron percentage in iron cored and iron coated wire is investigated (see Figure 3.24). Iron coated type wire (36% ratio of iron by volume) shows a 1.4 times improvement of actuator force with no increase in resistance. However, iron-cored and pure iron wire shows little improvement when resistance is accounted for.

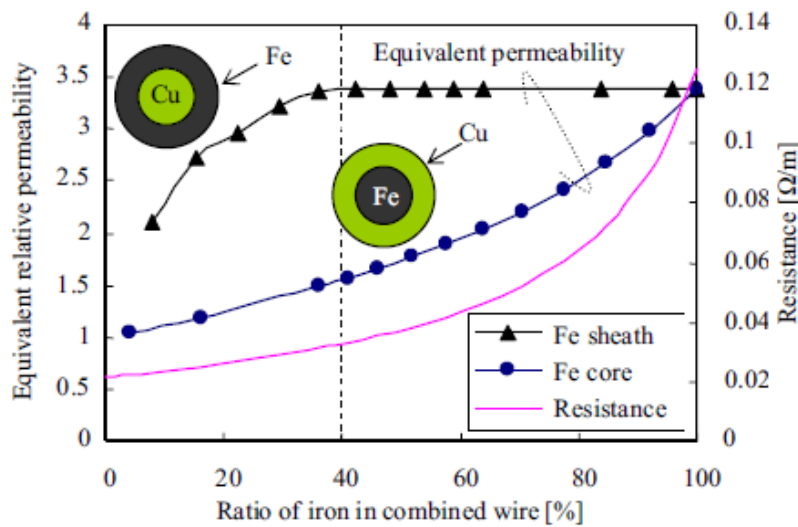


Figure 3.24: Effects of wire composition on air gap permeability and coil resistance [228]

Other ideas include using alternating steel and iron windings [229]. Alternatively, the small air gaps around the windings (assuming circular wire is used) could be filled with a highly permeable material such as iron. For example, the coil could be wound and simultaneously coated or afterwards injected under pressure with a mix of glue and iron powder to both give it rigidity and higher permeability. Simultaneously winding a larger diameter copper wire with a smaller diameter steel wire that fits in the cracks may increase the coil permeability without sacrificing the packing factor.

Most coil designs use rectangular cross sectional areas for the coil space. However, non-uniform coil windings [230] could be used to increase uniformity of force over stroke. Figure 3.25 shows non-uniform coils featuring graduated windings, either by winding axially at different densities (Figure 3.25a) or radially (Figure 3.25b).

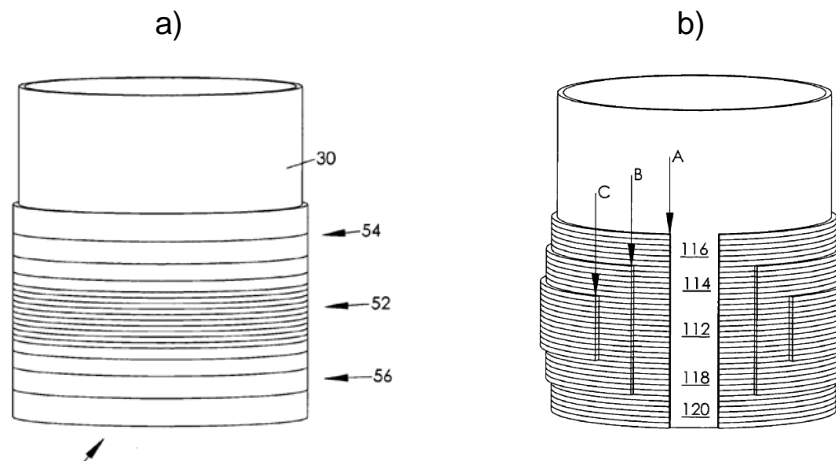


Figure 3.25: Graduated coil windings [230]

Coils also do not necessarily need to be made from wire. Some large range XY precision positioning systems use coils printed on circuit boards for multi-phase actuation [190]. Coils in large electromagnets (called “resistive magnets”) are made from layered plates with coolant pathways to achieve extremely high magnetic fields. The [National High Magnetic Field Laboratory](#) has a 45 Tesla sustainable field magnet (a world record holder) using this technology. Such coils, known as Bitter coils made from stacks of Bitter plates are shown in Figure 3.26a. As seen in Figure 3.26b [231], each plate layer has only one turn, meaning that large currents are necessary to achieve these high magnetic fields. It is usually desirable in actuator design to work with lower currents and therefore more windings, hence the conventional choice of many turns of small diameter wire wound on a bobbin. To achieve more windings using planar coils, several

successively smaller Bitter coils can be stacked inside each other and connected in series like in Figure 3.26a.

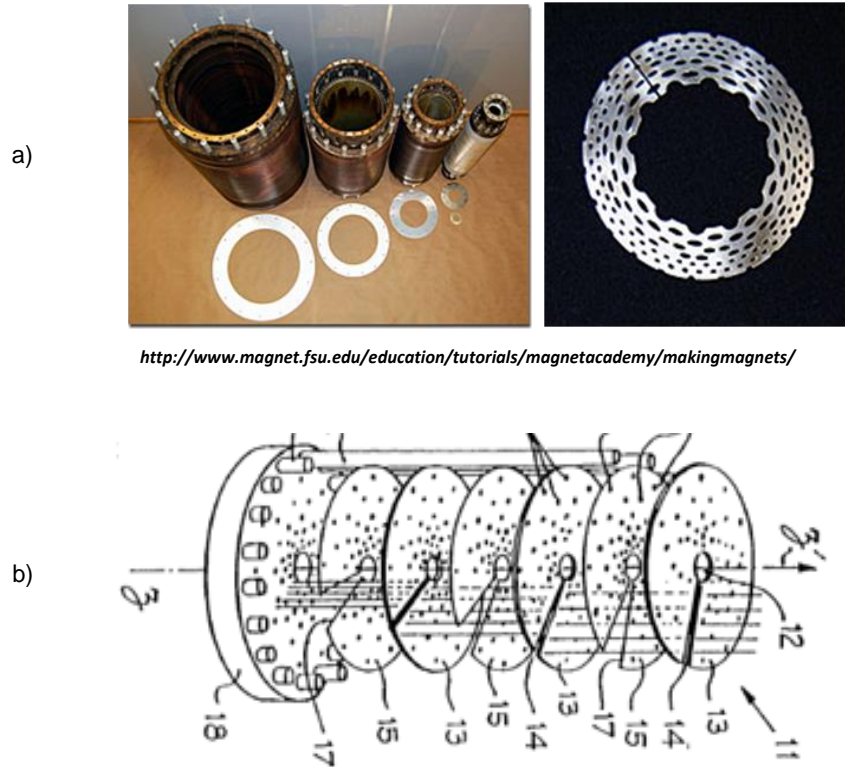


Figure 3.26: a) Bitter plate coils at the U.S. National High Magnetic Field Laboratory and b) Bitter coil patent [231]

## CHAPTER 4: Design considerations and methodologies

As described in the previous chapter, the non-slotted, traditional single phase MMA architecture was selected as the best potential candidate for achieving the desired nanopositioning performance outlined in Section 1.3. In this chapter, important actuator and system design considerations are first highlighted. Relations between actuator-level trade-offs and system-level trade-offs are discussed. Next, various design methodologies and figures of merit used in the prior art are examined. The effectiveness of these design approaches in addressing the actuator and system trade-offs is considered.

### 4.1 Actuator design considerations

This section describes several key MMA design considerations, namely force uniformity over the actuator stroke, use of a shorted turn, armature reaction, magnetic saturation, wire selection, magnet material, and off-axis attraction. Many more subtle design details beyond these which should also be considered. To better understand these details, a breakdown of the factors affecting the seemingly simple Lorentz force equation ( $F = il \times B$ ) is also presented. These topics are comprehensively described in [2].

#### 4.1.1 Force uniformity over stroke

The force profile over the stroke in a conventional MMA results from the superposition of two forces, the force between magnet and coils (Lorentz force,  $il \times B$ ) and force between magnet, pole pieces and back iron (reluctance or cogging force,  $1/2 i^2 dL/dx$ ) [17][232]. The Lorentz force is ideally constant over the mover stroke.

However, in practice this force is generally non-constant, forming an “umbrella” profile due to flux fringing. “Fringing” describes when magnetic field lines spread out in an air gap but are still part of the force-producing magnetic circuit. For completeness, flux “leakage” is when flux lines bypass the force-producing magnetic circuit, reducing overall circuit efficiency (analogous to shorting out a battery). Lower force at the ends of the stroke results in increased power input requirement, especially for flexure based systems where the spring force is largest at the end of the stroke. Force uniformity over the stroke can be improved by reducing the utilized actuator stroke. Alternatively, force uniformity over stroke can be increased by increasing the axial overhang length of the coils. The trade-off, however, is still an increased power requirement.

A quarter view of an MMA (Figure 4.1) shows two effects due to fringing that can reduce the force at the end of the stroke (i.e. increase non-uniformity over stroke). Figure 4.1a shows the MMA at center stroke, where most flux passes through the coil, despite fringing. However, as the mover reaches the end of the stroke in Figure 4.1b, in region I some fringing flux does not pass through the coil, reducing the force output. Additionally, in region II flux fringing from the return path can cross into the wrong coil, further reducing force output.

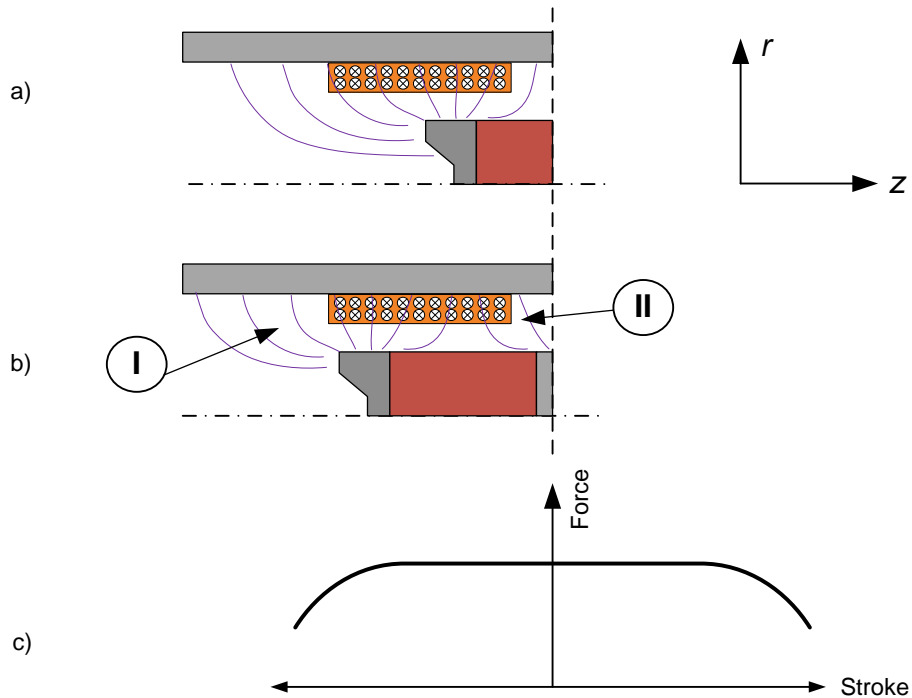


*Figure 4.1: Reduction in force and end of stroke due to fringing*

The second force which contributes to force uniformity over stroke is the reluctance force between the mover and the back iron. The result is the mover has the tendency to center itself axially with respect to the back iron. Figure 4.2 illustrates this effect (coils are not shown). It can be envisioned the magnetic flux has a lower reluctance path in Figure 4.2a as in Figure 4.2b. This means that for a displacement in the negative  $z$  direction, there will be a force in the positive  $z$  direction, and for a displacement in the positive  $z$  direction, there will be a force in the negative  $z$  direction. This results in a force profile of Figure 4.2c. This force is technically a cogging force; however it is much weaker than in slotted motors due to the larger air gaps and hence reduced magnetic fields. It is important to note that in the case where the back iron axial length is made very long, this cogging force is eliminated. It should also be noted that this force is not

seen in VCAs, as the non-ferromagnetic mover is not attracted to the back iron when the current is not applied to the coils.

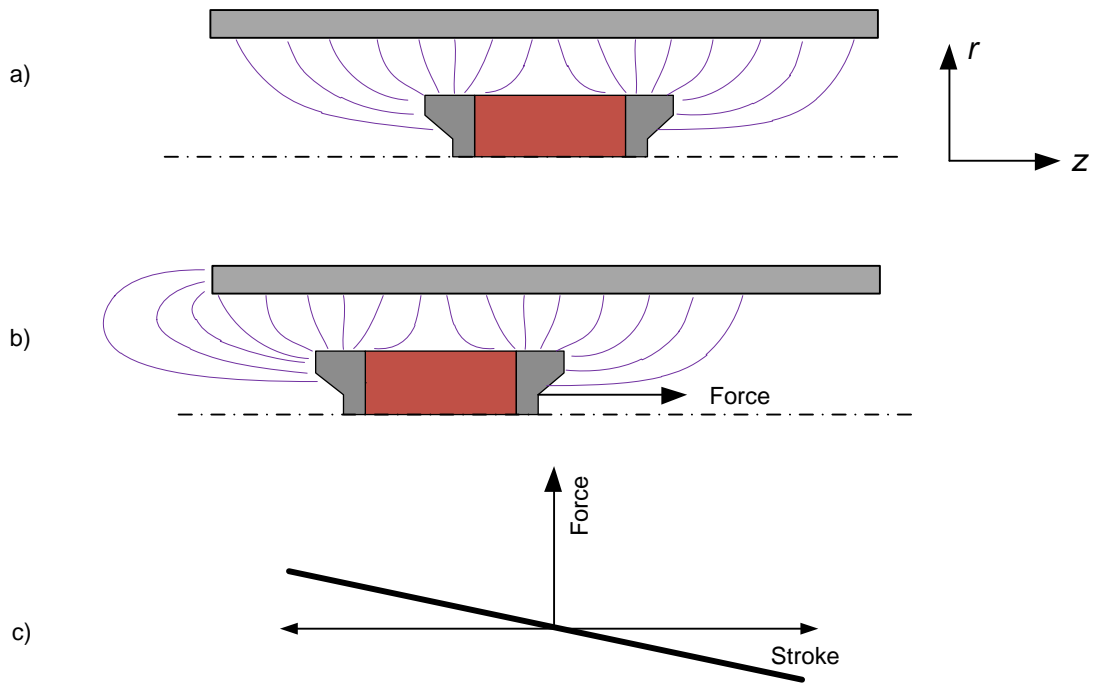


*Figure 4.2: Reluctance cogging force of MMA*

The reluctance and Lorentz forces superimpose resulting in a typical (albeit somewhat exaggerated here) force over stroke plot in an MMA as shown in Figure 4.3. The force over stroke is not axisymmetric, due to the reluctance cogging force between mover and back iron. Note that a constant current is applied over the entire stroke.

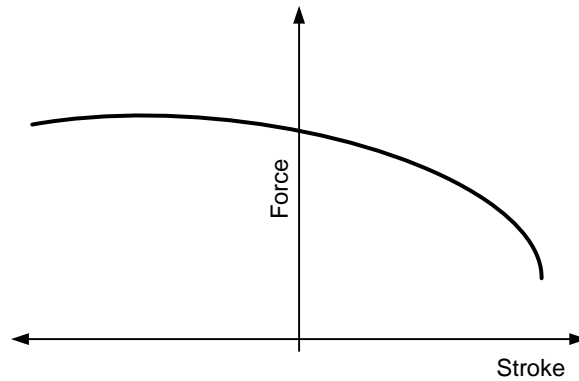


*Figure 4.3: Typical MMA force over stroke profile*

However, in a typical quasi-static scanning scenario, the desired force direction matches the travel direction as shown in Figure 4.4 (solid lines). This may mean, for example, that the current direction is positive for positive displacement, and negative for negative displacement. This leads to an axisymmetric force profile such as in Figure 4.4 (dotted line). In this case, the reluctance cogging force essentially increases the loss in force consistency over stroke due solely to fringing.

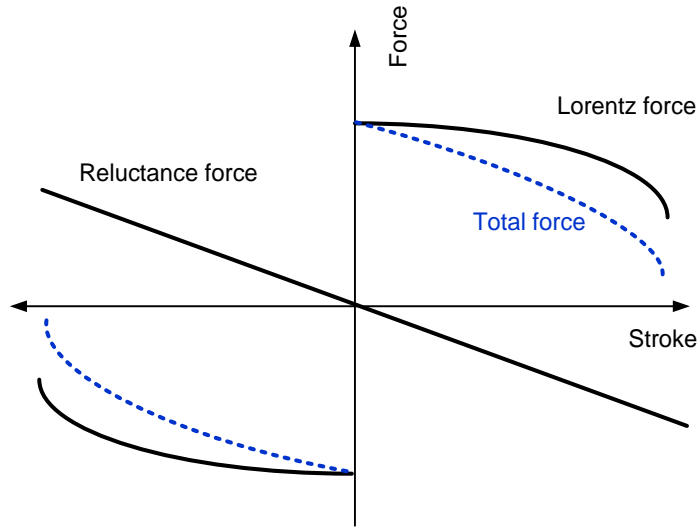


Figure 4.4: Force over stroke profile for scanning scenario

#### 4.1.2 Armature reaction

The effect of the armature magnetic field (i.e. magnetic flux from the coil in an MMA) on the main magnetic field (i.e. magnetic flux from the mover in an MMA) is called armature reaction or the push / pull effect [157][233]. Armature reaction describes the interaction of coil and magnet magnetic fluxes, and can result in the output force and force over stroke profile to change based on input current levels and polarity. This is often undesirable, as the actuator force output is no longer linear with respect to input current—one of the main advantageous characteristics cited for Lorentz force actuators. In MMAs of the traditional architecture, armature reaction is reduced because the flux in the oppositely wound coils tends to cancel out. The magnetic flux path from one coil passes through the other coil and vice versa, and due to this flux linkage and the opposite coil windings, the net magnetic flux is reduced. Also, designs with less magnetically permeable material tend to have lower armature reactions, as the coil flux path has a higher reluctance. This results in lower coil inductance as well. In some VCAs, the

armature reaction can be decreased by clever removal of iron material as shown in [233][215][227].

Armature reaction is illustrated in Figure 4.5 which shows a planar MMA featuring a bar magnet travelling inside a closed back iron. Coil windings are fixed to the top wall of the back iron. The mover stroke is the length of the coil. As shown in Figure 4.5a, the magnetic flux from the magnet forms two main loops within the back iron and air gap. The coil current is 0A. In Figure 4.5b the coil current is positive (e.g.  $i=1A$ ), which forms a flux loop in the back iron (the magnet and its magnetic flux paths are omitted for clarity). However, some coil magnetic flux loops around the coil through the air gap as shown. This coil flux affects the air gap flux density and hence the force output as shown in Figure 4.5c. For small coil current magnitudes, the force over stroke profile looks like that of  $i=0A$ . It is a symmetric force profile with a slight drop in force at the end of the stroke due to fringing, as expected for an MMA. However, as the coil current is increased, the coil flux increasingly affects the air gap density, resulting in a non-symmetric force profile (e.g. the  $i=+1A$  curve). The profile is mirrored for the reverse current (e.g. the  $i=-1A$  curve). The force profile slope increases with current magnitude. The effect of coil flux on air gap flux density can be visualized by superimposing the coil flux at the axial ends of the coil (i.e. the flux loop portion parallel to the air gap magnet flux or perpendicular to the motion direction) and the magnet flux. At one end of the stroke the magnet and coil flux will add, and at the other end of the stroke they subtract. This results in increased force at one end and decreased force on the other.

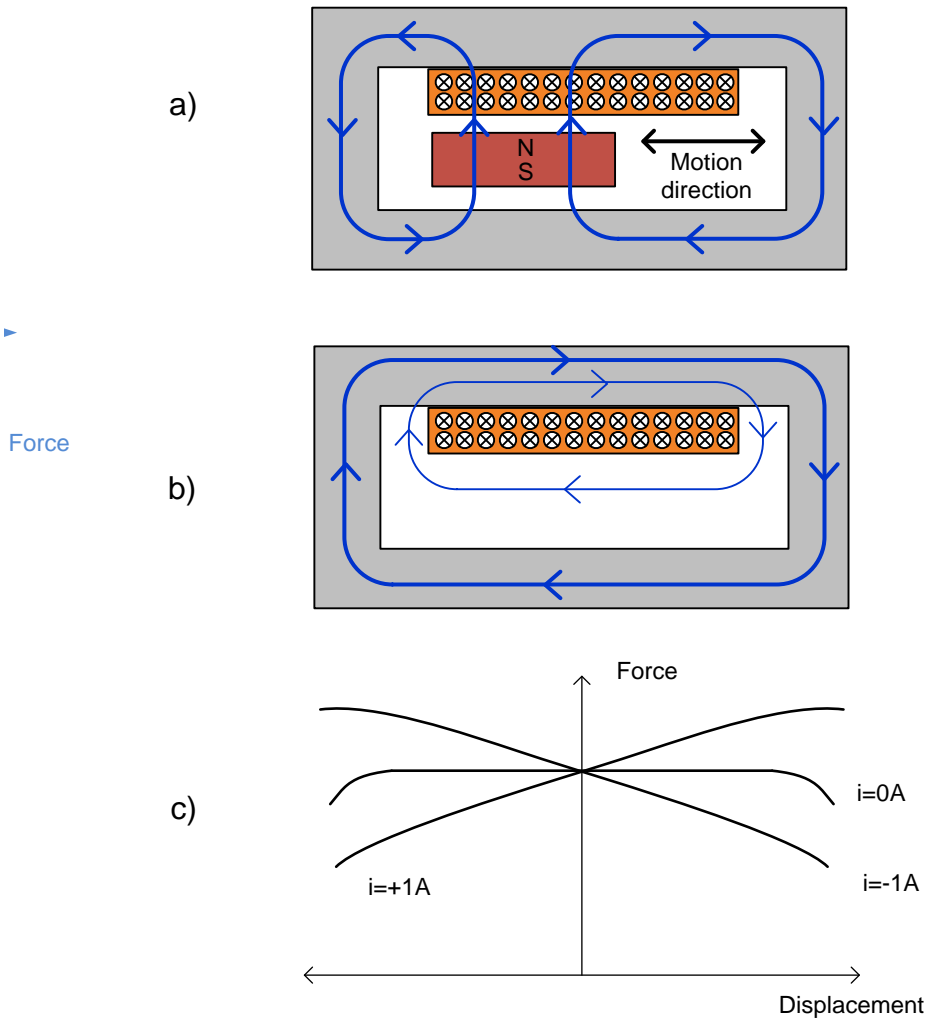


Figure 4.5: Armature reaction

#### 4.1.3 Shorted turn

Often a copper ring is placed concentric to the actuator coils which acts as a “shorted turn” [157][234][235]. A change in coil current and the resulting changing magnetic field will cause eddy currents in the shorted turn, which generate a magnetic field to oppose the change in coil current. This reduces the inductance and armature reaction of the coil. This method is analogous to using oppositely wound coils described

above, except that the shorted turn is not used for force generation unlike a second oppositely wound coil. Use of a shorted turn can be beneficial from a controls perspective and is often used in high speed voice coil designs. However, the eddy current resistive losses lower efficiency, reduce both the actuator specific force capability, and increase the magnitude of the input current [236]. This is similar to the resistive losses expected if only one of the two oppositely wound coils in the example above was wired to the amplifier and used for force generation. Additionally, these eddy currents can give rise to phase lag [237][238], thereby degrading the dynamic performance of the feedback loop. This was experimentally confirmed for the MMA designed in this work [239]. This shorted turn effect can be inadvertently caused by electrically conducting bobbins or magnets and can be reduced by laminations. The shorted turn can be placed anywhere in the armature flux circuit. Some other actuator designs utilizing a shorted turn are shown in [240].

#### 4.1.4 Wire selection

Actuator performance is in theory independent of wire diameter and only dependent on coil volume and geometry. Specifically, the time constant and power dissipation is unchanged by wire diameter [2][159]. However, this neglects any dependence of packing factor ( $S$ ), which is the ratio of coil volume occupied by copper to total coil volume. However, wire gauge choice significantly impacts the actuator voltage and current requirements and therefore the amplifier and electronics choices. [241] is a great resource from MWS Wire Industries explaining wire types, gauges, standards, and application information. Wire used to wind coils is known as “magnet wire” which is covered in an insulating (and often self-bonding) coating. Wire with a circular cross sectional area is most often used for its practicality, however other types of cross sections

are used as well to improve the packing factor, such as square or flattened (i.e. elliptical cross section) wire. The packing factor is approximately 0.62 for round wire and 0.79 for square wire if insulation is accounted for [2][158]. Ribbon wire or flattened round wire have packing factors between round and square wire. The resistance of the wire in a coil can be calculated by

$$R = \frac{\rho l_c}{A_{cu}} = \frac{\rho(Nl_t)^2}{SV_c} \quad (4.1)$$

where  $\rho$  is resistivity of the coil,  $l_c$  is total length of the wire,  $A_{cu}$  is conducting part of the coil,  $N$  is the number of turns,  $l_t$  is average wire length per turn,  $S$  is packing factor and  $V_c$  is total volume of the wire [2]. Thus, using square wire instead of round wire will increase  $S$  and the resistance and  $i^2R$  heat generated will be reduced. The trade-off is that winding coils using non round wire can be much more challenging.

#### 4.1.5 Magnetic saturation of circuit components

Ferromagnetic materials increase the net field strength of an applied magnetic field by bulk alignment of the material's magnetic domains. However, this increases only to the point at which all magnetic domains are aligned. Beyond this point, the material is known to be saturated and will no longer assist in increasing the magnetic flux of the circuit [2]. Therefore, it should be ensured that ferromagnetic components such as steel and iron in the MMA magnetic circuit do not saturate to avoid a reduced actuator force output.

#### 4.1.6 Magnet material

Characteristics of the permanent magnet significantly affect actuator performance. Good resources describing magnet material selection include [182][242][243][244][13], Chapter 1 in [4], as well as the actuator design resources listed in Section 4.3. Traditional magnetic material types are alnico, ceramic or ferrite, and rare earths. The traditional rare earth magnets are Neodymium Iron Boron (NdFeB or NIB) and Samarium Cobalt (SmCo).

Magnets are characterized by three main properties, namely 1. Residual Induction or Remanent Magnetization (symbol  $B_r$ , measured in Gauss). This indicates the strength of the magnet (i.e. its magnetic flux density). 2. Coercive Force or Coercivity (symbol  $H_c$ , measured in Oersteds). This describes the applied magnetic field strength at which the magnet becomes demagnetized by an external field (i.e. how difficult it is to demagnetize the magnet). 3. Maximum Energy Product (symbol  $BH_{max}$ , and measured in Gauss-Oersteds). This indicates overall energy density (i.e. how powerful the magnet is), or what volume of magnet material is required to project a given level of magnetic flux. Figure 4.6 shows the historical upward trend in magnet material performance. The highest is neodymium iron boron (NdFeB), with energy products ( $BH_{max}$ ) up to 52MGOe.

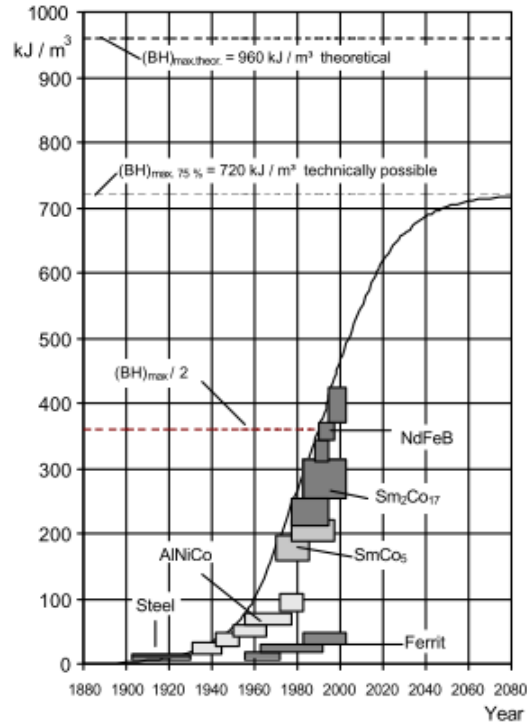


Figure 4.6: “Development of permanent magnet material” [174]

The relationship between  $B$  and  $H$  for a given magnet material and temperature is called its BH curve. Figure 4.7 shows a representative curve. Initially unmagnetized ferromagnetic material lies at the origin. Upon exposure to a coercive force in the positive  $H$  direction (e.g. by an electromagnet placed near the ferromagnetic material), the material exhibits flux density increasing along the dashed line, until the magnet is saturated. As the applied coercive force is then decreased, the magnet’s flux density decreases to its residual magnetization,  $B_r$ . For a given magnet arrangement and magnetic circuit (i.e. a given reluctance coercivity), the flux density will further decrease to a stable operating point. When the coercive force is applied in the negative  $H$  direction, the flux density decreases to zero, which is the magnet’s coercivity,  $H_c$ . As the field is further reversed, the magnet eventually saturates in the reverse direction, becoming fully magnetized with reverse polarity. If the magnet is not fully saturated, following the blue

dashed line, the magnet will lie along the blue hysteresis loop, called a minor loop. Infinite minor loops exist. If the operating point of a fully magnetized magnet is pushed below the knee by an external field, the magnet will be partially demagnetized and follow a minor loop (the  $B_r'$  line, as described next).

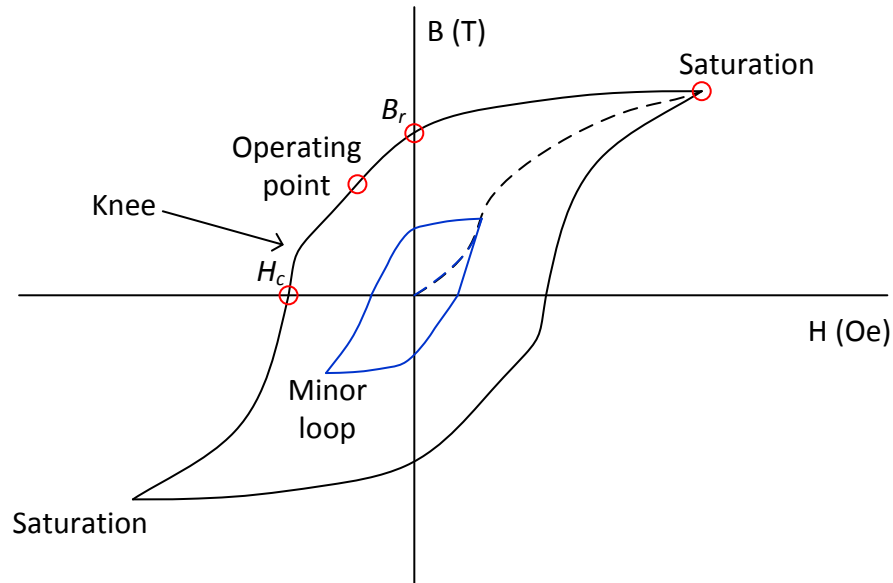


Figure 4.7: Representative magnetic hysteresis curve

The second quadrant of the BH curve is called the demagnetization curve and used for magnetic design (Figure 4.8). The actuator should be designed so that the net coercive force applied to the magnet during operation, comprising the reluctance load of the magnetic circuit and the coil magnetic field, does not demagnetize the magnet. This depends on the coil magnetic circuit, magnetic coercivity, and the “knee” of the demagnetization line (see [245][244]). The actuator geometrical arrangement results in a certain reluctance load on the magnet which is known as the “load line” (line  $a$ ). Where the load line and magnet’s demagnetization curve intersect gives the magnet’s operating point (point  $a'$ ). The coil magnetic field causes the load line to shift (line  $b$ ), moving the operating point to  $b'$ . If the load line and operating point (line  $c$ ), pushed, for example, by

a large applied coil field, slides below the knee in the demagnetization curve, there will be a loss in magnetization. The flux density will travel from point  $c'$  up a parallel lower line (blue), and will remain below a lower remanent magnetization  $B_r'$ . Therefore typically a good actuator design maintains the operating point above the knee in the magnetization curve, at the maximum actuator operating temperature, as discussed next.

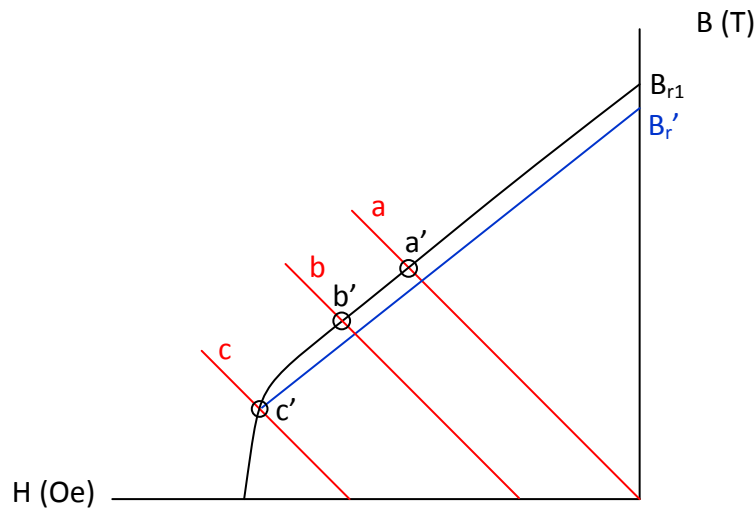
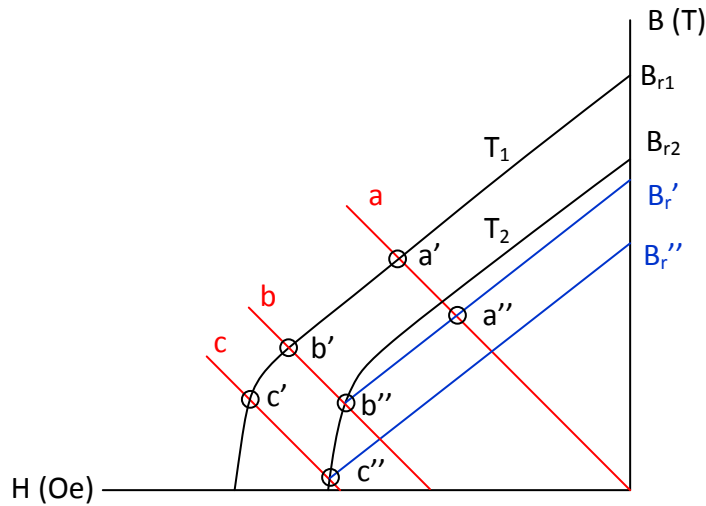


Figure 4.8: Demagnetization curve

Temperature also affects the magnet's demagnetization curve, which can result in undesired demagnetization, even if the magnet operating point lies safely above the knee in the demagnetization curve at room temperature [4], [244]. As shown in Figure 4.9, changes in temperature can shift the demagnetization curve so that the operating point for a given load line falls below the knee in the curve. When the temperature returns to its original state, there will be a loss in magnetic strength which can only be recovered by remagnetization. For example, at initial temperature  $T_1$  and no coil current, the load line is  $a$ , and the magnet lies at operating point  $a'$ . As coil current increases, the load line shifts to  $b$  and the operating point to point  $b'$ . This is still a safe operating point.

However, if the temperature of the magnet begins to rise during operation, the demagnetization curve shifts to  $T_2$ . The operating point is no longer safe, moving along load line  $b$  to point  $b''$ . Now, if the load line shifts back to  $a$ , the operating point moves to point  $a''$ , which is lower than the expected  $a'$ . The magnet remanence will be reduced to  $B_r'$ . Furthermore, in a poor design where the operating point may reach point  $c'$  at the initial temperature, a temperature change to  $T_2$  could significantly increase losses, reaching point  $c''$  and remaining below  $B_r''$ . To help designers, manufactures generalize temperature effects on magnets into three categories: reversible losses, irreversible but recoverable losses, and irreversible and unrecoverable losses, listed for various magnet types [243]. Increasing magnet temperature up to the maximum operating temperature ( $T_{max}$ ) will not cause irreversible loss in magnetization (essentially staying above the knee in the demagnetization curve for a large assumed applied coercive force). Beyond  $T_{max}$ , and up until the magnet's Curie temperature ( $T_c$ ), the magnet will lose magnetization, although the magnet could be remagnetized. Beyond the Curie temperature, however, the magnet will permanently lose magnetization, as it is now hotter than when originally sintered [246].  $T_{max}$  depends on the load line, and therefore differs between manufactures as they use different estimates.



*Figure 4.9: Temperature dependence of demagnetization curve*

In general, magnets with higher coercivity have lower Curie temperatures and therefore lower maximum operating temperatures. Alnico magnets are least affected by temperature, but are easily demagnetized. Rare earth magnets are not as easy to demagnetize as alnico, but the magnetic strength is more susceptible to temperature changes. The high remanent magnetization magnets such as NdFeB can have maximum operating temperatures as low as 80°C [247][246]. These modern magnets, due to their high coercivity, can withstand high armature fields without demagnetization. This means that heat dissipation is often essentially the limiting factor in actuator performance [160].

#### 4.1.7 Radial instability

Separation of the back-iron from the permanent magnet in an MMA introduces the risk of instability in the direction perpendicular to the motion axis [160][248][249][250]. This is due to reluctance forces acting between the mover and stator in the radial direction, ideally balanced in an unstable equilibrium. Small radial

perturbations, manufacturing tolerances, or magnetization non-uniformities can cause the mover to leave equilibrium and “snap in” to contact the side walls of the stator. This instability increases with increasing air gap flux density (i.e. increasing actuator force and / or decreasing air gap dimension). Therefore one drawback of designing an MMA for high actuator force can be higher risk of instability, placing additional demands on the bearing.

#### 4.1.8 Thermal management

Heat generation due to coil resistive losses is one of the main drawbacks of electromagnetic actuators. Consideration of thermal management is important in the design of electromagnetic actuators and is discussed in depth in [2]. During quasi-static operation, which represents the worst-case scenario of heat generation, most of the power sent to the actuator is converted to heat. Heat dissipation should not cause the temperature in the coil to affect the magnet wire insulation and bonding agent. Magnet wire is specified by thermal class (for example, NEMA standards 105°C, 155°C, 180°C, 200°C and 240°C). The wire should be maintained below this temperature to ensure operation and no loss in performance. See [241] for more information on wire insulation thermal ratings. The temperature rise of the permanent magnet must also remain below the magnet’s maximum operating temperature, as discussed in Section 4.1.6.

#### 4.1.9 Actuator design considerations map

A breakdown of the factors affecting the seemingly simple Lorentz force equation  $F = il \times B$  provides additional insight into actuator-level design trade-offs. Many links

between the geometric, electrical, and magnetic parameters can be seen in Figure 4.10<sup>3</sup>. The material and geometric parameters on the left affect electrical and magnetic parameters in the middle of the figure, which influence the air gap magnetic field, coil size, and coil current on the right. These give the actuator output force. Studying this network, interesting relations become apparent. For example, some geometric variables affect both the magnetic and electrical domains. The radius of the mover affects coil size and magnetic field. Likewise, the coil thickness affects coil length and air gap magnetic field. Looking at this model, there are no obvious variables or relations that lead to a simple yet comprehensive design methodology. This is largely why design of these actuators often rely more on engineer design judgment, experience, and rules of thumb. While already fairly complex, this breakdown does not account for other important performance factors such as the back iron reluctance force, wire packing factors, and coil overhang length. Dynamic considerations such as coil inductance and eddy current generation are also not accounted for.

---

<sup>3</sup>Special thanks to Cory Welch for this figure

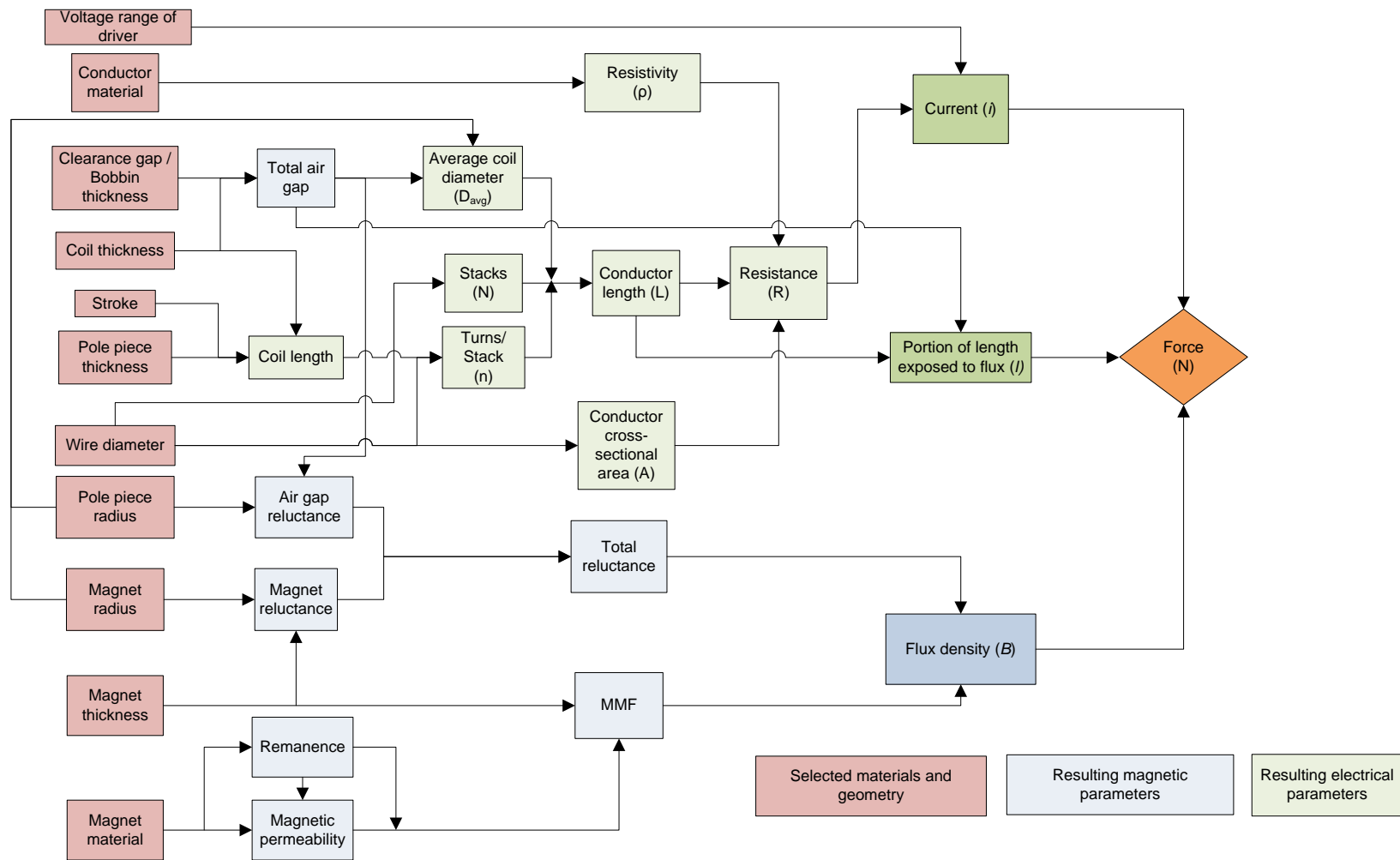


Figure 4.10: Actuator-level trade-offs in Lorentz force equation

## 4.2 System design considerations

Actuator performance, which depends on the above mentioned actuator design considerations, affects the overall nanopositioning system performance. Similarly, several system design considerations also affect actuator-level design specifications. These system-level design considerations are discussed here.

### 4.2.1 Open-loop bandwidth

Due to the absence of friction and backlash in an MMA as well as the components in the nanopositioning system, system motion quality is determined by its closed-loop tracking performance. Closed-loop tracking performance is primarily limited by noise and harmonic distortion in the electrical driver that supplies current to the actuator. Higher open-loop system bandwidth generally enables higher closed-loop performance, leading to better suppression of noise and / or distortion in closed-loop operation [251]. System open-loop bandwidth, which can be represented by the first natural frequency of the motion system, can be increased by increasing the flexure stiffness and decreasing the overall moving mass [252]. The noise and distortion in the electrical driver can also be reduced at the source by lowering the actuator power input.

### 4.2.2 Actuator force

The maximum achievable motion range is determined by the motion-direction stiffness of the bearing and the maximum actuator force, neglecting material yield considerations. For a given bearing stiffness, a larger stroke requires a larger actuator force. Additionally, for high scanning speed, the actuator also has to overcome inertial loads, which place further demands on the actuation force requirement. As described in

Chapter 1, external forces on the motion stage are considered negligible in comparison to the spring and inertial forces.

#### 4.2.3 Actuator force uniformity

As discussed in Section 4.1.1, non-uniformity in the MMA's force output over its stroke for a fixed current input also leads to higher order harmonics in output force and therefore position in open-loop as well as closed-loop operation [92]. While the adverse effect of these harmonics on the motion quality may be mitigated by a large open-loop bandwidth and therefore better closed-loop disturbance rejection, the actuator should also be designed to provide greater force-stroke uniformity.

#### 4.2.4 Mechanical load on flexure bearing

The MMA places several important mechanical load bearing requirements on the flexure bearing. The attraction forces between the magnet and the back iron and the cantilevered mass of the mover give off-axis forces and torques which must be constrained by the bearing to avoid the mover contacting the sidewall. This is illustrated in Figure 4.11. The flexure bearing has to provide a higher positive off-axis and rotational stiffness compared to the negative (or destabilizing) off-axis stiffness associated with the magnetic force between the moving magnet and the stationary back-iron as discussed in 4.1.7. It can be mitigated by a bearing design that provides higher positive off-axis stiffness compared to the negative off-axis stiffness of the actuator. However, high off-axis stiffness of a flexure bearing also implies high motion axis stiffness [253], [254].

The off-axis and rotational stiffness requirements of the bearing is also influenced by the mass and axial length of the MMA mover. In general, the mass of the mover is larger, and the length of the mover is axially longer, than a corresponding VCA.

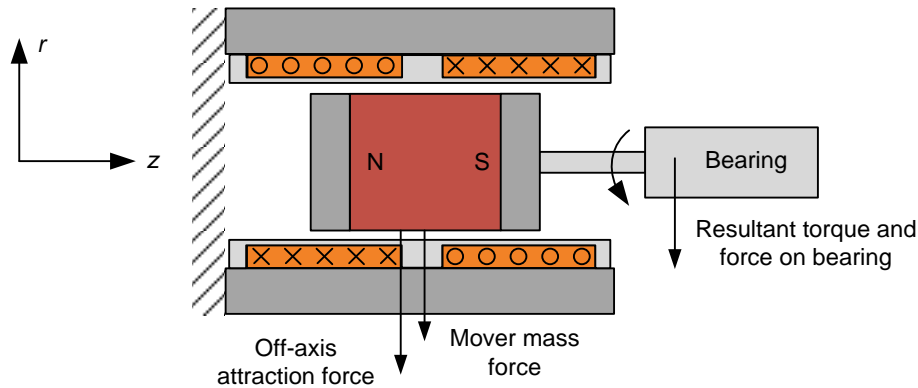


*Figure 4.11: Cantilevered mover mass and off-axis attractive forces increase loads on bearing*

#### 4.2.5 Thermal management

Temperature rise due to power dissipated as heat in the coil can be detrimental not only to actuator performance (as described in 4.1.8), however also to system performance. Individual system components, as well as the assembly of the motion system, can be affected. For example, given the coefficient of thermal expansion of aluminum of about  $24\mu\text{m}/\text{m}/^\circ\text{C}$ , thermal strains can be  $240 \times 10^{-6}$  for a temperature rise of  $10^\circ\text{C}$ . For aluminum, this can correspond to stress levels of 17MPa, which are high enough to produce in-plane or out-of-plane buckling of beams, distortions of the base plate, and over-constraints in the assembly. Invar or Super Invar are commonly used as a flexure materials due to their low coefficient of thermal expansion, which reduces risk of thermal strains and stresses. However, this choice leads to smaller motion range for the

same flexure bearing size due to the lower strength to modulus ratio of these two alloys. Also, the cost of these materials is significantly higher than aluminum.

Thermal expansion in the flexure resulting in displacement of the motion stage could be compensated using position feedback provided by the sensor. However, sensors are sensitive to thermal fluctuations, and if the sensor itself drifts due to the temperature change, it is not possible to correct in a feedback loop. For example, a temperature rise of 10°C of an encoder scale with a thermal expansion coefficient of  $\sim 0.6 \mu\text{m}/\text{m}/^\circ\text{C}$  from Renishaw [255] corresponds to a significant measurement error (or loss in accuracy) in the sensor of around 60nm.

Although the heat source (i.e. the current carrying coil) is located further away from the motion stage in an MMA, as compared to a VCA, the generated heat still has to be channeled away from the motion system. Proper heat management design must therefore be considered.

#### 4.2.6 System design considerations map

This discussion reveals several conflicting system and actuator requirements. For example, the force output of an MMA can be raised by increasing either the moving magnet mass or the input power, at the expense of open loop bandwidth and therefore motion quality [11]. Reducing the flexure stiffness in the motion direction allows a larger portion of the actuation force to be devoted to inertial loads, leading to higher operating speeds, however lower stiffness also reduces the open-loop bandwidth and compromises disturbance rejection capability. While greater force-stroke uniformity reduces the reliance on large open-loop bandwidth to provide the desired motion quality, it typically requires an axially longer coil, which in turn implies greater power consumption, heat

generation, and potential loss in positioning accuracy. Furthermore, increasing the actuator force also increases the actuator negative off-axis stiffness, which requires higher bearing off-axis stiffness and ultimately can increase motion-direction stiffness.

An attempt at mapping the interrelated MMA geometric trade-offs, their effect on the magnetic and electric domains and resulting actuator performance, and their effect on the system level performance, is shown in Figure 4.12. It can be seen, for example, that at the actuator level, increased air gap volume lowers flux density,  $B_g$ , but exposes more coil windings. Depending on the geometry, this could either increase or decrease the force output. The force output, in turn, affects system level performance such as speed, range, and motion resolution. Reducing wire diameter in the actuator increases the force constant,  $K_t$ , but increases resistance,  $R$ , and if the wire packing factor changes, these influence heat generation, which in turn affects overall motion quality. Actuator force increases with magnet remanence,  $B_r$ , but the magnet is more susceptible to heat, which can be abated by either lower actuator power generation or better system heat management. This figure does not show additional trade-offs such as off-axis attraction or force uniformity over stroke. Based on this and discussions in the previous sections, it is clear that appropriate design metrics and methodologies to relate the actuator-level geometrical parameters, actuator-level performance, and system-level performance is needed.

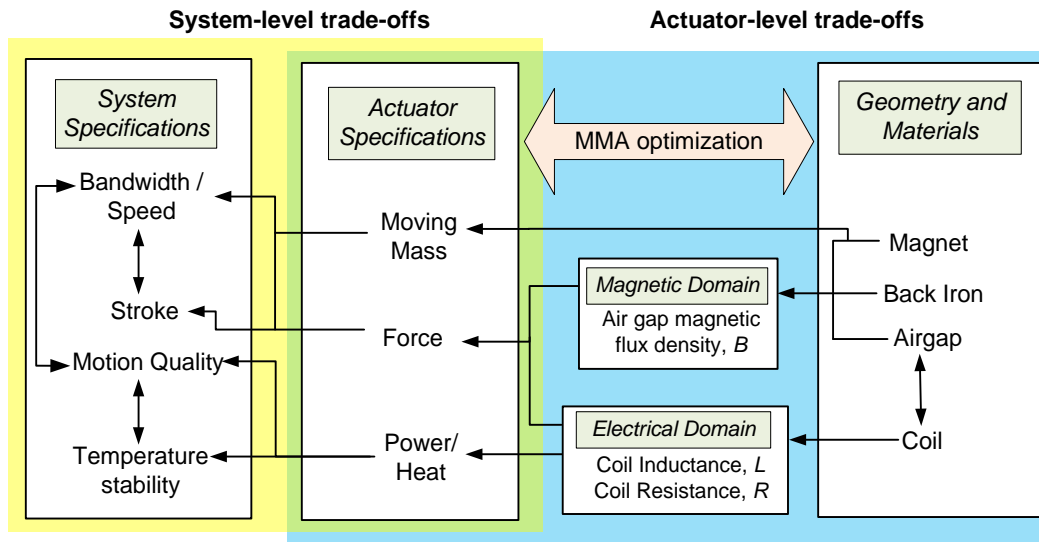


Figure 4.12: Actuator and system level trade-offs

### 4.3 Design methodologies

While there are many resources on electromagnetic actuator design and design methodologies, several classic and / or well-presented resources include [2] (see Chapter 5), and [3][256][159]. In general, these resources use analytical lumped-parameter modeling of the magnetic circuit to estimate air gap magnetic flux densities and corresponding actuator output force. Coil design is likewise carried out, considering wire diameter and material, and thermal management. These actuator parameters are chosen to meet mechanical and electrical requirements of a desired system motion or velocity profile, for a given control method and thermal and electrical driver constraints. It is also possible to directly substitute actuator level design variables into the system level equations of motion and voltage equation to enable more direct determination of actuator geometry and materials based on system requirements [2]. Once a design is deemed feasible, magnetic finite element analysis methods are used for increased accuracy. Design influences often include whether the actuator is operated in voltage or current

control, whether a shorted-turn is employed, and which magnetic materials are used. For example, in [2] an example designing a hard drive disk VCA is given. Starting with system level requirements (stroke, move time, voltage and current requirements, operating temperature, etc.) and estimated control method (bang-bang, triangular velocity profile), the required actuator force, actuator constant, maximum speeds, and maximum back EMF are calculated. This gives coil design parameters (coil resistance and wire size), which enables air gap length and air gap flux density estimations. This drives the design of the rest of the magnetic circuit, including magnet and steel dimension selection. Finally, inductance is analytically estimated based on coil flux paths through the actuator. This gives all values for the equations of motion and voltage equation to estimate design feasibility.

Several further resources on MMA design are also worth discussion. For example, [11] concentrates on power dissipation, moving mass and position dependency of the force of an MMA. Designs are evaluated based on their ability to achieve a force of 10N for a stroke of 1mm. Variation of the force with motion and the moving mass is also evaluated. The analysis, however, does not take system bandwidth into account per se, nor does it account for dissipated power. [219] also investigates MMA design for reciprocating systems, however it does not offer clear design metrics. Alternatively, some papers present highly detailed derivations and design guidelines (“general design frameworks”) of MMAs. In [173] the magnetic fields are solved analytically giving force, the winding back EMF and inductance, with mover position dependence. [257][258] are similar. However, design intuition is lost in the mathematical complexity.

#### 4.4 Figures of merit

Several existing figures of merit used in actuator design are discussed here. One figure of merit traditionally used is the *actuator constant*,  $K_a = F/\sqrt{P} = K_t/\sqrt{R}$ , which is defined as the actuator output force ( $F$ ) per unit square root of power ( $P$ ) consumed. It is equivalent to the force constant,  $K_t$ , (in N/A) per square root of resistance ( $R$ ) via Ohm's law. It captures the actuator-level tradeoff that the output force of an MMA cannot be indefinitely increased without increasing the power input and heat generated. However, this actuator constant only captures the quasi-static performance of the MMA since it does not incorporate the actuator's moving mass. As a result, it does not reflect on the dynamic performance of the MMA when used in a flexure-based nanositioning system.

Other figures of merit for MMAs that do capture some degree of dynamic performance include the *electrical time constant* and the *mechanical time constant*. The electrical time constant,  $\tau_e = L/R$ , is defined as the rise time of the current for a step voltage change and depends on the inductance ( $L$ ) to resistance ( $R$ ) ratio of the coil. While it does represent a tradeoff between the current rise-time (i.e. force rise-time) and heat generation, this tradeoff is readily overcome via the use of a current driver. The mechanical time constant,  $\tau_m = mR/K_t^2 = m/K_a^2$  is defined as the rise-time of the velocity for a step voltage change and depends on the actuator constant ( $K_a$ ) as well as the moving mass ( $m$ ). However, it does not reveal any inherent tradeoff associated with the construction and physics of the MMA.

Few other figures of merit beyond the actuator constant and time constants were identified in the literature discussing MMA design, especially for use in flexure based motion systems. In [2], equations 5-52 and 5-53 relate actuator geometry and material

properties to the rise time and power requirements for voice coil actuators. [154] discusses simple relations between flux density and coil heating, actuator size and flux density, and the force per mass ratio and dynamic response. [256] mentions the relation between magnet mass and mechanical work. However these basic guidelines also may be too general to produce an optimal design, and do not give insight into overall system performance.

## CHAPTER 5: Dynamic Actuator Constant

While many of the discussed design methodologies and figures of merit are time-tested and well known, they often rely heavily on engineering judgment and are iterative processes. Ideally there exists an actuator figure of merit which comprehensively determines system level performance in a more direct manner. For example, a parameter that relates actuator materials and dimensions to the actuator moving mass, force and power, and subsequently to the resulting system bandwidth, stroke, motion quality, and thermal considerations. This parameter would be a valuable figure of merit and simplify the design process. In this chapter, an attempt is made to systematically capture design limitations and performance tradeoffs of the MMA in a quantitative manner. The result is a novel figure of merit, the dynamic actuator constant,  $\beta$ , which enables normalized comparison and optimization of an MMA as well as captures the resulting basic system dynamic performance of a flexure based nanopositioning system actuated via the MMA. This parameter depends solely on actuator geometry and materials and is independent of actuator scaling, enabling the comparison of the dynamic performance between different MMAs of any geometry and size, and revealing inherent limitations in MMA performance.

The dynamic actuator constant addresses several key questions in actuator design. For example, what is an optimal actuator geometry? Is there an optimal geometry in general, or does it depend on the specific application? How large should an actuator be for a given application? What is the relation between power (affecting heat output), moving mass, and output force (affecting dynamic performance)—specifically,

increasing actuator force requires either larger moving mass, or higher power input—and how significant is this tradeoff? By investigating these questions, it was discovered that certain ratios of actuator properties remain constant regardless of dimension scaling, and was subsequently derived analytically to give the dynamic actuator constant. This constant is a normalizing factor which gives unprecedented quantitative insight into these questions and therefore gives the designer a powerful tool for MMA optimization.

Special thanks to Gaurav Parmar for his contributions to the analytical investigation of the dynamic actuator constant and effect on system performance.

## 5.1 Derivation

In order to capture dynamic performance, a figure of merit is needed that includes both the continuous output force and the actuator's moving mass (i.e. specific actuator work), as well as actuator power consumption. To quantitatively investigate the existence of such a figure of merit, the effect of geometric scaling on the actuator output force, power consumption, and moving mass is considered. This is done via derivation based on a lumped parameter model of a traditional MMA. The derivation of the lumped parameter model is based on standard procedures of lumped parameter analysis [2][3].

Figure 5.1 shows a lumped parameter model of an MMA with a traditional architecture. The dimensions  $l_m$ ,  $l_p$ ,  $r_m$ , and  $t_g$  denote the nominal magnet axial length, pole piece length, magnet radius, and magnetic air gap radial thickness, respectively. The coils are defined by length  $l_c$  and thickness  $t_c$ , separated by distance  $l_{cs}$ .  $\alpha$  is the geometric scaling factor. The back iron is referred to as the yoke in this analysis, with length  $l_y$  and thickness  $t_y$ . The following assumptions are made to simplify the analysis:

1. Any fringing and leakage flux is neglected
2. All the radial space between the pole pieces and the back iron ( $t_g$ ) is occupied by coils. In other words, the mechanical clearance between the pole piece and bobbin ( $t_{clear}$ ) is negligible compared the thickness of coil ( $t_c$ ).

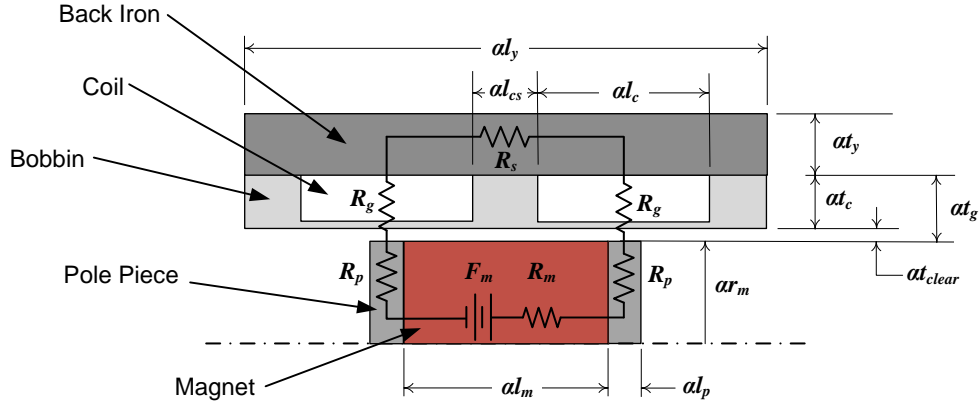


Figure 5.1: MMA simplified lumped parameter model

Assuming a linear region of the magnetization curve of the permanent magnet,

$$B_m = B_r + \mu_m H_m \quad (5.1)$$

where  $B_m$  and  $B_r$  are the magnetic flux density and remanent magnetization of the permanent magnet respectively,  $\mu_m$  is its permeability, and  $H_m$  is the magnetic field intensity inside the magnet. Using the integral form of Ampere's Law with no coil current gives,  $\oint H \cdot dl = 0$  which evaluated along the circuit gives

$$H_m \tilde{l}_m + H_p \tilde{l}_p + H_g \tilde{l}_g + H_y \tilde{l}_y = 0 \quad (5.2)$$

Subscripts  $m$ ,  $p$ ,  $g$ , and  $y$  denote the permanent magnet, pole piece, air gap and yoke respectively, and  $\tilde{l}$  represent the average length of the magnetic flux path. Substituting  $H_m$  from Equation (5.1) into Equation (5.2), gives

$$\frac{B_m \tilde{l}_m}{\mu_m} + \frac{B_p \tilde{l}_p}{\mu_p} + \frac{B_g \tilde{l}_g}{\mu_g} + \frac{B_y \tilde{l}_y}{\mu_y} = \frac{B_r \tilde{l}_m}{\mu_m} \quad (5.3)$$

where  $B$  is the average flux density along the path. Assuming no flux leakage, we can write

$$\Phi = B_m A_m = B_g A_g = B_p A_p = B_c A_c \quad (5.4)$$

where  $\Phi$  is the total magnetic flux through the circuit. Combining Equations (5.3) and (5.4) leads to

$$\Phi \left( \frac{\tilde{l}_m}{\mu_m A_m} + \frac{\tilde{l}_p}{\mu_p A_p} + \frac{\tilde{l}_g}{\mu_g A_g} + \frac{\tilde{l}_y}{\mu_y A_y} \right) = \frac{B_r I_m}{\mu_m} \quad (5.5)$$

or

$$\Phi (R_m + R_p + R_g + R_y) = F_m \quad (5.6)$$

$R$  and  $F_m$  represent the reluctance and the magneto-motive force respectively. The permeability of the permanent magnet and that of the air are approximately the same as that of vacuum. Also, the permeability of iron is more than 100 times greater than that of the vacuum, provided that the iron core and the pole piece do not saturate. Hence, the following additional assumptions can be safely made

$$\mu_y = \mu_p \gg \mu_{air} \approx \mu_m \approx \mu_0 \quad (5.7)$$

and therefore  $R_y$  and  $R_p$  can be neglected. Equation (5.6) reduces to

$$\Phi(R_m + R_g) = F_m \quad (5.8)$$

Based on standard lumped parameter magnetostatic analysis [3], and substituting in Equation (5.7), the magneto-motive force ( $F_m$ ) and the lumped reluctances of the magnet and the air gap ( $R_m$  and  $R_g$ ) are given by

$$F_m = \frac{\alpha B_r l_m}{\mu_0} \quad (5.9)$$

$$R_m = \frac{l_m}{\pi \alpha \mu_0 r_m^2} \quad (5.10)$$

$$R_g = \frac{\ln(1 + t_g / r_m)}{2\pi \alpha \mu_0 l_p} \quad (5.11)$$

Therefore, the resultant flux,  $\phi$ , and average magnetic flux density in the air gap,  $B_g$ , are given by

$$\phi = \frac{F_m}{R_m + 2R_g} \quad (5.12)$$

$$B_g = \frac{\phi}{2\pi \alpha^2 (r_m + t_g / 2) l_p} \quad (5.13)$$

The force output ( $F$ ) and power consumed i.e. dissipated as heat ( $P$ ), and the actuator moving mass ( $m_a$ ) can be determined to be

$$F = B_g i l_w = B_g i \frac{4\pi \alpha^3 l_p t_g (r_m + t_g / 2)}{d^2} = i \phi \frac{2\alpha t_g}{d^2} \quad (5.14)$$

$$P = i^2 R = i^2 \frac{\rho_c l_w}{A_w} = i^2 \rho_c \frac{16\alpha^3 l_p t_g (r_m + t_g / 2)}{d^4} \quad (5.15)$$

$$m_a = \rho_m \pi \alpha^3 r_m^2 l_m \quad (5.16)$$

where  $i$  is the coil current,  $R$  is the coil resistance,  $\rho_c$  is the resistivity of the coil wire,  $d$  is the wire diameter,  $A_w$  is the cross-sectional area of the wire,  $l_w$  is the total length of the wire in the air gap, and  $\rho_m$  is the mass density of the magnet. It should be noted that the magnetic flux density in the air gap varies in the radial direction. Each layer of the coil in turn experiences a different magnitude of the magnetic flux density. However radial magnetic flux density is presented only at the middle of the coil stack in Equation (5.15). This corresponds to the average flux density, which occurs at radius  $r = r_m + t_g/2$ . The Lorentz force contains a product of the magnetic flux density which varies inversely with radius  $r$ . Therefore, the circumferential length of the coil stack layer (which varies proportionally with  $r$ ) turns out to be independent of the variable  $r$  as seen in the first relation in Equation (5.14). Thus, there are no approximations made in this assumption. It should also be noted that the current ( $i$ ), force ( $F$ ), and power ( $P$ ), are all dynamic variables. Combining Equations (5.14), (5.15), and (5.16) gives

$$\frac{F}{\sqrt{P} \sqrt{m_a}} = \frac{B_r}{\left( \frac{l_m l_p}{r_m^2} + \ln \left( 1 + \frac{t_g}{r_m} \right) \right)} \sqrt{\frac{\pi l_m l_p t_g}{4 \rho_c \rho_m r_m^2 (r_m + t_g / 2)}} \quad (5.17)$$

In the above relation, the scaling factor  $\alpha$ , wire diameter  $d$ , and coil current  $i$  cancel out, and the left hand side term is found to be dependent on only the physical constants and nominal dimensions, which are constant for a given MMA architecture. This corroborates that the time constant and power dissipation is unchanged by wire diameter for fixed coil volume [2]. This relation also shows that the force output ( $F$ ) remains directly proportional to the square root of the actuator moving mass ( $m_a$ ) and the

square root of power consumed ( $P$ ), irrespective of the scale of the actuator ( $\alpha$ ). Therefore Equation (5.17) may be restated as follows

$$\frac{F}{\sqrt{P}\sqrt{m_a}} = \frac{K_t}{\sqrt{R}\sqrt{m_a}} = \beta \text{ (constant)} \quad (5.18)$$

where  $K_t$  is the force constant (force per unit current) of the MMA. The constant  $\beta$  (units of  $\sqrt{\text{Hz}}$ ), therefore, turns out to be an important figure of merit in the design of an MMA, and is hereafter referred to as the *dynamic actuator constant*. While this constant is related to the mechanical time constant ( $\tau_m = 1 / \beta^2$ ), it provides important design insight that the latter does not. It reveals an inherent trade-off associated with the force, moving mass, and the power consumption of an MMA, which cannot be overcome by varying the actuator size. It should be noted, however, that  $\beta$  varies when the relative proportions between the actuator's dimensions are changed.

Although several simplifying assumptions were made in the derivation of the dynamic actuator constant, (5.18) is found to be true even when these assumptions are removed in a finite element analysis (FEA) using Maxwell<sup>TM</sup>. This is shown in Figure 5.2. The ratio ( $K_t/\sqrt{R}$ ), which is the actuator constant, is plotted against the square root of the actuator moving mass ( $\sqrt{m_a}$ ) for different values of the scaling factor ( $\alpha$ ). The slope of the curve represents the dynamic actuator constant ( $\beta=14$ ), for the particular choice of actuator dimension proportions used in the analytical model.

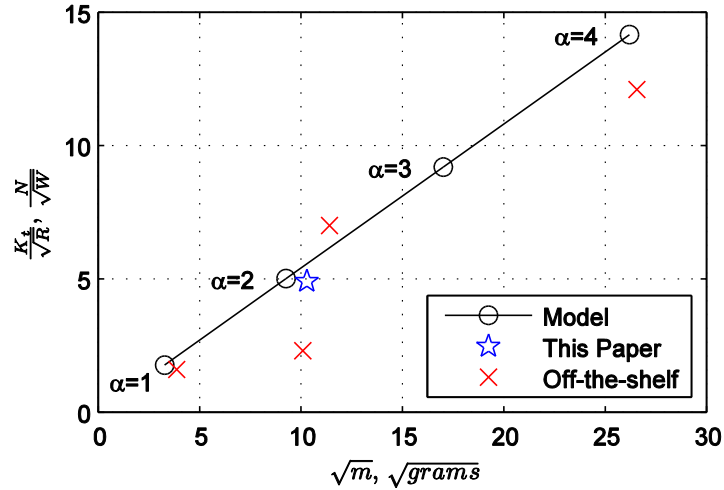


Figure 5.2: Effect of geometric scaling on MMA performance [83]

The design implications of the dynamic actuator constant and its independence on actuator scale are significant. For example, this enables an optimal MMA geometry to be first determined using arbitrary nominal design dimensions. Subsequently, the actuator size can be scaled to meet the required force constraints and / or be matched to the payload mechanical impedance. This greatly simplifies the design process and enables normalized comparison of MMA designs regardless of their size.

It should be noted that in practical design scenarios the mechanical air gap of an MMA may be constrained, at least to a minimum size. Typical manufacturing tolerances may limit the size to be no less than  $\sim 0.020''$ . Assuming a fixed minimum air gap size,  $\beta$  will increase as all other actuator dimensions are scaled and not remain constant as presented above. However, as scaling increases, the minimum mechanical air gap becomes negligible compared to other dimensions, and  $\beta$  will approach a constant as expected. Similarly, often it is desired that the stroke remains a constant length during MMA design and geometry optimization. For a fixed stroke length,  $\beta$  will increase as scale increases because the coil overhang (which is essentially an additional resistive

power loss) also remains a constant length. However, as scale increases further, the stroke overhang becomes of negligible length compared to the total coil length (i.e. the additional power losses due to the coil overhang become negligible compared to the rest of the coil), and  $\beta$  approaches a constant in this scenario as well.

## 5.2 Impact on motion system performance

When the MMA is employed in a flexure-based nanopositioning system, an important consequence of Equation (5.18) is that it places a fundamental limit on the system open-loop bandwidth ( $\omega_n$ ), desired scanning speed ( $\omega$ ), desired motion range ( $\pm\Delta_o$ ), power consumed ( $P$ ), and the moving masses (actuator  $m_a$  and motion stage  $m$ ). Assuming a sinusoidal motion profile ( $\Delta = \Delta_o \cos \omega t$ ), this limit may be derived by equating the actuation force with the spring and inertial forces

$$F = K_y i = (m + m_a) \left| \omega_n^2 - \omega^2 \right| \Delta \quad (5.19)$$

Where  $\omega_n^2 = K_y / (m + m_a)$  and  $K_y$  is the flexure stiffness. This indicates that when the desired scanning speed is less than the natural frequency of the system (i.e.  $\omega \ll \omega_n$ ), the required actuation force is dominated by the spring stiffness, and the actual scanning speed is less important. However, when the scanning speed is greater than the natural frequency ( $\omega \gg \omega_n$ ), the required actuation force is dominated by inertial loads and depends on the square of the scanning speed. These two conditions represent the worst-case actuation force requirements. As expected, the actuation force becomes very small around resonance ( $\omega \approx \omega_n$ ). Substituting  $\beta$  from Equation (5.18) and  $P = i^2 R$ , the minimum required actuation force may be restated as

$$\beta \cdot \frac{\sqrt{m_a}}{m + m_a} \geq \Delta \cdot \left| \omega_n^2 - \omega^2 \right| \cdot \frac{1}{\sqrt{P}} \quad (5.20)$$

This expression quantitatively captures the performance tradeoff that achieving large motion range, high resolution (enabled by good disturbance rejection due to high natural frequency), high scanning speed, and low power consumption (to minimize temperature rise and driver noise/distortion) are all at odds with respect to each other. The only way to simultaneously achieve these nanopositioning performance attributes is to use an MMA that provides a large  $\beta$  and minimize all moving masses in the system.

The mass ratio term in Equation (5.20) is a mechanical impedance factor which is maximized when the actuator mass and payload mass are equal. If the payload is negligible, then system dynamic performance increases with decreasing actuator mass, for a fixed power limit. For realistic ranges of actuator and payload mass in the scope of this work, this mass ratio term is near unity, leaving the dynamic actuator constant as the sole design metric for obtaining high dynamic performance.

This analysis quantitatively shows the system-level performance trade-offs discussed in 4.2. If, for example, the flexure bearing is designed to be stiffer to increase the open-loop bandwidth and improve disturbance rejection of the driver noise/distortion and actuator force-stroke non-uniformity, it would also require an increase in the actuation force in order to retain the same motion range. But, as per the MMA tradeoff given by relation (5.18), this can only be achieved by increasing the magnet mass, for a given power consumption limit. Ultimately, using a stiffer bearing will not lead to the desired increase in the open-loop bandwidth. Trying to improve disturbance rejection via controller design hurts the closed-loop system stability robustness [251]. Therefore, it becomes important to employ an electrical driver with minimal noise and distortion, and design the MMA with maximal force-stroke uniformity. Furthermore, while increasing the current and therefore power into the system will improve its overall performance, it

will also produce a temperature rise that is detrimental. Therefore, any increase in power has to be matched by a thermal management system that carries the heat out of the system to maintain its temperature.

In addition to the above closed-form and finite elements analysis, a survey of commercially available off-the-shelf MMAs further validates the significance of relation (5.18). The specifications of the surveyed actuators, along with the MMA designed and fabricated in this work, are presented in Table 5.1. The corresponding actuator manufacturer and model number is listed in Table 5.2. Most of the MMAs available are of the traditional architecture, however they have a wide variety of stroke length, sizes and geometrical proportions. Despite this variety, when the actuator constant ( $K_t/\sqrt{R}$ ) is plotted against the square root of the actuator moving mass ( $\sqrt{m_a}$ ) in Figure 5.3, almost all MMAs fall near or below the straight line with slope corresponding to  $\beta = 15$ . Only a few MMAs approach  $\beta = 20$ . This suggests that the dynamic actuator constant, in addition to being independent of the actuator size, cannot be increased beyond a certain limit even by optimizing the dimensional proportions. The optimal value and practical design implications are examined further in Section 11.1.1.

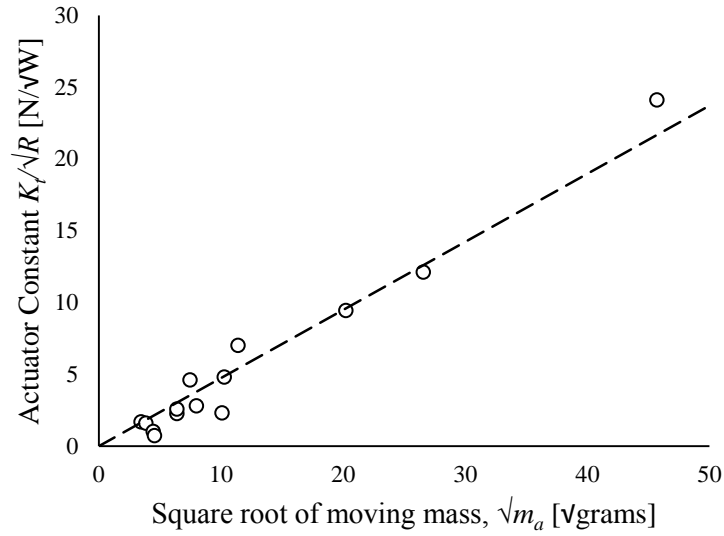


Figure 5.3: Dynamic actuator constant (slope) for off-the-shelf MMAs

The dynamic actuator constant is also plotted against actuator stroke in Figure 5.4. No clear trend except for a consistent upper limit of  $\sim 15\sqrt{\text{Hz}}$  is discernible, again alluding to an inherent limitation in MMAs regardless of actuator scaling and size.

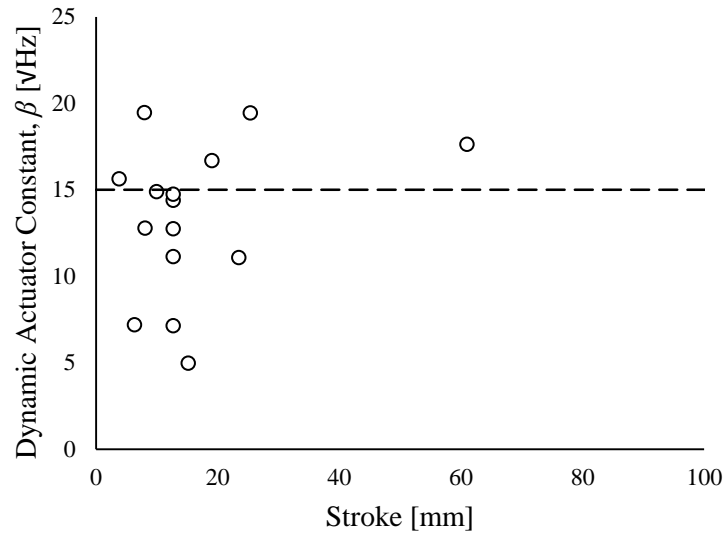


Figure 5.4: Dynamic actuator constant vs. stroke for off-the-shelf MMAs

Table 5.1: MMA performance specifications from various vendors

Performance Metric	Units	Actuator reference (see Table 5.2)														
		This work	1	2	3	4	5	6	7	8	9	10	11	12	13	14
Stroke, $\Delta$	mm	10.0	6.4	3.8	8.1	12.7	12.7	12.7	12.7	12.7	15.2	19.1	23.5	25.4	61.0	8.0
Continuous Force	N	20.0	9.2	2.2	2.2	80.0	2.2	2.2	45.0	3.6	1.8	200.0	4.5	12.5	1865.0	38.4
Peak Force	N	60.0	22.0	6.7	6.7	240.0	6.7	6.7	134.0	10.7	5.4	600.0	13.4	37.4	5594.0	259.0
Force Constant, $K_f$	N/A	32.0	6.2	3.2	3.5	38.6	7.4	2.3	26.7	8.5	1.3	83.6	9.7	4.6	229.0	8.3
Force-stroke non-uniformity	%	9	10	N/A	N/A	N/A	N/A	N/A	N/A	N/A	N/A	N/A	N/A	N/A	N/A	N/A
Continuous Power, $P$	W	20	16	2	2	44	1	5	22	2	6	68	2	8	383	30
Coil Resistance, $R$	Ohm	43.6	7.3	3.5	5.0	10.2	10.8	5.2	8.0	10.8	3.0	12.0	9.6	1.9	5.8	1.4
Actuator Constant, $K_f/\sqrt{R}$	N/ $\sqrt{W}$	4.8	2.3	1.69	1.6	12.1	2.3	1.0	9.4	2.6	0.7	24.1	2.8	4.6	95.1	7.0
Moving Mass, $m_a$	g	106	102	12	15	706	41	20	410	41	21	2088	64	56	29100	130
Actuator Mass	g	1930	226	49	109	2442	107	220	2050	107	75	5720	132	375	72000	N/A
Length	mm	88.9	47.6	42.4	70.5	120.7	96.3	69.5	132.5	106.0	70.5	176.0	66.0	87.0	721.4	33.0
Outer Diameter	mm	76.2	44.0	13.2	16.4	75.7	16.5	25.0	57.2	16.5	16.5	88.0	28.0	36.0	163.8	60.0
Volume	cm <sup>3</sup>	405.4	72.6	5.8	14.8	543.2	20.6	34.1	340.5	22.7	15.1	1070.5	40.6	88.6	15201.8	93.3
Inductance	mH	2.6	2.6	0.3	0.5	5.1	1.3	0.6	3.6	1.3	0.4	6.5	3.8	0.6	5.9	1.1
Electrical Time Constant, $\tau_e$	ms	0.1	0.4	0.1	0.1	0.5	0.1	0.1	0.5	0.1	0.1	0.5	0.4	0.3	1.0	0.8
Mechanical Time Constant, $\tau_m$	ms	4.5	19.4	4.1	6.1	4.8	8.1	19.7	4.6	6.2	40.5	3.6	8.2	2.6	3.2	2.6
Dynamic Actuator Constant, $\beta$	$\sqrt{Hz}$	14.9	7.2	15.6	12.8	14.4	11.1	7.1	14.7	12.7	5.0	16.7	11.1	19.4	17.6	19.5

*Table 5.2: MMA manufacturers and model numbers*

Table 5.1 reference	Company	Model Number
1	BEI Kimco Magnetics	LA16-19-001A
2	H2W Technologies	NCM02-05-005-4JB
3	H2W Technologies	NCM03-06-005-5JB
4	H2W Technologies	NCM05-28-180-2LB
5	H2W Technologies	NCM05-06-005-5JB
6	H2W Technologies	NCM05-10-005-2JB
7	H2W Technologies	NCM05-23-100-3LB
8	H2W Technologies	NCM05-06-008-5JB
9	H2W Technologies	NCM06-06-004-3JB
10	H2W Technologies	NCM08-35-450-3LB
11	H2W Technologies	NCM09-11-010-2X
12	H2W Technologies	NCM10-14-028-2BX
13	H2W Technologies	NCM24-60-4190-6LB
14	Magnetic Innovations	MI-MMA 6033

## CHAPTER 6: Electromagnetic modeling of an MMA

The moving magnet actuator is designed and optimized using the new figure of merit, the dynamic actuator constant,  $\lambda$ , and MMA design considerations also discussed previously. Designing using the dynamic actuator constant requires accurate prediction of the dynamic actuator constant for various MMA dimensions. In this chapter, the effectiveness of lumped parameter analytical modeling in predicting the dynamic actuator constant is investigated. The analytical model of an MMA presented previously captures the system trade-offs and scaling (giving rise to the dynamic actuator constant) and shows how MMA geometrical parameters affect system performance. However, the assumptions made in the model, especially the assumption of no fringing of magnetic flux in the air gap, could result in inaccurate predicted values of the dynamic actuator constant for various MMA geometries, preventing accurate design optimization. Although in this chapter the lumped parameter model was improved to achieve fairly accurate results, FEA was used for subsequent analysis due to its higher accuracy over a large range of dimensions.

The dynamic actuator constant depends on actuator force, power input, and moving mass. For a given MMA geometry, the latter two quantities are simple to estimate. However, the force output requires accurate prediction of the air gap magnetic flux density. Once known, this enables accurate calculation and summation of the force for each winding of the coil. Therefore, to enable optimal detailed MMA design, the goal is to develop an analytical model which accurately predicts the air gap magnetic flux density over a wide range of actuator dimensions.

Figure 6.1 shows predicted flux lines in an MMA solved using static finite element analysis (FEA), along with important nominal dimensions of the geometry. Air gap thickness,  $t_g = 7\text{mm}$ , pole piece thickness,  $t_p = 7\text{mm}$ , magnet radius,  $r_m = 16\text{mm}$ , and magnet thickness,  $t_m = 19\text{mm}$ , are chosen based on the voice coil used in previous work [259]. Magnetic flux passing through the coil is known as working flux as it contributes to the Lorentz force. As described in Section 4.1.1, magnetic flux that spreads away from the working flux is known as fringing flux. Flux that does not enter the coil regions is known as leakage flux. In an MMA, leakage flux can occur at both axial ends of the coil.

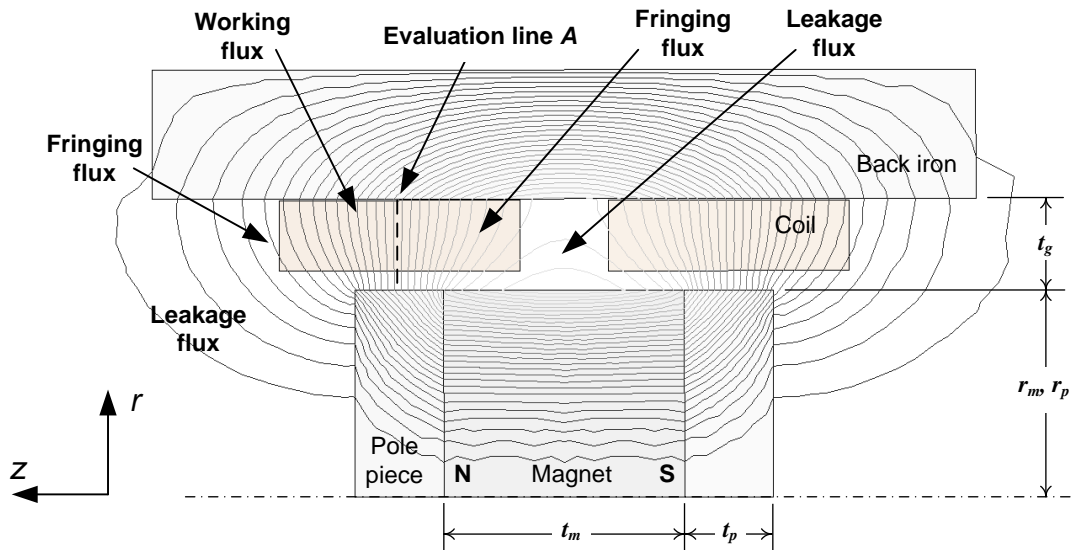


Figure 6.1: Flux lines in MMA and line evaluated for magnetic flux density calculations in various models

Results of each analytical model presented in this chapter are compared to FEA to evaluate accuracy. This is done by calculating the magnetic flux density at points along an evaluation line A in the air gap in Figure 6.1. The evaluation line is located at the axial midpoint of the pole piece. It was assumed that this location gives a good estimate of the flux density in the coil region. A more detailed comparison between the model and FEA

is also conducted, where the force on each coil winding is calculated separately using the magnetic flux density in the respective reluctance region and summed to give the total force. This force is compared to the force from the FEA model. However the main conclusions remained the same and are therefore only the results of magnetic flux density along the evaluation line are presented.

Magnetic flux fringing and flux leakage can cause discrepancies between analytical and FEA models in several ways. These are important considerations for improving the model.

1. Flux leakage is essentially a short in the magnetic circuit. As the flux leakage is in parallel with the magnet source, the overall circuit flux will most likely be higher than in a model that does not account for fringing. However, because the circuit flux is distributed between the various reluctances in parallel, the flux density in portions of the circuit which contribute to useful force may be lower than in a model that does not account for fringing.

2. As described in Section 5.1, reluctance ( $R$ ) in the air gap is dictated by the ratio of the average flux line path length ( $l$ ) and the cross sectional area through which it passes ( $A$ ) and permeability ( $\mu$ ), e.g.  $R = l/\mu A$  [2], [256]. In the air gap reluctance of the original closed form model (a cylindrical flux path in Figure 6.2), the only increase in cross sectional area is due to the change in radius (i.e. change in circumference). Integration of this  $1/r$  dependence of reluctance in the air gap gives the natural logarithm in Equation (5.11). The assumed flux path and reluctance does not change in the axial ( $z$ ) direction. However, due to fringing, the actual magnetic flux as shown by FEA in Figure 6.2 spreads out in the axial direction, so the reluctance cross sectional area will decrease closer to  $\sim 1/r^2$ , leading to a  $\sim 1/r$  dependence of reluctance instead.
3. The cross sectional area in the reluctance calculation is also used in calculating the magnetic flux density. This means that the air gap flux densities will also decrease in the air gap with increasing radial dimension faster compared to closed form models which do not account for fringing.
4. If the magnetic circuit comprises several reluctance paths in parallel, the air gap magnetic flux density could be calculated in each path separately, or as an average over several paths. This can give significantly different magnetic flux densities depending on how well the estimated reluctance regions match the real flux paths.

5. The Lorentz force depends on the magnetic flux density, wire length, and coil current. Ideally, the force on each wire loop is calculated separately with the magnetic flux density in that particular reluctance region and then summed over the entire coil. However various simplifying assumptions (e.g. assuming an average flux density at each coil winding layer, or an average flux density in the entire coil) could lead to reduced accuracy of predicted force.

### 6.1 Model neglecting magnetic fringing

The magnetic circuit for an analytical model assuming no fringing, based on that used in the previous chapter, is shown in Figure 6.2. The actual flux lines are clearly different than the assumed flux path of the model. Because leakage and fringing flux are not accounted for, this may contribute to an inaccurate prediction of the air gap magnetic flux density.

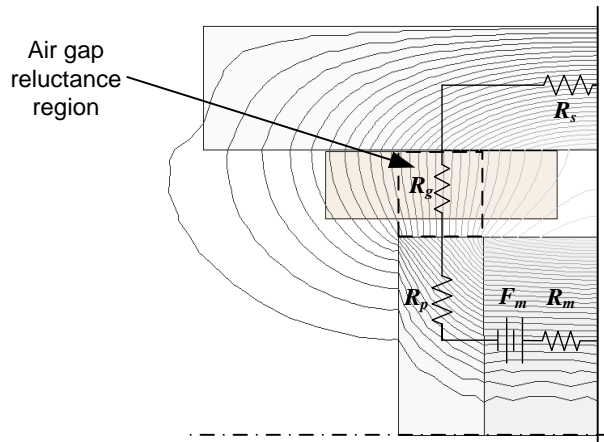


Figure 6.2: Actual flux paths compared to closed form model assumption

The magnetic flux density,  $B$ , is calculated along the evaluation line in the air gap by

$$B_g = \frac{\phi}{A(r)} = \frac{\phi}{2\pi(r_m + r)t_p} \quad (6.1)$$

where  $r$  is the radial distance from the radius of the pole piece and magnet. The magnetic flux,  $\phi$ , is calculated using the circuit analysis presented in the previous chapter. In Figure 6.3, the resulting magnetic flux density along the evaluation line is compared to FEA (initial analytical model curve). The model overestimates the magnetic flux density by almost 100%. However, it appears to accurately capture the rate at which the magnetic flux density decreases with increasing radius. This makes sense, as discussed in point 2 above, because the magnetic flux lines near the evaluation line do not fringe much. For example, by counting the number of flux lines entering the air gap reluctance region from the pole piece face (see Figure 6.2), one will notice that most lines remain within the reluctance region until leaving at the back iron boundary. This implies that the magnetic flux density in the reluctance region mainly changes because of the increasing radius (and therefore circumference).

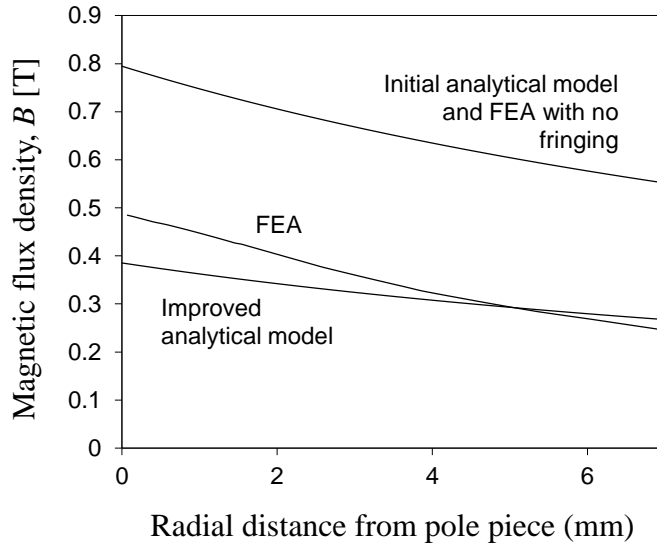


Figure 6.3: Magnetic flux density,  $B$ , in the air gap for various analytical models

To confirm that discrepancies between the FEA and analytical models are only due to inaccurate predictions of the flux path in fringing regions, an FEA model of the MMA was made with custom non-magnetically permeable material ( $\mu \ll \mu_0$ ) placed in all air gap regions except for the analytical model air gap reluctance region. This is shown in Figure 6.4. The non-permeable regions effectively eliminate flux fringing in the FEA model. The resulting FEA flux density overlaid within 0.5% of the analytical model with no fringing, as plotted in Figure 6.3. This confirms that discrepancies between FEA and analytical models are due to flux path estimation only.

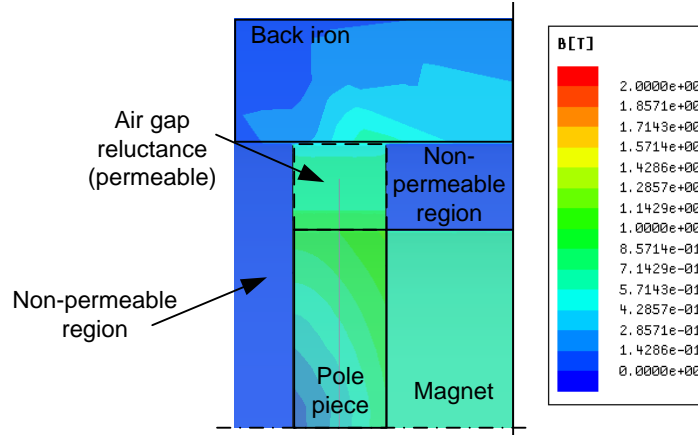


Figure 6.4: Validation of closed form model using non-permeable regions

## 6.2 Models incorporating magnetic fringing via Rotor's method

Roter's method [256] of reluctance estimation was implemented to improve the accuracy of the analytical model. As mentioned earlier, reluctance is proportional to the ratio of the average flux path length and flux cross-sectional area and material permeance. Roter's method proposes to instead use a ratio of average flux path length squared and average volume encasing the flux as shown in equation (6.2). This is because volume integrals can be easier to calculate.

$$R = \frac{l}{\mu A} = \frac{l^2}{\mu V} \quad (6.2)$$

In Roter's method, fringing paths are assumed to be either straight or circular. This often makes calculating reluctances easier while matching the actual fringing paths well. The method is known to approach < 10% error in total circuit flux for many different geometries. This hold true based on the experience in this work. It is found, however, that Roter's method often does not predict flux densities in specific locations in a circuit well.

### 6.2.1 Circular flux paths

The analytical model is improved by incorporating fringing reluctance paths consistent with Rotor's method [256]. Circular fringing paths are assumed, giving the reluctance regions 1-5 in Figure 6.5. Reluctance volumes are calculated using expressions in [256] and the reluctance using (6.2). The geometric mean ( $l = \sqrt{l_1 l_2}$ ) was used as the average path length. The outer boundary radius of region 4 is set to be either the length of the back iron, or the radius of the magnet ( $r_m$ ), whichever is smaller. Regions 2 and 3 are formed by quarter circles with a radius equal to the air gap ( $t_g$ ). Leakage path region 5 fills the space remaining. The additional fringing reluctance regions are incorporated into the circuit in parallel to give the total circuit magnetic flux. The magnetic flux passing through the cross sectional area of the reluctance regions gives the magnetic flux density.

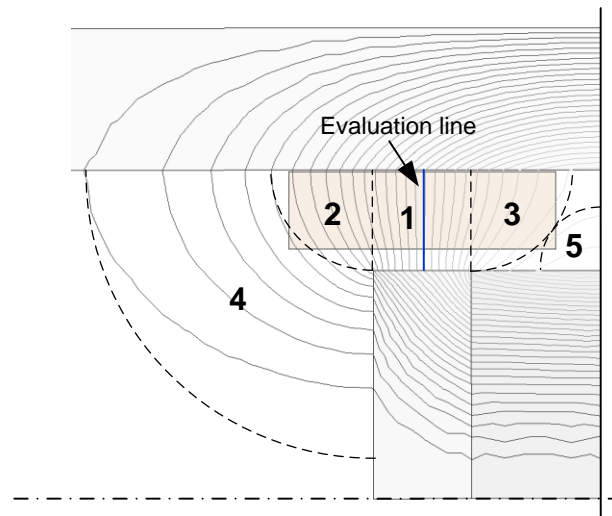


*Figure 6.5: Improved closed form model using circular fringing paths*

The resulting magnetic flux density on the evaluation line in region 1 in the air gap is compared with FEA in Figure 6.6. As discussed in point 1 above, the total magnetic flux of the analytical model increased as expected (from 0.6mWb to 0.9mWb)

due to parallel reluctance paths. However the circuit flux is still underestimated compared to FEA. The magnetic flux splits between the different parallel regions which results in an overall decrease in magnetic flux density in the coil regions 1-3 compared to the initial analytical model. The magnetic flux density along the evaluation line can be calculated using region 1 or by combining regions 1-3 (see discussion point 4 above). Both results are shown in Figure 6.6. The model overestimates the decrease of magnetic flux density when regions 1-3 are used. As discussed in point 3, this implies that the cross sectional area of the reluctance volume increases with increasing radius faster than the flux actually spreads. Conversely, it underestimates the decrease of magnetic flux density when only region 1 is used. This implies that the flux leaves reluctance region 1 due to fringing, consistent with the initial analytical model. For this geometry the average error in magnetic flux density along the evaluation line was significant, at 34%. The error magnitude stays consistent for various geometries. Therefore this model is deemed not adequate for use in the detailed design. One cause of the inaccuracy is that reluctance regions 3 and 5 did not well match the actual paths of the flux lines. This is apparent when studying Figure 6.5.

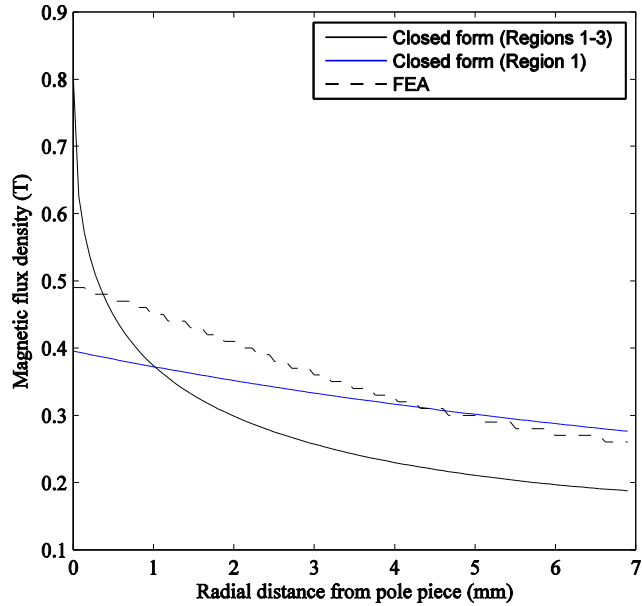


Figure 6.6: Magnetic flux density along evaluation line for lumped parameter model with circular geometries

### 6.2.2 Improved magnetic leakage estimation

To better capture the actual flux paths, the reluctance circuit (Figure 6.7) incorporating a parallelogram reluctance region in the air gap between the coils is introduced. The cross sectional area in reluctance region 3 decreases more slowly for increasing radial position than the quarter circle in Figure 6.5, yet faster than the cylinder in Figure 6.2. This may address the inaccurate decrease in magnetic flux density noted in the previous model. The bounds of the parallelogram reluctance region 5 are determined by the pole piece corner location and axial midpoint of the MMA. This model improves the accuracy of the magnetic flux density prediction in the air gap, however it is not a drastic (<10% improvement), and still led to ~30% error for many different geometries.

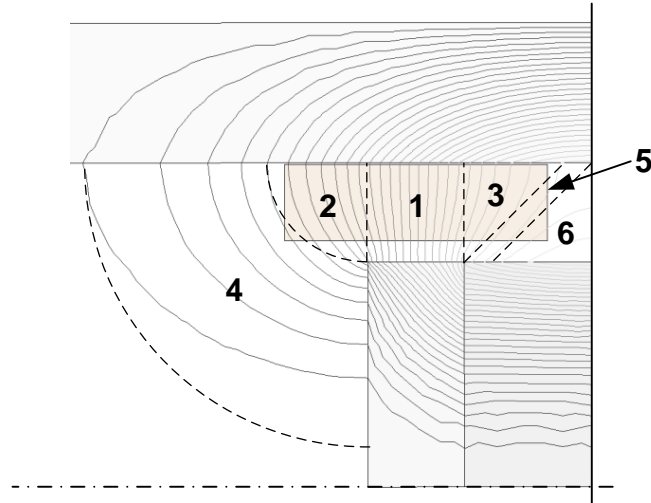


Figure 6.7: Closed form model using parallelogram reluctance region between coils

### 6.2.3 Improved magnetic fringing estimation

The inaccuracies suggest that a better approximation of the flux fringing is still needed. Specifically, if the dependence of flux fringing on air gap thickness is known, the flux density could be more accurately calculated. Therefore the geometrical relationship between the flux lines and air gap thickness is investigated. It is confirmed using FEA that magnetic flux lines in the MMA air gap spread out proportional to the air gap thickness. Therefore, the magnetic flux density also changes with this rate. While this method is primitive (literally counting flux lines in FEA plots for various geometries!), it was surprisingly consistent and significantly improved model results.

Figure 6.8 shows the method used to approximate the dependence of fringing on air gap thickness ( $t_g$ ). The variable  $a$  denotes an arbitrary axial length along the pole piece (selected to be 25% of the pole piece thickness,  $t_p$ ). The variable  $b$  denotes a length on the inner wall of the back iron. The length  $b$  is defined as the minimum length along which

all flux lines that leave through length  $a$  also cross through  $b$ . For example, in Figure 6.8 there are 4 flux lines that leave the pole piece face along length  $a$ , and  $b$  is the length through which the 4 flux lines enter the back iron.

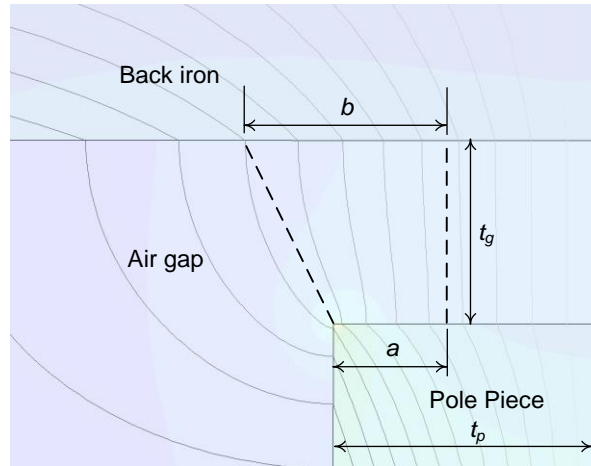


*Figure 6.8: Method of investigating the dependency of magnetic flux fringing on air gap size ( $t_g$ )*

Figure 6.9 shows the distance that the fringing flux spreads ( $a - b$ ) for various MMA geometries and air gap lengths,  $t_g$ . The best fit line gives the following relation

$$b - a \cong 0.4t_g \quad (6.3)$$

showing a linear dependence between magnetic flux fringing and air gap thickness. The relation is incorporated into the analytical model using the variables  $a$  and  $b$  as shown in Figure 6.10.

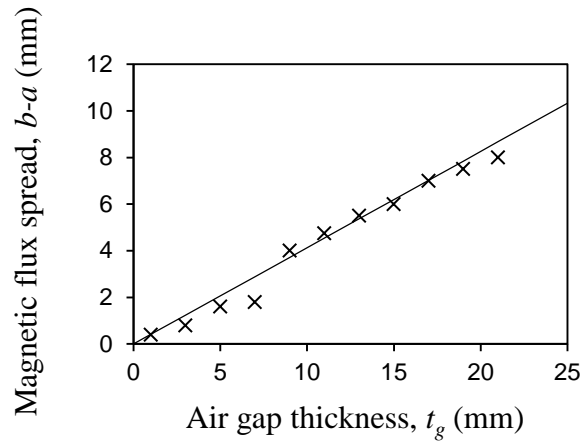


Figure 6.9: Magnetic flux fringing distance dependence on air gap thickness

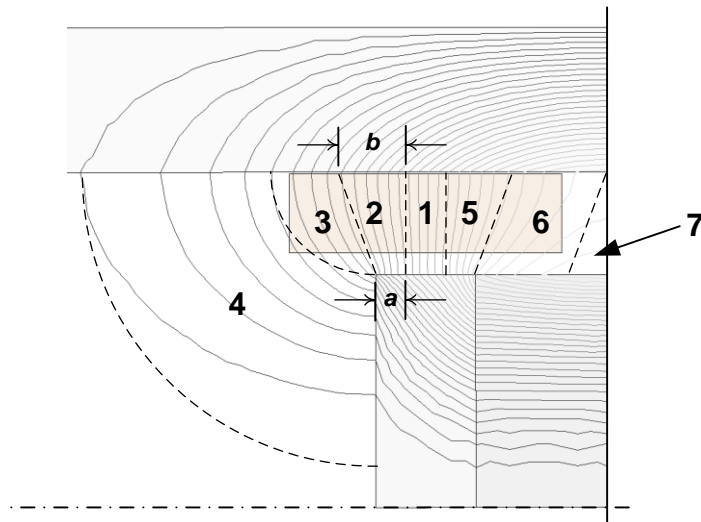


Figure 6.10: Analytical model incorporating flux fringing dependence on air gap thickness,  $t_g$

In this model, the estimated magnetic flux density is much improved. Figure 6.11 shows the magnetic flux density on the evaluation line for several different MMA geometries. The geometries are varied widely, for example the air gap thickness is varied between 3mm and 25mm. The results for the MMA dimensions used at the start of the

chapter are in Figure 6.11c (this is also plotted in Figure 6.3 to compare with the initial analytical model). However, the magnetic flux density magnitude is still underestimated, especially for smaller air gap sizes (Figure 6.11a-d). The likely source of this error is from regions 6 and 7 and from the region 4. In these regions, the spread of flux does not match well with the actual flux lines. Interestingly, if regions 6 and 7 are neglected, the slope does not fit as well, however the error in flux density magnitude is less than 10% over a large dimension ranges:  $3mm < t_g < 25mm$ ,  $4mm < r_m < 20mm$ ,  $15mm < t_m < 35mm$ ,  $7mm < t_p < 30mm$ . This suggests that the total circuit reluctance is not captured accurately, especially for smaller air gap thicknesses, despite capturing fringing well.

While the radial dependency of magnetic flux density in the air gap is captured better, the magnitude is still significantly inaccurate (~30%) for many geometries. Therefore, in the rest of this work FEA is employed. It may be that the limitations of the lumped parameter method have been approached. Exploring different reluctance geometries to better capture the end fringing effects could further improve the analytical model accuracy. Improving this lumped parameter circuit model would be rewarding future work, however, it is anticipated that a closed form model using magnetic potential methods [173][257][258] may be more useful due to their high accuracy despite higher complexity. The MATLAB code implementing this model can be found in APPENDIX A: Analytical MMA model MATLAB code.

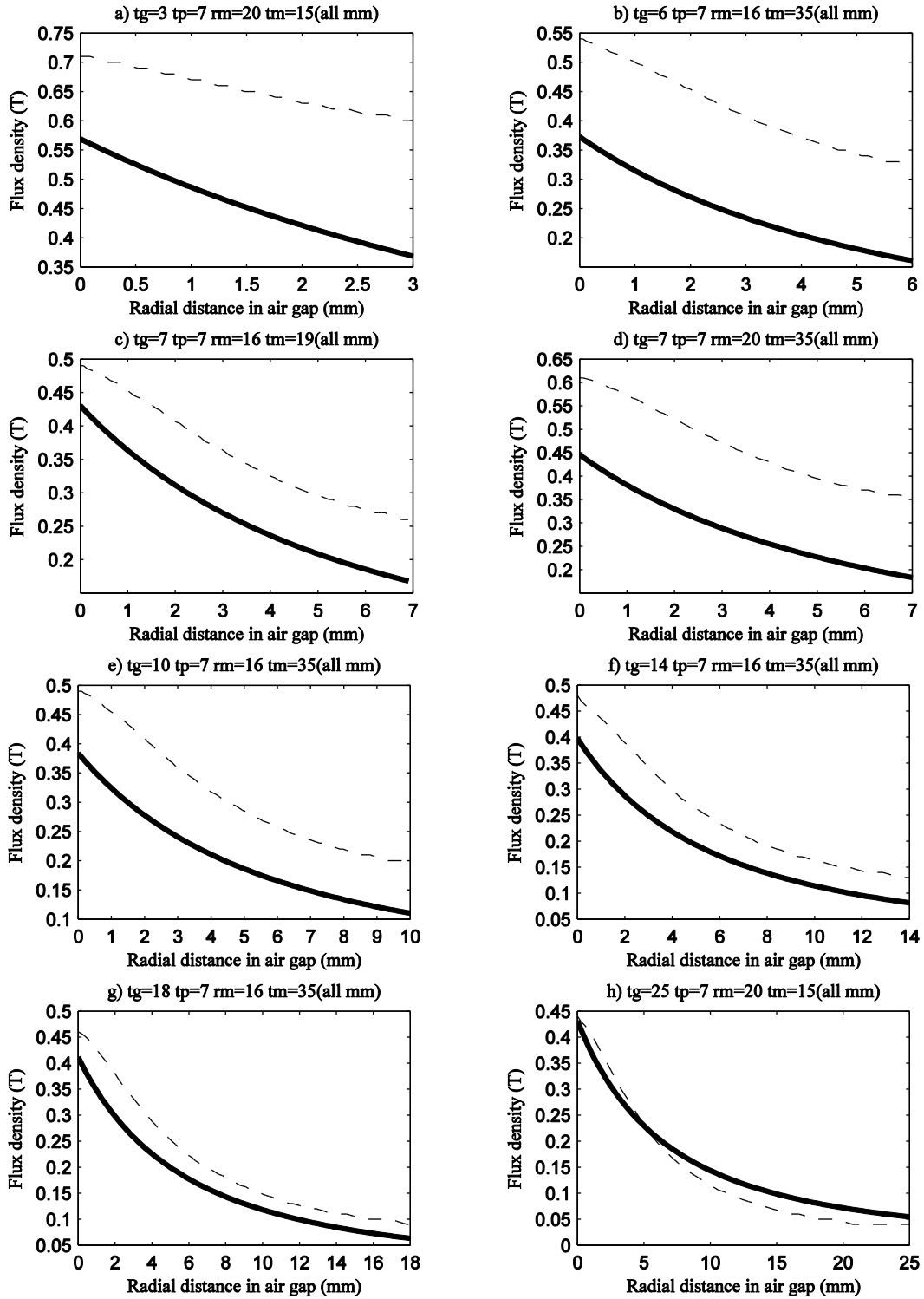
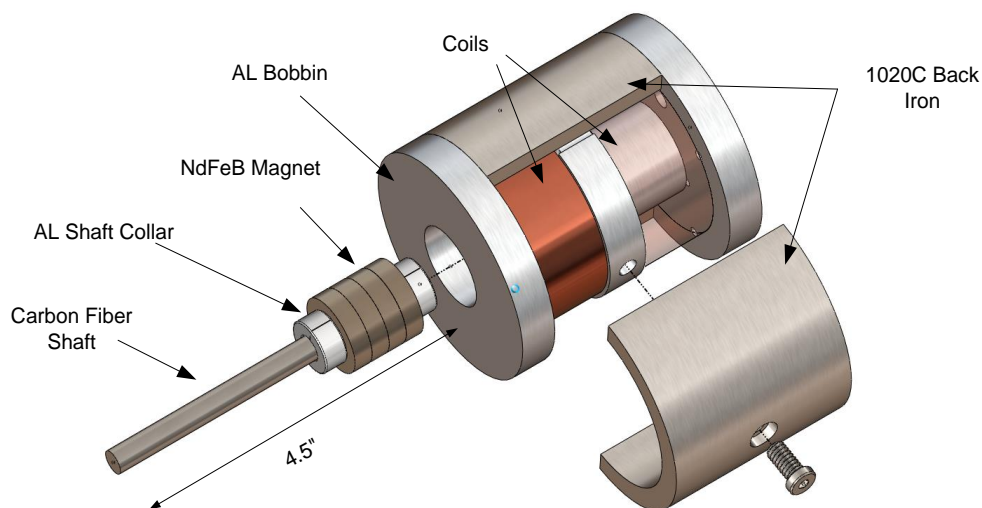


Figure 6.11: Results of improved closed form model showing air gap flux density,  $B$ , along evaluation line for various geometries. Nominal MMA dimensions are in c)

## CHAPTER 7: Actuator design and fabrication

The detailed design and fabrication of the moving magnet actuator is described here, including selection of actuator dimensions, magnet type, wire, mechanical mounting, and assembly considerations. Fabrication of the MMA is carried out in-house by the author and general guidelines and tips are given. The final CAD design is shown in Figure 7.1 and the fabricated prototype in Figure 7.2. The predicted performance of the final design is shown in Table 7.1. Final experimental results are given in Chapter 10.



*Figure 7.1: CAD rendition of MMA*

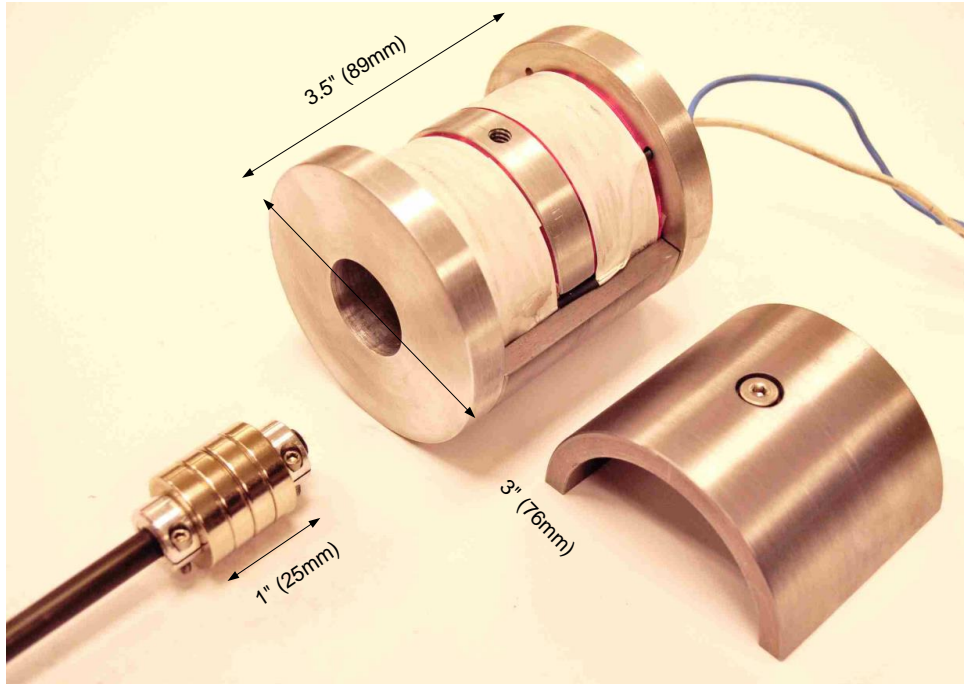


Figure 7.2: Fabricated MMA prototype

Table 7.1: MMA final design specifications

Parameter	Value	Units
Dynamic actuator constant	14	Hz <sup>1/2</sup>
Actuator constant	4.5	NW <sup>-1/2</sup>
Force constant	31.5	NA <sup>-1</sup>
Max. cont. force	17	N
Stroke	10	mm
Moving mass	106	g
Force-stroke non-uniformity	9	%
Resistance	43.6	Ω
Inductance	2.6	mH
Radial / Axial size	∅ 76.2 /	mm
Total mass	2300	g
Air gap magnetic flux	0.1 – 0.3	T

## 7.1 Detailed design

The MMA dimensions and materials are selected in a systematic manner to maximize the dynamic actuator constant,  $\beta$ , while maintaining high force-stroke uniformity. All results presented in this section are using Maxwell<sup>TM</sup> FEA software. The final topology of the MMA is shown in Figure 7.3 and selected dimensions are listed in Table 7.2. A methodical design process to maximize the dynamic actuator constant is followed, starting with the only known variable, the stroke length of 10mm.

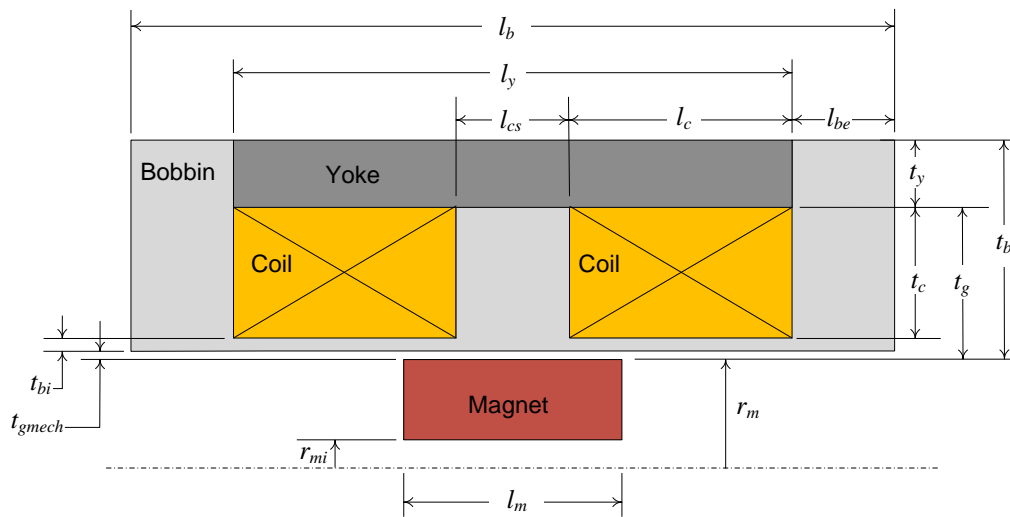


Figure 7.3: MMA topology

Table 7.2: Selected MMA dimensions

Dimension	Symbol	Value mm (in.)
Magnet outer radius	$r_m$	12.7 ( $\frac{1}{2}$ )
Magnet inner radius	$r_{mi}$	4 ( $\frac{5}{32}$ )
Magnet axial length	$l_m$	25.4 (1)
Coil radial thickness	$t_c$	15
Coil axial length	$l_c$	26
Coil separation	$l_{cs}$	13.2
Bobbin axial length	$l_b$	88.9 ( $3\frac{1}{2}$ )
Bobbin extension	$l_{be}$	12.7 ( $\frac{1}{2}$ )
Bobbin radial thickness	$t_b$	25.4 (1)
Bobbin inner wall thickness	$t_{bi}$	1.5
Yoke length	$l_y$	63
Yoke thickness	$t_y$	7.6
Total air gap	$t_g$	17.8
Mechanical air gap	$t_{gmech}$	0.5
Wire diameter	$d$	0.455 (25AWG)

### 7.1.1 Pole piece

An initial design consideration is whether to include steel pole pieces at the axial ends of the mover. While conventionally used in MMA designs, it was not known whether the beneficial increase in force and / or force uniformity overcomes the drawback of increased mover mass, considering the dynamic actuator constant. Figure 7.4 shows the dynamic actuator constant vs. mover position for a conventional MMA with and without pole pieces. The dimensions used for the simulation are  $r_m=16\text{mm}$ ,  $t_g=6\text{mm}$ ,  $l_c=19\text{mm}$ ,  $t_m=19\text{mm}$ ,  $t_p=7\text{mm}$ . Removing pole pieces increases the dynamic actuator constant without significantly altering the force uniformity over stroke. Interestingly, removal of the pole pieces does reduce the force constant ( $K_f$ ) yet due to the

reduced moving mass it leads to an overall higher value of  $\beta$ . This finding is consistent for several other dimensions as well. Therefore pole pieces are not incorporated into the MMA design.

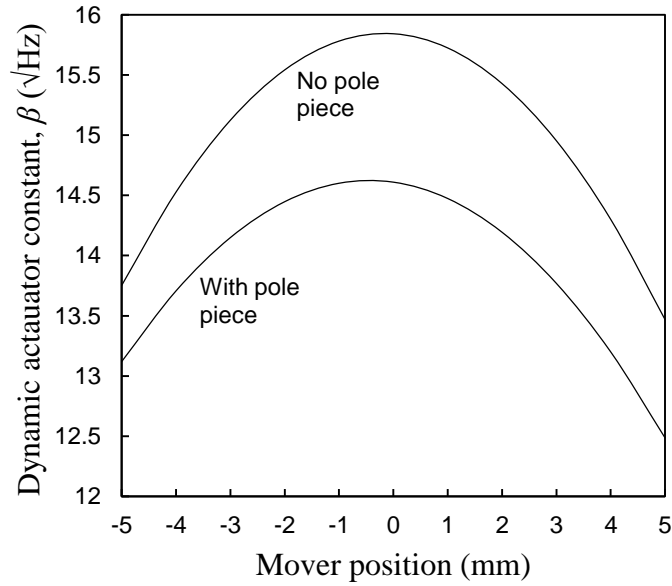


Figure 7.4: Effect of pole piece on the dynamic actuator constant

### 7.1.2 Magnet length

To ensure the magnet is enclosed by coils, in Figure 7.5 it can be seen that the minimum magnet length ( $l_m$ ) is dictated by the desired stroke ( $\Delta_o$ ) and the coil separation ( $l_{cs}$ ), given by Equation (7.1).

$$l_m \geq 2\Delta_o + l_{cs} \quad (7.1)$$

The coil separation should be large enough so that fringing flux from one face of the magnet does not pass through the opposite coil when the magnet is at maximum stroke. This maintains higher force uniformity over the stroke. Assuming a circular flux

fringing path ( $r_f$ ), the coil separation ( $l_{cs}$ ) in Figure 7.5 should be at least the thickness of the coil ( $t_c$ ), related by

$$l_{cs} \geq r_f \cong t_c \quad (7.2)$$

Assuming a maximum coil thickness of 15mm, the minimum coil separation is chosen to be 15mm. However, due to fabrication constraints the prototype coil separation is 13.2mm. For a desired stroke of  $\Delta_o = \pm 5\text{mm}$ , the magnet length of 25.4mm (1in.) is selected. This is a readily-available commercial magnet length.

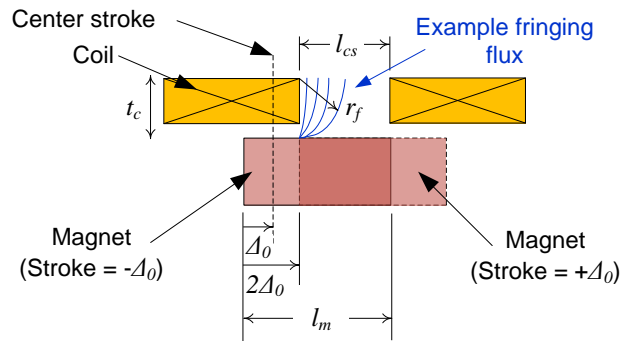


Figure 7.5: Magnet length and coil separation requirements

### 7.1.3 Magnet radius and coil thickness

While the dynamic actuator constant,  $\beta$ , is invariant with geometric scaling, it does vary with the dimensional proportions of the actuator. Therefore, once the magnet length is chosen, the magnet radius ( $r_m$ ) and the coil thickness ( $t_c$ ) can be selected to maximize  $\beta$ . The coil length ( $l_c$ ) and back iron length are initially set to be very long ( $> 100\text{mm}$ ) to eliminate any force-stroke non-uniformity trade-offs as discussed next in Section 7.1.4. Neodymium-Iron-Boron (NdFeB) magnet material and a shaft mass of 15g are assumed for calculating the moving mass. Figure 7.6 shows the effect of varying the magnet radius and coil thickness on  $\beta$  for a fixed coil length ( $l_c$ ). With increasing magnet

radius, the incremental gains in  $\beta$  decrease. For a given magnet radius, there is an optimal coil thickness, corresponding to a peak in the  $\beta$  curve. It should be noted that the coil length and moving mass shown are the final optimized values chosen in the next sections. With the initial extended coil length and back iron length, matching curves result except that the magnitude of  $\beta$  is lower. This enables optimal selection of magnet radius and coil thickness before knowing the optimal coil length. Based on this plot, and taking manufacturing constraints and standard magnet sizes into account,  $r_m$  and  $t_c$  are chosen to be 12.7mm and 15mm, respectively. Similar trade-offs between  $\beta$  and coil thickness ( $t_c$ ) exist in selecting the inner radius of the magnet ( $r_{mi}$ ). This dimension is 4mm and is based on available magnet sizes as described next.

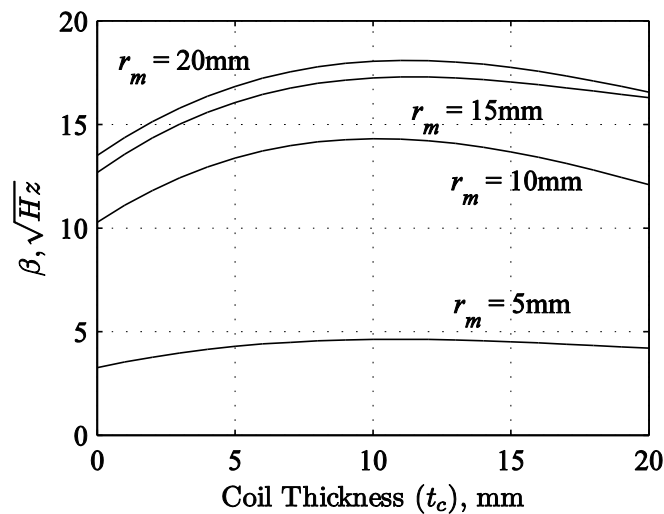


Figure 7.6: Variation in dynamic actuator constant ( $\beta$ ) with varying coil thickness and magnet radius

The magnet comprises a stack of four commercially available Grade 52 Neodymium-Iron-Boron axial magnets [260] as shown in Figure 7.7. The main advantage is the high remanent magnetization ( $B_r = 1.45\text{T}$ ), which directly affects  $\beta$  as seen in Equation (5.17). One drawback of this magnet is its low maximum operating temperature

of 80°C (due to a low Curie temperature), but this risk is mitigated by the thermal management system described in Chapter 8. The total actuator moving mass is 106g.



*Figure 7.7: N52 NdFeB grade ring magnet [260] from K&J Magnetics, Inc.*

#### 7.1.4 Coil length

Due to magnetic flux fringing, it is assumed that the air gap flux path width increases by the radius of the magnet. Therefore the coil length ( $l_c$ ) is dictated by the stroke and the magnet radius as

$$l_c \geq 2\Delta_o + r_m \rightarrow l_c \geq 22.7\text{mm} \quad (7.3)$$

It should be noted however, that a better assumption would be to use the coil thickness instead of the magnet radius. Increasing the length of the coils improves the force-stroke uniformity but only at the cost of an increase in the coil resistance, which reduces the dynamic actuator constant,  $\beta$ . As shown in Figure 7.8, the coil length is chosen to be 26mm to achieve a high value of  $\beta$  while ensuring that the drop in force at the ends of the stroke is less than 10%. It should be remembered that force is proportional to  $\beta$  for fixed power input and mover mass. The selected coil length gives that  $\beta$  is predicted to be  $\sim 15\sqrt{\text{Hz}}$ .

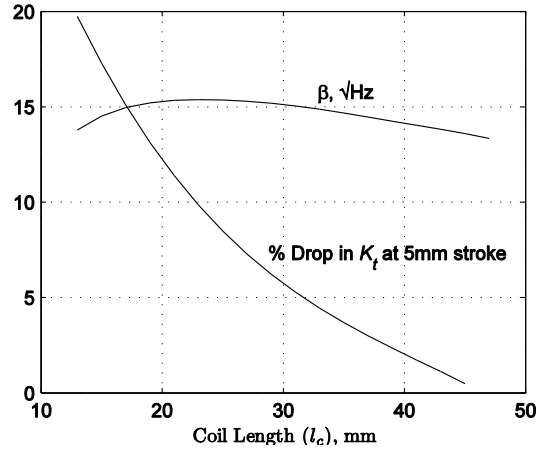


Figure 7.8: Percentage drop in force constant ( $K_t$ ) at the ends of the stroke and dynamic actuator constant ( $\beta$ ) vs. coil length ( $l_c$ )

#### 7.1.5 Wire gauge

As shown in Section 5.1,  $\beta$  is only dependent on coil volume and is independent of the wire diameter ( $d$ ). Reducing  $d$  increases the coil resistance  $R$ , however it also increases  $K_t$  due to greater number of turns, thereby keeping  $\beta$  invariant. However, the choice of wire diameter presents a tradeoff between voltage and current for a fixed power input. Figure 7.9 shows this trade-off for a fixed power level of 20W (dictated by the power amplifier specifications [239]). 25AWG wire with a diameter of 0.455mm is chosen to keep the required voltage below 25V, a limit imposed by the power supply. This resulted in maximum continuous current of 0.56A and coil resistance of 43.6 $\Omega$ .

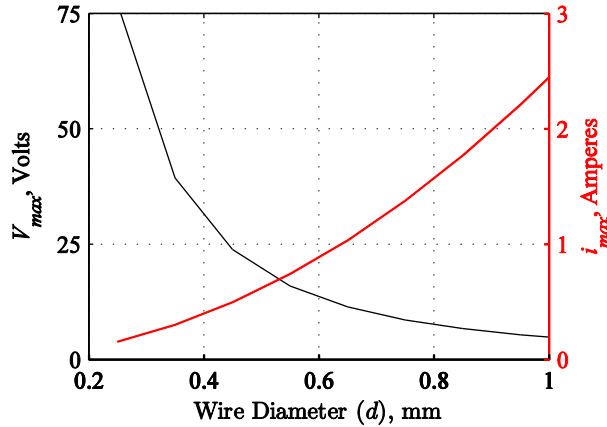


Figure 7.9: Maximum continuous current and voltage requirement vs. wire diameter

#### 7.1.6 Back iron

The back iron (i.e. yoke) thickness ( $t_y$ ) is chosen such that the magnetic flux density in the iron remains below saturation for all values of coil current. Under maximum current input,  $t_y$  is increased until the magnetic flux density in the back iron drops below  $\sim 1.2\text{T}$ , which is safely below saturation levels. Therefore a thickness of 7.6mm (0.3in) is chosen.

Increasing the length of the back iron ( $l_y$ ) reduces the axial reluctance force between the magnet and the back iron. As discussed in Section 4.1.1, this force acts in addition to the Lorentz force and tends to restore the magnet towards the center of the stroke. The dimension of 65mm was chosen to maximize the length, limited by the width of the bobbin ends used for the thermal management system design. The resulting Lorentz and axial reluctance force are plotted in Figure 7.10 for  $i = 1\text{A}$  and  $i = 0\text{A}$ , respectively. While the Lorentz force component is symmetric with respect to zero stroke position, the overall force–stroke profile of the MMA turns out to be nonsymmetrical due to the force between the magnet and the back iron. The predicted stiffness due to this

reluctance force is 0.2N/mm. This latter force component is unique to MMAs and does not exist in VCAs, in which the magnet and back iron are rigidly attached.

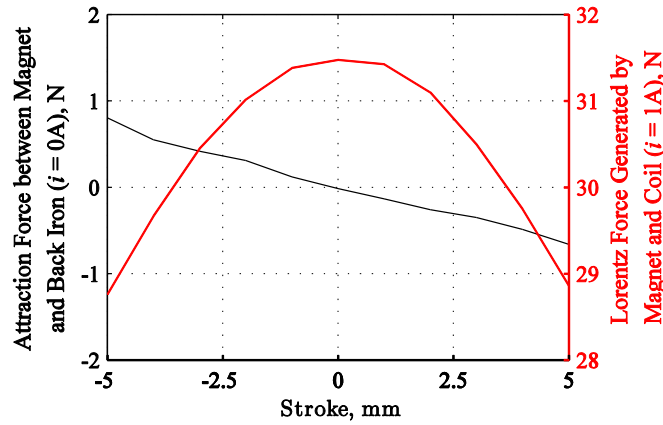


Figure 7.10: Mover force vs. stroke for  $i = 0A$  and  $i = 1A$  coil current

The resulting magnetic flux density in the MMA at nominal mover position is shown in Figure 7.11. Flux density in the air gap is 0.1 – 0.3T.

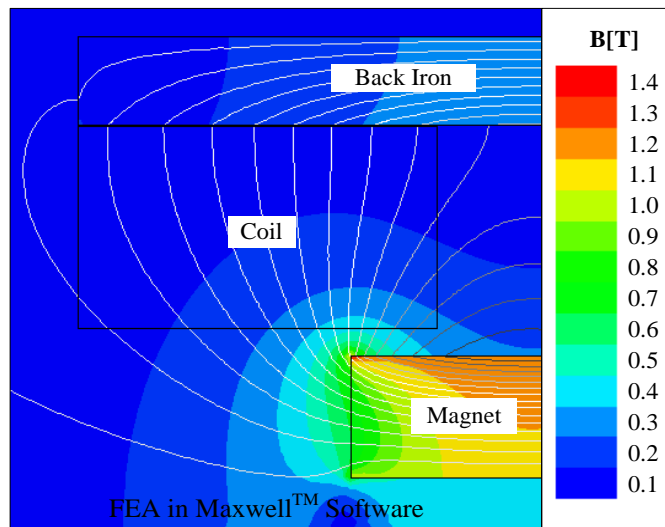


Figure 7.11: Flux Density in the MMA

Grade 1020C steel is selected as the material due to its availability and good magnetic characteristics, including a saturation flux density of 1.6T.

### 7.1.7 Coil bobbin

The magnetic circuit and therefore the dynamic actuator constant are influenced by several practical mechanical considerations involving the bobbin design. Increasing the air gap between the magnet and coils decreases the dynamic actuator constant. Therefore the mechanical air gap ( $t_{gmec}$ ) and bobbin wall thickness ( $t_{bi}$ ) should be minimized. The mechanical air gap is chosen to be 0.5mm, limited by manufacturing and assembly tolerances to avoid contact between the mover and stator. An error budget was made considering worst-case scenario tolerance stacking between the mover and stator during assembly. The bobbin inner wall thickness is selected to be 1.5mm (60 thou). This dimension is chosen to be comfortably large to avoid risk of structural failure, although it could be smaller given that the material is relatively stiff. During fabrication, the wall thickness was further reduced to 1mm once it was found to be structurally rigid. The radial thickness of the bobbin ( $t_b$ ) is selected to be 48.8mm based on the magnet, coil and back iron dimensions.

Aluminum 6061 is chosen for the bobbin material. One advantage is its high thermal conductivity to effectively remove heat from the coils. In addition, Aluminum has good machinability, and it serves as a shorted turn which can be advantageous (see Section 4.1.3 for discussion).

The bobbin length ( $l_b$ ) is chosen to optimize thermal management. Several factors are considered. 1. Aluminum has a high thermal conductivity. 2. The coils are wound so that there is a small air gap between the windings and the steel yoke. This protects the coils from wear and damage. 3. As described in Section 8.2.3, an aluminum thermal housing is designed to provide an interface between the MMA and heat pipes. The housing should have tight contact to the MMA in order to lower contact resistance. The

housing achieves this by lightly clamping the MMA between two symmetrical halves. Due to tolerances, a design in which both the yoke and the bobbin tightly interface the thermal housing is not possible. Depending on the tolerances, either the yoke or the bobbin will have good contact, while the other has a poor contact.

Given these factors, two main design concepts for the bobbin and housing interface are considered. In the first concept (Figure 7.12a), the thermal housing clamps the yoke and the primary heat transfer path is from the center of the bobbin radially outwards through the steel yoke. In the second concept (Figure 7.12b) the thermal housing clamps the ends of the bobbin. The primary heat transfer path is from the ends of the coils radially outwards through the aluminum bobbin. The total thermal resistance of the heat transfer paths are represented by  $R_1$  and  $R_2$ , where  $R_2 = R_2'/2$ .

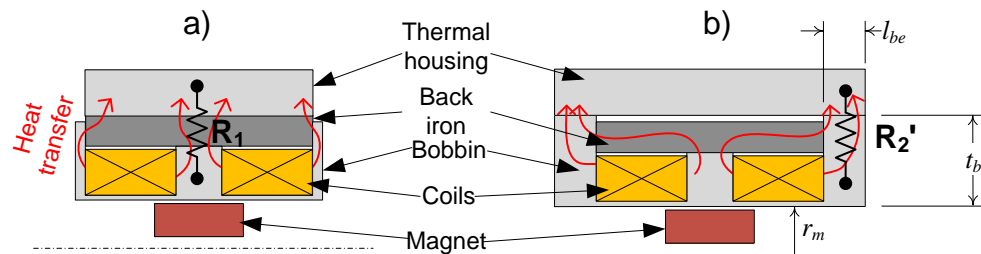


Figure 7.12: Bobbin design considerations

The main drawback of the first concept is the much lower thermal conductivity of steel ( $\sim 40\text{W/m/K}$ ) as compared to Aluminum ( $\sim 215\text{W/m/K}$ ) as well as the air gap between the coils and yoke. These factors could potentially lead to a high thermal resistance of the heat transfer path. Therefore the minimum bobbin extension length ( $l_{be}$ ) is estimated in the second concept which would result in an equal thermal resistance of the yoke in the first concept, assuming heat was evenly distributed through its entire

length. If the minimum bobbin extension length is reasonable then it makes more sense to choose the second concept. The thermal resistances are compared in equation (7.4), resulting in relation (7.5) between the minimum bobbin extension length ( $l_{be}$ ) and the thermal conductivity of steel ( $k_s$ ) and Aluminum ( $k_{Al}$ ), and the length of the yoke ( $l_y$ ).

$$R_1 \geq R_2 \rightarrow \frac{\ln\left(\frac{r_m + t_b}{r_m}\right)}{2\pi k_s l_y} \geq \frac{1}{2} \frac{\ln\left(\frac{r_m + t_b}{r_m}\right)}{2\pi k_{Al} l_{be}} \rightarrow \frac{1}{k_s l_y} \geq \frac{1}{2k_{Al} l_{be}} \rightarrow 2k_{Al} l_{be} \geq k_s l_y \quad (7.4)$$

$$l_{be} \geq \frac{k_s}{2k_{Al}} l_y \quad (7.5)$$

This implies that the bobbin extension should be greater than or equal to  $0.1l_y \approx 6\text{mm}$ . This is reasonable, and the bobbin extension was therefore chosen to be half an inch (12.7mm) to be well above the minimum length. This results in a total bobbin length ( $l_b$ ) of 89mm (3.5 in).

#### 7.1.8 Off-axis attraction forces

The flexure bearing must provide adequate off-axis stiffness to counter the negative off-axis stiffness of the moving magnet. Therefore the off-axis attraction force is calculated via FEA assuming a maximum off-axis mover displacement in the mechanical air gap (based on the dimension  $t_{clear}$ ). Figure 7.13 shows the setup used in FEA. The off-axis force is 0.65N for a radial displacement of the mover by 0.5mm. For further discussion see Section 9.1.4.

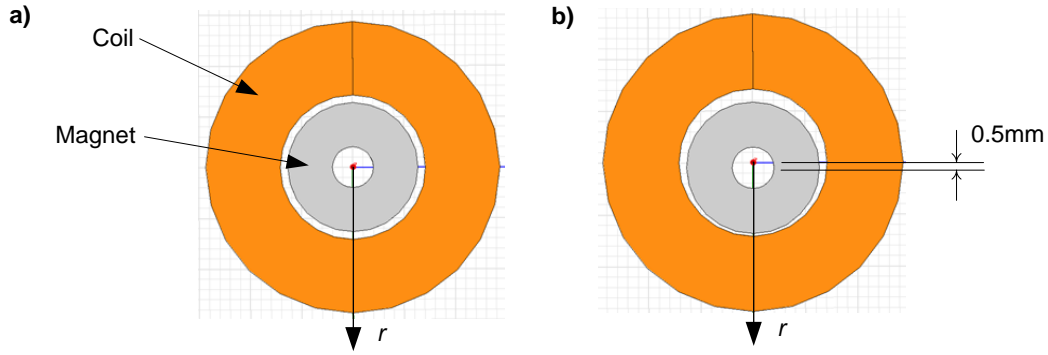


Figure 7.13: Magnet in a) nominal position and b) misaligned by 0.5mm in radial direction

### 7.1.9 Mover shaft

The MMA mover shaft connects the magnets to the motion stage. It should be lightweight, stiff, non-magnetically permeable, and have low heat transfer and thermal expansion coefficients so that any heat transferred via convection and radiation from the coils to the mover does not reach the motion stage. As an initial selection criterion, the minimal shaft stiffness was calculated. Assuming a simple cantilevered beam of circular cross-section, the deflection is equal to

$$\delta = \frac{Pl^3}{3EI} = \frac{4Pl^3}{3\pi Er^4} \leq 0.5mm \quad (7.6)$$

where  $P$ ,  $l$ ,  $E$ ,  $I$  and  $r$  are the maximum radial off-axis attraction force, shaft length, Young's modulus, area moment of inertia and shaft radius, respectively. The deflection must be less than the mechanical air gap thickness of 0.5mm to avoid collision. Solving for the minimum required Young's modulus gives Equation (7.7)

$$E \geq \frac{4Pl^3}{3\pi r^4 \delta} \quad (7.7)$$

The shaft length is assumed to be 102mm (4in.) and the shaft radius 4mm. The magnet mass is again assumed to be 100g. With a safety factor of 2, this results in a minimum required Young's modulus of 5GPa. Materials that fit the Young's modulus criterion and the others listed above are evaluated. Aluminum, while non-magnetic and having a low mass density ( $2.7 \text{ g}\cdot\text{cm}^{-3}$ ), is not selected due to its high thermal conductivity and fairly high thermal expansion coefficient ( $237 \text{ W}\cdot\text{m}^{-1}\cdot\text{K}^{-1}$  and  $23 \mu\text{m}\cdot\text{m}^{-1}\cdot\text{K}^{-1}$ , respectively). Austenitic (3XX grade) stainless steels, due to nickel content, are largely non-magnetic and have high stiffness, however have too high of mass density ( $7.8 \text{ g}\cdot\text{cm}^{-3}$ ). This would have added  $\sim 40\text{g}$  to the mover, or a 50% increase. Alumina silicate ceramics such as MACOR were also considered, due to low mass density ( $2.5 \text{ g}\cdot\text{cm}^{-3}$ ) and very low thermal conductivity ( $1.46 \text{ W}\cdot\text{m}^{-1}\cdot\text{K}^{-1}$ ) and thermal expansion coefficient ( $12.6 \mu\text{m}\cdot\text{m}^{-1}\cdot\text{K}^{-1}$ ). Due to its brittleness, the flexure strength criterion was also considered, which it passed (94MPa far below the maximum allowable 3GPa). Extruded-type (pultruded) carbon fiber shaft is also considered. This composite shaft is commonly used for hobby kite applications. It has high stiffness, very low mass (4g) and is non-magnetically permeable. Although extruded carbon fiber has a high thermal conductivity along the fibers, due to the small cross sectional area, the shaft actually has a high effective thermal resistance. Based on these considerations, the carbon fiber shaft from [Goodwinds](#) is selected.



*Figure 7.14: Pultruded carbon fiber shafts from Goodwin.com*

#### 7.1.10 Summary

Based on this design process, the selected MMA parameters are given in Table 7.2. The MMA is predicted to have a  $\beta$  value of  $14\sqrt{\text{Hz}}$  and an actuator constant of  $4.5\text{N}/\sqrt{\text{W}}$ . This results in an achievable actuation force of 17N for a power constraint of 20W. Additional actuator performance parameters are shown in Table 7.1.

### 7.2 **Practical design considerations**

A CAD model of the MMA based on the selected dimensions is shown in Figure 7.1a. The MMA prototype shown in Figure 7.1b was fabricated and assembled in-house by the author. Some details of the fabrication process and “tips and tricks” learned during the process are included here.

#### 7.2.1 Mover

Two Aluminum shaft collars constrain the magnets to the carbon fiber mover shaft (Figure 7.15). This enables adjustment and / or replacement of the magnets during testing. To assemble, first one shaft collar is tightened to the shaft. Then the magnets and other end shaft collar are slid onto the shaft and preloaded against the first shaft collar before tightening. This eliminates backlash or slipping of the magnet axially between the

shaft collars. The steel bolts that were supplied with the shaft collar are swapped for nylon bolts to avoid any disruption of the magnetic field. The shaft collars are lightweight (4g each). Nylon shaft collars are also investigated to eliminate eddy currents, however the clamping force is not as strong. Structural adhesives such as 3M 2214 are often used to bond magnets to mover shafts and other components in commercial MMAs. Some commercial MMAs use a metal mover shaft with a step to a larger diameter against which the magnets are constrained via a tapped hole and bolt on the other end of the shaft.



*Figure 7.15: Shaft collars constrain magnets to carbon fiber shaft*

### 7.2.2 Back iron

The back iron is designed as two symmetric “clamshell” halves so the mover and bobbin can be easily assembled with the motion stage and bearing without the iron being in the vicinity of the strong magnetic force generated by the permanent magnet. See Figure 7.1, Figure 7.16, and overall assembly pictures in Chapter 10. Without this feature, assembly is very difficult. Due to off-axis attraction, the forces required to insert the mover into a single-piece tubular back iron are enormous (this was done with an earlier MMA prototype and it required several people and many attempts). Recessed 1/4”-20 bolts secure the back iron halves to the bobbin. The through-holes for these bolts also function as a sighting-hole into the center of the bobbin to see the mover once it is inserted into the bobbin. This enables easy axial alignment of the mover (i.e. to center the

mover axially with respect to the bobbin). 1/16” spacing between the back iron halves ensures a snug fit with the bobbin regardless of manufacturing tolerances.

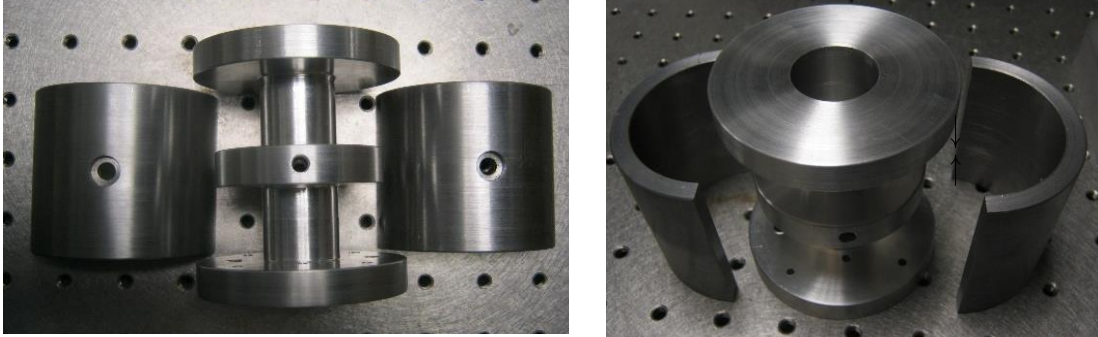


*Figure 7.16: Back iron split in two “clam shells” for simplified assembly with bobbin*

### 7.2.3 Bobbin

As shown in Figure 7.17, the bobbin is aligned radially with respect to the flexure bearing and mover with a dowel pin (see Section 9.2). Tapped holes on the bobbin provide axial constraint from 1/4”-20 bolts in the flexure bearing. The back face of the bobbin has entry- and exit-holes for coil wire for winding. Radial grooves along the coil cavity walls recess wire run down to the bottom of the cavity to begin winding. Otherwise the coils would form a bump around the wire. Axial grooves recess wire run between the coil cavities to avoid contacting the back iron. The aluminum is anodized which electrically insulates the bobbin. This eliminates the risk of shorting if the insulation becomes worn and contacts the bobbin. Insulation is most likely to be worn down on sharp edges of the bobbin so care is taken to round all edges.

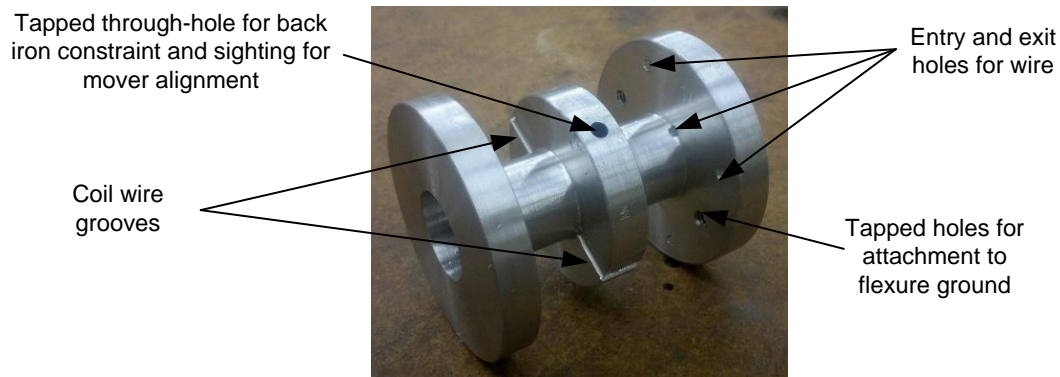


*Figure 7.17: Bobbin details*

### 7.3 Fabrication

All MMA components are fabricated by the author. Various comments on the fabrication process are listed here. Some are obvious to any skilled machinist. Others may be more subtle and particular to MMA design.

#### 7.3.1 Bobbin

- Make sure the coil cavity furthest away from the chuck is turned first, so that there is adequate mechanical support from the bobbin material. If the coil cavity nearest the chuck is turned first, the bobbin will flex and potentially yield when the cantilevered second coil cavity is turned due to the thin wall. This may prohibit achieving the desired dimensions.
- Holes through the end of the bobbin should be drilled in the initial round stock before the coil cavities are turned. This ensures that the drill bit will not be damaged by hitting corners as could happen if the coil cavities and other final dimension on the bobbin were turned first.

- Make sure stock material is long enough so that all bobbin features can be created without removing and reversing the stock in the lathe chuck. This avoids time consuming re-centering.
- Reverse the cutting tool mounting direction to reach inside deep coil grooves.
- A large (3/4") drill bit was used to drill the initial bobbin center cavity. The end of the drill bit is tapered, however, leaving a chamfer at the bottom of the bobbin. The chamfer is removed and the final inner wall diameter is achieved using a cutting tool and boring bar extended down the inside of the cavity. This must be done with care as it is not possible to see the bottom of the bobbin.
- Apply emery tape or Scotch Brite on the bobbin with a fairly slow spindle speed for a good final surface finish.

### 7.3.2 Coil winding

- The bobbin was wound using a lathe at slow spindle speeds. A makeshift spool holder kept the wire from getting tangled, as shown in Figure 7.18a and b.
- Make sure all portions of wire exposed to corners or edges are either wrapped with electrical tape or encased in shrink wrap. Also make sure all bobbin surfaces and edges are filed down. The wire insulation will wear off quite easily, potentially shorting the entire coil before being even fully wound!
- The wire was fed by hand as shown in Figure 7.18c. Layer winding was attempted. It was important to maintain constant tension on the wire otherwise it will unravel.

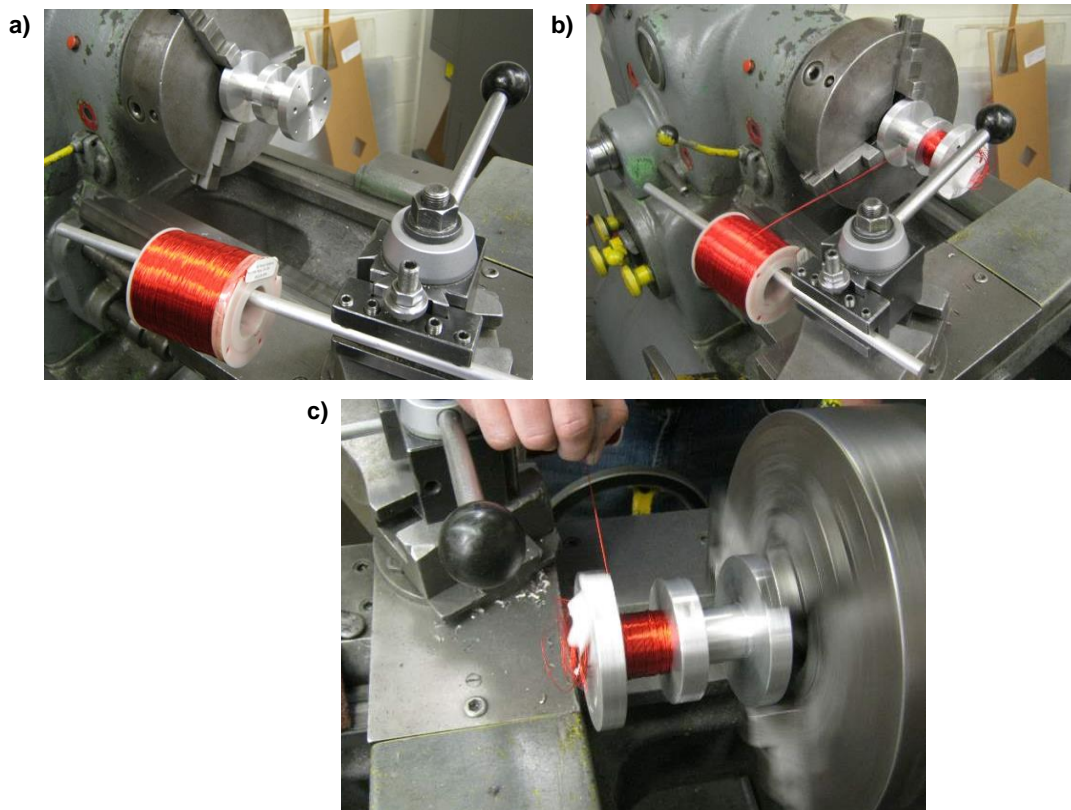


*Figure 7.18: a) coil winding initial setup b) start of first coil and c) hand-guided layer-winding*

- The wire creates layers very uniformly in the middle of the wire cavities, often on its own. A dowel was also sometimes used to keep the windings pressed against each other while winding. It is difficult to uniformly stack the windings at the axial ends of the coil cavity, especially after a number of stacks had been wound. This is because when the wire reverses, sometimes it would leave a gap or raised layer near the edge, where a subsequent winding could fall into or “climb” over. This would cause unevenness in the height of the stacks. There did not seem to be an ideal way of avoiding this. Often times the spindle would be reversed and the trouble spot re-wound. Over many turns bumps or uneven windings could be averaged out.
- Once all of the stacks had been wound, Loc-tight activator and glue was applied to the top stack. This held all stacks together. It may be advantageous to add glue on each layer while winding to prevent lower winding layers from humming / singing. A tight layer of electrical tape also maintains a good coil shape and creates less of a mess than glue. This is shown in Figure 7.19.

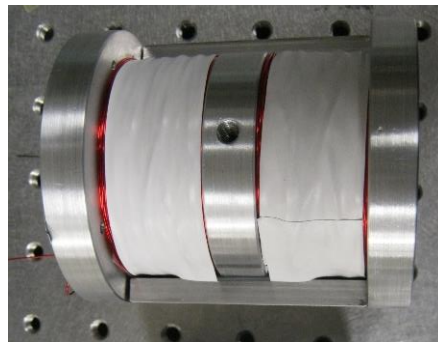


*Figure 7.19: Wound bobbin wrapped with electrical tape*

### 7.3.3 Back iron

- Cylindrical tube stock close to the final back iron inner and out diameter dimensions, instead of round stock is used. This avoids machining the inner diameter and saves significant machining time. Pre-formed steel tube from [speedymetals.com](http://speedymetals.com) was purchased.
- Before cutting the iron core into halves make sure to achieve a good surface finish. Sanding and polishing evenly is difficult once separated. With the single-piece back iron in the lathe chuck with a low spindle speed, use a file to remove any large divots/marks (make sure to clean file with file card after each pass). Using emery tape achieve a fairly good finish. Then use sandpaper increasing in fineness and finally end using steel wool for great surface finish quality.

### 7.3.4 Magnets

- Magnets are brittle and fracture very easily. They should not be press fit or be used as a structural component. Resources [242], [273] are good for practical design and fabrication considerations.

## CHAPTER 8: Thermal management system

As discussed in Section 1.3.4, thermal management is a critical aspect of precision motion system design, particularly in nanopositioning systems. Heating can cause internal stresses and deformation of the bearing, and cause drift in the sensor location and signal output. During steady-state operation, most of the power input to the MMA is dissipated as heat in the coils. This represents the worst-case scenario of heat generation. In the MMA, heating can decrease the remanence of the permanent magnet which reduces force output, and increase coil resistance which reduces power efficiency. It is particularly important that heat dissipated from the coils does not reach the motion stage, where the sample and the sensor are located. All these factors potentially adversely affect the precision and accuracy of the nanopositioning system. This chapter describes a thermal management system (TMS) based on latent heat transfer which is designed to mitigate these problems. The TMS is designed to dissipate 20W of heat while maintaining the temperature of the motion stage within the targeted range of  $\pm 1^{\circ}\text{C}$ . Thermal management concept selection is first discussed, followed by the detailed design process and then fabrication. Other relevant published work where authors are concerned with temperature variation and have built some kind of thermal management system include [60], [92], [261]–[267].

Special thanks to Yangbing Lou, Yilong Wen, and Yi Chen for their significant contributions to the design, manufacturing and experimental testing of the thermal management system.

The final design and fabricated TMS prototype are shown in Figure 8.1 and Figure 8.2. The TMS effectively transfers heat generated in the MMA coils from the aluminum housing around the MMA, to a separate cooling unit housing water-sealed ice-packs, using copper heat pipes that serve as low thermal resistance paths. The heat generated in the coils is absorbed by ice as it transitions to water, without any rise in its temperature. The aluminum housing and racks containing ice-packs are thermally insulated via a double-layered acrylic box in order to minimize any thermal fluctuations to the environment. The critical components of the TMS (heat pipes, ice packs, and aluminum racks) are designed using a lumped-parameter thermal model to ensure that the steady-state coil bobbin temperature remains near room temperature for at least 4 hours of operation under constant 20W power input to the actuator.

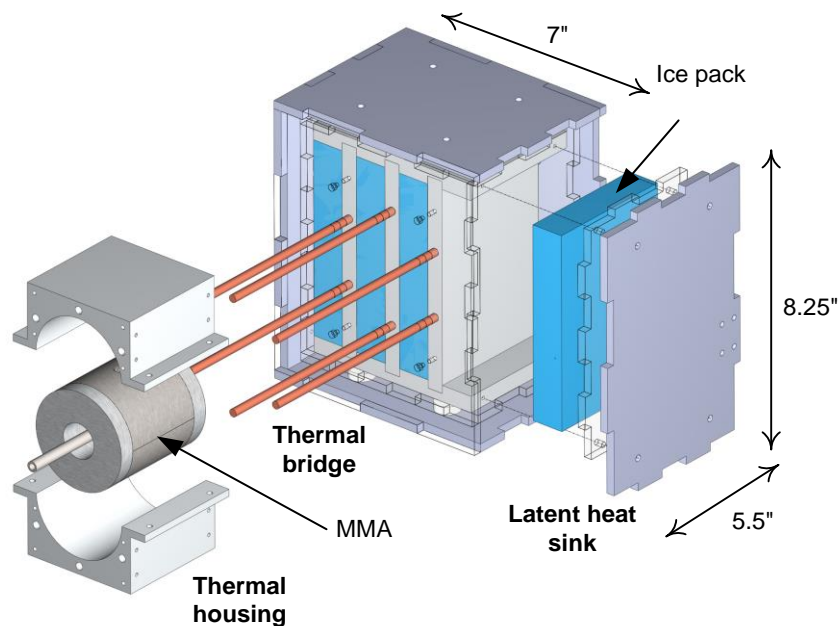
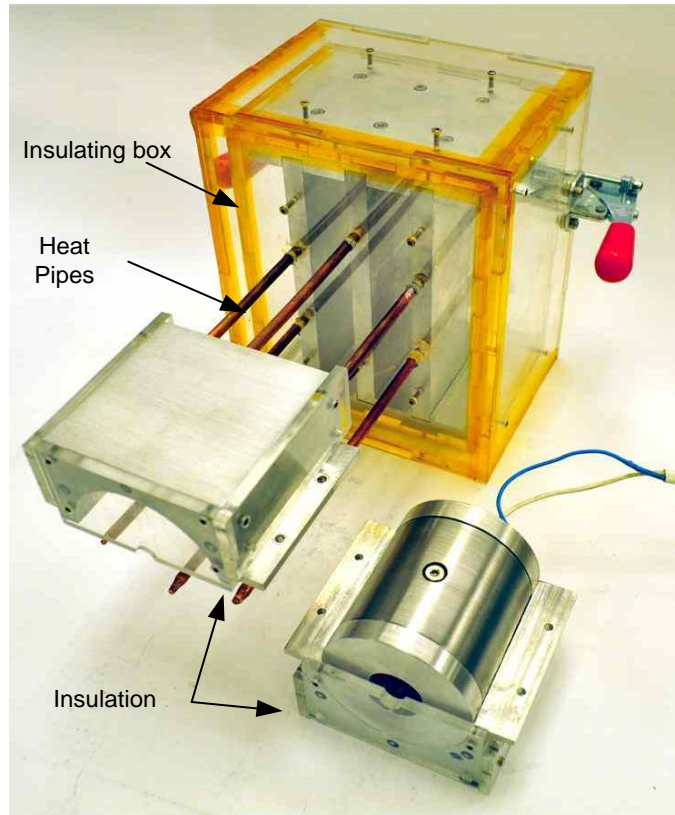


Figure 8.1: CAD rendition of thermal management system



*Figure 8.2: Fabricated TMS prototype*

## **8.1 Concept selection**

As shown in Figure 8.3, there are three paths that heat dissipated from the actuator coils can travel between the MMA and the motion stage: 1. Conduction through the ground of the bearing. 2. Conduction through the mover shaft. 3. Convection through the air. Radiation transfer is neglected due to the relatively low temperatures, although consideration of radiation is important in design for vacuum conditions.

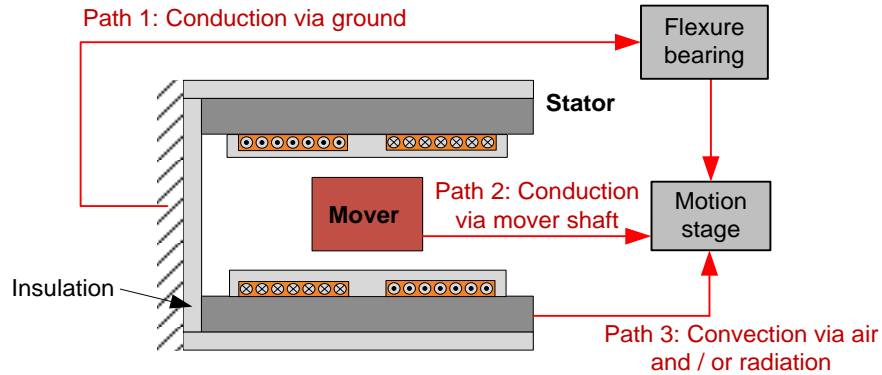


Figure 8.3: Primary heat transport paths between MMA and motion stage

An ideal thermal management system would maximize the thermal resistance of each path, and remove all heat generated at the MMA directly. As discussed in Section 7.1.9, the carbon fiber MMA shaft provides high thermal resistance and therefore acts as an effective heat barrier between the MMA and the motion stage of the flexure bearing (path 2). Additionally, the bearing can be designed for high thermal resistance via insulating materials or truss-like structures to reduce conduction paths (path 1). Insulating materials can also be used between the MMA and bearing (also path 1). In a vacuum environment, the convection path to the motion stage (path 3) is eliminated. This means that all thermal paths to the motion stage and surrounding sensitive areas may have a relatively high thermal resistance. Therefore, if the thermal management system is designed to effectively remove all heat from the coils at the source, good temperature stability of the bearing and motion stage will be maintained. This forms the chosen design strategy of the TMS.

To remove heat directly from the MMA, active and passive thermal management methods are considered. Active thermal management uses external electrical power to enhance heat transfer rates, often from forced convection with a fan or imposed temperature gradients from thermoelectric chips based on the Peltier effect [268]. The

advantage of active thermal management is enhanced and controllable heat transfer rates. However, these methods can introduce disturbances to the motion system from airflow and they add net additional heat to the system. Both degrade motion quality. Peltier effect-based cooling is also ultimately limited by the overall heat dissipation rate of the entire system, and due to their low power efficiencies, they also add significant additional heat. In applications where vacuum is not required, heat can be removed via the room's active temperature control system, however due to the large thermal capacitance the temperature cannot be quickly controlled.

Passive thermal management, on the other hand, does not use additional external power to remove heat. One advantage is that passive thermal management methods do not introduce motion disturbance to the positioning system, as typical passive methods rely on natural convection to surrounding air. The disadvantage is that passive thermal management options generally have lower heat transfer rates than active systems. Also, passive convection does not work in vacuum conditions. An additional passive heat management option uses a pre-cooled thermal mass or absorption of latent heat in a material's phase change to absorb heat from the actuator. While this method is ultimately no different than active refrigeration because the thermal mass must be actively cooled, the cooling of the thermal mass and absorption of heat are decoupled in terms of time. For example, a thermal mass can be actively cooled, and then heat from the actuator is absorbed while the cooling system is turned off. This method has the advantage of potentially large heat transfer rates in a vibration-free manner.

It was determined that latent heat based thermal management systems can remove significantly more heat in the same packaging size than other methods. Given this and the other above-mentioned advantages, the passive TMS based on the latent heat transfer

concept is chosen. In this concept, four main system components and functionalities are required as shown in Figure 8.4. Heat travels from the MMA through a thermally-conducting housing interfacing with the MMA, and then to a latent heat sink through a thermal bridge. As described in the following section, and seen in Figure 8.1, the housing is Aluminum and clamps the MMA. Copper heat pipes form the thermal bridge between the housing and the latent heat sink which comprises sealed ice-packs. The detailed design of the specific components is discussed next.

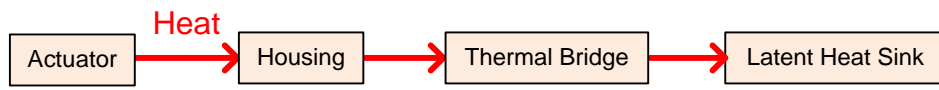


*Figure 8.4: TMS functionality diagram with main system components*

## **8.2 Detailed design**

The heat sink is designed first to absorb the worst-case scenario heat generation over an acceptable time duration of operation. Next, the thermal housing and thermal bridge are designed to interface with the MMA and effectively move heat to the heat sink.

### **8.2.1 Latent heat sink**

The final design of the heat sink is shown in Figure 8.5. The heat sink features ice packs enclosed in an Aluminum rack, into which the heat pipes of the thermal bridge are mounted. The rack distributes heat from the heat pipes to the ice packs. The assembly is enclosed in double-layered insulating wall, which opens at the rear for removal of the ice packs and is secured using toggle clamps.

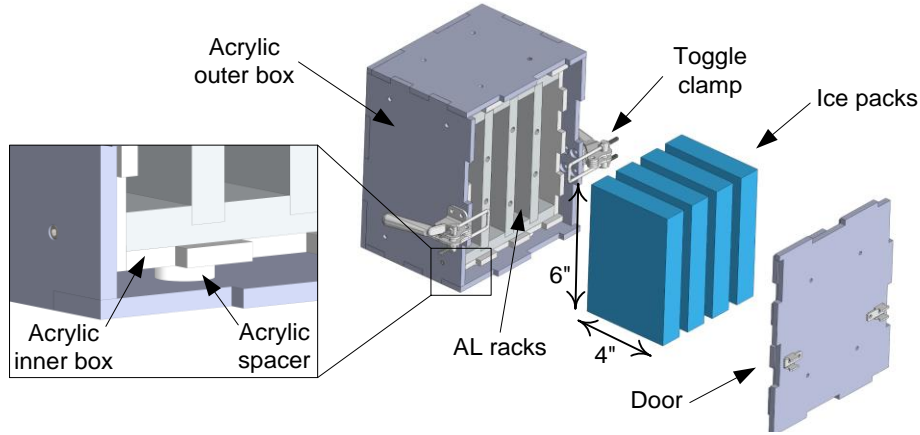


*Figure 8.5: Latent heat sink*

Frozen water is selected as the working fluid due to its high latent heat capacity, its benign properties, and availability. To avoid risk of leakage, sealed individual ice packs are chosen [269]. The mass of water in each pack is  $\sim 0.3\text{kg}$ . Worst-case scenario of 20W continuous power dissipation from the actuator results in roughly 40 minutes usage time per ice pack as shown in Table 8.1. Therefore, a heat sink design using 4 heat packs was selected to give a best-case-scenario 2.5 hour usage time.

*Table 8.1: Working time per ice pack*

Latent heat (kJ/kg)	Mass of water (kg)	Energy for phase change (kJ)	Worst-case input power (W)	Time (min.)
334	0.14	46	20	38

These calculations assume that no heat is transferred from the ice packs to the surrounding air, which would decrease the heat sink effectiveness and capable working time. Therefore, the heat lost to the surroundings should be minimized. The ice packs are enclosed in a double layered insulation box as shown in Figure 8.5. The inner and outer boxes are made of acrylic, separated by acrylic spacers (inset) to give an air buffer zone between the walls. The walls were designed with interlocking teeth to simplify the assembly. They are cut from acrylic sheets using a laser cutter.

Separation between the acrylic wall layers should be selected so that the air layer between the walls forms an effective insulation layer. To check the effectiveness, the walls are assumed to be vertical as shown in Figure 8.6. As detailed in [270], for Rayleigh numbers below  $\sim 1000$  there is no free convection and can be therefore treated as conduction between the acrylic walls. This would represent the best-case insulating scenario. With air as the enclosed fluid, and the acrylic wall exposed to ambient air at  $T_0 = 25^\circ\text{C}$  and the acrylic wall exposed to the ice pack at  $T_{icepack} = 0^\circ\text{C}$ , the distance between the walls,  $L$ , was chosen. With  $L=0.25\text{in.}$ , the Rayleigh number is 890, thus ensuring a well-insulating air layer.

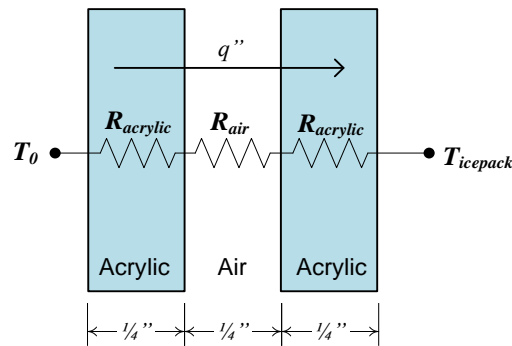


Figure 8.6: Heat sink insulated walls

The thermal resistance per unit area of the wall circuit in Figure 8.6 is given in (8.1).

$$R'' = 2R''_{acrylic} + R''_{air} = \frac{2L}{k_{acrylic}} + \frac{L}{k_{air}} \quad (8.1)$$

where the thermal conductivity of acrylic is  $k_{acrylic} \simeq 0.2\text{Wm}^{-1}\text{K}^{-1}$  and that of air is  $k_{air} = 0.024\text{Wm}^{-1}\text{K}^{-1}$ . This results in a total wall insulation of  $R'' = 0.33\text{Km}^2\text{W}^{-1}$ . Without

the insulating layer, the thermal resistance per unit area between the inner wall and air would be roughly  $R'' = 0.17 \text{Km}^2\text{W}^{-1}$ , calculated for a vertical plate with natural convection empirical relations pg. 571 in [270]. The insulation doubles the thermal resistance and is therefore deemed to be sufficient.

### 8.2.2 Thermal bridge

The heat from the MMA should be transported with minimal losses to the latent heat sink via a thermal bridge. The main requirement is that the thermal bridge has low thermal resistance to maximize heat transfer. The final design is shown in Figure 8.1, comprising six heat pipes. Heat pipes are selected for their very low thermal resistance, high heat load capacity, and passive, vibration-free operation.

Figure 8.7 shows the heat pipe working principle and setup with the TMS. A heat pipe is a hollow closed vessel. Inside of the pipe resides a working fluid in a near-vacuum. The inner walls are lined with a wicking material. Heat applied to one end (the evaporator) vaporizes the fluid, creating a pressure gradient in the pipe. This pressure gradient forces the vapor to flow along the pipe to a cooler section where it condenses giving up its latent heat of vaporization. The working fluid is then returned to the evaporator by the capillary forces developed in the wick structure. This results in high heat transfer rates, often 10-100 times higher than an equivalently sized copper rod.

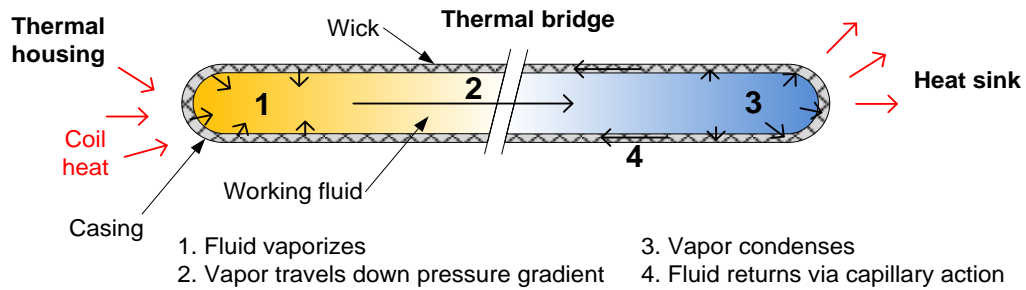


*Figure 8.7: Heat pipe working principle*

In this design, in which the temperature range is most likely between 0 and 125°C, water as a working fluid is recommended [271][272]. A mesh wick type was chosen for its low thermal resistance over a variety of lengths [272]. The chosen heat pipe dimensions are 6mm diameter, 270mm long from [Enertron](#). These are chosen based on availability and low thermal resistance of ~3K/W. For comparison, a solid copper pipe of the same cross section would have a thermal resistance of ~17K/W. Several heat pipes are placed in parallel to further reduce overall thermal resistance of the thermal bridge. The number of heat pipes was selected to be six using an analytical thermal model of the TMS as described in 8.2.4.

### 8.2.3 Thermal housing

The aluminum bobbin of the actuator is designed to effectively transfer the heat radially outwards from the coils (see Section 7.1.7) to the outer faces of the bobbin. From there the heat enters the thermal housing and then the thermal bridge. The thermal housing is made of two symmetrical halves that tightly clamp the MMA as shown in Figure 8.8. This improves the heat transfer between the actuator and the housing. A 1/16” gap between the two halves ensures tight clamping of the actuator. Without the gap, the housing halves may not clamp tightly due to manufacturing tolerances. Heat pipes are

inserted into holes in the thermal housing. A light interference fit ensures good heat transfer. Silicone-free heat sink compound from McMaster was also applied in the holes. The housing assembly is enclosed by acrylic plates to reduce heat transfer to the surroundings. The acrylic plates also fit around the mover shaft. Slots in the rear plates allow easy assembly with the MMA wire leads.

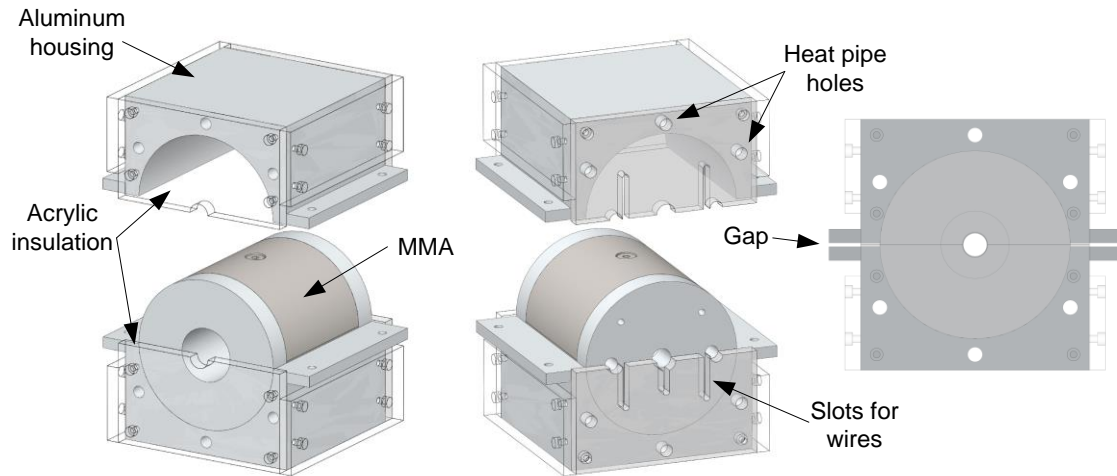


*Figure 8.8: Thermal housing*

#### 8.2.4 TMS thermal model

A lumped parameter thermal network for the MMA and TMS is developed to evaluate the steady-state temperature of the coil and bobbin. The model is also used to select the number of heat pipes,  $n$ , used in the thermal bridge. The model is validated using Solidworks Thermal Simulation Tool. The overall system model is shown in Figure 8.9. The resistance of each component is described below.

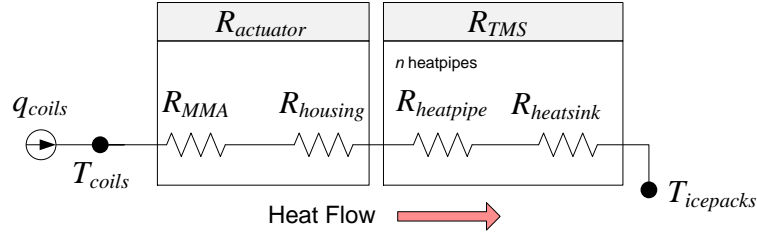


Figure 8.9: System thermal resistance network

Using the above model, the temperature of the coils is given by (8.2)

$$T_{coils} = q_{coils} \sum R + T_{icepacks} = q_{coils} (R_{actuator} + R_{tms}) + T_{icepacks}, \quad (8.2)$$

where  $R_{actuator}$  is given in (8.7) and  $R_{tms} = \frac{R_{heatpipe} + R_{heatsink}}{n}$ .

#### Thermal resistance of the actuator ( $R_{actuator}$ )

The thermal resistance of the MMA and the housing were combined to give the total actuator thermal resistance,  $R_{actuator}$ , as shown in Figure 8.10. The resistance network consists of five parallel heat conduction paths. The heat travels radially outwards from the coil. Two paths are in the axial ends of the bobbin, two are in the yoke, and one in the middle both in the bobbin and yoke. It is assumed that the thermal housing is cylindrical, with a thickness  $t_h = 0.5\text{in}$  (12.7mm). The air gap between the iron and thermal housing is assumed to be  $g = 0.5\text{mm}$ . Several geometric relations are apparent, giving  $t_b = t_c + t_y$ ,  $r_c = r_m + t_c$ ,  $r_y = r_m + t_b$ , and  $r_h = r_m + t_b + t_h$ . The thickness of the air gap between the mover and bobbin, as well as the inner bobbin wall thickness are neglected.

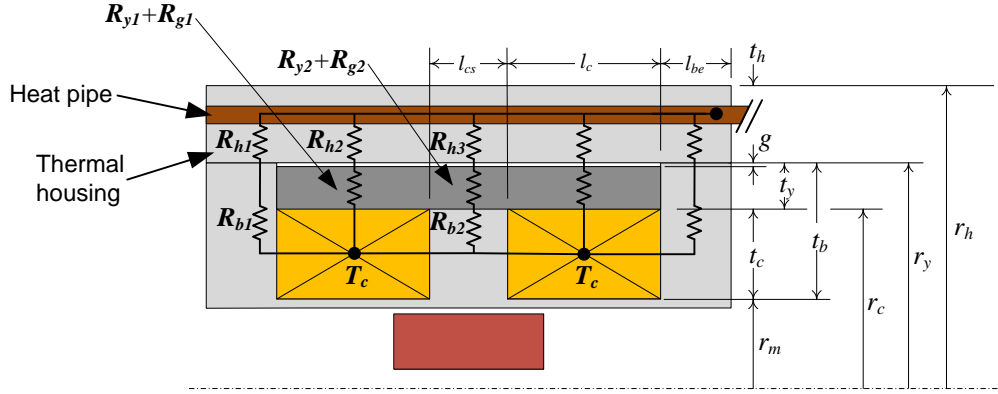


Figure 8.10: Thermal resistance of the MMA and housing

The individual resistances of the heat transfer paths are given below,

$$R_{b1} = \frac{\ln(r_y/r_m)}{2\pi k_{Al} l_{be}}; R_{b2} = \frac{\ln(r_c/r_m)}{2\pi k_{Al} l_{cs}} \quad (8.3)$$

$$R_{y1} = \frac{\ln(r_y/r_c)}{2\pi k_s l_c}; R_{y2} = \frac{\ln(r_y/r_c)}{2\pi k_s l_{cs}} \quad (8.4)$$

$$R_{g1} = \frac{\ln(r_y/(r_y - g))}{2\pi k_a l_c}; R_{g2} = \frac{\ln(r_y/(r_y - g))}{2\pi k_a l_{cs}} \quad (8.5)$$

$$R_{h1} = \frac{\ln(r_h/r_y)}{2\pi k_{Al} l_{be}}; R_{h2} = \frac{\ln(r_h/r_y)}{2\pi k_{Al} l_c}; R_{h3} = \frac{\ln(r_h/r_y)}{2\pi k_{Al} l_{cs}} \quad (8.6)$$

where the dimensions are listed in Table 7.2, and the thermal conductivities of 1020C steel, air, and 6061 Aluminum in units of W/m/K are  $k_s = 51$ ,  $k_a = 0.024$  and  $k_{Al} = 170$ , respectively. The total thermal resistance of the MMA and housing is given by (8.7).

$$R_{actuator} = \frac{1}{\frac{2}{R_{b1} + R_{h1}} + \frac{2}{R_{y1} + R_{g1} + R_{h2}} + \frac{1}{R_{b2} + R_{y2} + R_{g2} + R_{h3}}} \quad (8.7)$$

### Thermal resistance of the thermal management system ( $R_{TMS}$ )

The thermal resistance of the thermal management system,  $R_{TMS}$ , depends on the thermal resistance of the heat pipes, heat sink, and on the number of heat pipes. The effective thermal conductivity of the heat pipes,  $k_{hp}$ , is 3200W/m/K, and the length ( $l_{hp}$ ) and radius ( $r_{hp}$ ) of the heat pipe are 270mm and 3mm, respectively. The thermal resistance of an individual heat pipe,  $R_{heatpipe}$  can be expressed as

$$R_{heatpipe} = \frac{l_{hp}}{k_{hp} \pi r_{hp}^2} \quad (8.8)$$

Each heat pipe interfaces with the ice packs in the heat sink as shown in Figure 8.1 and Figure 8.5. A lumped parameter thermal model of the heat transfer between each heat pipe and the ice pack is shown in Figure 8.11. Heat from the heat pipe conducts through the Aluminum structure and through the 1/8" ice pack plastic wall. As the ice begins to melt, a thin water layer develops between the plastic and ice. This will further increase the thermal resistance, assuming the layer is too thin for significant natural convection to occur. This was modeled as a 0.25" layer of water through which the heat conducts to the ice.

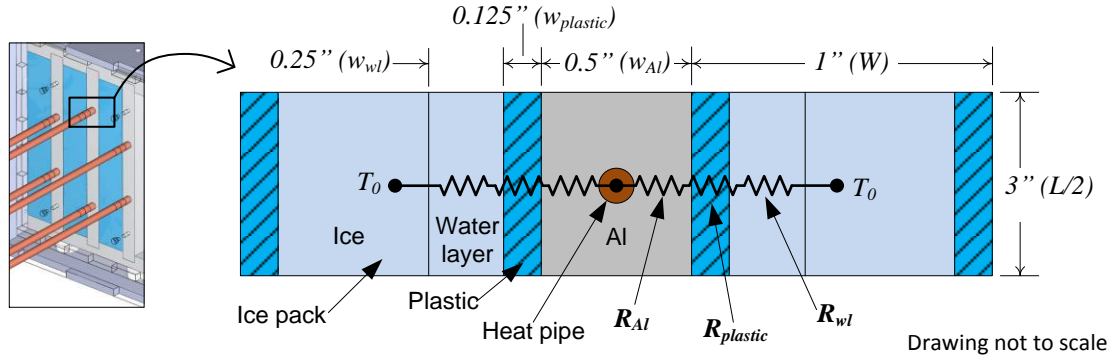


Figure 8.11: Thermal model of the heat sink

Based on the above model, the individual thermal resistances are

$$R_{Al} = \frac{\frac{w_{Al}}{2}}{k_{Al} H \frac{L}{2}}; R_{plastic} = \frac{w_{plastic}}{k_{plastic} H \frac{L}{2}}; R_{wl} = \frac{w_{wl}}{k_{water} H \frac{L}{2}} \quad (8.9)$$

where the length ( $L$ ), width ( $W$ ) and height ( $H$ ) of the ice packs (see Figure 8.5) are 6, 1 and 4 inches, respectively. The thermal conductivity of the plastic ( $k_{plastic}$ ) is assumed to be 0.147 W/m/K and that of water ( $k_{water}$ ) 0.569 W/m/K.

The total thermal resistance of the heat sink, which occurs between the heat pipe and ice pack, is therefore

$$R_{heatsink} = \frac{R_{Al} + R_{plastic} + R_{wl}}{2} \quad (8.10)$$

### Number of heat pipes ( $n$ )

Inserting relations (8.7), (8.8) and (8.10) into the thermal model of the thermal management system, relation (8.2), gives the predicted coil temperature depending on the number of heat pipes in the thermal bridge. The results are shown in Figure 8.12. Six heat

pipes are selected to maintain the coil temperature at a predicted 18°C. This is below room temperature and is chosen because factors such as thermal contact resistance and heating from the ambient air were not accounted for. An even number of heat pipes also enabled symmetry of heat pipes in the heat sink. The MATLAB code implementing this model can be found in APPENDIX B: Analytical thermal model for selection of heat pipes.

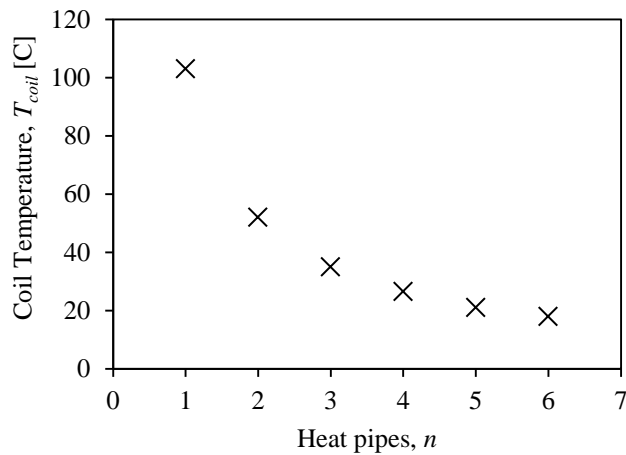


*Figure 8.12: Predicted coil temperature versus number of heat pipes*

### **8.3 Fabrication**

The TMS is fabricated in-house by the author and others acknowledged at the beginning of this chapter. General machining guidelines are followed. The thermal housing is machined from a single block of 6061 Aluminum. The large hole was bored using a lathe and the halves were separated using a cutting blade on a mill. All acrylic components were cut using a laser cutter. Figure 8.13 shows pictures of the TMS during the fabrication process.

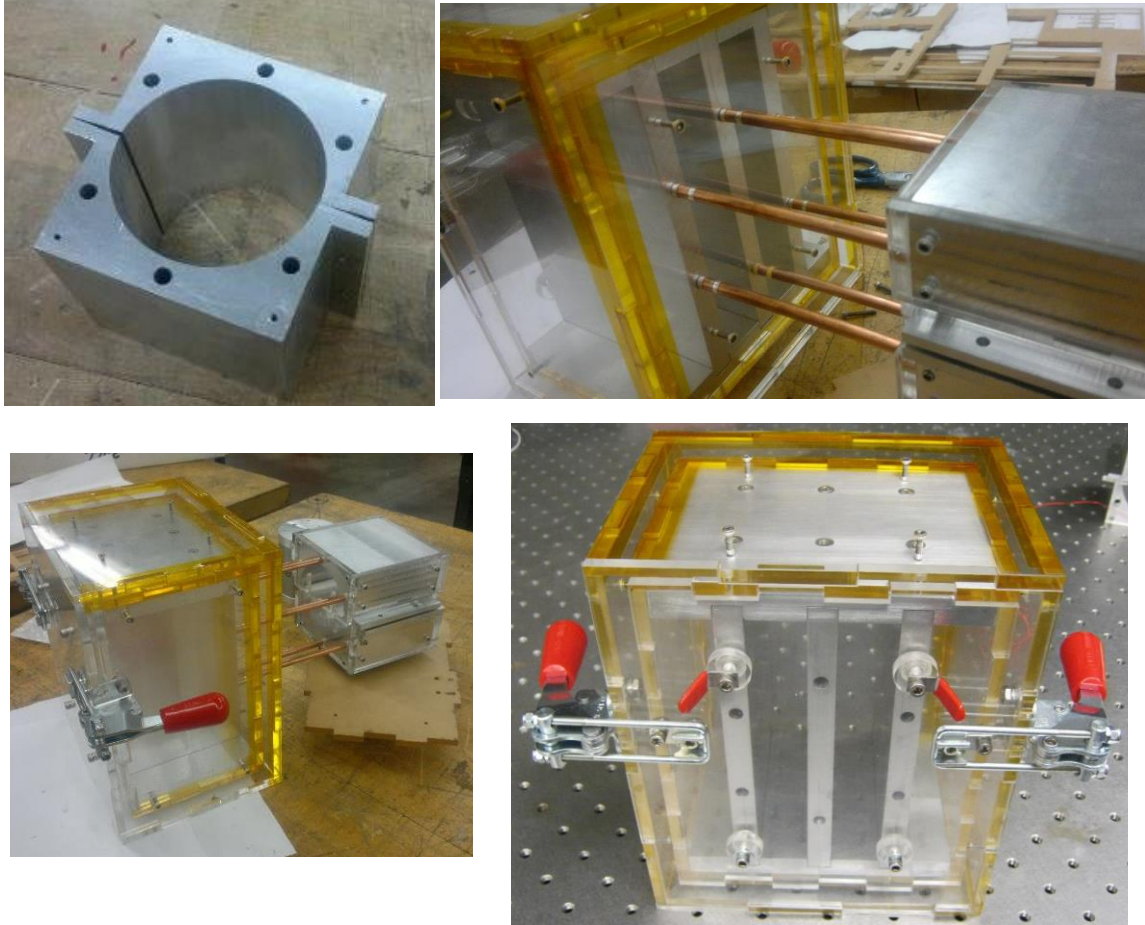


*Figure 8.13: Fabricated thermal management system (ice packs not shown)*

## CHAPTER 9: Double-parallelogram flexure bearing

A single-axis symmetric double-parallelogram (DP) flexure bearing is designed to provide frictionless and backlash-free motion guidance over the entire range of motion of the MMA. This flexure design provides uniform motion direction stiffness over a relatively large stroke and high bearing stiffness in all other translation and rotation directions [254][274][275]. In this chapter, first the detailed design is discussed, followed by practical design considerations and fabrication. The bearing assembly in CAD interfacing with the MMA and thermal management system (TMS) is shown in Figure 9.1. The fabricated bearing is shown in Figure 9.2 and the dimensions are given in Table 9.1.

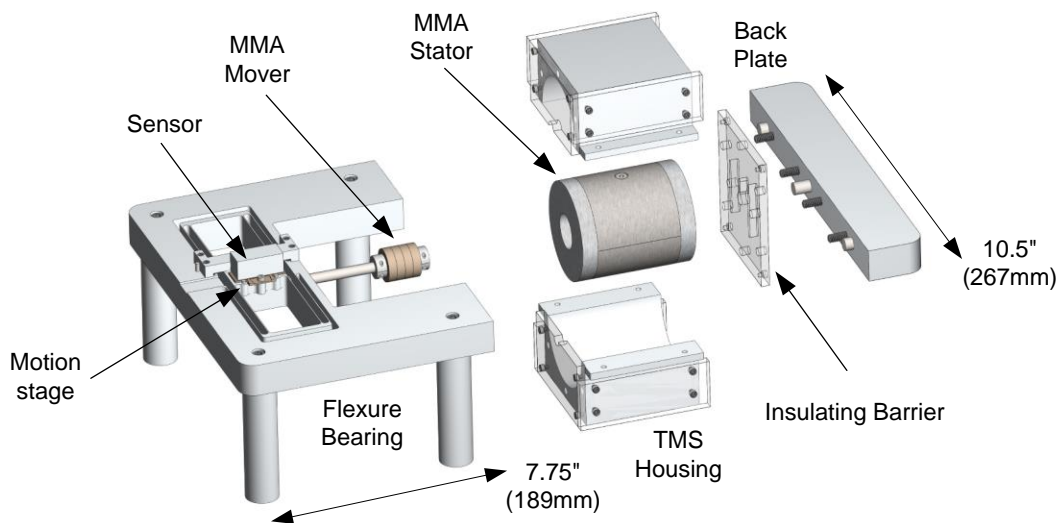
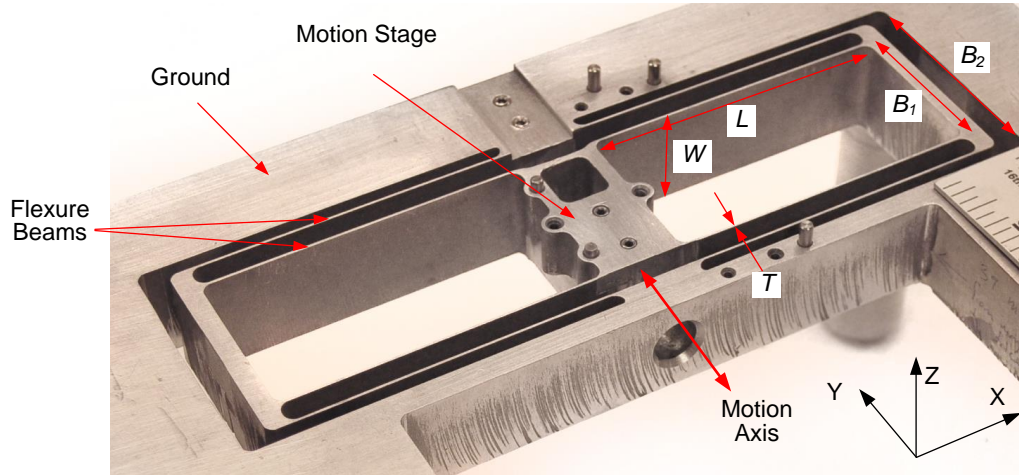
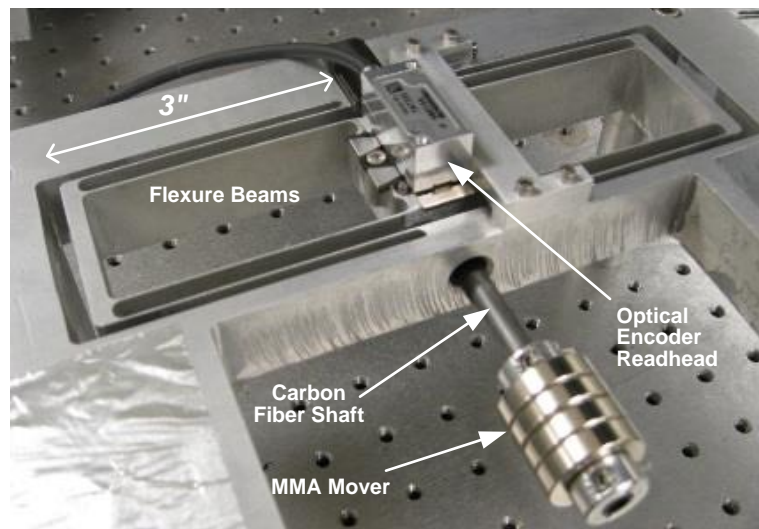


Figure 9.1: Flexure bearing and MMA assembly in CAD



*Figure 9.2: Fabricated flexure bearing*



*Figure 9.3: Flexure bearing with MMA mover and encoder assembly*

## 9.1 Detailed design

This section describes the design of the flexure bearing. Bearing design and analysis is based on prior closed-form results [254].

### 9.1.1 Material selection

Material choice affects most aspects of flexure bearing performance. Aluminum 6061 (grade T-651) is selected given its overall good flexure characteristics, including high yield strength to modulus ratio, strength-to-modulus ratio, lack of cold-working stresses, long term phase stability, low cost, availability, and machinability [254]. The temper designation indicates heat treatment to relieve internal stresses so that the flexure elements do not deform after machining.

### 9.1.2 Motion stage design

The motion stage interfaces with the shaft of the actuator mover and holds the optical encoder scale for feedback control. As discussed in Section 1.3.3 and Section 5.2, for a given actuator moving mass it is beneficial to minimize the mass of the motion stage. Therefore special care is taken to minimize the mass. A CAD model shows the motion stage cross section in Figure 9.4a and the fabricated result in Figure 9.4b. The mover shaft is constrained axially and radially via a sleeve bushing clamped using set screws in threaded holes (A). Another good solution is a keyless bushing (for example, from Fenner Drives), however is not chosen due to space constraints (the outer diameter is significantly larger than the mover shaft—almost as large as the plate thickness—and keyless bushings require a wrench for tightening which imposes additional space constraints). The mover shaft passes through a clearance hole (H) in the ground portion of the bearing. The optical encoder scale is aligned via dowel pins in holes (B) and secured via mounting clips bolted into threaded holes (C). To minimize mass, the mounting locations for the holes extrude from the motion stage only where required (D). The optical encoder read-head mounting block (see Figure 10.1 for system assembly) is aligned via dowel pins in holes (E) on ground and constrained via bolts in threaded holes

(F). A pocket (G) in the motion stage further reduces mass. The resulting mass of the motion stage is  $m = 42\text{g}$ . With the mass of the motion stage, optical encoder scale, sleeve bushing, mover shaft, and MMA, the total moving mass is 148g.

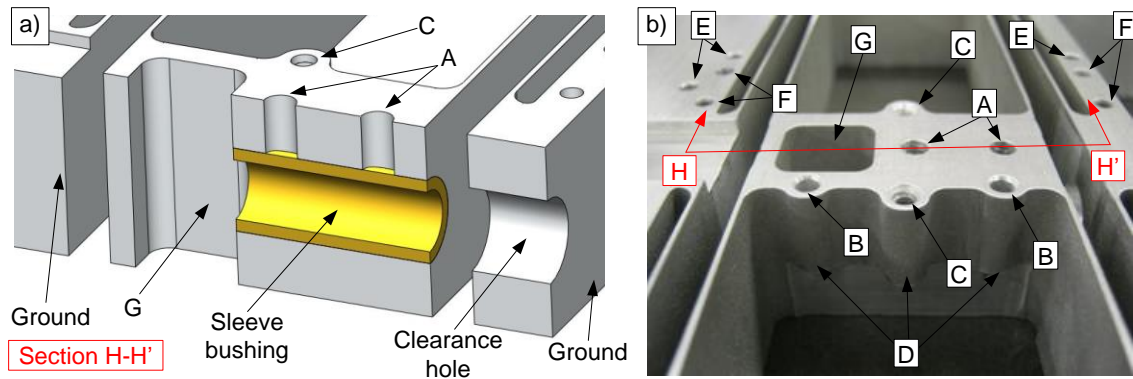


Figure 9.4: a) CAD cross section and b) fabricated motion stage

### 9.1.3 Beam dimensions

With the overall moving mass ( $m + m_a$ ), dynamic actuator constant ( $\beta$ ), power consumption limit ( $P$ ), and desired stroke ( $\Delta_o$ ) and scanning speed ( $\omega$ ) all known, (5.19) predicts that the maximum achievable natural frequency ( $\omega_n$ ) is 27Hz. This implies a maximum flexure stiffness of  $\sim 4\text{N/mm}$  which the flexure should be designed for. The beam dimensions are selected as described below to achieve this motion direction stiffness while maintaining high stiffness in the non-motion directions. The bearing topology is shown in Figure 9.5 and the corresponding selected dimensions are shown in Table 9.1.

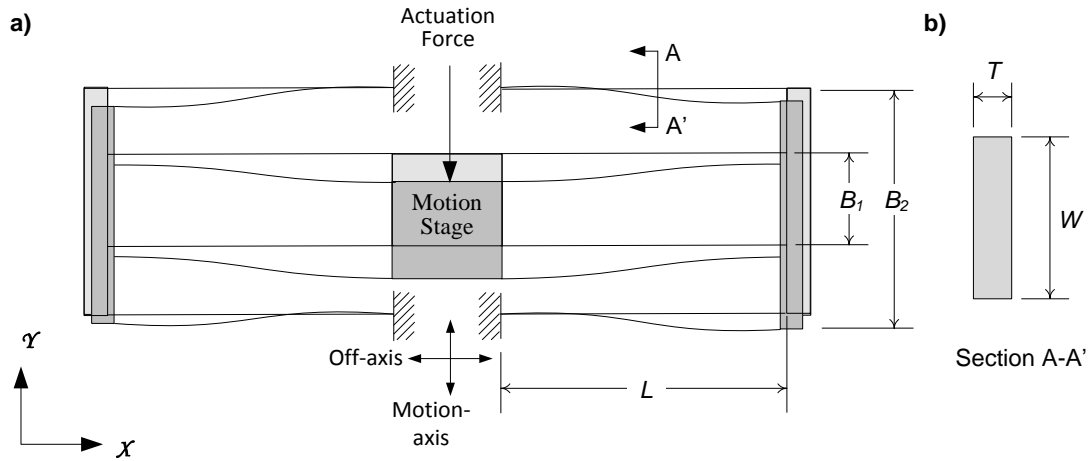


Figure 9.5: Double parallelogram flexure bearing topology and dimensions

Table 9.1: Bearing specifications

Parameter	Symbol	Value	Units
Stroke	$\Delta_0$	$\pm 5$	mm
Motion direction 1 <sup>st</sup> resonant mode	$\omega_0$	25	Hz
Motion stage mass	$m$	42	g
Beam width	$W$	25.4	mm
Beam thickness	$T$	0.75	mm
Beam length	$L$	80	mm
Inner beam separation	$B_1$	39	mm
Outer beam separation	$B_2$	52.5	mm
Motion direction stiffness	$K_y$	3.43	N/mm
Vertical off-axis stiffness (at $\Delta = 5\text{mm}$ )	$K_x$	149.6	N/mm
Horizontal off-axis stiffness (at $\Delta = 5\text{mm}$ )	$K_z$	70.6	N/mm

The linear stiffness values of the DP flexure bearing in the motion direction ( $K_y$ ), in-plane off-axis direction ( $K_x$ ), and out-of-plane direction ( $K_z$ ) depend upon the beam dimensions as

$$K_y \approx \frac{WT^3E}{L^3} \quad (9.1)$$

$$K_x \approx \frac{WTE}{L} \quad (9.2)$$

$$K_z \approx \frac{W^3TE}{L^3} \quad (9.3)$$

where  $E$  is the Young's modulus of the material, and  $W$ ,  $T$  and  $L$  are the width, thickness and length of the beam, respectively. The stiffness relations shown above are not independent. Therefore, to maximize the stiffness in the bearing directions, the beams dimensions are chosen to minimize the following stiffness ratios

$$\frac{K_y}{K_x} \approx \frac{T^2}{L^2} \quad (9.4)$$

$$\frac{K_y}{K_z} \approx \frac{T^2}{W^2} \quad (9.5)$$

Clearly, it is beneficial to minimize the beam thickness ( $T$ ) and maximize the beam width ( $W$ ) and beam length ( $L$ ). The prior two are limited by the capability of the water-jet machining process and set to be 0.75mm and 25.4mm respectively. Using wire EDM, smaller values of  $T$  could be achieved, however water-jet is selected due to its in-house availability and lower cost. Finally, the beam length ( $L$ ) is selected to be 80mm to provide  $\pm 5$ mm motion range with the motion direction stiffness of 3.43N/mm. An additional  $\pm 1$ mm range of travel is added to ensure the full desired range without contact.

The separation between the inner and outer beams ( $B_1$  and  $B_2$ ) influence the mass of the motion stage, however reducing them significantly compromises the yaw motion stiffness (in rotation about  $z$ ) of the stage. This stiffness is approximated as

$$yaw \approx T^2 \left( \frac{1}{B_1^2} + \frac{1}{B_2^2} \right) \frac{\Delta_0}{L} \quad (9.6)$$

Small iterations of the motion stage design were made to ensure that  $B_1$  and  $B_2$  were selected to be small as possible without significantly compromising the increased yaw. Pitch (rotation about  $x$ ) stiffness and roll (rotation about  $y$ ) stiffness are assumed to depend largely on beam width ( $W$ ), which is maximized as discussed above.

The maximum allowable tip displacement for an S-shape beam deformation can be derived from the maximum yield criteria as [276]

$$\Delta_0 \leq \frac{1}{3\eta} \frac{S_y}{E} \frac{L^2}{T} \quad (9.7)$$

where  $\eta$  is the factor of safety,  $S_y$  is the material yield strength and  $\Delta_0$  is the maximum allowable tip displacement. With the above dimensions and stroke, and Aluminum 6061 as the bearing material, the factor of safety against yield is 4.

#### 9.1.4 Off-axis stability

FEA is used to validate the motion direction stiffness ( $K_y$ ) and yield strength calculation, and check that the bearing can constrain potential off-axis forces from the mover. An appropriate mesh (4mm size tetra elements, with minimum element size of 0.5mm) is created in Hypermesh software and Abaqus solves the loading conditions with non-linear, large displacement analysis conditions. The mesh is shown in Figure 9.6a. A 3 7/16" mover shaft imbedded 0.5" into the motion stage was included in the model with

material property of ceramic (230GPa, 0.25 Poisson's ratio). The bearing material properties were set to 68GPa and 0.3 Poisson's ratio.

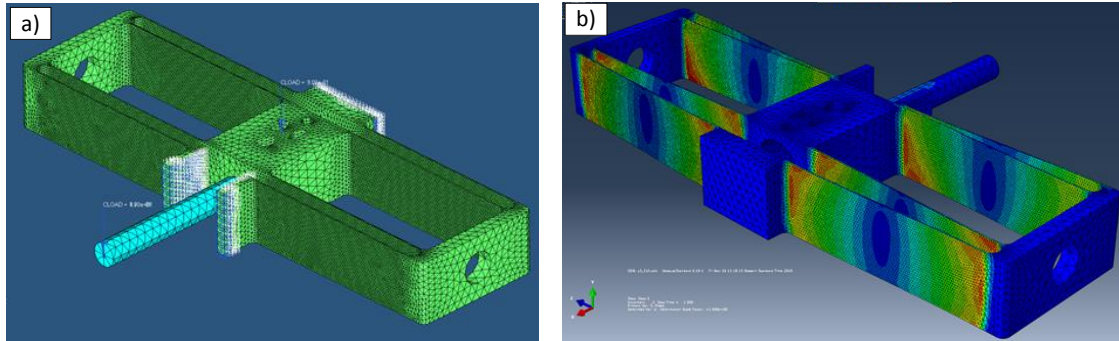


*Figure 9.6: Bearing mesh and loading conditions for FEA a) and stress analysis b)*

The FEA results in  $K_y$  of 3.4N/mm, matching the analytical results. Yielding condition is also satisfied. As shown in Figure 9.6b, the maximum von Mises stress is 74MPa which is sufficiently below the yield strength Aluminum (~240MPa).

The potential off-axis attraction forces from the MMA must be mitigated by a higher positive off-axis stiffness of the flexure bearing compared to the negative off-axis stiffness associated with the actuator (see Section 4.1.7). The stiffness of the bearing in the X and Z directions is determined via FEA to compare with the MMA's negative stiffness of 1.3N/mm described in Section 7.1.8. It should be noted that because the MMA applies a moment on the motion stage, the X direction stiffness is perhaps better described by  $K_{\theta Z}$  and the Z direction by  $K_{\theta X}$ . Stiffness of the bearing in the X and Z directions are the smallest at the maximum motion stage displacement. Therefore the first load step displaces the bearing to a 5mm displacement. The second load step applies point loads at the end of the shaft in the X and Z directions (see Figure 9.6a). The Z direction load case additionally accounts for the magnet mass. The measured

displacements of the end of the shaft resulted in linear stiffness values of 149.6N/mm in the X direction ( $K_{\theta Z}$ ) and 70.6N/mm in the Z direction ( $K_{\theta X}$ ). The stiffness of the bearing and actuator are compared in Figure 9.7, confirming stability of the magnet-back iron assembly. The quadratic off-axis actuator attraction force is significantly lower than the bearing constraint force, especially within the physical air gap space. Larger displacements would regardless not be physically possible due to the mover hitting the wall.

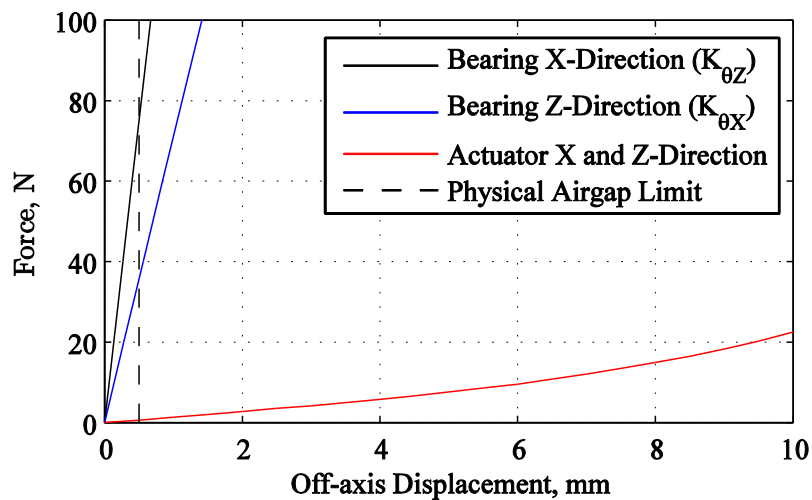


Figure 9.7: Stiffness comparison of actuator and bearing showing off-axis stability

#### 9.1.5 Bearing dynamics

With these dimensions the bearing is predicted to have a first natural frequency of 25Hz. Primary stiffness of the flexure bearing (3.43N/mm) combined with the magnetic stiffness of the magnet / back-iron assembly (0.16N/mm) gives a total motion direction stiffness of 3.59N/mm. With a total moving mass of 148g, this gives  $\omega_n \approx \sqrt{3590/0.148}/2\pi = 24.8$  Hz.

A finite element modal analysis in ANSYS is performed to predict subsequent natural frequencies and associated mode shapes of the overall mechanical structure of the flexure bearing, mover shaft and mover. The first four modes shapes are shown in Figure 9.8. These modes correspond to experimental results in 10.4. Figure 9.8a shows the first mode at 22.4Hz. It is an in-plane in-phase motion of the motion stage and secondary stages. This corresponds to the first pole at 25Hz in the experimental results. Figure 9.8b shows the second mode at 82.0Hz. The motion stage is stationary while the secondary stages resonate. This corresponds to the first two zeros at 89Hz and 93Hz in experimental results. Figure 9.8c shows the third mode which occurs at 86.3Hz. It is an in-plane out-of-phase motion of the motion stage and secondary stages and corresponds to the two second poles at 91Hz and 98Hz in the experimental results. Figure 9.8d shows the fourth mode at 152.8Hz. It is an out of plane rocking mode due to twisting of beams. This corresponds to the third pole at 118Hz of the experimental results. The discrepancy is most likely because the finite joint stiffness values between motion stage and shaft and between shaft and magnets are assumed infinite in FEA.

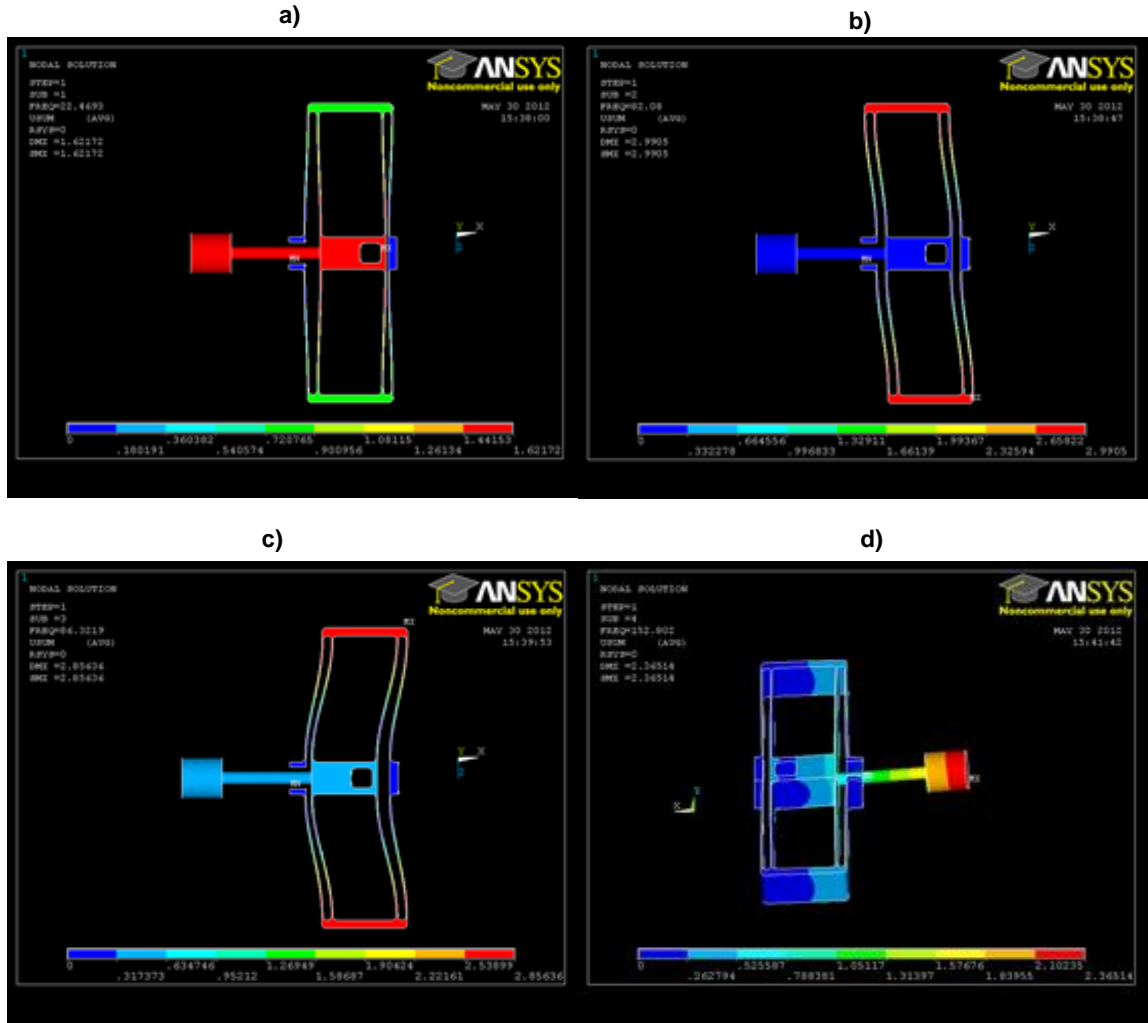
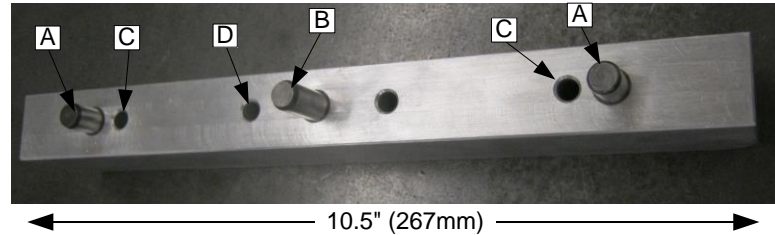


Figure 9.8: First four natural frequency modes of mover integrated with flexure bearing at a) 22.4Hz b), 82Hz c), 86.3Hz, and d) 152.8Hz

## 9.2 Practical design considerations

The bearing is designed with a removable back plate so that the MMA can be easily assembled with the bearing (see Figure 9.9). The fabricated back plate is shown in Figure 9.9. Dowel pins enable alignment between the back plate and bearing (A) and

between the MMA and back plate (B). Clearance holes for bolts provide constraint between back plate and bearing (C) and between the back plate and the MMA (D).



*Figure 9.9: Removable flexure bearing back plate*

### **9.3 Fabrication**

As with the MMA and TMS, the flexure bearing is fabricated in-house by the author and general machining guidelines were followed. Various comments on the fabrication process are listed here. Again, some are obvious to any skilled machinist, others may be more subtle and particular to this design.

- The bearing pattern is cut from the Aluminum plate using an OMAX water-jet machine and finishing operations on standard milling machine.
- The flexure pattern was cut out over an inch away from the edges of the Aluminum stock to ensure that the beams were away from potential residual stresses from cutting down stock to size.
- The water-jet tool-path was manually configured to ensure that the motion stage and pockets are cut before the beams are cut to maintain rigidity.

- The tool-path is designed to eliminate any excess material remaining attached to the beams as they are cut out. The tool-path begins on the inside of the beams then works outwards until the double parallelogram flexure units are all cut out.
- Cutting time with the water jet machine was over an hour for this pattern.
- Two perpendicular edges of the bearing perimeter were cut using the highest cut quality (i.e. slowest cutting speed). These edges were used as datum planes for milling operations. All other holes and edges use lower cut quality to shorten cut time except along the beams, where a high quality was used.
- Small bridges of material were left not cut out between the motion stage and ground so that the motion stage would be rigidly constrained while machining. The bridges were removed by hand using a small hack saw after all machining was complete to enable the motion stage to freely move.
- The parallel edges of the inner walls of the bearing ground where the MMA resides are used to set a datum plane along the centerline of the bearing for all alignment dowel holes. This maintained symmetry about the motion axis and proper alignment of the MMA to the motion stage.

Pictures of the completed flexure bearing are shown in Figure 9.10 below. A steel mover shaft and shaft collars are shown, without the magnets.

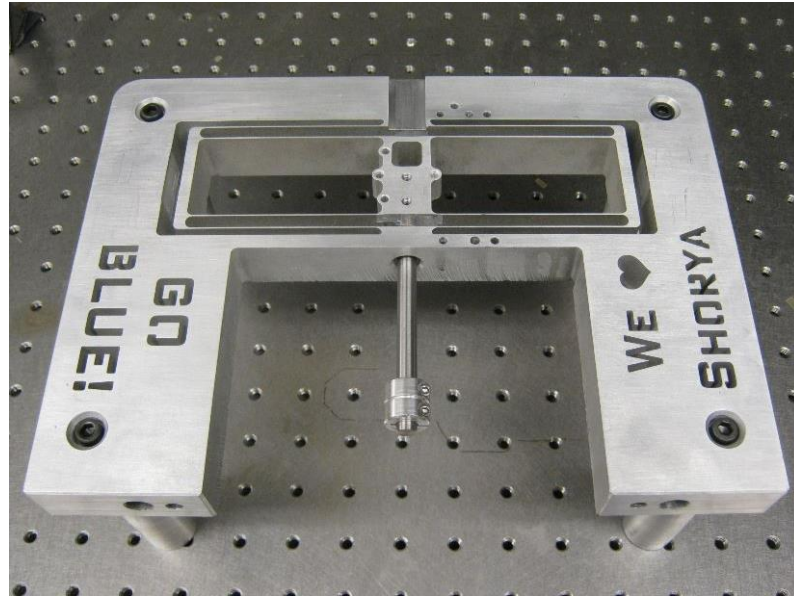


*Figure 9.10: Bearing and mover assembly (top) and removable MMA attachment plate (bottom)*

## CHAPTER 10: Experimental Results

An experimental setup comprising the moving magnet actuator (MMA), flexure bearing, thermal management system (TMS), and position sensor, driver, and control system is assembled for testing. First, the characteristics and performance of the MMA and TMS are measured and validated. This includes measurement of the actuator force output, motion range, and temperature rise of the motion stage during operation with and without the thermal management system. Next, the system's nanopositioning capability is tested. This requires the characterization of the overall motion system, controller design, and then measurement of the motion system positioning resolution and dynamic response. With preliminary controller design the potential of MMAs in large range, high speed nanopositioning is confirmed. Further details are described in [239].

Special thanks to Gaurav Parmar for his contributions of the open-loop system characterization, controller design, and closed-loop performance measurements. Special thanks to Yi Chen for his significant contributions to the experimental testing of the thermal management system.

The key experimental performance results of the single-axis nanopositioning system are summarized in Table 10.1.

*Table 10.1: Motion system experimental results*

<b>Specification</b>	<b>Value</b>	<b>Units</b>
Motion range	10	mm
Open-loop natural frequency	25	Hz
Max. continuous power	20	W
Temperature stability	0.5	°C
Closed-loop resolution	20/4	nm(pp)/nm(RMS)

### **10.1 Experimental setup**

The nanopositioning system experimental setup, comprising the MMA, TMS, flexure bearing, and position sensor, is shown in Figure 10.1. An off-the-shelf 5nm resolution linear optical encoder from Renishaw is selected for position measurement of the motion stage (RELM scale, Si-HN-4000 Read-head, and SIGNUM Interface). As shown in Figure 10.1 (inset), the motion stage holds the MMA mover shaft and optical encoder scale (A). Dowel pins (B) provide alignment of the encoder scale with respect to the motion stage. The optical encoder readhead (C) is mounted and aligned using three ground-mounted dowel pins (D). As described in 7.1.9, the mover shaft is aligned and secured to the motion stage via a sleeve collar (E).

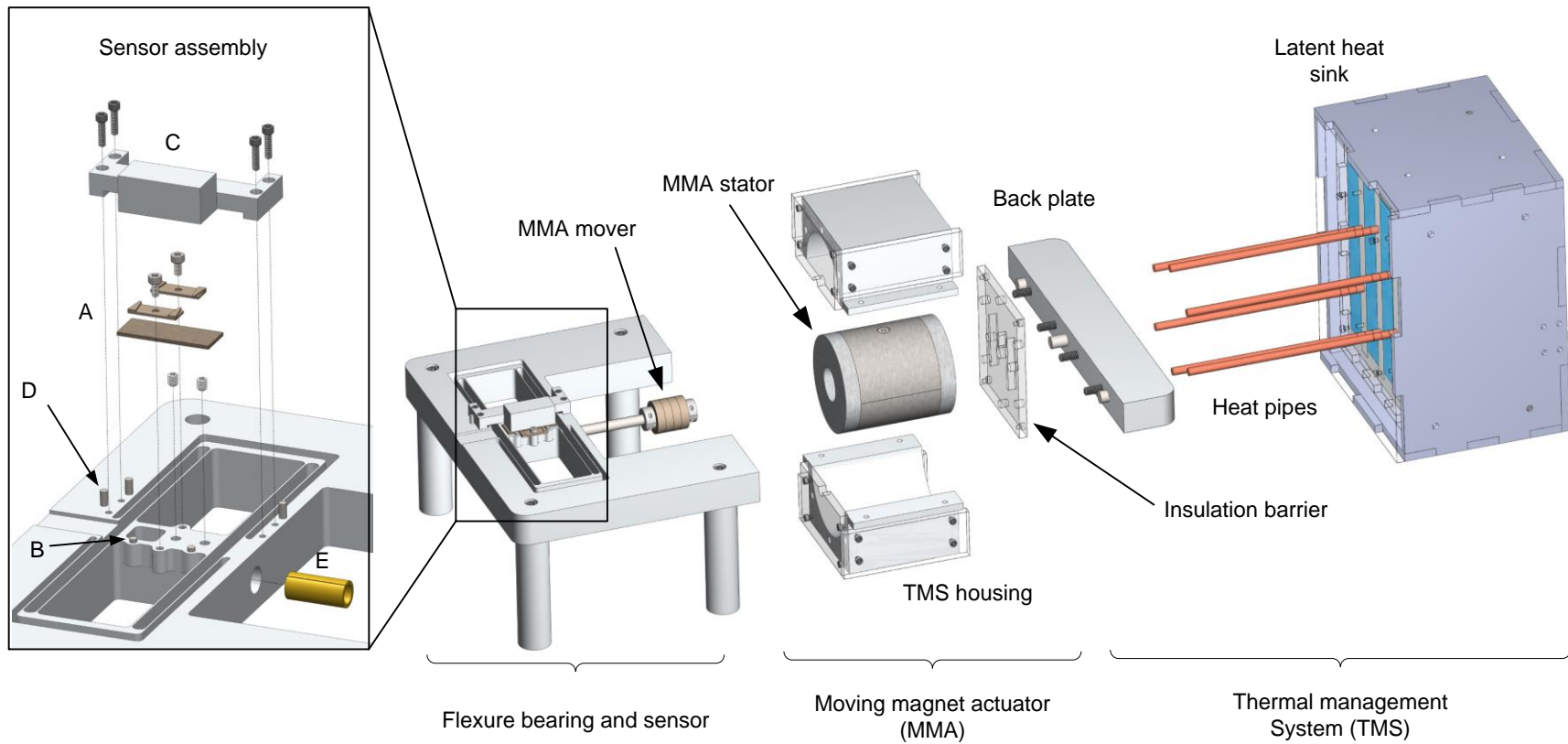


*Figure 10.1: Detailed CAD of motion system assembly*

The final, fabricated single-axis nanopositioning system assembly is shown in Figure 10.2. The full experimental setup including the motion system, current driver and feedback control hardware is schematically shown in [239]

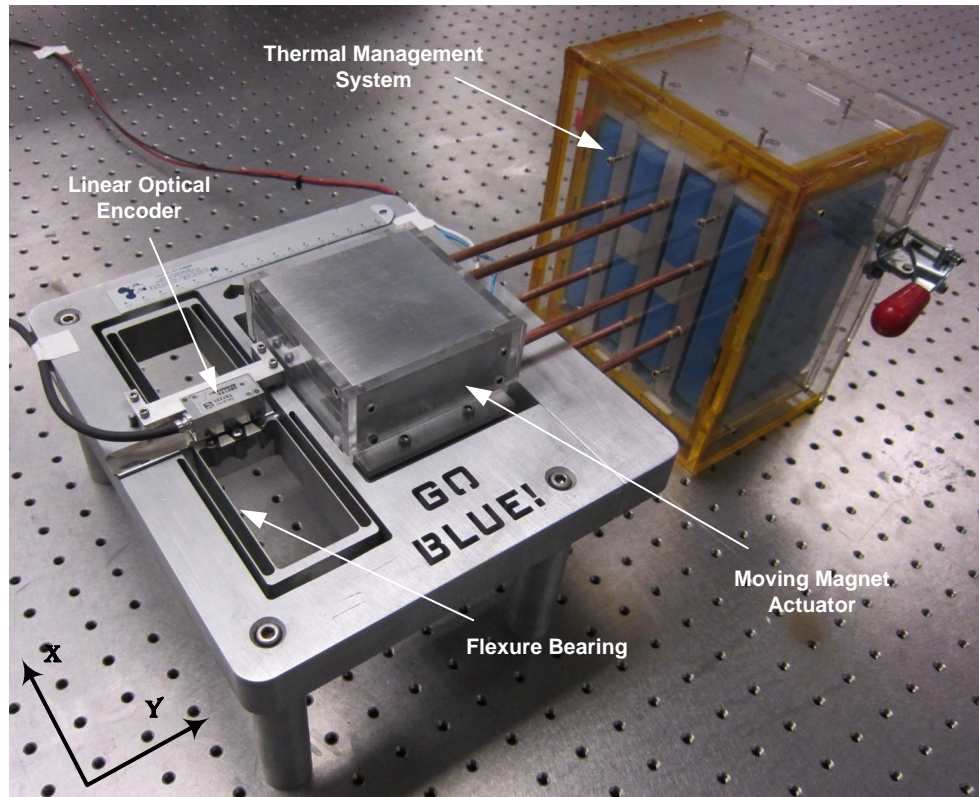


*Figure 10.2: Single-axis nanopositioning system prototype*

A custom-made driver, based on the MP111 power-OpAmp from Cirrus Logic, designed and tested by Gaurav Parmar in [239] signed to achieve high signal-to-noise-ratio (110dB) and low total harmonic distortion ( $-90\text{dB}$ ). This driver was operated in the current mode with a gain of  $1\text{A/V}$  to provide direct control of the actuation force over a 1KHz bandwidth. This driver is rated for 20W power; higher power tends to further deteriorate the noise and harmonic distortion. The feedback controller was implemented

on real-time hardware from National Instruments (PXI-8106, PXI-6289) at a loop-rate of 5KHz.

## 10.2 Moving magnet actuator

The MMA stroke and force characteristics are validated. Next, the effect on dynamic performance of the choice of bobbin material is measured. These tests and results are described in this section.

### 10.2.1 MMA static force characteristics

The MMA force is measured using a load-cell (Model # ELFF-T4E-20L from Measurement Specialties) in a temporary setup (Figure 10.3). The load-cell is threaded into a split Aluminum shaft to measure forces transmitted along the shaft.

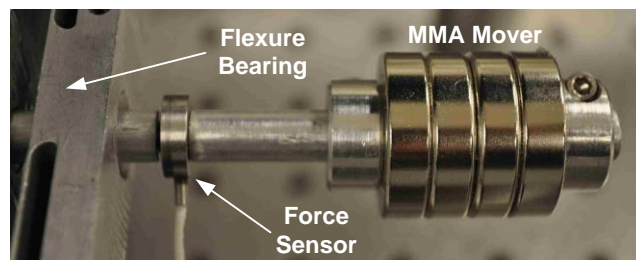


*Figure 10.3: Setup for MMA force measurement*

With the mover constrained via clamps at the nominal position ( $\Delta = 0\text{mm}$ ), the MMA force is plotted with respect to the coil current in Figure 10.4a. The slope of this line provides the measured force constant  $K_b$ , of 32.5N/A. This is within 3.5% of the value (31.5N/A) predicted by FEA. This difference is most likely due to a discrepancy between number of winding turns employed in the prototype coils and the FEA model. The measured Lorentz force-stroke non-uniformity, plotted in Figure 10.4b, is within

10% over the entire  $\pm 5\text{mm}$  stroke. The constant force offset in this plot is due to the above-mentioned discrepancy in the force constant.

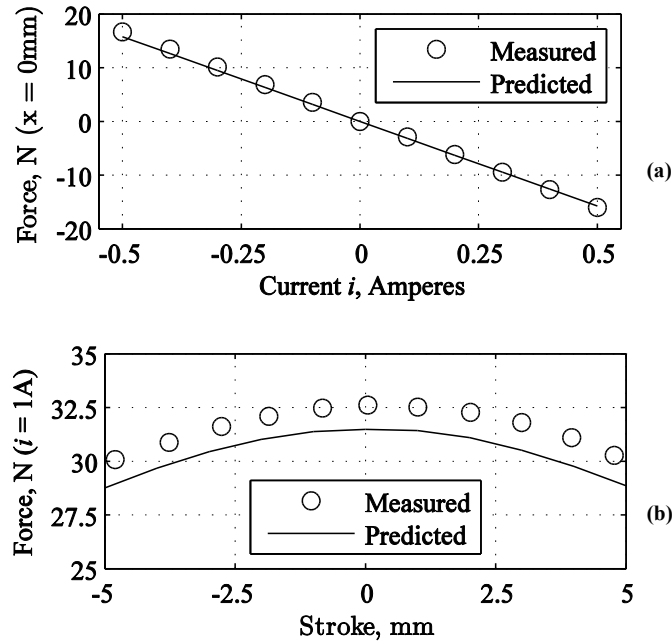


Figure 10.4: (a) Measured force constant (b) Measured force-stroke non-uniformity

### 10.2.2 Effect of bobbin material on dynamic response

The MMA bobbin material was chosen as Aluminum (see Section 7.1.7). To experimentally study the possible effects on the dynamic performance due to eddy currents in the bobbin, a plastic bobbin was manufactured and the open-loop frequency response from the driver command to the measured position was compared in [239]. Eddy currents in the Aluminum bobbin lead to additional damping in the first resonance mode of the system as well as higher phase lag at higher frequencies. The higher frequency phase lag near crossover frequency degrades the dynamic performance in terms of achievable phase margin and disturbance rejection in the closed-loop operation.

### 10.3 Thermal management system

As discussed in Section 1.3.4 and Chapter 8, temperature stability in the nanopositioning system during operation is critical. The temperature of the optical encoder scale, the motion stage, and the MMA bobbin are measured using thermocouples from Extech. A step current command to the actuator is applied and the temperature rise over time is recorded. Due to the change of the resistivity, the input power under of the actuator under constant current varied up to 20%. Thus the heat generation rate is between 20W to 24W. Figure 10.5 shows the measured coil bobbin and motion stage temperatures for an MMA power input of 20W, with and without the TMS. The motion stage, which is the most sensitive location in the motion system, remains within 0.5°C of room temperature over the entire testing period, once steady-state is reached. This demonstrates the effectiveness of the proposed TMS in maintaining temperature stability.

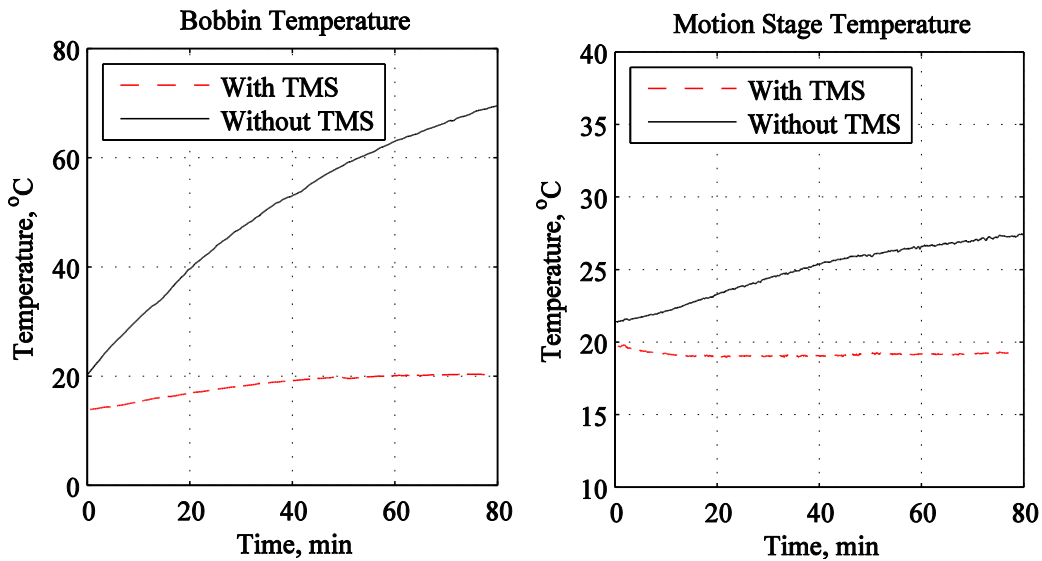


Figure 10.5: Temperature rise of the coil bobbin and the motion stage with ( - - ) and without ( — ) the thermal management system

The temperature of the encoder scale, which is mounted to the motion stage, is also measured. This is important because a finite temperature rise of the motion stage

does not guarantee a significant temperature rise and resulting expansion of the encoder scale itself. Figure 10.6 shows the temperature rise of the scale, with and without the TMS. The discrepancy in initial temperatures is due to a change in ambient temperature. With the TMS, the temperature fluctuates within  $0.5^{\circ}\text{C}$  as expected. Without the TMS the temperature rises  $3^{\circ}\text{C}$  and continues. A  $3^{\circ}\text{C}$  temperature rise causes the 10 mm long Invar encoder scale (thermal expansion coefficient of  $0.6\ \mu\text{m}/\text{m}/^{\circ}\text{C}$ ) to expand by 18 nm. This again highlights the effectiveness of the TMS in eliminating thermal errors.

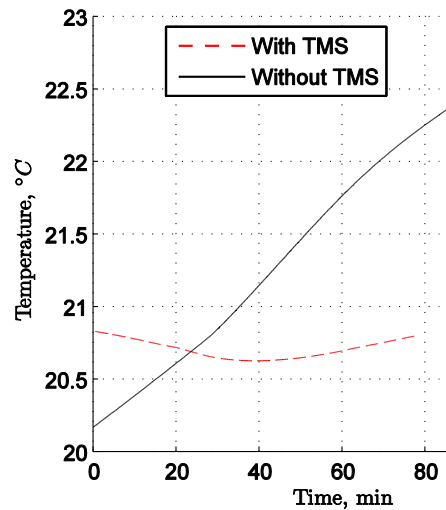


Figure 10.6: Effect of TMS on optical encoder scale temperature

## 10.4 Nanopositioning

Following experimental validation of the individual components, the capabilities of the nanopositioning system are tested here. First, the open-loop frequency response of the system is measured, followed by controller design and implementation. Both point-to-point and scanning type motion profiles are tested for nanopositioning performance capability.

### 10.4.1 System characterization

The open-loop frequency response of the nanopositioning system is measured using a dynamic signal analyzer (Model 20-22A from SigLab). Figure 10.7 shows the resulting transfer function between the command to the current driver and the motion stage displacement. As expected, the first natural frequency of the system is found to be 25Hz. Damping at this resonance peak primarily comes from eddy currents in the Aluminum bobbin, as described above. The resonant peaks at higher frequencies are discussed in 9.1.5.

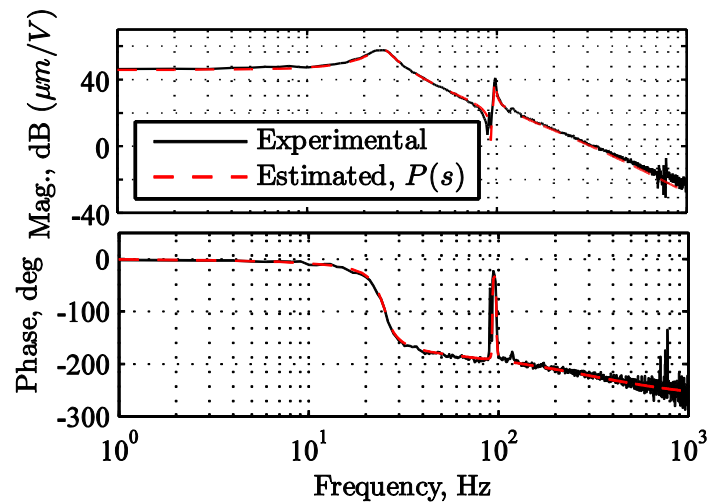


*Figure 10.7: Open-loop frequency response*

### 10.4.2 Nanopositioning performance

To achieve high speed and high motion quality, the nanopositioning system is operated in closed-loop control. This attenuates noise and disturbance from the actuator driver, position sensor, data-acquisition hardware, and ground vibrations, all of which limit the achievable motion quality. Additionally, closed-loop operation enables command tracking over a desired frequency range, by mitigating the effects of harmonic

distortion in the current driver and the force-stroke non-uniformity of the MMA. Such command tracking over large motion range is possible as long as the driver and power supply are not saturated. The closed loop architecture is shown in Figure 10.8.

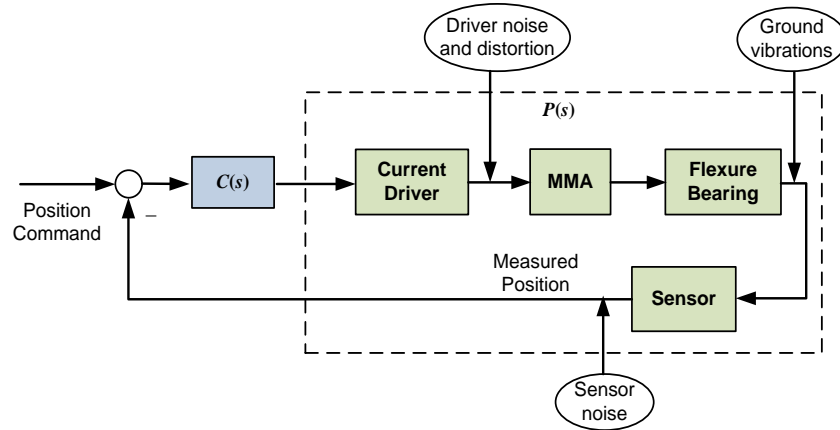


Figure 10.8: Feedback architecture

To design a linear feedback controller, a fifth-order transfer function,  $P(s)$ , is fit to the open-loop frequency response (see Figure 10.7).  $P(s)$  is given by

$$P(s) = \frac{1.06 \times 10^{10}}{(s + 2000)(s^2 + 36.94s + 2.46 \times 10^4)} \times \frac{(s^2 + 4.54s + 3.40 \times 10^5)}{(s^2 + 6.38s + 3.76 \times 10^5)} \quad (10.1)$$

This open-loop transfer function is used design a lag-lead controller,  $C(s)$ , to achieve acceptable closed-loop stability and performance. The lag part includes an integrator and a higher frequency zero to achieve zero steady state error and the lead part increases the phase near gain crossover frequency. The final controller transfer function is shown below.

$$C(s) = \frac{0.92(s^2 + 37s + 2.46 \times 10^4)}{s(s + 1 \times 10^4)} \quad (10.2)$$

The frequency response of the resulting closed-loop transfer function is given by

$$T(s) = \frac{P(s)C(s)}{1 + P(s)C(s)} \quad (10.3)$$

and the experimentally obtained closed-loop frequency response is shown in Figure 10.9. The phase margin and gain margin for the loop transfer function are  $59^\circ$  and 21dB, respectively. The small signal closed-loop bandwidth (-3dB) of the system is approximately 150Hz.

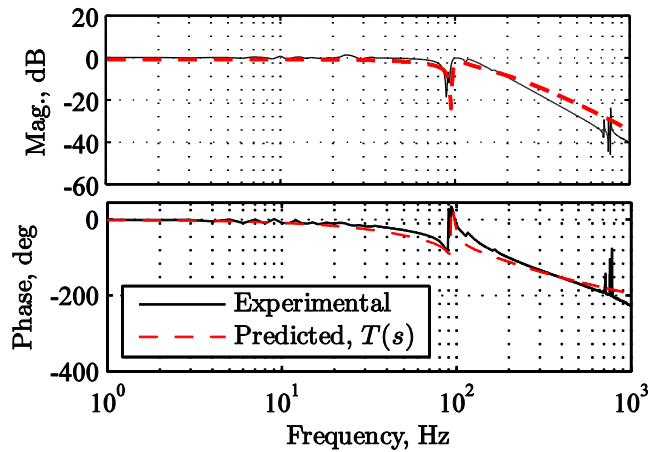
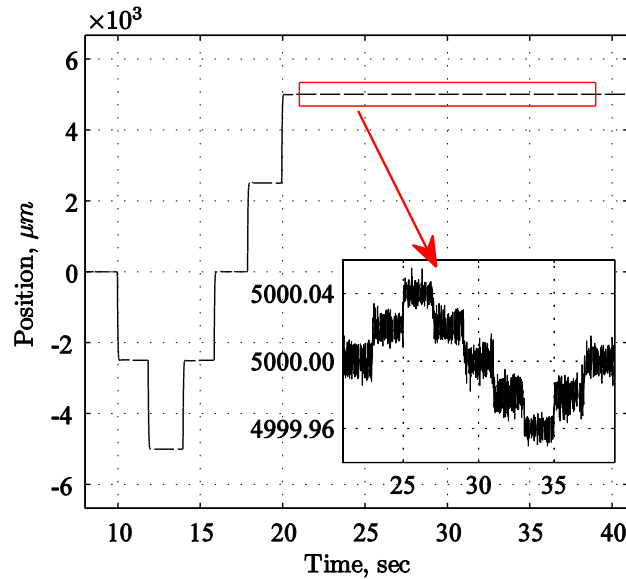


Figure 10.9: Closed-loop frequency response

The nanopositioning system is tested for point-to-point positioning performance with steps commands of 2.5mm and 20nm. The measured position response is shown in Figure 10.10. In this test, a steady-state positioning error of 20nm (peak-to-peak) or 4nm (RMS) is achieved over the entire 10mm motion range. This confirms the desired nanometric motion quality and large motion range.



*Figure 10.10: Motion stage response to 2.5mm and 20nm step commands*

In addition to point-to-point positioning, nanopositioning systems are also employed in scanning type applications where the motion profile is dynamic in nature, as discussed in Section 1.3. To evaluate the dynamic tracking performance, a 3mm and 2Hz sinusoidal signal is applied as the command. The resulting tracking error is observed to be as high as  $\pm 60\mu m$ , which is clearly inadequate in terms of targeted motion quality. Tracking error further worsens as the command frequency is increased. This large tracking error is due to the strong higher-order harmonics arising from the driver and the actuator non-linearities [91]. The 25Hz open-loop bandwidth of the present system proves to be inadequate in suppressing these effects in the closed-loop operation. This problem is further investigated in [91] and [239]. Significant improvement in performance is achieved using iterative learning control methods.

## CHAPTER 11: Innovations in Actuator Design

As described in Section 5.2, and based on the nanopositioning performance described in Section 10.4, this work motivates the design of MMAs that offer greater values of the dynamic actuator constant ( $\beta$ ) while maintaining high force uniformity over its stroke. One way to achieve this is through conception and optimization of new MMA architectures. In this chapter, several concepts are presented in the domains of MMA architecture and coil design which hold promise for larger  $\beta$  values. Additionally, concepts for improved VCA and coil designs are presented. These concepts are described in pending patent [277].

### 11.1 Concentric coil ring magnet (CCRM) moving magnet actuator

In this section, the basic concept and promising embodiments of a novel MMA is introduced to meet the objective of maximizing the dynamic actuator constant. To maximize the dynamic actuator constant, the MMA design must maximize force output, minimize power consumption, and minimize moving mass. Force output corresponds to reducing magnetic flux fringing, maintaining good perpendicularity of flux to coil windings (maximizing Lorentz force cross product), and minimizing magnetic air gaps and other circuit reluctances. Power corresponds to ensuring that all coil windings are used for force generation (maximizing power efficiency), and designing for optimal magnetic circuit efficiency. Furthermore, minimizing moving mass corresponds to using high remanence magnets, eliminating pole pieces, and using lightweight material for structural elements. In addition to having a large value of the dynamic actuator constant,

the MMA must also feature good force uniformity over the stroke, have low off-axis attractive forces, and allow adequate mechanical integration with the mover.

### 11.1.1 Optimal MMA topology

With these requirements in mind, an MMA topology shown in Figure 11.1 is proposed to best achieve these goals, albeit first in an idealized manner, not taking certain practical design considerations into account. The topology features a rectangular magnet and coil separated by an air gap of negligible size. The magnet of depth  $w$  and mass density  $\rho$  is oriented perpendicular to the coil windings. It is assumed that there is no flux fringing. The coil is fixed and the magnet moves in the direction shown. The only moving entity is the magnet which minimizes moving mass. The magnetic flux lines leave the north face of the magnet, pass through the coil, and return to the south end of the magnet. The reluctance of the flux return path is assumed to be zero, with no fringing. The coil is a single strand conductor (i.e. packing factor of unity) with wire length  $w$ , current density  $J$ , and electrical resistivity  $\chi$ .

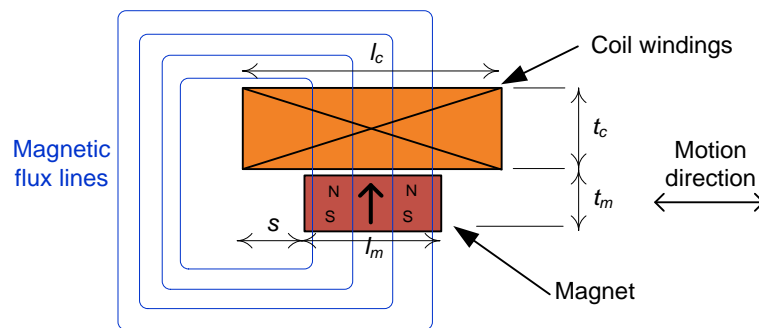


*Figure 11.1: Optimal MMA magnetic circuit arrangement with ideal assumptions*

The magnet is of length  $l_m$  and moves over a stroke of length  $s$ . The ideal length of the coil,  $l_c$ , is therefore given as

$$l_c = l_m + 2s \quad (11.1)$$

The magnetomotive force,  $F_m$ , magnet reluctance  $R_m$ , and air gap (i.e. coil cavity) reluctance  $R_g$  are given by

$$F_m = \frac{B_r t_m}{\mu_m} \quad (11.2)$$

$$R_m = \frac{t_m}{\mu_m l_m w} \quad (11.3)$$

$$R_g = \frac{t_c}{\mu_0 l_m w} \quad (11.4)$$

where  $B_r$  is remanence of the magnet,  $\mu_m$  is the permeance of the magnet, and  $\mu_0$  is the permeance of the air. The resultant circuit magnetic flux,  $\phi$ , and average magnetic flux density in the air gap,  $B_g$ , are given by

$$\phi = \frac{F_m}{R_m + R_g} = \frac{B_r t_m l_m w}{\frac{\mu_0}{\mu_m} t_c + t_m} = \frac{B_r l_m w}{1 + \frac{\mu_0}{\mu_m} \frac{t_c}{t_m}} \quad (11.5)$$

$$B_g = \frac{\phi}{l_m w} = \frac{B_r}{1 + \frac{\mu_0}{\mu_m} \frac{t_c}{t_m}} \quad (11.6)$$

The air gap magnetic flux density depends on the magnet remanence, the ratio between magnet and vacuum permeability, and the ratio between coil and magnet thickness. For small air gap compared to magnet thickness, the air gap flux density approaches that of the magnet.

The force output ( $F$ ), power consumed i.e. dissipated as heat ( $P$ ), and the actuator moving mass ( $m_a$ ) are given by

$$F = B_g i w = B_g (J t_c l_m) w = \frac{B_r J t_c l_m w}{1 + \frac{\mu_0 t_c}{\mu_m t_m}} \quad (11.7)$$

$$P = i^2 R = (J t_c l_c)^2 \frac{\chi w}{t_c l_c} = J^2 \chi t_c l_c w \quad (11.8)$$

$$m_a = \rho l_m t_m w \quad (11.9)$$

The dynamic actuator constant  $\beta$  is therefore

$$\beta = \frac{F}{\sqrt{P} \sqrt{m_a}} = \frac{\frac{B_r J t_c l_m w}{1 + \frac{\mu_0 t_c}{\mu_m t_m}}}{\sqrt{J^2 \chi t_c l_c w} \sqrt{\rho l_m t_m w}} = \frac{B_r}{\sqrt{\chi \rho}} \frac{\sqrt{t_c t_m}}{t_m + \frac{\mu_0}{\mu_m} t_c} \frac{1}{\sqrt{1 + 2 \frac{s}{l_m}}} \quad (11.10)$$

According to (11.10),  $\beta$  is governed by the magnet remanent flux density, magnet mass density, and wire resistivity, the ratio of magnet and coil thicknesses, and the ratio of stroke to magnet length.

When the stroke  $s$  is small compared to the magnet length  $l_m$ , and assuming  $\mu_m = \mu_0$ , the optimal magnet and coil dimensions are  $t_m = t_c$ . This gives the optimal MMA  $\beta$  value described by (11.11).

$$\beta = \frac{B_r}{2\sqrt{\chi \rho}} \quad (11.11)$$

### 11.1.2 Concentric coil radial magnet (CCRM) module

Starting with the optimal theoretical arrangement in Figure 11.1, several modifications are made to reach a basic MMA topology which accounts for practical design considerations and holds promise to achieve higher values of the dynamic actuator constant. Unlike an idealized planer conductor in Figure 11.1, in practical designs the coil should be a cylindrical shape to avoid unused portions of the coil. This would otherwise decrease power efficiency and lower the dynamic actuator constant. Furthermore, the magnet should be cylindrical (i.e. ring shaped) to reduce fringing. This is because only the two axial faces of a ring magnet have fringing compared to all four sides of a bar magnet. Decreased fringing increases the force output for a given magnet (i.e. moving) mass, thereby increasing the dynamic actuator constant. Taking these considerations into account, we arrive at a cylindrical version of the optimal magnetic circuit in Figure 11.2, featuring a radially-magnetized ring magnet located concentrically inside of a cylindrical coil winding.

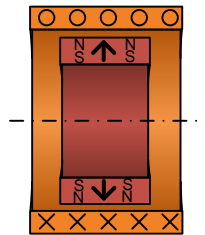


*Figure 11.2: Cylindrical version of optimal circuit arrangement*

Next, we realize that in practical designs there will be magnetic flux entering the interior (south) face of the ring magnet which should either have a minimal reluctance path or be utilized for force generation. As a method to reduce the flux path reluctance, a magnetically permeable back iron can be placed concentrically inside the magnet ring. However, this implies an adequate air gap between the inner back iron and the magnet to

enable the magnet to move freely along the motion axis. This air gap should be small to minimize the air gap reluctance, however this increases undesirable off axis forces between the ring magnet and back iron. These forces for a small (e.g. 20 thousands) air gap can be prohibitively large. Therefore, instead, this the air gap is made larger, and a second coil winding in the air gap is added. This reduces the off axis attractive forces while also producing a useful Lorentz force. In fact, due to smaller off axis attractive forces, the air gap can be made smaller than otherwise would be necessary, giving a net benefit in terms of magnetic circuit efficiency. This thought process results in the arrangement of Figure 11.3a, consisting of a cylindrical, radially magnetized magnet sandwiched between a set of concentric coil windings. The inner back iron is removed and not featured in this arrangement.

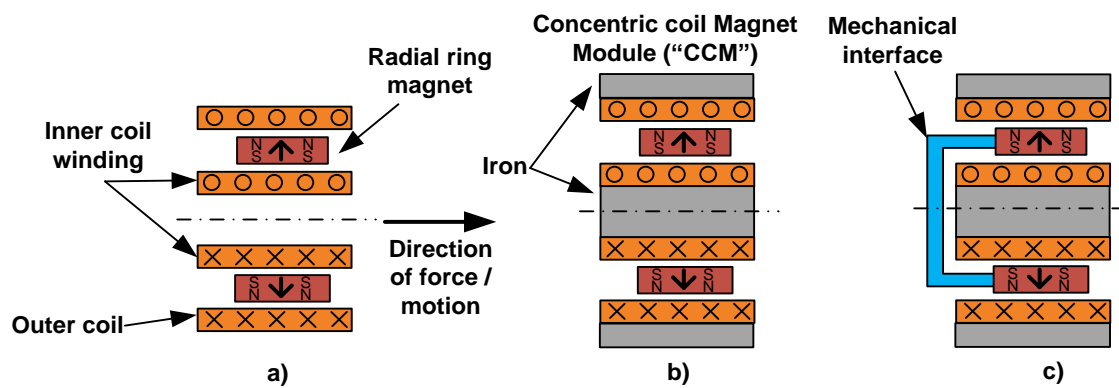


Figure 11.3: Radial magnet concentric coil MMA building block

The final ideal assumption of the theoretical model which must be addressed in practical designs is the magnetic flux path between the coils after leaving the magnet. The reluctance of this flux path must be reduced to maximize the force output and dynamic actuator constant. Therefore a ferromagnetic back iron is added to the magnetic circuit, featuring a rod inserted in the inner coil and a tube over the outer coil. This results

in the basic optimal MMA topology shown in Figure 11.3b. This is termed a concentric coil magnet module, or CCRM. This module best approximates an ideal circuit arrangement while accounting for practical design requirements. The inner and outer back iron components can be joined via various permutations of the CCRM which are described in the next sections. The CCRM modules can be arranged in parallel, in series, or in combinations thereof. The preferred embodiment consists of one CCRM module with an open face back iron design. It is important to note that a back iron can be omitted at the expense of output force (i.e. dynamic actuator constant) if cogging should be eliminated, as discussed in 3.1.1. In all designs, a mechanical interface on the magnet is added such as in Figure 11.3c. Such a connector is required to interface the magnets with the payload.

#### 11.1.3 Single CCRM open face MMA (preferred embodiment)

This section presents various permutations of the optimal concentric coil (CCRM) MMA topology. The preferred embodiment is shown first in this section. All presented MMA configurations also maintain the benefits of conventional MMAs discussed in 2.6.2, such as good heat dissipation, compact size, no moving wire leads, and good mechanical interface. These concepts hold promise to achieve significantly higher values of the dynamic actuator constant and dynamic performance compared to the examined off-the-shelf MMAs.

In this embodiment, the inner and outer back iron of the concentric coil module (CCRM) are joined via a ferromagnetic back plate, effectively closing one end of the MMA (Figure 11.4). This MMA features a radially-oriented ring magnet (A), concentric

coil windings (B), center pole piece (C) and back-iron with a closed end (D). The magnetic flux travels primarily through the closed face and back wall.

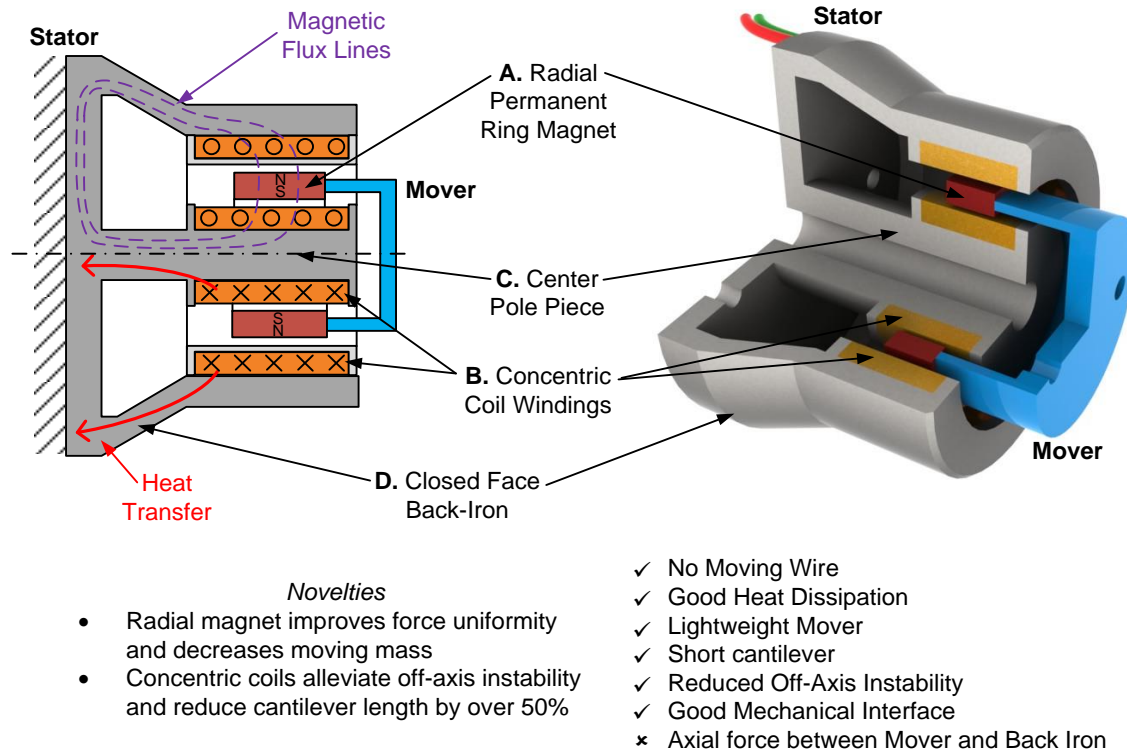


Figure 11.4: MMA featuring radial magnet and concentric coil windings cross-section (left) and CAD rendition (right)

Based on the CCRM optimal magnet configuration, this MMA has many potential advantages over other conventional MMA topologies. The radially-oriented magnet is advantageous as compared to axially-oriented magnets in the conventional MMAs in that the magnetic flux naturally travels radially through the coils, alleviating the need for pole pieces on the mover. This reduces the reluctance path of the magnetic circuit, as well as the actuator's moving mass, thereby improving the dynamic actuator constant and dynamic performance. This magnet orientation decreases fringing of the magnetic flux in

the air gap which increases force-stroke uniformity. Outer diameter is swept to make reluctance force symmetric.

The concentric coil windings are advantageous as they allow a flux path that reduces the overall length of the actuator. Furthermore, they function to maintain significant distance between the magnet and center pole piece as well as the magnet and back iron to decrease attractive forces between them. This results in low off axis attraction forces. Both of these features reduce mechanical loading on the bearing.

One drawback of this configuration is that the closed back iron, which allows a low reluctance flux path, also introduces an axial force (i.e. cogging force) between the mover and back iron even in the absence of current in the coil. This in turn affects the force uniformity over the actuator stroke. However, this effect can be mitigated or reduced by proper design of the back iron. The back iron diameter is swept to make reluctance force symmetric.

This design may have significant armature reaction and coil inductance as the coil flux path has fairly low reluctance. However, the one open face breaks the coil reluctance path and therefore is not a primary concern, especially compared to other designs presented below with both ends closed.

The center core is potentially at risk of saturation because all flux from the magnet passes through one inner iron cross section.

This design provides easy mechanical access to the mover. Figure 11.5 shows the MMA with an envisioned mover made of non-magnetically permeable and electrically non-conductive plastic to eliminate reduction of magnetic field and eddy current damping.

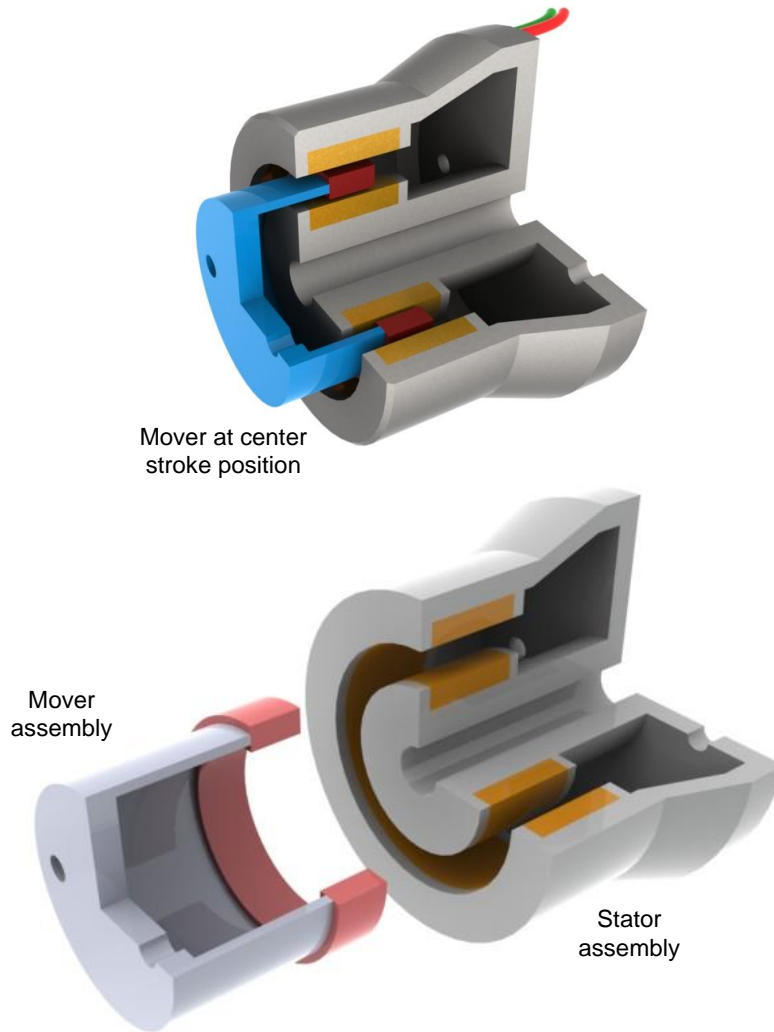


*Figure 11.5: CAD model of envisioned MMA*

The configuration in Figure 11.6 is similar to that of Figure 11.4 however the mover features two concentric ring magnets instead of one and the stator features three concentric coil windings instead of two. This is essentially two CCRM's spaced radially, sharing a common coil. The main benefit of this embodiment is the highly uniform radial magnetic flux passing between the two ring magnets. This highly uniform field both increases the overall output force as well as improves force uniformity over the actuator's

stroke compared to a single CCRM. Potential drawbacks include higher armature reaction and more complex bobbin and mover mechanical design.

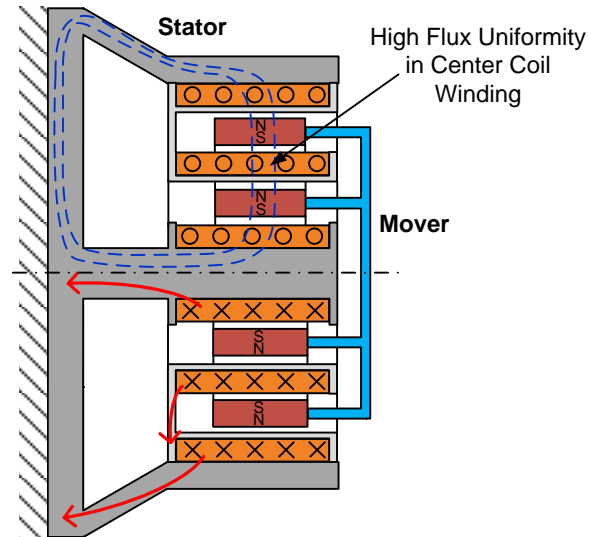


Figure 11.6: Triple coil embodiment

#### 11.1.4 Integrated thermal management

In general, all presented MMA designs feature good thermal management. The closed back iron provides good thermal mass and provides easy access to sections of the back iron where the heat can be removed. However, for better thermal control and to enable larger power output this design can be integrated with heat pipes. One concept is to add heat pipes to a highly thermally conductive structure attached to the coils to drastically increase heat transfer. This concept is shown in Figure 11.7. The MMA integrated with a diaphragm flexure bearing and thermal management system is shown in Figure 11.8.

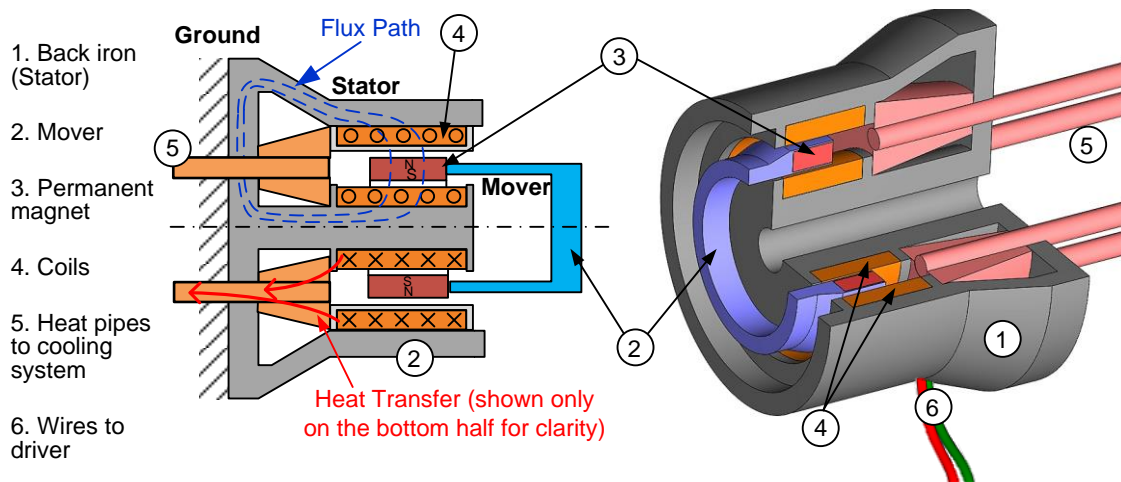


Figure 11.7: Single CCRM MMA with integrated thermal management

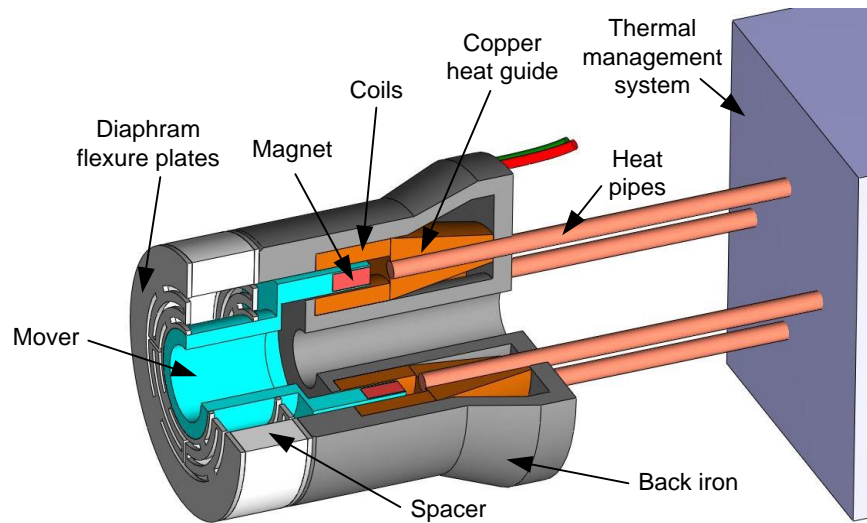
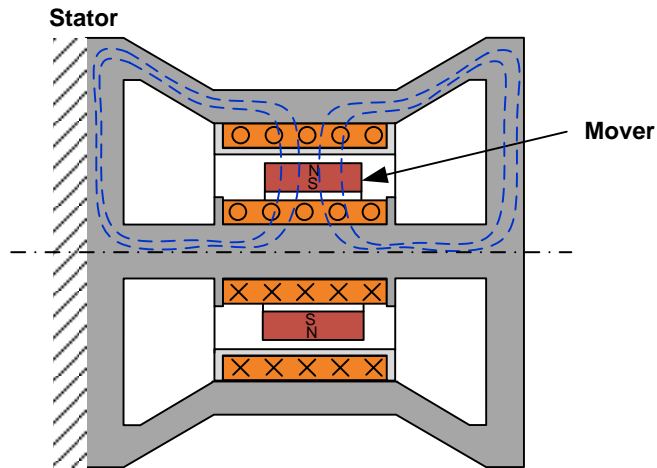


Figure 11.8: Single CCRM MMA with integrated diaphragm flexure bearing and thermal management system

### 11.1.5 Single CCRM closed face MMA design

One disadvantage of the open face design above is that all magnetic flux must go through the same path of the center core which could cause magnetic saturation. This

may be addressed by closing both faces to create two parallel flux loops. Half of the flux goes through each end which significantly reduces saturation in the center core due to the permanent magnet flux.



*Figure 11.9: Single CCRM closed face MMA design*

However, the closed faces also reduce the reluctance of the coil magnetic circuit. Therefore this design can suffer from high armature reaction and have high coil inductance. This may cause saturation of the center core due to the coil current and overcome benefits in the permanent magnet circuit. The coil induced flux adds to the magnet flux, resulting in a localized area of high magnetic field density and potential saturation. This design has good force-stroke uniformity and is symmetric. However, it may be affected by coil current (i.e. armature reaction) as discussed above. Finally, in this design it is more challenging to access the magnet mover than when one side of the architecture is open.

### 11.1.6 Axially spaced dual CCRM MMA designs

One method to reduce potential for armature reaction and high coil inductance is to use oppositely wound coils like in conventional MMAs ( explained in 4.1.2). This can be realized by joining two CCRM modules axially as in Figure 11.10. The two sets of fixed coils are wound oppositely, and magnets are also magnetized with opposite polarities. One ring magnet is north polarity on the radial outside face and south on radial inside face, and the other magnet is south polarity on the radial outside face, and north on the inside face. This permutation features no ferromagnetic back-iron, which eliminates cogging at the expense of decreased force output and uniformity over stroke (see 3.1.1). Example permanent magnet magnetic flux lines are shown with significant fringing. The ring magnets are joined via a tubular mover.

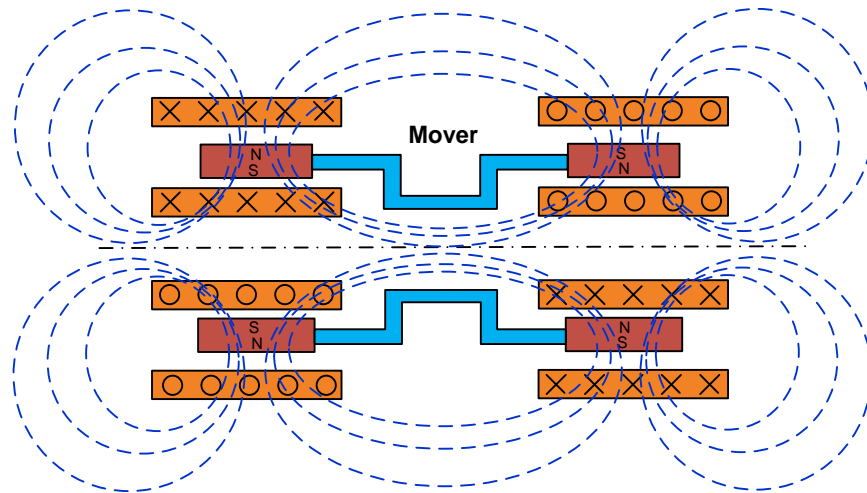


*Figure 11.10: Ironless axially spaced dual CCRM MMA*

The embodiment shown in Figure 11.11 features a ferromagnetic center core and back-iron. This reduces reluctance of the permanent magnet magnetic circuit, forming a primary flux loop between the two ring magnets as shown. This increases force

generation and reduces fringing, however some cogging is introduced. Mechanical interfacing with the mover is also more difficult. Heat transfer is improved via the back iron.

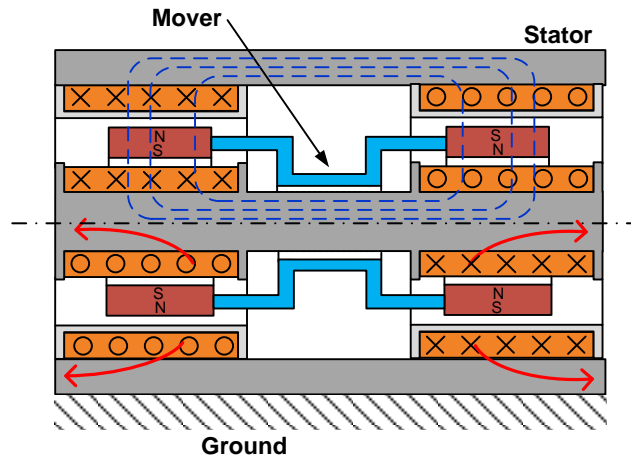


*Figure 11.11: Axially spaced dual CCRM MMA with center core and back iron*

This design can be improved by introducing ferromagnetic end plates as shown in Figure 11.12. This enables the formation of three primary magnetic flux loops with the permanent magnet. Splitting the magnetic flux paths drastically reduces saturation potential in the center core. This design therefore has potential for high force output, good force-stroke uniformity, and low armature reaction and coil inductance. Mechanical interface of this design is challenging, however. It requires access to the magnet through one side of the back iron caps without disrupting the flux line distribution shown.

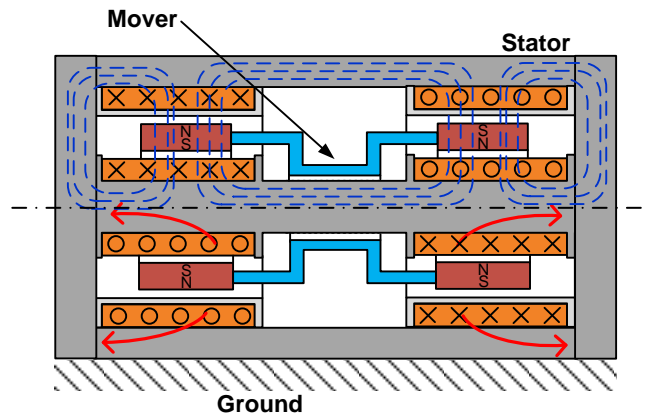


*Figure 11.12: Axially spaced dual CCRM closed face MMA design*

#### 11.1.7 Radially spaced dual CCRM MMA designs

An alternate method to reduce armature reaction via oppositely wound coils with significant flux linkage is to place oppositely wound coils concentric to each other – that is, to space the CCRM modules radially instead of axially. Figure 11.13 shows one embodiment of this concept consisting of a ferromagnetic core around which two similarly wound coils sandwich a radially magnetized ring magnet inside of a tubular back iron. This forms the first CCRM. Around the back iron are placed two more similarly wound coils (albeit wound in the opposite direction as the first coils) which sandwich a second radially magnetized ring magnet of opposite polarity. A second tubular back iron encloses the coils to form the second CCRM. A ferromagnetic back plate completes the two primary magnetic circuits as shown. While magnetic flux from both ring magnets adds in the middle back iron, there is less likelihood for saturation due to the larger radius and hence larger cross sectional area as compared to the center core. Furthermore, radially placed oppositely wound coils may reduce net coil magnetic flux in the center core compared to the axially spaced CCRM designs, potentially improving

performance. Due to the open face of this design, mechanical access to the mover is simplified. This design is also axially much shorter, at the expense of a larger diameter.

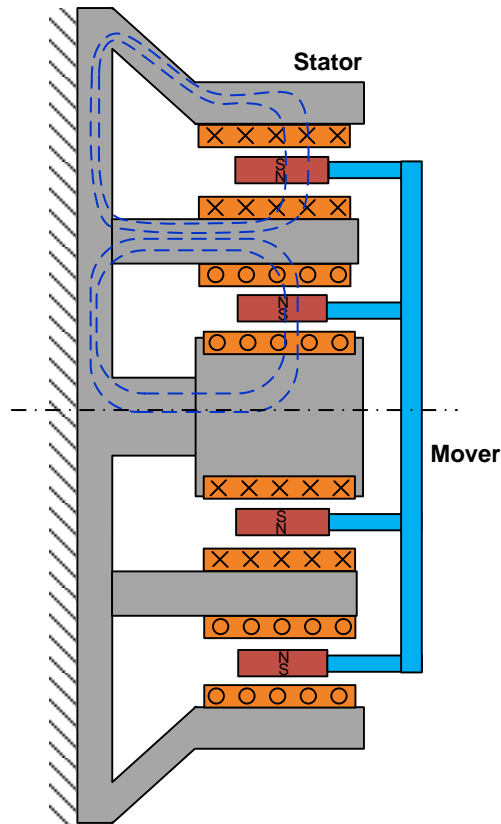


*Figure 11.13: Radially spaced dual CCRM open face MMA*

Magnetic saturation is most likely to occur in the center core. Therefore a second ferromagnetic plate can be added to close the face of the inner CCRM as shown in Figure 11.14. This opens a third primary permanent magnet flux circuit as shown to reduce the flux density in the center core. The mover interfaces with the inner ring magnet via through holes in the front plate.

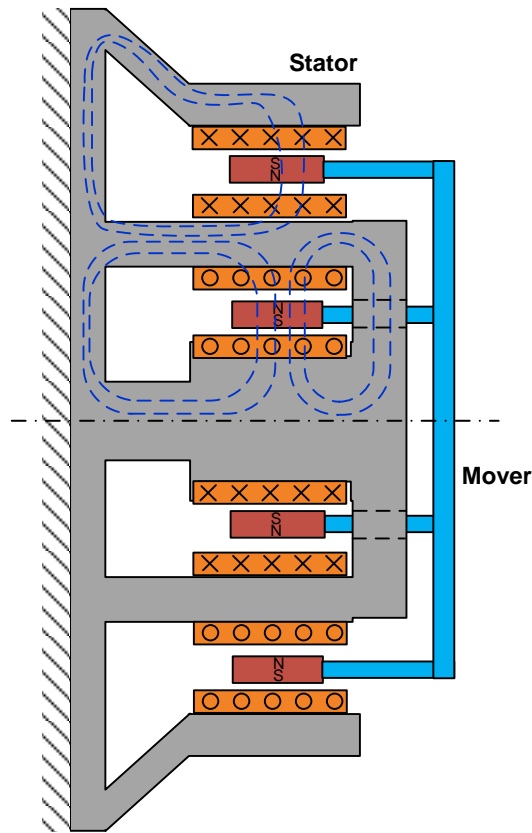


*Figure 11.14: Radially spaced dual CCRM semi-closed-face MMA*

### 11.1.8 Planar topologies

In general, all of the presented embodiments of the CCRM MMA can also be configured in a planar instead of cylindrical manner. This is envisioned by considering half of the cross sections of any of the above cylindrical designs, and extruding it to a planar design. Some of the benefits of the ideally cylindrical CCRM are lost, notably that not all of coil winding is utilized for force generation which decreases power efficiency and hence the dynamic actuator constant. The bar magnet also has increased fringing, potentially decreasing force output and the dynamic actuator constant. However, these

embodiments may give several benefits, including more compact packaging and simplified manufacturing, especially of the magnets, which can be conventional planar bar magnets instead of ring magnets. Also the planar designs in general still maintain the benefits of the cylindrical configurations, as the magnet orientation features relatively low flux fringing, requires no pole pieces, has minimal off-axis attraction (in this case, in the vertical direction), and has low cogging due to the open ends of the back iron. The magnets can also be mounted near the motion stage and the small actuator length minimizes any cantilever from the motion stage.

One planar embodiment is shown in Figure 11.15 comprising two oppositely polarized bar magnets (mover) sandwiched between four coils and two ferromagnetic plates (stator). This is analogous to the cylindrical configuration in Figure 11.11.

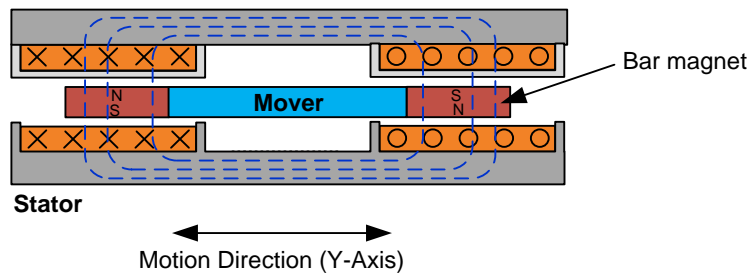


*Figure 11.15: Single-Axis Planer MMA*

An interesting embodiment not seen in cylindrical CCRM MMA designs is, however, realized in planar designs. The planar design above which provides single axis (i.e. Y axis) linear actuation can also be utilized as a highly effective dual axis (i.e. XY plane) MMA. Rotating one coil (in this case the upper) 90° so that the current flows along the Y axis as in Figure 11.16, enables the actuator 2-axis (XY) motion. The upper

and lower coils are not wired together in this case, each having its own separately controlled current driver. Current in the upper coil results in force and motion in the left-to-right (Y direction) and by current in the lower coil results in motion in and out of the page (X direction). Simultaneously driving both coils controls motion of the mover in all directions within the XY plane.

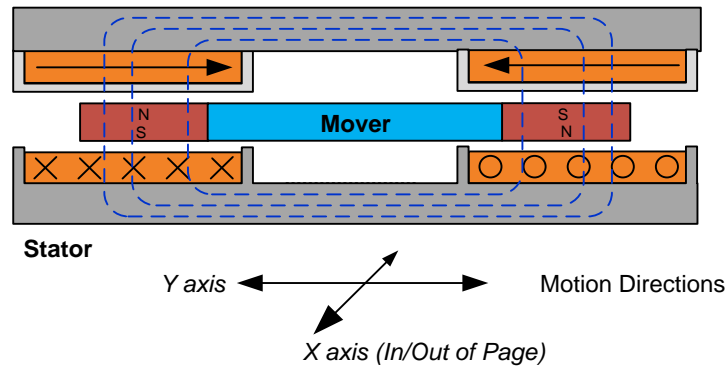


*Figure 11.16: Dual axis planar MMA*

## 11.2 Actuator integration with motion system

Performance of the motion system may be improved and complexity reduced by integrating the function of the motion guidance bearing and actuator. By using a magnetically permeable motion stage and flexure beams, the actuator magnet and coil may be compactly integrated within the bearing, such as in Figure 11.17a. Figure 11.17b shows an additional embodiment where the motion stage itself assumes the role of center pole piece. These arrangements may save packaging space, reduce the likelihood of center pole piece saturation, decrease the motion stage size constraints, and simplify manufacturing and assembly.

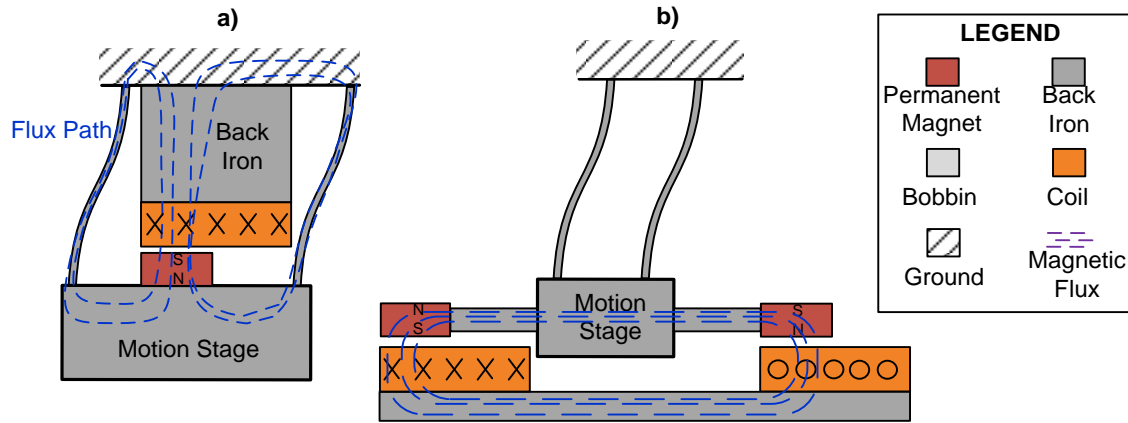


Figure 11.17: Integrated actuator and motion bearing configurations

### 11.3 Coil designs

This section discusses pertinent innovative coil design concepts. The dynamic actuator constant increases with actuator power efficiency which can be increased by improved packing and utilization factors of the coil. Likewise, the actuator force uniformity over stroke profile can also be improved via coil design.

#### 11.3.1 MMA featuring non-uniform coil windings

As shown in Figure 11.18, a non-uniform coil winding shape can be used to increase force uniformity over stroke. In conventional coils, coil thickness (i.e. winding layers) is maintained constant, and fringing of the magnetic field contributes to a drop in force at the end of the stroke (left). However, additional coil windings at the ends of the coils can compensate for fringing losses and maintain uniform force over stroke (right). This improvement comes at the cost of higher coil resistance and a lower dynamic actuator constant value if measured at the center stroke. The dynamic actuator constant

may increase at the ends of the stroke, however. Non-uniform coil windings can be used in all of the proposed MMA architectures.

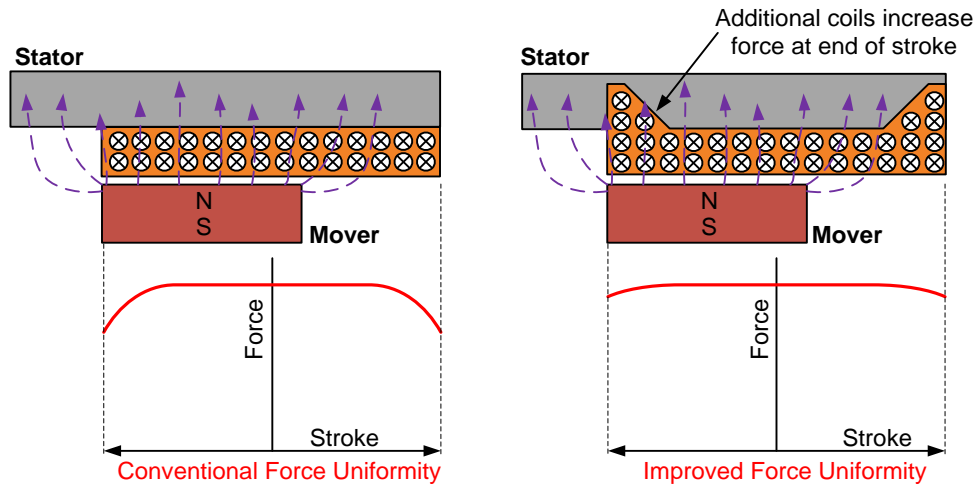
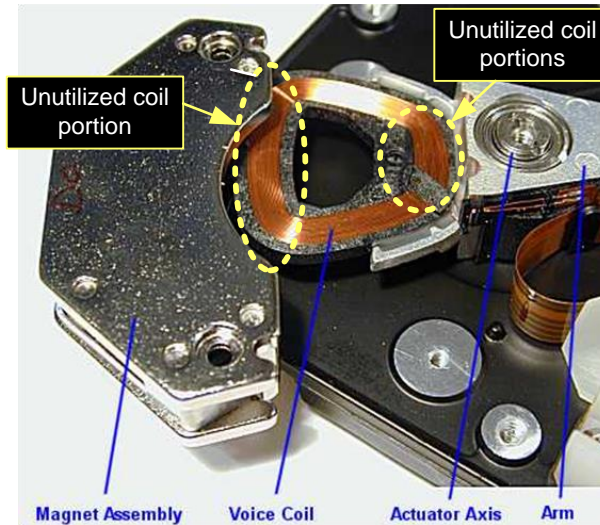


Figure 11.18: Non-uniform coil increase force uniformity over stroke profile

### 11.3.2 High-efficiency planar coils

Planar coils, such as those used in the XY planar MMA above, are commonly used in voice coil actuators in hard drives. An example of these voice coils is shown below in Figure 11.19. They are made in a similar fashion to cylindrical voice coils by winding wire on a bobbin. Planar actuator designs have the disadvantage in that portions of the coil are not used to generate force—often roughly half of the coil—unlike in cylindrical designs which use the entire winding. The unused portions of the coils in the hard drive actuator example are circled in Figure 11.19 in green. The unutilized portions of planar coils reduce power efficiency and therefore the dynamic actuator constant.



*Figure 11.19: Planar voice coil in hard drive read head mechanism [278]*

An approach using stacked conductive plates in alternating patterns may increase the efficiency of planar coils while also improving their manufacturability. In this idea, alternating layers of conductive material and thin insulator layers form a conductive “spiral”, with narrower conductive paths in the working air gap where high packing density is desirable, and wider, lower resistance conductive paths in the non-utilized portions of the coil. The wider conduction paths decrease the total coil resistance and therefore increase overall coil efficiency. This layout is depicted in Figure 11.20, showing multiple winding layers which alternate as: a conductive clockwise layer, a layer of insulation, a counter-clockwise conductive layer, insulation, a clockwise layer, and so forth.

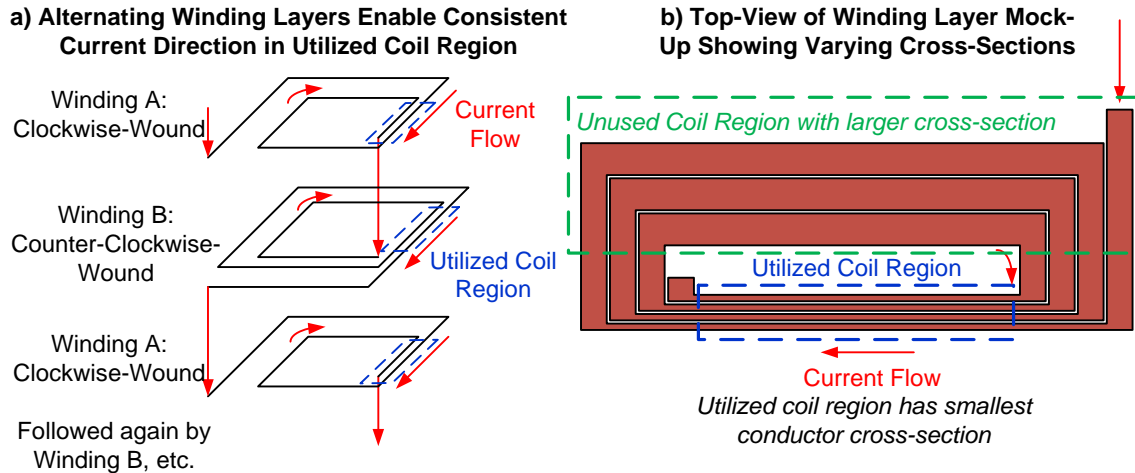


Figure 11.20: Planar coil winding pattern (a) and layout (b)

These coils may be manufactured using standard equipment and processes. For example, macro-scale coils can be made using water jet or CNC milling operations to cut the patterns in copper or aluminum sheets. Conventional PCB layouts could be stacked as well. For micro-scale coils standard MEMS processes can be used to achieve the same patterns. The layers are stacked with similarly-cut insulating layers in between, and then glued or pressed together to form the completed coil.

#### 11.4 Voice coil actuator concepts

As described earlier in Section 2.6.1, voice coil actuators, despite their many desirable qualities, are potentially not suitable for large range nanopositioning in this work because they suffer from motion disturbance due to moving wire leads as well as reduced accuracy due to significant heat transfer from the moving coil to the motion stage and the flexure beams. These problems, however, may be eliminated by the concepts presented in this section.

### 11.4.1 Flexure coil leads

An auxiliary conductive flexure beam connected to the coil can transmit actuator drive current as well as remove heat from the coil, yet maintain frictionless and disturbance-free motion unlike conventional lead wire. An example is shown in Figure 11.21. A voice coil actuator with the back iron and magnet form the stator and the coil forms the mover. The coil is attached to the motion stage which is guided by conventional flexure beams. The auxiliary electrically conducting flexure beam provides current to the coil and removes  $i^2R$  heating. A potential material is Beryllium Copper which is an excellent flexure material and also a very good electrical and thermal conductor. Flexures have the benefit of low stiffness in the motion direction and high stiffness in the other (bearing) directions, so the flexure coil lead would add negligible mechanical stiffness and damping in the motion direction.

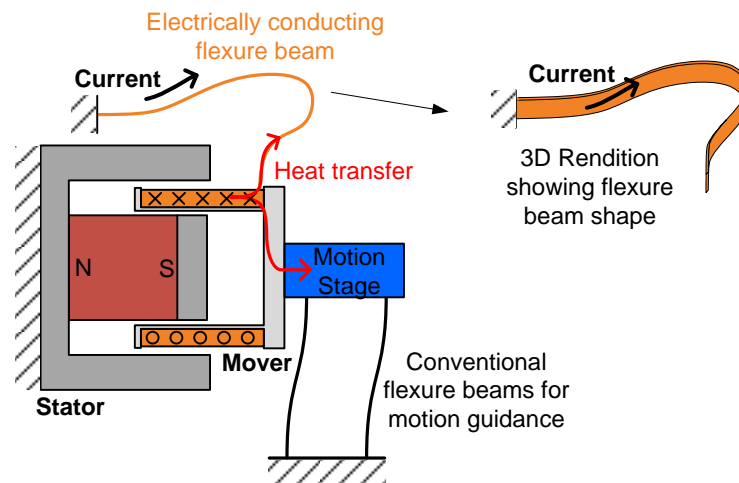
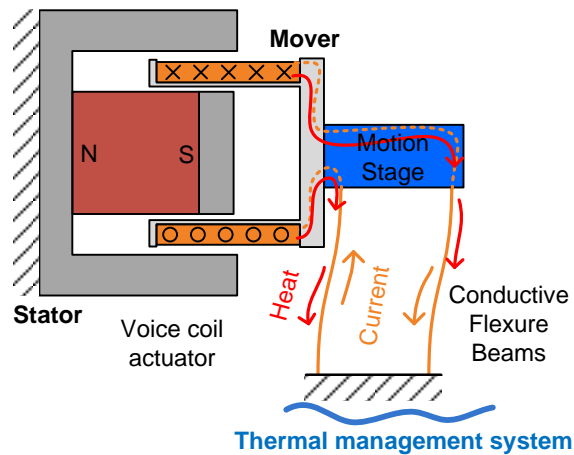


Figure 11.21: Flexure beam voice coil electrical wire leads

### 11.4.2 VCA for nanopositioning

In this concept, a flexure bearing made of Aluminum, which is highly electrically and thermally conductive, itself simultaneously provides disturbance-free motion guidance, power supply, and heat dissipation to a heat sink, all in one compact package. This gives a VCA fully suited for nanopositioning, as the main VCA drawbacks of moving coil leads and poor thermal management are all overcome. This concept is shown in Figure 11.22.



*Figure 11.22: Flexure beams for motion guidance, power supply, and heat transfer*

## CHAPTER 12: Conclusion

This work analytically and experimentally establishes the limits of motion performance enabled by moving magnet actuators (MMA) in flexure-based nan positioning systems. Actuator performance index analysis and a survey of prior art suggests MMA to be an overall good, if not best, candidate for achieving high performance nan positioning over the desired large (~10mm) range. A new MMA figure of merit, referred to as the dynamic actuator constant, is introduced that captures inherent trade-offs between the actuator specifications, and limits the first natural frequency of the nan positioning system. The dynamic actuator constant describes the fundamental performance limits for all MMAs, regardless of size or design. This significantly simplifies the MMA design process, enabling determination of an optimized MMA geometry and relates it to system level dynamic performance. The significance of this constant is experimentally validated via the fabrication and testing of a single-axis nan positioning system. The design of a single axis flexure bearing and position sensing setup is described. A novel thermal management system is designed to greatly abate the heat dissipation problem associated with MMAs.

Promising results for large-range point-to-point nan positioning are shown. However, dynamic tracking with nanometric motion quality is not attained due to harmonic distortion in the driver, force-stroke non-uniformity of the MMA, and limited natural frequency of the overall system.

The limitation of overall system open-loop natural frequency motivates future work to design MMAs that offer greater values of the dynamic actuator constant while maintaining low force-stroke non-uniformity. This is accomplished via the conception and optimization of new MMA architectures, and other innovations in VCA and coil designs.

Although this work focuses on the application of MMAs in nan positioning systems, the discussion is relevant to any flexure-based motion system that employs a linear electromagnetic actuator, as well as to electromagnetic actuator design and actuator selection in general.

## REFERENCES

- [1] D. Griffiths, *Introduction to Electrodynamics*, 3rd ed. Upper Saddle River, NJ: Prentice Hall, 1999.
- [2] H.-D. Chai, *Electromechanical Motion Devices*. Upper Saddle River, NJ: Prentice Hall, 1998.
- [3] E. P. Furlani, *Permanent magnet and electromechanical devices: materials, analysis, and applications*. Academic Press, 2001.
- [4] “G2 Consulting Course on Magnetics.” [Online]. Available: <http://www.consult-g2.com/>.
- [5] O. Gomis-Bellmunt and L. Campanile, *Design rules for actuators in active mechanical systems*. 2010.
- [6] “Product Model # 4022 Moving Magnet Actuator Series.” Magnetic Innovations BV.
- [7] N. Bianchi, S. Bolognani, D. D. Corte, and F. Tonel, “Tubular linear permanent magnet motors: an overall comparison,” *Conf. Rec. 2002 IEEE Ind. Appl. Conf. 37th IAS Annu. Meet. (Cat. No.02CH37344)*, vol. 2, pp. 1266–1273, 2002.
- [8] “Product Model # NCM02-17-035-2F.” H2W Technologies, Inc.
- [9] G. P. Gogue and J. J. Supak Jr., “Voice-coil actuators,” *PCIM 1989 conference*, Long Beach, California, USA, 1989.
- [10] B. Black, M. Lopez, and A. Morcos, “Basics of voice coil actuators,” *Power Convers. Intell. motion*, vol. 19, pp. 44–46, 1993.
- [11] N. H. Vrijsen, J. W. Jansen, and E. A. Lomonova, “Comparison of linear voice coil and reluctance actuators for high-precision applications,” in *14th International Power Electronics and Motion Control Conference*, 2010, pp. S329–S336.
- [12] R. Banik and D. G. Gweon, “Design and optimization of voice coil motor for application in active vibration isolation,” *Sensors Actuators, A Phys.*, vol. 137, no. 2, pp. 236–243, 2007.

- [13] T. Morcos, “The Straight Attraction: Part One,” *Motion Control*, pp. 29–33, Jun-2000.
- [14] D. S. Georgescu, “Considerations about the actual stage of linear electric motors with mobile coil,” *Sixth International Conference on Electromechanical and Power Systems*. Chisinau, Rep. Moldova, 2007.
- [15] M. G. E. Schneiders, J. Makarovic, M. J. G. van de Molengraft, and M. Steinbuch, “Design considerations for electromechanical actuation in precision motion systems,” in *16th IFAC World Congress*, 2005.
- [16] “Voice Coil Actuators An Applications Guide.” Bei Kimko Magnetics.
- [17] J. Janssen, J. Paulides, E. A. Lomonova, and A. J. A. Vandenput, “Cogging force reduction in tubular permanent magnet actuators,” in *Electric Machines & Drives Conference*, 2007, pp. 1–6.
- [18] Y. Zhang, Q. Lu, M. Yu, and Y. Ye, “A Novel Transverse-Flux Moving-Magnet Linear Oscillatory Actuator,” *IEEE Trans. Magn.*, vol. 48, no. 5, pp. 1856–1862, 2012.
- [19] S. Kim, M. Song, N. Park, J. Yoo, Y. Park, K. Park, K. Sangyong, S. Myeong-Gyu, P. No-Cheol, Y. Jeonghoon, P. Young-Pil, and P. Kyoung-Su, “Optimal Design of Moving-Magnet Type Actuators for Optical Disk Drives Considering Effect of Coil Electromagnet,” *IEEE Trans. Magn.*, vol. 45, no. 5, pp. 2228–2231, 2009.
- [20] N. Chen, Y. J. Tang, Y. N. Wu, X. Chen, and L. Xu, “Study on static and dynamic characteristics of moving magnet linear compressors,” *Cryogenics (Guildf.)*, vol. 47, no. 9–10, pp. 457–467, 2007.
- [21] K. a. Poornima, “Moving magnet loudspeaker system with electronic compensation,” *IEE Proc. - Circuits, Devices Syst.*, vol. 40, no. 4, p. 250, 2001.
- [22] T. Nast, J. Olson, P. Champagne, B. Evtimov, D. Frank, E. Roth, and T. Renna, “Overview of Lockheed Martin cryocoolers,” *Cryogenics (Guildf.)*, vol. 46, no. 2–3, pp. 164–168, Feb. 2006.
- [23] “Product Model # BROADBAND LINEAR AMPLIFIER P200.” FLC Electronics AB.
- [24] “Product Model # NCM08-17-050-2LB.” H2W Technologies, Inc.

- [25] “Miniature Linear Bearing Assemblies,” *The Precision Alliance*. [Online]. Available: <http://onlinecatalog.tpa-us.com/category/miniature-linear-guides>.
- [26] W. West and D. Mcmillan, “The design of a loud-speaker,” *Wirel. Sect. Inst. Electr. Eng.*, vol. 15, no. 44, pp. 53 – 67, 1940.
- [27] S. Hwang, H. Lee, K. Hong, B. Kang, and G. Hwang, “New Development of Combined Permanent-Magnet Type Microspeakers Used for Cellular Phones,” *IEEE Trans. Magn.*, vol. 41, no. 5, pp. 2000–2003, 2005.
- [28] H. Takewa, S. Saiki, S. Kano, and a. Inaba, “Slim-type speaker for flat-panel televisions,” *IEEE Trans. Consum. Electron.*, vol. 52, no. 1, pp. 40–46, Feb. 2006.
- [29] A. Madni, J. Vuong, and M. Lopez, “A smart linear actuator for fuel management system,” in *Automation Congress, 2002 Proceedings of the 5th Biannual World*, 2002, pp. 615–624.
- [30] F. Baronti, A. Lazzeri, and F. Lenzi, “Voice coil actuators: From model and simulation to automotive application,” in *Industrial Electronics, 2009. IECON '09. 35th Annual Conference of IEEE*, 2009, pp. 1805–1810.
- [31] H. Hong and L. Rodrigues, “Modeling and controller design for a voice coil actuated engine valve,” in *Proceedings of 2005 IEEE Conference on Control Applications, 2005. CCA 2005.*, 2005, pp. 1234–1239.
- [32] R. Wakeland, “Use of electrodynamic drivers in thermoacoustic refrigerators,” *J. Acoust. Soc. Am.*, vol. 107, no. 2, pp. 827–32, Feb. 2000.
- [33] A. S. Gaunekar, K. . Narayankhedkar, and S. L. Bapat, “Dynamic and thermodynamic analysis of doubly motorized miniature Stirling cryocooler using double coil linear motors,” *Cryogenics (Guildf)*., vol. 34, no. 1, pp. 43–50, Jan. 1994.
- [34] G. Savioz and Y. Perriard, “A miniature short stroke linear actuator and its position control for a haptic key,” in *2009 IEEE Energy Conversion Congress and Exposition, ECCE 2009*, 2009, no. 9671, pp. 2441–2446.
- [35] J. McBean, “Voice coil actuators for human-robot interaction,” *Intell. Robot. Syst. 2004.*, pp. 852–858, 2004.
- [36] R. Fair and H. R. Bolton, “Analysis and design of electromagnetic moving coil vibration generators,” in *Electrical Machines and Drives, 1993. Sixth International Conference on (Conf. Publ. No. 376)*, 1993, pp. 529–534.

- [37] J. Jeong and D.-G. Gweon, "Optimal design of rotary-type voice coil motor using multisegmented magnet array for small form factor optical disk drive," *Japanese J. Appl. Physics, Part 1 Regul. Pap. Short Notes Rev. Pap.*, vol. 46, no. 5 A, pp. 2912–2914, 2007.
- [38] Y. Hirano and J. Naruse, "Dynamic characteristics of a voice coil motor for a high performance disk drive," *IEEE Trans. Magn.*, vol. 25, no. 4, pp. 3073–75, 1989.
- [39] Y. A. Mah, H. Lin, Q. H. Li, and S. X. Chen, "Design of a high bandwidth moving-coil actuator with force couple actuation," *IEEE Trans. Magn.*, vol. 35, no. 2, pp. 874–878, Mar. 1999.
- [40] K. Kim, D. Gweon, H. S. Jung, S. Lee, M. Hong, and M. G. Lee, "A Stage Based on Voice Coil Motor with High Speed and Long Range for Laser Micro/Nano Fabrication," *Key Eng. Mater.*, vol. 346, pp. 757–760, 2007.
- [41] K. Yongdae, S. Byounguk, Y. Woosub, J. Jongkyu, L. Jonghyun, and P. Kyihwan, "Voice coil motor nano stage with an eddy current damper," in *2008 10th International Conference on Control, Automation, Robotics and Vision (ICARCV 2008)*, 17-20 Dec. 2008, 2008, pp. 1714–1717.
- [42] M. Binnard, J. Gery, and A. Hazelton, "High Efficiency Voice Coil Motor," *US Pat. App. 12/050,675*, 2008.
- [43] A. Taberner and N. Ball, "A portable needle-free jet injector based on a custom high power-density voice-coil actuator," in *Proceedings of the 28th IEEE EMBS Annual International Conference*, 2006, pp. 5001–5004.
- [44] H. C. Yu, T. Y. Lee, S. J. Wang, M. L. Lai, J. J. Ju, D. R. Huang, and S. K. Lin, "Design of a voice coil motor used in the focusing system of a digital video camera," *Ieee Trans. Magn.*, vol. 41, no. 10, pp. 3979–3981, 2005.
- [45] J.-D. Hsu and Y.-Y. Tzou, "Modeling and design of a voice-coil motor for auto-focusing digital cameras using an electromagnetic simulation software," in *Power Electronics Specialists Conference, 2007. PESC 2007. IEEE*, 2007, pp. 939–944.
- [46] L. P. Maguire, S. Szilagy, and R. E. Scholten, "High performance laser shutter using a hard disk drive voice-coil actuator," *Rev. Sci. Instrum.*, vol. 75, no. 9, pp. 3077–3079, 2004.
- [47] R. Olaru and C. Astratini-Enache, "Analysis and design of a moving-magnet type linear actuator with repulsive magnetic forces," *Int. J. Appl. Electromagn. Mech.*, vol. 38, pp. 127–137, 2012.

- [48] R. E. Clark, D. Howe, and G. W. Jewell, "The Influence of Magnetization Pattern on the Performance of a Cylindrical Moving-Magnet Linear Actuator," *IEEE Trans. Magn.*, vol. 36, no. 5, pp. 3571–3574, 2000.
- [49] D. Howe, "Magnetic actuators," *Sensors Actuators A Phys.*, vol. 81, no. 1–3, pp. 268–274, Apr. 2000.
- [50] M. Scanlon, "Moving Magnet Actuator with Counter-Cogging End-Ring and Asymmetrical Armature Stroke," *US Pat. App. 14/042,308*, 2013.
- [51] J. J. Cathey, D. A. Topmiller, S. A. Nasar, and S. Member, "A Tubular Self-Synchronous Motor for Artificial Heart Pump Drive," *IEEE Trans. Biomed. Eng.*, vol. 33, no. 3, pp. 315–319, 1986.
- [52] E. Shahoian, "Moving magnet actuator for providing haptic feedback," *US Pat. 6,982,696*, 2006.
- [53] N. Baker and M. Mueller, "Permanent magnet air-cored tubular linear generator for marine energy converters," *Electron. Mach.*, no. 1, pp. 862–867, 2004.
- [54] M.-Y. Chen, M.-J. Wang, and L.-C. Fu, "A novel dual-axis repulsive Maglev guiding system with permanent magnet: modeling and controller design," *IEEE/ASME Trans. Mechatronics*, vol. 8, no. 1, pp. 77–86, 2003.
- [55] R. Seung-Kook and P. Jong-Kweon, "Development of a miniature air-bearing stage with a moving-magnet linear motor," *Int. J. Precis. Eng. Manuf.*, vol. 9, no. 1, pp. 19–24, 2008.
- [56] S. Verma, H. Shakir, K. Won-Jong, and W.-J. Kim, "Novel electromagnetic actuation scheme for multi-axis nanopositioning," *Ieee Trans. Magn.*, vol. 42, no. 8, pp. 2052–2062, 2006.
- [57] P. Estevez, A. Mulder, and R. H. M. Schmidt, "Mechatronics 6-DoF miniature maglev positioning stage for application in haptic," *MECHATRONICS*, pp. 2–9, 2012.
- [58] J. Zhu, H. Lu, and Y. Guo, "Development of electromagnetic linear actuators for micro robots," *Electr. Mach. Syst.*, pp. 3673–3679, 2008.
- [59] S. Awtar and G. Parmar, "Design of a Large Range XY Nanopositioning System," *ASME 2010 Int. Des.*, vol. 2010, no. 44106, pp. 1–13, 2010.

- [60] S. Devasia, E. Eleftheriou, and S. O. R. Moheimani, “A survey of control issues in nanopositioning,” *IEEE Trans. Control Syst. Technol.*, vol. 15, no. 5, pp. 802–823, 2007.
- [61] M. Culpepper and G. Anderson, “Design of a low-cost nano-manipulator which utilizes a monolithic, spatial compliant mechanism,” *Precis. Eng.*, vol. 28, pp. 469–482, 2004.
- [62] A. Sinno, P. Ruaux, L. Chassagne, S. Topçu, Y. Alayli, G. Lerondel, S. Blaize, A. Bruyant, and P. Royer, “Enlarged atomic force microscopy scanning scope: novel sample-holder device with millimeter range,” *Rev. Sci. Instrum.*, vol. 78, no. 9, p. 095107, Sep. 2007.
- [63] K. Salaita, Y. Wang, and C. A. Mirkin, “Applications of dip-pen nanolithography,” *Nat. Nanotechnol.*, vol. 2, no. 3, pp. 145–55, Mar. 2007.
- [64] G. Dai, F. Pohlenz, H. U. Danzebrink, M. Xu, K. Hasche, D. Gaoliang, X. Min, and G. Wilkening, “Metrological large range scanning probe microscope,” *Rev. Sci. Instrum.*, vol. 75, no. 4, pp. 962–969, 2004.
- [65] M. Van De Moosdijk, E. Van Den Brink, and K. Simon, “Collinearity and stitching performance on an ASML stepper,” *Proc. SPIE*, vol. 4688, pp. 858–866, 2002.
- [66] N. B. Hubbard, M. L. Culpepper, and L. L. Howell, “Actuators for micropositioners and nanopositioners,” *Appl. Mech. Rev.*, vol. 59, no. 6, pp. 324–334, 2006.
- [67] W. O’Brien, “Long-range motion with nanometer precision,” *Photonics Spectra*, vol. 39, no. June, pp. 80–81, 2005.
- [68] “Product Model # P-541.2 – P-542.2 Piezo XY Nanopositioning Stage, PhysikInstrumente.” .
- [69] “P-620.2 – P-629.2 PIHera XY Piezo Stage.” [Online]. Available: <http://www.physikinstrumente.com/en/products/prdetail.php?sortnr=202400>.
- [70] “Queensgate Instruments NPS-XY-100 Two Axis 100µm x 100µm Stage.” [Online]. Available: <http://www.nanopositioning.com/products/nanomechanisms/nps-xy-100a>.
- [71] “Mad City Labs Nano-Bio Series.” [Online]. Available: <http://www.madcitylabs.com/nanobioseries.html>.

- [72] A. Slocum, *Precision machine design*. Englewood Cliffs, N.J.: Prentice Hall, 1992.
- [73] M. Kosinskiy, Y. Liu, S. Ahmed, M. Scherge, and J. Schafer, "Tribology of nanopositioning characterization of precision linear bearings on nanometre scale," *VDI BERICHTE*, no. 1950, pp. 215–224, 2006.
- [74] S. Vorndran, "Nanopositioning: fighting the myths," *OLE*, pp. 25–27, Nov-2004.
- [75] K. Fan, Y. Fei, X. Yu, W. Wang, and Y. Chen, "Study of a noncontact type micro-CMM with arch-bridge and nanopositioning stages," *Robot. Comput. Integr. Manuf.*, vol. 23, pp. 276–284, 2007.
- [76] "nPoint NPXY400A." [Online]. Available: [http://www.npoint.com/pdf/specifications/SPECIFICATION\\_NPXY400A.PDF](http://www.npoint.com/pdf/specifications/SPECIFICATION_NPXY400A.PDF).
- [77] "Discovery Technology NanoDirect NTS10." [Online]. Available: [http://www.dti-nanotech.com/docs/NTSseries\\_Brochure.pdf](http://www.dti-nanotech.com/docs/NTSseries_Brochure.pdf).
- [78] "piezosystem jena piezo positioner series PXY 200." [Online]. Available: [http://www.piezosystem.com/piezo\\_actuator\\_nanopositioning/piezo\\_actuators\\_nano\\_stages\\_positioning\\_equipment/xy\\_positioner/series\\_pxy\\_200/](http://www.piezosystem.com/piezo_actuator_nanopositioning/piezo_actuators_nano_stages_positioning_equipment/xy_positioner/series_pxy_200/).
- [79] H. Danzebrink and L. Koenders, "Advances in scanning force microscopy for dimensional metrology," *Ann. CIRP*, vol. 55, no. 2, 2006.
- [80] S. Lenhert, P. Sun, Y. Wang, H. Fuchs, and C. A. A. Mirkin, "Massively Parallel Dip-Pen Nanolithography of Heterogeneous Supported Phospholipid Multilayer Patterns," *Small*, vol. 3, no. 1, pp. 71–75, 2007.
- [81] J. Kramar, "Nanometre resolution metrology with the molecular measuring machine," *Meas. Sci. Technol.*, vol. 16, no. 11, pp. 2121–2128, Nov. 2005.
- [82] S. Jordan, "Forecast for 2007: Nano Gets Big," *Photonics Spectra*, 2007.
- [83] D. Hiemstra, G. Parmar, and S. Awtar, "Performance Tradeoffs Posed by Moving Magnet Actuators in Flexure-Based Nanopositioning," *IEEE/ASME Trans. Mechatronics*, vol. 19, no. 1, pp. 201 – 212, 2012.
- [84] S. Vorndran, "Piezoelectric technology eases navigation in the nanoworld," *Laser Focus world*, no. June, 2005.
- [85] S. Awtar and G. Parmar, "Physical and control systems design challenges in large range nanopositioning," *IFAC Sym. Mechatron. Syst.*, 2010.

- [86] K. S. Chen, D. L. Trumper, and S. T. Smith, "Design and control for an electromagnetically driven X-Y- stage," *Precis. Eng.*, vol. 26, no. 4, pp. 355–369, 2002.
- [87] J. Kwang Suk and B. Yoon Su, "Contact-Free Moving-Magnet Type of Micropositioner With Optimized Specification," *Magn. IEEE Trans.*, vol. 38, no. 3, pp. 1539–1548, 2002.
- [88] M. Holmes, R. Hocken, and D. Trumper, "The long-range scanning stage: a novel platform for scanned-probe microscopy," *Precis. Eng.*, vol. 24, no. 3, pp. 191–209, Jul. 2000.
- [89] S. Awtar and G. Parmar, "Design of a large range XY nanopositioning system," *J. Mech. ...*, pp. 1–13, 2013.
- [90] S. Smith and R. Seugling, "Sensor and actuator considerations for precision, small machines," *Precis. Eng.*, vol. 30, pp. 245–264, 2006.
- [91] G. Parmar, K. Barton, and S. Awtar, "Large dynamic range nanopositioning using iterative learning control," *Precis. Eng.*, 2014.
- [92] P. Schellekens, N. Rosielle, and H. Vermeulen, "Design for precision: current status and trends," *CIRP Ann.*, vol. 47, no. 2, 1998.
- [93] J. Huber, N. Fleck, and M. Ashby, "The selection of mechanical actuators based on performance indices," *R. Soc. Eng. Sci.*, vol. 453, no. 1965, pp. 2185–2205, 1997.
- [94] L. Lim, "Long range and high axial load capacity nanopositioner using single piezoelectric actuator and translating supports," *Int. J. Precis. Eng.*, 2007.
- [95] D. Wood, J. S. Burdess, A. J. Harris, S. Road, S. Building, and M. Court, "Actuators and their mechanisms in microengineering," *Eng. Sci. Educ. J.*, vol. 7, no. 1, pp. 3–5, 1998.
- [96] F. L. Langley and P. H. Mellor, "High-specific output bidirectional moving magnet actuator for use in active vibration control of rotorcraft," *IET Electr. Power Appl.*, vol. 5, no. 1, pp. 100–110, 2011.
- [97] K. Uchino, "Piezoelectric actuators 2006," *J. Electroceramics*, vol. 20, no. 3–4, pp. 301–311, Jul. 2007.
- [98] P. D. A. Thomas R Hicks, *The NanoPositioning Book*. Woodland Road, Torquay TQ2 7AY: Queensgate Instruments Ltd, 1997.

- [99] “PICA Stack Piezo Actuators.” Physik Instrumente.
- [100] K. Mccarthy, “Limitations of Piezos.” [Online]. Available: <http://www.dovermotion.com/WhitePapersPage.aspx>.
- [101] “Piezo actuator catalog.” Noliac, Inc.
- [102] “Application Note: Selection guide for piezo actuators.” Cedrat Technologies, 2009.
- [103] “Piezoelectric Actuators Catalog.” Physik Instrumente.
- [104] J.-J. Kim, Y.-M. Choi, D. Ahn, B. Hwang, D.-G. Gweon, and J. Jeong, “A millimeter-range flexure-based nano-positioning stage using a self-guided displacement amplification mechanism,” *Mech. Mach. Theory*, vol. 50, pp. 109–120, Apr. 2012.
- [105] J. Schutte, L. H. Joubert, and J. M. Strauss, “Constrained optimisation of a transverse flux PM linear generator,” *2012 XXth Int. Conf. Electr. Mach.*, pp. 595–599, Sep. 2012.
- [106] E. Furukawa, M. Mizuno, and T. Doi, “Development of a flexure-hinged translation mechanism driven by two piezoelectric stacks,” *JSME Int. journal. Ser. C, Dyn. Control. Robot. Des. Manuf.*, vol. 38, no. 4, pp. 743–748, 1995.
- [107] H. Jaeger, J. Parker, and C. Peclat, “Mechanically amplified piezoelectric transducer,” *US Pat. 8,154,173*, 2012.
- [108] “P-602 PiezoMove Flexure Actuator.” Physik Instrumente.
- [109] “Flextensional piezoelectric actuator user manual.” Dynamic Structures And Materials, Llc.
- [110] “Flextensional piezoelectric actuators,” *Dynamic Structures LLC* . .
- [111] “Piezoelectric actuators,” *Cedrat Technologies*. [Online]. Available: <http://www.cedrat-technologies.com/en/mechatronic-products/actuators/apa.html>.
- [112] S. C. Woody and S. T. Smith, “Performance comparison and modeling of PZN, PMN, and PZT stacked actuators in a levered flexure mechanism,” *Rev. Sci. Instrum.*, vol. 75, no. 4, p. 842, 2004.

- [113] J. Li, R. Sedaghati, J. Dargahi, and D. Waechter, "Design and development of a new piezoelectric linear Inchworm actuator," *Mechatronics*, vol. 15, no. 6, pp. 651–681, Jul. 2005.
- [114] "Piezo LEGS Linear 6N Datasheet." PiezoMotor AB.
- [115] S. Johansson, M. Bexell, and P. Lithell, "Fine walking actuator," *US Pat. 6,337,532*, 2002.
- [116] "N-111 NEXLINE OEM Linear Actuator Datasheet." Physik Instrumente.
- [117] H. Marth, "Piezo linear drive with a group of piezo actuator stacks as well as method for operating such a drive," *US Pat. 6,800,984*, 2004.
- [118] N. Shimizu and T. Kimura, "An ultrahigh vacuum scanning tunneling microscope with a new inchworm mechanism," *J. Vac. Sci. Technol. A*, vol. 8, no. 1, p. 333, Jan. 1990.
- [119] B. Zhang and Z. Zhu, "Developing a linear piezomotor with nanometer resolution and high stiffness," *IEEE/ASME Trans. Mechatronics*, vol. 2, no. 1, pp. 22–29, Mar. 1997.
- [120] T. Higuchi, Y. Yamagata, K. Furutani, and K. Kudoh, "Precise positioning mechanism utilizing rapid deformations of piezoelectric elements," in *Proceedings of IEEE Micro Electro Mechanical Systems, 1990. An Investigation of Micro Structures, Sensors, Actuators, Machines and Robots.*, 1990, no. 5, pp. 222–226.
- [121] "Stepping Piezo Actuators Application Note." Cedrat Technologies.
- [122] F. Barillot and F. Claeysen, "Fine positioning system using an inertial motor based on a mechanical amplifier," *US Pat. 8,004,153*, 2011.
- [123] Y. Okamoto and R. Yoshida, "Development of linear actuators using piezoelectric elements," *Electron. Commun. Japan (Part III Fundam. Electron. Sci.)*, vol. 81, no. 11, pp. 11–17, Nov. 1998.
- [124] T. Morita, R. Yoshida, Y. Okamoto, M. K. Kurosawa, and T. Higuchi, "A smooth impact rotation motor using a multi-layered torsional piezoelectric actuator.," *IEEE Trans. Ultrason. Ferroelectr. Freq. Control*, vol. 46, no. 6, pp. 1439–45, Jan. 1999.
- [125] "The Nanomotor Datasheet." Klocke Nanotechnik.

- [126] “For imparting microscopic/macroscopic movements to an object,” *US Pat. 5,325,010*, 1994.
- [127] D. W. Pohl, “Dynamic piezoelectric translation devices,” *Rev. Sci. Instrum.*, vol. 58, no. 1, p. 54, 1987.
- [128] M. Kurosawa, H. Yamada, and S. Ueha, “Hybrid transducer type ultrasonic linear motor,” *Jpn. J. Appl. Phys.*, vol. 28, pp. 158 – 60, 1989.
- [129] M. K. Kurosawa, Y. Tsuchitoi, and T. Higuchi, “Transducer for high speed and large thrust ultrasonic linear motor using two sandwich-type vibrators,” *IEEE Trans. Ultrason. Ferroelectr. Freq. Control*, vol. 45, no. 5, pp. 1188–1195, 1998.
- [130] “PILine Ultrasonic Piezo Motors: OEM Motors, Technical Data.” Physik Instrumente.
- [131] W. Wischnewskiy, S. Kovalev, and O. Vyshnevskyy, “New ultrasonic piezoelectric actuator for nanopositioning,” in *9th International Conference on New Actuators*, 2004.
- [132] “HR-1 Servo Motor Datasheet.” Nanomotion Ltd.
- [133] “Linear Piezo Motor LPM20-3 Datasheet.” Cedrat Technologies.
- [134] B. Albert and S. K. Hsu, “Transducer,” *US Pat. 3,292,019*, 1966.
- [135] S. P. Salisbury, D. F. Waechter, R. B. Mrad, S. E. Prasad, R. G. Blacow, and B. Yan, “Design considerations for complementary inchworm actuators,” *IEEE/ASME Trans. Mechatronics*, vol. 11, no. 3, pp. 265–272, Jun. 2006.
- [136] D. F. Waechter, S. Salisbury, R. Ben Mrad, S. E. Prasad, R. G. Blacow, and B. Yan, “Complementary inchworm actuator for high-force high-precision applications,” in *Proc. SPIE 5390, Smart Structures and Materials 2004: Smart Structures and Integrated Systems*, 2004.
- [137] W. G. May, “Piezoelectric electromechanical translation apparatus,” *US Pat. 3,902,084*, 1975.
- [138] R. A. Bizzigotti, “Electromechanical translation apparatus,” *US Pat. 3,902,085*, 1975.
- [139] “Burleigh Inchworm Motor Technology Application Note.” EXFO Burleigh Products Group.

- [140] G. Powers, Q. Xu, and J. Fasick, "Nanometer resolution actuator with multimillimeter range and power-off hold," *Smart Struct. Mater.*, 2003.
- [141] S. Kleindiek, "Electromechanical positioning unit," *US Pat. 5,994,820*, 1999.
- [142] K. Uchino, "Piezoelectric ultrasonic motors: overview," *Smart Mater. Struct.*, vol. 273, 1998.
- [143] V. Snitka, V. Mizariene, and D. Zukauskas, "The status of ultrasonic motors in the former Soviet Union," *Ultrasonics*, vol. 34, no. 2–5, pp. 247–250, Jun. 1996.
- [144] V. Snitka, "Ultrasonic actuators for nanometre positioning," *Ultrasonics*, vol. 38, pp. 20–25, 2000.
- [145] T. Nishimura, H. Hosaka, and T. Morita, "Resonant-type Smooth Impact Drive Mechanism (SIDM) actuator using a bolt-clamped Langevin transducer," *Ultrasonics*, vol. 52, no. 1, pp. 75–80, Jan. 2012.
- [146] T. Morita, H. Murakami, T. Yokose, and H. Hosaka, "A miniaturized resonant-type smooth impact drive mechanism actuator," *Sensors Actuators A Phys.*, vol. 178, pp. 188–192, May 2012.
- [147] M. Suzuki, "Resonant-Type Smooth Impact Drive Mechanism Actuator with Two Langevin Transducers," *Adv. Robot.* 26, 2012.
- [148] J. Zheng, S. Takahashi, S. Yoshikawa, K. Uchino, and J. W. C. de Vries, "Heat Generation in Multilayer Piezoelectric Actuators," *J. Am. Ceram. Soc.*, vol. 79, no. 12, pp. 3193–3198, 1996.
- [149] H. Nakano, "Angstrom positioning system using a giant magnetostriction actuator for high power applications," *Power Convers. Conf. 2002. PCC Osaka*, pp. 1102–1107, 2002.
- [150] S. F. Tsodikov and V. I. Rakhovskii, "Linear And Angular Measurements: Magnetostriction Power Actuators For Superprecision Positioning," *Meas. Tech.*, vol. 40, no. 5, pp. 56–62, 1997.
- [151] F. Claeysen, N. Lhermet, and R. Le Letty, "Actuators, transducers and motors based on giant magnetostrictive materials," *J. Alloys Compd.*, vol. 258, pp. 61–73, Aug. 1997.
- [152] H. Janocha, "Application potential of magnetic field driven new actuators," *Sensors Actuators A Phys.*, vol. 91, no. 1–2, pp. 126–132, 2001.

- [153] F. Claeysen, "Magnetostrictive actuators compared to piezoelectric actuators," in *Proceedings of the SPIE European Workshop on Smart Structures in Engineering and Technology*, 2003, pp. 194–200.
- [154] H. R. Bolton, "Design aspects of electromagnetic actuators," in *IEE Colloquium 'Magnetic Materials for Sensors and Actuators' (Digest No.1994/183)*, 1994, vol. 6, pp. 1–6.
- [155] C. Dawson and H. Bolton, "Performance prediction of a wide-angle limited-motion rotary actuator," *Proc. Inst. Electr. Eng.*, vol. 125, no. 9, pp. 895–898, 1978.
- [156] C. Astratini-Enache and R. Olaru, "Moving magnet type actuator with ring magnets," *J. Electr. Eng.*, vol. 61, no. 7, pp. 144–147, 2010.
- [157] S. Jang and S. Jeong, "Reduction of armature reaction and inductance in the moving coil linear actuator for a high performance drive," in *Magnetics Conference, 2002. INTERMAG Europe 2002. Digest of Technical Papers. 2002 IEEE International, 2002*.
- [158] L. M. Livshitz and Y. Vaknin, "Moving Coil Linear Actuator," *US Pat. 3,743,870*, 1973.
- [159] J. Stupak Jr., G. Gogue, and J. Stupak, "Voice-coil actuators: insight into the design," in *Official Proceedings of the 16th International Intelligent Motion Conference*, 1989, pp. 241–253.
- [160] B. Lesquesne, "Permanent magnet linear motors for short strokes," *IEEE Trans. Ind. Appl.*, vol. 32, no. 1, pp. 161–168, 1996.
- [161] J. Frandsen, "Method of making a multi-coil/multi-magnet actuator," *US Pat. 4,692,999*, 1987.
- [162] W. Youm, J. Jung, S. Lee, K. Park, Y. Woosub, J. Jongkyu, Q. L. Sung, and P. Kyihwan, "Control of voice coil motor nanoscanners for an atomic force microscopy system using a loop shaping technique," *Rev. Sci. Instrum.*, vol. 79, no. 1, pp. 13706–13707, 2008.
- [163] T. J. Teo, I. M. Chen, G. Yang, and W. Lin, "A flexure-based electromagnetic linear actuator," *Nanotechnology*, vol. 19, no. 31, pp. 1–10, Aug. 2008.
- [164] S. Fukada and K. Nishimura, "Nanometric positioning over a one-millimeter stroke using a flexure guide and electromagnetic linear motor," *Int. J. Precis. Eng. Manuf.*, vol. 8, pp. 49–53, 2007.

- [165] “BEI Kimco Model # LA15-26-000A.” [Online]. Available: [http://www.beikimco.com/product.php?part\\_id=LA15-26-000A](http://www.beikimco.com/product.php?part_id=LA15-26-000A).
- [166] “BEI Kimco Model # LA12-17-000A.” [Online]. Available: [http://www.beikimco.com/product.php?part\\_id=LA12-17-000A](http://www.beikimco.com/product.php?part_id=LA12-17-000A).
- [167] V. Kordonskii and S. Demchuk, “Heat transfer in electrodynamic transducers,” *J. Eng. Phys.*, vol. 59, no. 6, pp. 1499–1504, 1990.
- [168] J. de Boeij, E. Lomonova, J. L. Duarte, and a. J. a. Vandenput, “Contactless power supply for moving sensors and actuators in high-precision mechatronic systems with long-stroke power transfer capability in x–y plane,” *Sensors Actuators A Phys.*, vol. 148, no. 1, pp. 319–328, Nov. 2008.
- [169] J.-Y. Chang, “Hard disk drive seek-arrival vibration reduction with parametric damped flexible printed circuits,” *Microsyst. Technol.*, vol. 13, no. 8–10, pp. 1103–1106, Mar. 2007.
- [170] B. M. M. Chen, T. H. H. Lee, P. Kemaio, and C. Guoyang, “Improvement on a hard disk drive servo system using friction and disturbance compensation,” in *Advanced Intelligent Mechatronics, 2003. AIM 2003. Proceedings. 2003 IEEE/ASME International Conference on*, 2003, vol. 2, no. Aim, pp. 1160–1165 vol.2.
- [171] C. Jen-Yuan, “Minimization of flexible cable settling PES in high TPI hard disk drives via mechatronic integration,” *IEEE Trans. Magn.*, vol. 45, no. 11, pp. 4956–4961, 2009.
- [172] H. Ono, J. Mochizuki, and T. Hisano, “Novel hard disk drive actuator control method to solve micro jog problem,” in *SICE Annual Conference, 2008*, 2008, pp. 2555–2561.
- [173] J. Wang, G. W. Jewell, D. Howe, and W. Jiabin, “A general framework for the analysis and design of tubular linear permanent magnet machines,” *IEEE Trans. Magn.*, vol. 35, no. 3, pp. 1986–2000, May 1999.
- [174] K. Hameyer and M. Nienhaus, “Electromagnetic acutators - current developments and examples,” *Actuator - International Conference and Exhibition on New Actuators and Drive Systems*. Bremen, Germany, 2002.
- [175] “BEI Kimco Model # LA16-19-001A.” [Online]. Available: [http://www.beikimco.com/product.php?part\\_id=LA16-19-001A](http://www.beikimco.com/product.php?part_id=LA16-19-001A).

- [176] “H2W Model # NCM03-20-089-2LB.” [Online]. Available: <http://www.h2wtech.com/Pages/Product-Detail.aspx?prodid=230>.
- [177] W. Kim, S. Verma, and H. Shakir, “Design and precision construction of novel magnetic-levitation-based multi-axis nanoscale positioning systems,” *Precis. Eng.*, vol. 31, pp. 337–350, 2007.
- [178] S. Verma, K. Won-jong, and J. Gu, “Six-axis nanopositioning device with precision magnetic levitation technology,” *IEEE/ASME Trans. Mechatronics*, vol. 9, no. 2, pp. 384–391, 2004.
- [179] S. T. Smith, D. G. Chetwynd, and S. Harb, “A simple two-axis ultraprecision actuator,” *Rev. Sci. Instrum.*, vol. 65, no. 4, p. 910, 1994.
- [180] K. Shirey, S. Banks, R. Boyle, and R. Unger, “Design and qualification of the AMS-02 flight cryocoolers,” *Cryogenics (Guildf.)*, vol. 46, pp. 143–148, 2006.
- [181] M. Watada and K. Yanashima, “Improvement on characteristics of linear oscillatory actuator for artificial hearts,” *IEEE Trans. Magn.*, vol. 29, no. 6, pp. 3361–3363, 1993.
- [182] T. Morcos, “The Straight Attraction: Part Two,” *Motion Control*, pp. 24–28, 2000.
- [183] G. W. McLean, “Review of recent progress in linear motors,” *IEE Proc. B Electr. Power Appl.*, vol. 135, no. 6, pp. 380–416, 1988.
- [184] B. Yao, Y. Hong, C. Hu, and Q. Wang, “Precision motion control of linear motor drive systems for micro/nano-positioning,” in *2007 First International Conference on Integration and Commercialization of Micro and Nanosystems*, 2007, no. 50528505, pp. 1605–1614.
- [185] W. Kim and B. Murphy, “Development of a novel direct-drive tubular linear brushless permanent-magnet motor,” *Int. J. Control. Autom. Syst.*, vol. 2, no. 3, pp. 279–288, 2004.
- [186] S. Jang, S. Lee, and I. Yoon, “Design criteria for detent force reduction of permanent-magnet linear synchronous motors with Halbach array,” *IEEE Trans. Magn.*, vol. 38, no. 5, pp. 3261–3263, Sep. 2002.
- [187] J. Choi, H. Kim, and S. Jang, “Thrust calculations and measurements of cylindrical linear actuator using transfer relations theorem,” *IEEE Trans. Magn.*, vol. 44, no. 11, pp. 4081–4084, 2008.

- [188] Z. Zhu, P. Hor, and D. Howe, “Novel linear tubular brushless permanent magnet motor,” *Electr. Mach.*, no. 444, pp. 91–95, 1997.
- [189] H. Luo, J. Wu, and W.-S. Chang, “Minimizing thrust fluctuation in moving-magnet permanent-magnet brushless linear DC motors,” *IEEE Trans. Magn.*, vol. 43, no. 5, pp. 1968–1972, 2007.
- [190] X. Lu, “6D direct-drive technology for planar motion stages,” *CIRP Ann. Technol.*, vol. 61, no. 1, pp. 359–362, 2012.
- [191] M. Tano, W. Gao, S. Kiyono, Y. Tomita, K. Makino, and H. Morita, “Precision positioning of a Sawyer motor-driven stage by a surface encoder,” *J. Phys. Conf. Ser.*, vol. 13, pp. 90–93, Jan. 2005.
- [192] F. Claeysen, O. Sosnicki, and G. Magnac, “Moving Iron Controllable Actuators.” Cedrat Technologies SA.
- [193] N. Bianchi, S. Bolognani, and F. Tonel, “Design criteria of a tubular linear IPM motor,” in *IEMDC 2001. IEEE International Electric Machines and Drives Conference*, 2001, pp. 1–7.
- [194] B. Gysen and E. Lomonova, “Analytical and numerical techniques for solving Laplace and Poisson equations in a tubular permanent-magnet actuator: Part I. Semi-analytical framework,” *IEEE Trans. Magn.*, vol. 44, no. 7, pp. 1751–1760, 2008.
- [195] M. Godkin, “Linear voice coil actuator as a bi-directional electromagnetic spring,” *US Pat. 8,193,885*, 2012.
- [196] A. Goto, T. Okamoto, and A. Ikariga, “A new linear actuator utilizing flux concentration type permanent magnet arrangement,” in *2010 International Conference on Electrical Machines and Systems (ICEMS)*, 2010, pp. 1500 – 1505.
- [197] Y. Hirabayashi, T. Oyama, S. Saito, and H. Sohno, “Moving magnet-type actuator,” *US Pat. 5,434,549*, 1995.
- [198] S. Yoon, I. Jung, and K. Kim, “Dynamic analysis of a reciprocating linear actuator for gas compression using finite element method,” *IEEE Trans. Magn.*, vol. 33, no. 5, 1997.
- [199] D. Ebihara and M. Watada, “Development of a single-winding linear oscillatory actuator [artificial heart application],” *IEEE Trans. Magn.*, vol. 28, no. 5, pp. 3030–3032, 1992.

- [200] S. Braune and S. Liu, "Design of a novel moving magnet linear motor for use as a valve actuator," in *31st Annual Conference of the IEEE Industrial Electronics Society*, 2005, pp. 2041–2046.
- [201] R. Karunanithi, S. Jacob, A. S. Gour, C. Damu, M. Das, and A. S. Singh Gour, "Development of moving magnet type linear motor for dual piston compressor for pulse tube cryocooler," in *AIP Conf. Proc. (USA)*, 2012, vol. 525, pp. 525–531.
- [202] W. Wang and X. Yong-Ming, "Research on Linear Motor for Linear Compressor," *Adv. Mater. Res.*, vol. 383–390, pp. 1350–1355, 2012.
- [203] Q. Li, F. Ding, and C. Wang, "Novel bidirectional linear actuator for electrohydraulic valves," *Magn. IEEE Trans.*, vol. 41, no. 6, pp. 2199–2201, 2005.
- [204] K. H. Kim and D. G. Gweon, "Design of a bidirectional actuator for a nanopositioning system with a permanent magnet and an electromagnet," *Rev. Sci. Instrum.*, vol. 76, no. 12, pp. 5–8, 2005.
- [205] R. Carreras and T. Froeschle, "Permanent magnet transducing," *US Pat. 5,216,723*, 1993.
- [206] Z. Li and B. R. Varlow, "Optimal design of autorecloser electromagnetic actuator," *Electr. Power Appl. IEE Proc.*, vol. 147, no. 5, p. 431, 2000.
- [207] N. Takanashi and T. Honda, "A Metal-Based High-Resonant-Frequency Optical Scanner with a Moving-Magnet Actuator for Non-Resonant Large-Angle Scanning," *SID Symp. Dig. Tech. Pap.*, vol. 42, no. 1, pp. 547–550, 2011.
- [208] T. Yamada, S. Koganezawa, K. Aruga, and Y. Mizoshita, "A high-performance and low-profile moving-magnet actuator for disk drives," *Ieee Trans. Magn.*, vol. 30, no. 6, pp. 4227–4229, 1994.
- [209] S. X. Chen, R. Wood, and Y. Mah, "Design of a dual moving-magnet motor for a hard disk drive actuator," in *1997 IEEE International Magnetism Conference (INTERMAG '97), 1-4 April 1997*, 1997, 5th ed., vol. 33, pp. 3871–3873.
- [210] J. Corey and G. Yarr, "Linear electrodynamic machine," *US Pat. 5,389,844*, 1995.
- [211] N. Vitale, "Permanent magnet linear electromagnetic machine," *US Pat. 4,937,481*, 1990.
- [212] W. Jiabin, D. Howe, and L. Zhengyu, "Design optimization of short-stroke single-phase tubular permanent-magnet motor for refrigeration applications," *IEEE Trans. Ind. Electron.*, vol. 57, no. 1, pp. 327–334, 2010.

- [213] X. Chen, Z. Q. Zhu, and D. Howe, "Modeling and analysis of a tubular oscillating permanent magnet actuator," in *2008 IEEE Industry Applications Society Annual Meeting*, 2008.
- [214] M. G. Lee, S. Q. Lee, and G. Dae-Gab, "Analysis of Halbach magnet array and its application to linear motor," *Mechatronics*, vol. 14, pp. 115–128, 2004.
- [215] M. Godkin, "The latest developments in the field of voice coil actuators," in *11th European Space Mechanisms and Tribology Symposium*, 2005, 591st ed., pp. 341–345.
- [216] C. Petrescu and R. Olaru, "Study of a mini-actuator with permanent magnets," *Adv. Electr. Comput. Eng.*, vol. 9, no. 3, pp. 54–57, 2009.
- [217] M. Godkin, "Linear voice coil actuator with compensating coils," *US Pat. 6,713,904*, 2004.
- [218] "H2W Technologies, Inc. Product Model # NCM01-07-001-2X," pp. 6–7.
- [219] R. Clark and D. Smith, "Design optimisation of moving-magnet actuators for reciprocating electro-mechanical systems," *IEEE Trans. Magn.*, vol. 31, no. 6, pp. 3746–3748, 1995.
- [220] J. Mitchell, J. Wang, R. Clark, and D. Howe, "Analytical modeling of the air-gap field in reciprocating moving-magnet actuators," *J. Magn. Magn. Mater.*, vol. 276, pp. e1783–e1785 Analytical, 2004.
- [221] S. Markon, E. Kazan, and A. Onat, "Moving magnet type linear motor," *US Pat. 8,502,421*, 2013.
- [222] M. Godkin and J. Kimble, "Moving coil linear actuator with interleaved magnetic circuits," *US Pat. 4,808,955*, 1989.
- [223] A. Hirata, "Voice coil linear actuator, apparatus using the actuator, and method for manufacturing the actuator," *US Pat. 6,856,049*, 2005.
- [224] D. Gillott and J. Simes, "PERMANENT MAGNET TRANSLATIONAL MOTOR WITH AUXILIARY ELECTROMAGNET," *US Pat. 3,863,082*, 1975.
- [225] D. Adler, "Linear actuator," *US Pat. 4,075,517*, 1978.
- [226] F. Morinigo and K. Stuart, "Ferromagnetic wire electromagnetic actuator," *US Pat. 5,309,050*, 1994.

- [227] J. Bourque and L. Wedman, "Linear positioning system," *US Pat. 4,456,934*, 1984.
- [228] M. Sanada and S. Morimoto, "Experimental Verification of Thrust Improvement in Voice Coil Linear Actuator using Combined Wire of Copper and Iron," *Conf. Rec. 2007 IEEE Ind. Appl. Conf. 2007. 42nd IAS Annu. Meet.*, pp. 490–494, 2007.
- [229] N. Sharron and B. S. Jr, "Electric generator with two rotors," *US Pat. 4,612,470*, 1986.
- [230] R. Calderwood and E. Stiles, "Audio speaker with graduated voice coil windings," *US Pat. 7,492,918*, 2009.
- [231] G. Aubert, "Coreless solenoidal magnet," *US Pat. 4,808,956*, 1989.
- [232] H. Lu, J. Zhu, and Z. Lin, "A Miniature Short Stroke Linear Actuator — Design and Analysis," *IEEE Trans. Magn.*, vol. 44, no. 4, pp. 497–504, 2008.
- [233] A. Morcos and A. Morreale, "Performance enhancement of closed-ended magnetic circuits by selective removal of material," *US Pat. 5,677,963*, 1997.
- [234] M. A. Moser, "Shorted turn effects in rotary voice coil actuators," *IEEE Trans. Magn.*, vol. 32, no. 3, pp. 1736–1742, May 1996.
- [235] A. Brende and R. Luoma, "Linear moving coil actuator," *US Pat. 4,439,699*, 1984.
- [236] R. Clark, G. Jewell, and D. Howe, "Dynamic modeling of tubular moving-magnet linear actuators," *J. Appl. Phys.*, vol. 93, no. 10, pp. 8787–8789, 2003.
- [237] J. W. Jansen, E. a. Lomonova, and J. M. M. Rovers, "Effects of eddy currents due to a vacuum chamber wall in the airgap of a moving-magnet linear actuator," *J. Appl. Phys.*, vol. 105, no. 7, 2009.
- [238] J. M. M. Rovers, J. Achterberg, M. J. C. Ronde, J. W. Jansen, J. C. Compter, E. A. Lomonova, C. M. M. van Lierop, and M. J. G. van den Molengraft, "The deformation of the moving magnet plate of a commutated magnetically levitated planar actuator," *Mechatronics*, vol. 23, no. 2, pp. 233–239, Feb. 2013.
- [239] G. K. Parmar, "Dynamics and Control of Flexure-based Large Range Nanopositioning Systems," University of Michigan, 2014.
- [240] J. Sim, "Voice coil motor," *US Pat. 5,177,383*, 1993.
- [241] "Technical Data Book." MWS Wire Industries.

- [242] “MAGCRAFT Permanent Magnet Selection and Design Handbook.” Magcraft.
- [243] “High Performance Permanent Magnets.” Magnet Sales & Manufacturing Inc.
- [244] D. Hyre, “Following Load Lines to your Operating Points, an engineer’s Reluctance to optimize: Coercing the most out of your Magnets.” Dyne Analytics.
- [245] G. P. Gogue and J. J. Supak Jr., “G2 Consulting Chapter 11: Actuators.” [Online]. Available: <http://www.consult-g2.com/>.
- [246] “Temperature and Neodymium Magnets.” [Online]. Available: <http://www.kjmagnetics.com/blog.asp?p=temperature-and-neodymium-magnets>.
- [247] J. M. D. Coey, *Rare-Earth Iron Permanent Magnets*. New York: Oxford University Press, 1996.
- [248] P. Patt, “Frictionless motor material testing,” *US Pat. 6,405,599*, 2002.
- [249] “Application Guide: Linear Motors.” Aerotech Inc.
- [250] A. C. Smith, “Magnetic forces on a misaligned rotor of a PM linear actuator,” in *Int. Conf. Elec. Mach.*, 1990, pp. 107–108.
- [251] J. S. Freudenberg Looze, D. P., *Frequency Domain Properties of Scalar and Multivariable Feedback Systems*, vol. 70, no. 1. Berlin : Springer-Verlag, 1988, p. 77.
- [252] S. Garrett, R. Keolian, and R. Smith, “High-efficiency moving-magnet loudspeaker,” *US Pat. 6,307,287*, 2001.
- [253] S. Awtar and A. Slocum, “Constraint-based design of parallel kinematic XY flexure mechanisms,” *Trans. ASME J. Mech. Des.*, vol. 129, no. 8, pp. 816–830, 2007.
- [254] S. Awtar, A. H. Slocum, and E. Sevincer, “Characteristics of beam-based flexure modules,” *Trans. ASME. J. Mech. Des.*, vol. 129, no. 6, pp. 625–639, 2007.
- [255] “RELM high accuracy linear encoder.” Renishaw.
- [256] H. C. Rotors, *Electromagnetic devices*. Wiley, 1941.
- [257] B. L. J. Gysen, K. J. Meessen, J. J. H. Paulides, and E. A. Lomonova, “General formulation of the electromagnetic field distribution in machines and devices using fourier analysis,” *Ieee Trans. Magn.*, vol. 46, no. 1, pp. 39–52, 2010.

- [258] D. Trumper, W. Kim, and M. Williams, "Design and analysis framework for linear permanent-magnet machines," *IEEE Trans. Ind. Appl.*, vol. 32, no. 2, 1996.
- [259] "LA16-16-000A Datasheet." Bei Kimko Magnetics.
- [260] "RX054-N52 Ring Magnet Datasheet." K&J Magnetics.
- [261] P. Klapetek, M. Valtr, and M. Matula, "A long-range scanning probe microscope for automotive reflector optical quality inspection," *Meas. Sci. Technol.*, vol. 22, no. 9, Sep. 2011.
- [262] S. Box, "Design and Temperature Control of Nanometre Precision," *Mikroniek*, vol. 48, no. 3, pp. 12–16, 2008.
- [263] R. Lamers, "Keep your cool in precision machine design," *Mikroniek*, no. 3, pp. 27–33, 2011.
- [264] T. a. M. Ruijl, "Thermal effects in precision systems: Design considerations, modelling, compensation and validation techniques," *Diam. Light Source Proc.*, vol. 1, no. MEDSI-6, p. e60, Apr. 2011.
- [265] B. Gashi, "Meeting Report of the First Meeting of the Special Interest Group on Thermal Effects in Precision Engineering," in *7th euspen International Conference*, 2007, no. December 2006.
- [266] J. Bryan, "International Status of Thermal Error Research," *CIRP Ann. - Manuf. Technol.*, vol. 39, no. 2, pp. 645–656, 1990.
- [267] R. Lamers, "When Precision Cannot Stand the Heat," *Mikroniek*, vol. 50, no. 5, pp. 39–43, 2010.
- [268] P. Klapetek, M. Valtr, and M. Matula, "A long-range scanning probe microscope for automotive reflector optical quality inspection," *Meas. Sci. Technol.*, vol. 22, no. 9, p. 094011, Sep. 2011.
- [269] "Eutectic Ice Packs." [Online]. Available: <http://www.kegworks.com/eutectic-ice-packs-898-p21720>.
- [270] F. Incropera, D. Dewitt, T. Bergman, and A. Lavine, *Fundamentals of Heat and Mass Transfer*, 6th ed. John Wiley & Sons, 2007, p. 589.
- [271] H. Xie and A. Ali, "The use of heat pipes in personal computers," in *IEEE 1998 InterSociety Conference on Therind Phenomena*, 1998, pp. 442–448.

- [272] “Application Note: How to select a heat pipe.” Enertron, Inc.
- [273] M. T. Thompson, “Practical issues in the use of NdFeB permanent magnets in maglev, motors, bearings, and eddy current brakes,” *Proc. IEEE*, vol. 97, no. 11, pp. 1758–1767, 2009.
- [274] R. V. Jones, *Instruments and Experiences: Papers on Measurement and Instrument Design*. New York, NY, USA: John Wiley & Sons, 1988.
- [275] Smith S.T., *Flexures: Elements of Elastic Mechanisms*. Gordon and Breach Science Publishers, 2000.
- [276] S. Awtar, “Synthesis and Analysis of Parallel Kinematic XY Flexure Mechanisms. Chapter 7. Experimental Measurements,” 2004.
- [277] S. Hiemstra, D., Parmar, G., Welch, C., and Awtar, “Electromagnetic Actuators and Component Designs Therefor,” *US Appl. Number 61801212*, 2013.
- [278] C. M. Kozierok, “Construction and Operation of the Hard Disk.” [Online]. Available: [http://www.pcguide.com/ref/hdd/op/z\\_000874voicecoil.jpg](http://www.pcguide.com/ref/hdd/op/z_000874voicecoil.jpg).

## APPENDIX A: Analytical MMA model MATLAB code

```
%% Determining flux density in coil gap for a cylindrical MMA
% David B. Hiemstra
% August 10, 2012
% Please email me at davidbh@umich.edu for the FEAResults data set

clear all
clc
format('short')
load FEAResults %Import all FEA data sets

%% Constants
mu0=1.25663706*10^(-6);%permeability of free space [m kg s^-2 A^-2]
muAir=mu0;%air
mu1010=825.9*mu0;%AISI 1010
mu1018=529*mu0;%AISI 1018
mum=1.0998*mu0;%NeFeB mag

%% Magnet Properties
Br=1.23;%remanence [T]

%% Actuator Geometry
%all units are meters [m]

% FEA Data sets
% FEA_B_tg3tp7rm20tm15
% FEA_B_tg3tp7rm20tm30
% FEA_B_tg6tp7rm16tm35
% FEA_B_tg7tp7rm12tm35
% FEA_B_tg7tp7rm16tm19
% FEA_B_tg7tp7rm16tm35
% FEA_B_tg7tp7rm20tm35
% FEA_B_tg7tp7rm8tm35
% FEA_B_tg10tp7rm16tm35
% FEA_B_tg10tp7rm20tm20
% FEA_B_tg11tp30rm16tm25
% FEA_B_tg11tp30rm16tm60
% FEA_B_tg14tp7rm16tm35
% FEA_B_tg18tp7rm16tm35
% FEA_B_tg25tp7rm20tm15

FEAfilename='FEA_B_tg14tp7rm16tm35'; %Specify which FEA data to compare with
```

```

currentFEAdata=eval (FEAfilename);
tgpos=strfind (FEAfilename, 'tg');
tppos=strfind (FEAfilename, 'tp');
rmpos=strfind (FEAfilename, 'rm');
tmpos=strfind (FEAfilename, 'tm');

tg=str2num (FEAfilename ((tgpos+2):(tppos-1)))/1000; %Extracts geometry values from
file name
tp=str2num (FEAfilename ((tppos+2):(rmpos-1)))/1000;
rm=str2num (FEAfilename ((rmpos+2):(tmpos-1)))/1000;
tm=str2num (FEAfilename ((tmpos+2):(tmpos+3)))/1000;

rp=rm;%pole piece radius
%rm=0.01588;%magnet radius
%tm=0.035;%magnet thickness
%tp=0.007;%pole piece thickness
%tg=0.014;%gap thickness
tclear=0.0005;%clearance gap thickness
tb=0.0015;%bobbin thickness
OCl=0.140;%outer core length
OCt=0.01;%outer core thickness
OCri=rp+tg;%outer core inner radius
OCro=OCri+OCt;%outer core outer radius
OCext=0.100;%outer core overhang

r=currentFEAdata(:,1)/1000;% x-values for plots

if tg >= tm/2
    display('tg >= tm/2')
end

%% Constants for reluctance calculations
a=0; %length along pole piece where flux spreads out for given tg
b=0; %length along outer core inner wall where the spreading flux hits for given tg
fs2=b-a; %flux spread

if a >= tp/2
    display('a >= tp/2')
    fs1=tp/2;
else
    fs1=a;
end

Rmag=tm./ (mum*pi*rm.^2);%magnet reluctance
Rcore=(tm+tp) ./ (mu1010*pi*(OCro.^2-OCri.^2));%outer core reluctance
Rpole=rp./ (mu1010*2*pi*rp*tp);%pole piece reluctance

%% Reluctances
%% R1
if fs1==tp/2
    R1=inf;
    A1=0;

```

```

else
    R1=log((rp+tg)./rp) / (2*pi*(tp-2*fs1)*muAir);
    A1=(tp-2*fs1).*2.*pi.*(rp+r);
end

%% R2 NOT USED!!

V2=2*pi*(tg*(rp*fs2/2+rp*fs1)+tg^2*(fs2/3+fs1/2));
%L2=(tg+sqrt((tg^2)+(fs2)^2))/2;
L2=sqrt(tg*sqrt(tg^2+fs2^2));
R2=L2^2 / (muAir*V2);

A2=2.*pi.*(rp+r).(fs2.*r/tg+fs1);

%% R3
x3=sqrt(tg.^2-(tg-r).^2)-fs2.*r./tg;
A3=2.*pi.*(rp+r).*x3;

V3=pi*tg^2*(pi/2*(rp+tg)-2/3*tg)-pi*fs2*(rp*tg+2/3*tg^2);

%L3=((pi/2)*tg+sqrt((tg^2)+(d)^2))/2;
L3=sqrt((pi/2)*tg*sqrt((tg^2)+fs2^2));
R3=L3^2 / (muAir*V3);

%% R4
e=rp;
V4=pi*((OCri*pi/2)*(tg+e)^2-(2/3)*(tg+e)^3)...
    -pi*((OCri*pi/2)*(tg)^2-(2/3)*(tg)^3);
%L4=(pi/4)*(2*tg+e);
L4=(pi/2)*sqrt(tg*(tg+e));
R4=L4^2 / (muAir*V4);

%% R5
if tg >= tm/2
    fs2prime=tm/2;
else
    fs2prime=tg;
end

x5=sqrt(tg.^2-(tg-r).^2); %make sure to change from 3!!
A5=2.*pi.*(rp+r).*x5;

V5=pi*tg^2*(pi/2*(rp+tg)-2/3*tg); %make sure to change from 3!!

%L3=((pi/2)*tg+sqrt((tg^2)+(d)^2))/2;
L5=sqrt((2*pi*tg/4)*(tg));
R5=L5^2 / (muAir*V5);

%% R7
x7=sqrt(tg^2+(tm/2)^2);
r7=x7-tg;

```

```

V7=2*pi*(rp+4*r7/(3*pi))*pi*r7^2/4;
L7=sqrt(((2*pi*r7)/4)*(tm/2-r7));
R7=L7^2 / (muAir*V7)/(r7/tm); %divided by r7/tm because only portion of magnet
is used

%% Circuit calculations
Rair=1/(1/R1+1/R2+1/R3+1/R4+1/R5+1/R7);
Rcircuit=Rair+Rmag/2+Rpole+Rcore/2;

MMFtotal=(Br*tm)/mum;%magnetomotive force [A-turns]
MMFcircuit=MMFtotal/2;

phi_total=(MMFcircuit)./Rcircuit;%flux [Wb]

MMFdropMag=phi_total*(Rmag/2);%find individual MMF drops
MMFdropAir=phi_total*Rair;
MMFdropPole=phi_total*Rpole;
MMFdropCore=phi_total*(Rcore/2);

phi1=MMFdropAir/R1;
phi2=MMFdropAir/R2;
phi3=MMFdropAir/R3;
phi4=MMFdropAir/R4;
phi5=MMFdropAir/R5;
phi7=MMFdropAir/R7;

%% Flux densities
B=(phi1+phi3+phi5)./(A1+A3+A5);
B2=(phi1)./(A1);

perdiff=100*abs(B(:)-currentFEAdata(:,2))./B(:);% % difference b/t CF and FEA
MeanBMinBMaxB = [mean(perdiff) min(perdiff) max(perdiff)]

perdiff=100*abs(B2(:)-currentFEAdata(:,2))./B2(:);% % difference b/t CF and FEA
MeanBMinBMaxB2 = [mean(perdiff) min(perdiff) max(perdiff)]

%plots %plot CF vs. FEA

%% Plot
plot(r*1000,B,'k-','LineWidth',1.5)
hold on
plot(r*1000,B2,'b-','LineWidth',1.5)

plot(r*1000,currentFEAdata(:,2),'k--','LineWidth',1.5)
%hold off

xlabel('Distance from pole piece (mm)')
ylabel('Flux density (T)')
legend('Closed Form Regions 1-3','CF Region 1','FEA')
%axis([0 7 0 1]);

```

```

%% Coil constants
I=5;%current [A]
dwire=0.00072;%wire diameter [m]
N=7;%number of stacks
stroke=0.006;%actuator stroke length [m]
n=floor((2*stroke+tp)/dwire);%turns per stack
coilength=2*stroke+tp;%coil length [m]

%% Calculate force on coils -- tentative
% plot(gapIterations-rp, (B1_newCircuit))
% B1_newCircuit=(phi1+phi2)./(Agap1+Agap2);

% plot(gapIterations-rp,B1,FEAresults(:,1)/1000,FEAresults(:,2))
% figure(1)
% plot(gapIterations-rp,B1,gapIterations-rp,FEAresults(:,2))
% hold on
% xlabel('Distance from pole piece (m)')
% ylabel('Flux density (T)')

% y(i) = B1(1);

% end
%
% figure(2)
% plot(x,y);
%
% perdiff_newCircuit=100*abs(B1_newCircuit(:)-FEAresults(:,2))./B1_newCircuit(:);

% %%
% %lower geometric limit [m]
% lower=0.01;
% %upper geometric limit [m]
% upper=0.04;
% %step size [m]
% step=0.001;
% %iterations
% iterations=(upper-lower)/step;
%
% %iteration vector
% x=(lower:step:upper);
%
% % for i=1:length(x)
% %
% % tm=x(i);

% %-----Flux density-----
%
% %%
% %*****tweak/change*****
% %Flux spread approximation (thickness direction)

```

```

% slope=( (OClength-tp) /2) /tg;
% %%
%-----
% %Effective thickness as a function of stack number
% tpEff=zeros(1,N);
% for q=1:N
%     tpEff(q)=tp+2*slope*(tclear+tb+((2*q-1)/2)*dwire);
% end
%
% % Area of the gap for each stack number
% Agap=zeros(vecLength,N);
% AgapNoFringe=zeros(vecLength,N);
%
% for i=1:N, p=1:vecLength;
%     Agap(p,i)=2*pi*(rp(p)+tclear+tb+((2*i-1)/2)*dwire)*tpEff(i);
%     AgapNoFringe(p,i)=2*pi*(rp(p)+tclear+tb+((2*i-1)/2)*dwire)*tp;
% end
%
% phiMat=zeros(vecLength,N);
% phiInv=phi';
%
% for k=1:N
%     phiMat(:,k)=phiInv;
% end
%
% Bgap=phiMat./Agap;
% BgapNoFringe=phiMat./AgapNoFringe;
%
% Bcompare=(Bgap(:,3)+Bgap(:,4))/2;
% BcompareNoFringe=(BgapNoFringe(:,3)+BgapNoFringe(:,4))/2;
%
% -----Force-----
% %%
%-----
% %*****tweak/change*****
% %portion of coils exposed to flux
% expo=floor((coilength/2)/dwire);
%
% %average "flux angle"
% theta=1;
% %%
%-----
% %Force as a function of stack number
% forceStackNoB=zeros(vecLength,N);
%
% for i=1:N, p=1:vecLength;
%     forceStackNoB(p,i)=2*pi*(rp(p)+tclear+tb+((2*i-1)/2)*dwire)*N*expo*I*theta;
% end
%
% forceStack=forceStackNoB.*Bgap;
% forceStackNoFringe=forceStackNoB.*BgapNoFringe;
%
% %Net force due to all stacks

```

```

% forceNet=sum(forceStack,2);
% forceNetNoFringe=sum(forceStackNoFringe,2);
%
% -----Plot-----
%
% figure(1)
% plot(rm,Bcompare,rm,BcompareNoFringe)
% title('Effect of magnet radius on flux density at the middle
stack','fontsize',12)
% xlabel(varLabel)
% ylabel('Flux density at the middle stack (T)')
%
% figure(2)
% plot(rm,forceNet,rm,forceNetNoFringe)
% title('Effect of magnet radius on net force','fontsize',12)
% xlabel(varLabel)
% ylabel('Net force at 5 A (N)')
%
% display('Force of current design (N)')
% forceNet(16)

```

## APPENDIX B: Analytical thermal model for selection of heat pipes

```
%Thermal Model for selection of heat pipes
%David B. Hiemstra
%August 2012
%Thermal Model
clc;
clear all;

%% Geometry
rm = 12.7/1000;
tc = 15/1000;
ty = 7.6/1000;
th = 12.7/1000;
tb = tc+ty;
rc = rm+tc;
ry = rm+tb;
rh = rm+tb+th;
lcs = 13.2/1000;
lc = 26/1000;
lbe = 12.7/1000;
g = 1/1000;

lhb = 0.1651/2; %half length of heat box struts
% Ahb = 0.0075; %4*25.4/1000 * 0.0127; % actual thickness 0.0127; %cross sectional
area of heat box struts
Ahb = (12.7/1000-6/1000)*(101.6/1000);
Aconv = 12.7/1000*(101.6/1000);

lhp = 270/1000; %-0.091440; 174.75mm 7*25.4/1000; %250/1000; %0.0795; %
rhp = 3/1000;

%% Constants
ks = 50; %conductivity steel W/m/K
kAl = 170; %conductivity al
ka = 0.024; %conductivity air
khp = 3200; %conductivity heat pipe
kp = 0.147; %kplastic
kw = 0.569; %kwater
qcoils = 20; %W

%% Rbobbin + Rhousing = Ractuator
Rb1 = log(ry/rm)/(2*pi*kAl*lbe);
Rb2 = log(rc/rm)/(2*pi*kAl*lcs);
```

```

Ry1 = log(ry/rc)/(2*pi*ks*lc);
Ry2 = log(ry/rc)/(2*pi*ks*lcs);
Rg1 = log(ry/(ry-g))/(2*pi*ka*lc);
Rg2 = log(ry/(ry-g))/(2*pi*ka*lcs);
Rh1 = log(rh/ry)/(2*pi*kAl*lbe);
Rh2 = log(rh/ry)/(2*pi*kAl*lc);
Rh3 = log(rh/ry)/(2*pi*kAl*lcs);

Ra = 1/(2/(Rb1+Rh1)+2/(Ry1+Rg1+Rh2)+1/(Rb2+Ry2+Rg2+Rh3));

%% Rheatpipe
Rhp = lhp/(khp*pi*rhp^2);

%% Rheatsink

% hiecpack = 100; %50-1000 for free conv
% Licepack = 6*25.4/1000;
% Hiecpack = 4*25.4/1000;
% Wicepack = 1*25.4/1000;
% Aicepack = 2*Licepack*Hiecpack + 2*Wicepack*Hiecpack + 2*Licepack*Wicepack;
% Rconv2 = 1/(hiecpack*Aicepack);%convection to icepack

% hair = 10; %2-25 free conv gas
% Lbox = 7*25.4/1000;
% Hbox = 8.25*25.4/1000;
% Wbox = 5.5*25.4/1000;
% Abox = 2*Lbox*Hbox + 2*Wbox*Hbox + 2*Lbox*Wbox;
% Rwalls = 0.33/Abox; %Km2/W
% Rconv1 = 1/(hair*Abox);
% R1 = Rwalls + Rconv1;
% R2 = Rconv2;
% R3 = Rmma + Rbridge;
% Tatm = 0;
% Ticepack = 0;

ww1 = 0.25*25.4/1000;
wp = 0.125*25.4/1000;
wAl = 0.5*25.4/1000;
W = 1*25.4/1000;
L = 6*25.4/1000;
H = 4*25.4/1000;

RA1 = wAl/2/(kAl*H*L/2);
Rp = wp/(kp*H*L/2);
Rw1 = ww1/(kw*H*L/2);
Rhs = (RA1 + Rp + Rw1)/2;

%% Totals
Ticepacks = 0;
n = 8; %number heat pipes
Rtms = (Rhp + Rhs)/n;
Tcoils = qcoils*(Ra + Rtms)+Ticepacks

```